Development, testing, and ocean mapping application of three-dimensional baroclinic hydrodynamic ocean modeling at a variety of scales

by

Ahmadreza Alleosfour

Bachelor of Science, Persian Gulf University, 2005
Master of Science, Tarbiat Modares University, 2008

A Dissertation Submitted in Partial Fulfillment
of the Requirements for the Degree of

Doctor of Philosophy

in the Graduate Academic Unit of Geodesy and Geomatics Engineering

Supervisor: Ian Church, Ph.D., Geodesy and Geomatics Engineering.

Examining Board: John Hughes Clarke, Ph.D., Geodesy and Geomatics Engineering
Robbie Kingdon, Ph.D., Geodesy and Geomatics Engineering
Kevin Wilcox, Ph.D., Mechanical Engineering

External Examiner: Katleen Robert, PhD, School of Ocean Technology, Fisheries and Marine Institute, Memorial University

This dissertation is accepted by
the Dean of Graduate Studies

THE UNIVERSITY OF NEW BRUNSWICK

December 2024

©Ahmadreza Alleosfour, 2024

ABSTRACT

To investigate the improvement in representing the general circulation and baroclinic condition of the Bay of Fundy and Minas Basin, two high-resolution 3D baroclinic hydrodynamic models have been developed using Finite-Volume Community Ocean Model (FVCOM). The effect of surface forcing resolution is assessed by prescribing two commonly used atmospheric forcing models in the region.

The model simulations are validated against the available observations and collected Conductivity, Temperature, and Depth (CTD) data during a benthic habitat campaign in July 2018, the tidal constituents, Sea Surface Temperature (SST) data from satellite, and historical published current meter data. The models show a good agreement in capturing the tide both in the Bay of Fundy and Minas Basin and represented some improvement against the operational models in the region. In addition, the improvement in representing the baroclinic condition of the Bay both at the surface and water column is reported. The coarse prescribed surface forcing resulted in a warmer surface temperature in the Bay, while the higher resolution one generated a better agreement with the observations.

Also, the model simulations have been implemented in an innovative approach to evaluate the partitioning of the hydrographic survey domain and provide insight into the multibeam echosounder depth uncertainty due to using a synthetized CTD profile, based on different criteria and limitations of hydrographic survey vessels for both Minas Basin and Saint John Harbor.

DEDICATION

To my wife, for your unwavering support, encouragement, endless patience, and all the sacrifices you have made. Your love and belief in me have been my greatest strength.

To my parents and my in-laws, for your guidance, wisdom, and unconditional love. Your values and support have been the foundation upon which I have built my journey.

Last but not least, to my beautiful daughter, Sofia, whom I have yet to meet, you are my hope and inspiration. I dedicate this work to the future we will share and the dreams we will pursue together.

ACKNOWLEDGEMENTS

I would like to thank Dr. Ian Church for supervising this project and providing invaluable information, Dr. Susan Haigh for facilitating the model compilation and going over the concepts, and Dr. John Hughes Clarke for his insight on the improvement of the model applications.

The following people also provided me with essential information and help during my thesis.

- Dr. Craig Brown at Dalhousie University for supporting the fieldwork and providing invaluable feedback for my project.

- Serguei Vassilev at Digital Research Alliance of Canada, ACENET, for troubleshooting the model compilation on HPC.

- Everyone within the Ocean Mapping Group and the Department of Geodesy and Geomatics Engineering supported me during my study.

- ArcticNet and Amundsen Science for making a dream come true by being on-board of CCGS Amundsen in the Arctic.

- COMREN for supporting me in going to the Canadian Hydrographic Conferences.

Table of Contents

ABSTRACT ii

DEDICATION iii

ACKNOWLEDGEMENTS iv

Table of Contents v

List of Tables viii

List of Figures xi

List of Symbols, Nomenclature or Abbreviations xviii

Chapter 1: Introduction 1

Chapter 2: Background 5

2.1 Study Area 5

2.1.1 Bay of Fundy 5

2.1.2 Minas Basin 12

2.2 Surface Forcing 13

2.3 Hydrography Survey Design 17

Chapter 3: Methodology 23

3.1 Bathymetry and Coastline 23

3.2 Three-dimensional Baroclinic Hydrodynamic Model 25

3.2.1 Finite-Volume Coastal Ocean Model 25

3.2.2 Mesh Generation 26

3.2.3 Surface Forcing 28

3.2.3.1 HRDPS 29

3.2.3.2 NARR 31

3.2.4 Model Initialization and Open Boundary Forcing 35

3.2.4.1 Bay of Fundy Model 36
3.2.4.2 Minas Basin Model 38
3.3 Model Calibration and Validation 40
3.3.1 Model Calibration of Bottom Roughness 40
3.3.2 Tidal Validation 41
3.3.2.1 Amplitude and Phase of Constituents 41
3.3.2.2 Tidal Current Ellipse 43
3.3.3 Baroclinic Validation 45
3.3.3.1 Skill Assessment for Surface Temperature Structure 45
3.3.3.2 Skill Assessment of the Vertical Structure 46
3.4 Hydrographic Survey Planning and Uncertainty 50
3.4.1 Sound Speed Error Estimation 51
3.4.2 Tide 57
3.4.3 Surface Currents 58
3.4.4 Weighted Criteria Matrix 59

Chapter 4: Analysis 66
4.1 Bay of Fundy 66
4.1.1 Model Calibrations 66
4.1.2 Model Validation- Currents 70
4.1.2.1 Predicted Tidal Currents 70
4.1.2.2 Water Column Variability with HRDPS Surface Forcing 72
4.1.2.3 Baroclinic Model Skill Assessment for Temperature 76
4.1.2.4 Baroclinic Model Skill Assessment for Salinity 80
4.1.2.5 Sea Surface Temperature Variability 83
4.1.3 Impact of Surface Forcing on the Ray-Tracing Error 91
4.2 Minas Basin Model 95
4.2.1 Model Calibration 95
4.2.2 Model Validation 98
4.2.2.1 Predicted Tidal Current 98
4.2.2.2 Sea Surface Temperature Variability in Minas Basin 99
4.2.2.3 Salinity and Temperature Variability in the Water Column 100

4.3 Hydrography Survey Planning 105
4.3.1 Saint John Harbor 105
4.3.2 Minas Basin 114

Chapter 5: Discussion 125

Chapter 6: Conclusion 137

References 140

Appendix A 156

Appendix B 179

Curriculum Vitae

List of Tables

Table 1. Data used in both the NCEP-DOE Global Reanalysis and in the North American Regional Reanalysis from Global Reanalysis 2 (GR2), Mesinger et al. 2006..... 33

Table 2. Data added or improved upon for the North American Regional Reanalysis from Mesinger et al. 2006..... 33

Table 3. Minimum bathymetry standards for the safety of navigation hydrographic survey,(*IHO-S-44_v_6.*)..... 52

Table 4. The model amplitude(m) and phase (Degree-local) comparison against the CHS published constituents and discrepancies (CHS-Model) for M_2 with a bottom coefficient of 0.001 and a minimum drag of 0.01..... 67

Table 5. The model amplitude(m) and phase (Degree-local) comparison against the CHS published constituents and discrepancies (CHS-Model) for N_2 with a bottom coefficient of 0.001 and a minimum drag of 0.01..... 68

Table 6. The model amplitude(m) and phase (Degree-local) comparison against the CHS published constituents and discrepancies (CHS-Model) for S_2 with a bottom coefficient of 0.001 and a minimum drag of 0.01..... 68

Table 7. The model amplitude(m) and phase (Degree-local) comparison against the CHS published constituents and discrepancies (CHS-Model) for K_1 with a bottom coefficient of 0.001 and a minimum drag of 0.01..... 69

Table 8. The model amplitude(m) and phase (Degree-local) comparison against the CHS published constituents and discrepancies (CHS-Model) for O_1 with a bottom coefficient of 0.001 and a minimum drag of 0.01..... 69

Table 9. Model data comparison of the depth-average tidal ellipse for M_2. The location of sites is in Figure 8 (Units of semi-major and minor are in m/s and the difference in angles are in degrees). 72

Table 10. Bottom layer temperature skill assessment for GOFS3.1, FVCOM_HRDPS, FVCOM_NARR, and GoMOFS against the 98 CTS casts. 78

Table 11. Middle layer temperature skill assessment for GOFS3.1, FVCOM_HRDPS, FVCOM_NARR, and GoMOFS against the 98 CTS casts. 79

Table 12. Surface layer temperature skill assessment for GOFS3.1, FVCOM_HRDPS, FVCOM_NARR, and GoMOFS against the 98 CTD casts. 80

Table 13. Bottom layer salinity skill assessment for GOFS3.1, FVCOM_HRDPS, FVCOM_NARR, and GoMOFS against the 98 CTD casts. 81

Table 14. Middle layer salinity skill assessment for GOFS3.1, FVCOM_HRDPS, FVCOM_NARR, and GoMOFS against the 98 CTD casts. 82

Table 15. Surface layer salinity skill assessment for GOFS3.1, FVCOM_HRDPS, FVCOM_NARR, and GoMOFS against the 98 CTD casts. 83

Table 16. The model Amplitude (m) and Phase (°, local) comparison against the CHS published constituents and discrepancies (CHS-Model) for M_2 with a bottom coefficient of 0.001m and minimum drag of 0.025. 95

Table 17. The model Amplitude(m) and Phase (°, local) comparison against the CHS published constituents and discrepancies (CHS-Model) for N_2 with a bottom coefficient of 0.001m and minimum drag of 0.025. 96

Table 18. The model Amplitude(m) and Phase (°, local) comparison against the CHS published constituents and discrepancies (CHS-Model) for S_2 with a bottom coefficient of 0.001m and minimum drag of 0.025. 97
Table 19. The model Amplitude(m) and Phase (°, local) comparison against the CHS published constituents and discrepancies (CHS-Model) for K_1 with a bottom coefficient of 0.001m and minimum drag of 0.025. 97
Table 20. The model Amplitude(m) and Phase (°, local) comparison against the CHS published constituents and discrepancies (CHS-Model) for O_1 with a bottom coefficient of 0.001m and minimum drag of 0.025. 97
Table 21. Model data comparison of the depth-averaged tidal ellipse for M_2. The location of sites is in Fig. 8 (Units of Semi-major and minor are in m/s and the difference in angles are in degrees). 98
Table 22. Model data comparison of the depth-averaged tidal ellipse for M_2 for the Bay of Fundy and Minas Basin model against the observations at C1 and C2. 99
Table 23. The RMSE (magnitude of bias) and AE (cold or warm bias) of temperature for the two model configurations for the upper and mouth of the Bay, were retrieved from Tables 10, 11, and 12. 131

List of Figures

Figure 1. Bay of Fundy and the location of Evandale Point (black star). 6

Figure 2. The three-bathymetry dataset in the model domain, a) where the pink domain is the CHS-NONA 100-m bathymetry, the dark blue domain is the Ocean Mapping Group bathymetry in the Saint John River, and the blue sections are digitized from CHS Charts. The figure at b) shows the resolution of CHS-NONNA 100-m in the Minas Basin. 24

Figure 3. Unstructured mesh generated by SMS and location of two high-resolution spots. 27

Figure 4. Mesh resolution for the Bay of Fundy model. 28

Figure 5.The computational domain for continental HRDPS (2.5 km in red), RDPS (10 km in blue), Gulf of St. Lawrence, and other experimental domains (in dashed blue), from Milbrandt et al. 2016. 30

Figure 6.The NARR domain and 32-km terrain elevation(m), from Mesinger et al. 2006. 32

Figure 7. The mesh resolution for the Minas Basin model. 38

Figure 8. Location of tidal constituent analysis for the Bay of Fundy and Minas Basin (blue circles)..... 42

Figure 9. The location of tidal current data (green circles) is used in Tables 7, 8, 20, and 21 (C1 to C9). 44

Figure 10. Location of moored current meters in the Bay of Fundy, Minas Basin, and Chignecto Bay, from Bedford Institute of Oceanography, from Godin, 1968. 44

Figure 11. SST definition by GHRSST group, from Minnet and Kaiser-Weiss, 2012. ... 46

Figure 12. CTD casts from DFO, WOD, and NSCC fieldwork during July and August 2018. The color-coded points represent the head (red), middle (green), and mouth of the Bay (blue) that are being used for baroclinic assessment of the model in the water column..... 48
Figure 13. Sound propagation in ocean layers retrieved from Li et al. 2018. 53
Figure 14. Constant sound speed ray tracing method, retrieved from Li et al. 2018..... 54
Figure 15. a) Sound speed profiles used for raytracing, one as the true CTD profile and the other as a synthesized profile, b) the absolute bias for depth, and c) horizontal bias, Masetti et al. 2017..... 55
Figure 16. Under-keel clearance definition. The UKC is the instantaneous under-keel clearance, T is the instantaneous water level, d is the vessel draft, h is the vessel heave, the CD is the Chart Datum, and Z is the sounding referenced to the CD..... 58
Figure 17. Predicted drift polygon, from Chenier et al. 2018..... 59
Figure 18. The weighted normalized depth higher than 5 meters at a one-time stamp. The dark red areas are regions with depths shallower than 5 meters, while the blue areas are deep parts. 63
Figure 19. The weighted normalized surface current speed lower than 1 m/s at a one-time stamp. The blue areas are the regions where the surface speed is less than one and close to zero (dark blue) and the red areas are very high surface current speed regions (close to or higher than 1 m/s)..... 63
Figure 20. The weighted normalized depth (>5 m) and surface current speed (<1 m/s) at the one-time stamp. The white areas are the places where the combination of both criteria does not satisfy values higher than 31. 64

Figure 21. The IHO order 1 results, based on using the sound speed profile from the open boundary node (orange node at the first time step as synthesized CTD). The blue area is accepted, red is rejected, and white areas are excluded from raytracing. 65
Figure 22.The percentage of depth error for using the sound speed profile at the open boundary node (at the first time step). The dark brown area is excluded from the error calculation since it did not satisfy the weight criteria. 65
Figure 23. The temperature (top) and salinity (bottom) from FVCOM_HRDPS and FVCOM_NARR comparison against CTD cast at the head of the Bay of Fundy. The first column (a), second (b), and third (c) columns represent the lowest, medium, and highest RMSE from FVCOM_HRDPS against CTD casts, respectively. 74
Figure 24. The temperature (top) and salinity (bottom) from FVCOM_HRDPS and FVCOM_NARR comparison against CTD casts at the middle of the Bay of Fundy. The first column (a), second (b), and third (c) columns represent the lowest, medium, and highest RMSE from FVCOM_HRDPS against CTD casts, respectively. 75
Figure 25. The temperature (top) and salinity (bottom) from FVCOM_HRDPS and FVCOM_NARR comparison against CTD casts at the entrance of the Bay of Fundy. The first column (a), second (b), and third (c) columns represent the lowest, medium, and highest RMSE from FVCOM_HRDPS against CTD casts, respectively. 76
Figure 26. STD, RMS, and R for the SST at the Bay entrance for the model run with HRDPS and NARR. 84
Figure 27. STD, RMS, R for the SST at the middle of Bay for the model run with HRDPS and NARR. 85

Figure 28. STD, RMS, R for the SST at the head of Bay for the model run with HRDPS and NARR..... 86
Figure 29. STD, RMS, R for the SST at the Minas Basin for the model run with HRDPS and NARR..... 87
Figure 30. The histogram equalized the mesh edges in meters and showed two sections, a) with high(high_res) and b) low(low_res) resolution mesh..... 88
Figure 31. Taylor plot for the Head of Bay at "A" section with higher resolution..... 90
Figure 32. Taylor plot for the Head of Bay at "B" section with coarse resolution..... 90
Figure 33. The depth percentage error by using the FVCOM_HRDPS model profile..... 91
Figure 34. The accepted or rejected model profile after raytracing using FVCOM_HRDPS output at order 1a at a 70-degree swath angle. Red dots are rejected, and blue dots are accepted. 92
Figure 35. The depth percentage error by using the FVCOM _NARR model profile. 93
Figure 36. The accepted or rejected model profile after raytracing using FVCOM _NARR output at order 1a at a 70-degree swath angle. Red dots are rejected, and blue dots are accepted..... 94
Figure 37. Taylor plot for Minas Basin comparing GHRSST against the SST from Minas and BoF models. 100
Figure 38. Temperature (left column) and Salinity (right column) profiles for the Minas_model (blue) and MVP data (orange) at a and c) Minas Basin on May 6th at 19:23 and 20:17, b) Minas Passage on May 13th at 23:09. 103
Figure 39. Temperature (left column) and Salinity (right column) profiles for the Minas_model (blue) and MVP data (orange) at a) Minas Passage on May 13 at 23:49, b)

Minas Channel on May 14th 00:29, and c) entrance of Minas Passage on May 14th at 01:43. 104
Figure 40. The normalized depth to 5 meters on 2018-08-15 at a) 02:00 at the start of the flood and b) at 05:00 at the flood, c) at 08:00 start of ebb, and d) at 11:00 at ebb. 106
Figure 41. The percentage of time in half tidal cycle with a total depth greater than 5m. 107
Figure 42. The weighted normalized surface current speed was less than 1 m/s on 2018-08-15 at a) 02:00 at the start of the flood b) at 05:00 at the flood, c) at 08:00 start of ebb, and d) at 11:00 at ebb. 108
Figure 43. The percentage of time in half tidal cycle with surface current speed lower than 1 m/s. 109
Figure 44. The weighted normalized total depth and surface current speed on 2018-08-15 at a) 02:00 at the start of the flood and b) at 05:00 at the flood, c) at 08:00 start of ebb, and d) at 11:00 at ebb. 110
Figure 45. The percentage of depth error introduced by using a modeled profile (as synthetic CTD cast, orange dot) on 2018-08-15 at a) 02:00 the start of the flood and b) at 05:00 at the flood, c) at 08:00 start of ebb, and d) at 11:00 at ebb. 111
Figure 46. The IHO exclusive order was accepted or rejected on 2018-08-15 at a) 02:00 at the start of the flood and b) at 05:00 at flood, c) at 08:00 start of ebb, and d) at 11:00 at ebb. The red and blue colors are accepted and rejected orders, and the white areas did not pass the base layer criteria. 112
Figure 47. The percentage of half tidal cycle that the survey would satisfy exclusive order based on the first CTD cast. 113

Figure 48. The normalized depth to 5 meters on 2018-08-15 at a) 02:00 at the start of the flood and b) at 05:00 at the flood, c) at 08:00 start of ebb, and d) at 11:00 at ebb. 115
Figure 49. The percentage of time in half tidal cycle with a total depth higher than 5m. 115
Figure 50. The normalized surface current speed to 1m/s on 2018-08-15 at a) 02:00 at the start of the flood and b) at 05:00 at the flood, c) at 08:00 start of ebb, and d) at 11:00 at ebb. Dark blue is the area with a surface speed lower than 1m/s and green and red have a higher surface speed than 1m/s. 116
Figure 51. The percentage of time in half tidal cycle with surface current speed lower than 1m/s. 117
Figure 52. The percentage of time in half tidal cycle with surface current speed lower than 1m/s and depth higher than 5 m. 118
Figure 53. The weighted normalized total depth and surface current speed on 2018-08-15 at a) 02:00 at the start of the flood and b) at 05:00 at the flood, c) at 08:00 start of ebb, and d) at 11:00 at ebb. The white areas have weighted normalized values of less than 31. 119
Figure 54. The percentage of depth error introduced by using a modeled profile (the orange dot as synthetic CTD cast) at the entrance of Minas Basin on 2018-08-15 at a) 02:00 the start of the flood and b) at 05:00 at the flood, c) at 08:00 start of ebb, and d) at 11:00 at ebb. 120
Figure 55. The IHO order 1a was accepted or rejected on 2018-08-15 at a) 02:00 at the start of the flood and b) at 05:00 at flood, c) at 08:00 start of ebb, and d) at 11:00 at ebb.

The red is rejected, the blue is accepted, and the white did not satisfy the depth and surface speed criteria..... 121
Figure 56. The percentage of depth error introduced by using a modeled profile (as CTD cast) at the middle of Minas Basin on 2018-08-15 at a) 02:00 the start of the flood and b) at 05:00 at the flood, c) at 08:00 start of ebb, and d) at 11:00 at ebb. 123
Figure 57. The IHO order 1a was accepted or rejected on 2018-08-15 at a) 02:00 at the start of the flood and b) at 05:00 at flood, c) at 08:00 start of ebb, and d) at 11:00 at ebb. The red is rejected, the blue is accepted, and the white did not satisfy the depth and surface speed criteria..... 124

List of Symbols, Nomenclature or Abbreviations

GHRSST: Group of High-Resolution for Sea Surface Temperatures

NARR: North American Regional Reanalysis

HRDPS: High-Resolution Deterministic Prediction System

GoMOFS: Gulf of Maine Operational Forecast System

BoF: Bay of Fundy

NCEP: National Center for Environmental Prediction

FVCOM: Finite-Volume Community Ocean Model

Chapter 1: Introduction

More than 90% of the world's trade is carried by sea (Kosowska-Stamirowska, Ducruet, & Rai, 2016), which is the most cost-effective method of transportation, and this alone shows the important role of maritime transportation in the world's economy. Consequently, more modernization and automation are needed to provide up-to-date information about this dynamic environment. In the hydrography world, the need for automation has become more pronounced in all of its stages, such as pre-planning, hydrography design, and postprocessing and providing the final products. The capability of autonomous systems has increased rapidly, both in the ocean and terrestrial environment. These autonomous features provide different advantages. They could reduce the operational costs, manpower requirement, and time to produce the results. Also, they enhance the capability of the survey by improving the responsiveness and data quality control and easing the accessibility of different parts of the ocean. Finally, the workforce could be more focused on the tasks that require their expertise instead of on the repetitive, laborious tasks.

These advantages could be achieved by overcoming the challenges we are facing in the ocean environment. Although the multibeam echo sounders benefit from a remarkable increase in swath coverage by collecting the oblique soundings, it comes at a cost which is bending the sounding path in the oblique angle (Beaudoin, 2010). According to Snell's Law, this bending capability of sound path relies on the speed of sound in the different ocean layers and since it is determined by temperature, salinity, and pressure, any spatiotemporal variations from these variables affect the speed of sound which finally

could result in sounding bias. According to the level of the required accuracy of the survey and the threshold of error, the surveyor should decide to do the Sound Velocity Profiler (SVP) sampling accordingly. The issue here is that there is no clear rule as to how often to collect sound speed profiles in coastal areas where the environment is very dynamic. To avoid exceeding the allowable error tolerance defined by international and national survey standards defined by International Hydrographic Organization (IHO), we should try not to contaminate the collected sounding by the refraction-induced depth bias from inadequate sound speed cast frequency to capture the spatio-temporal variability of the marine environment (Beaudoin, 2010; Lucieer, Huang, & Siwabessy, 2016; Wilson, Beaudoin, & Smyth, 2013). To overcome the poorly captured variability of the environment, either we should reduce the sonar swath angular sector, which impacts the survey efficiency, or over-sampling the water column by Moving Vessel Profiler (MVP), with a high risk of loss and costs (Masetti et al., 2017).

Even with the current advances in seafloor mapping systems, poor awareness of the oceanographic conditions of the survey environment impacts the final product and operational efficiency (Lurton et al., 2015; Mayer et al., 2018). However, this issue could be tackled by utilizing the local and global scales operational ocean models which provide us with the key environmental variables, such as temperature, and salinity (Masetti et al., 2020). The potential application of oceanographic variability knowledge can help during the planning phase to reduce the number of large uncertainty front crossings by designing a specific survey direction. Also, either we can change the survey time or change the swath coverage if the estimated uncertainty for the outer part of the swath is too large based on the specification of the survey. The other application of the proposed routine could be

defining the calibration site with minimum environmental variability or in the case of high variability, providing the best instrument suggestion to capture the water column variability. Also, while performing autonomous hydrography, a preferred method is to undertake the risk assessments for the survey area and prioritize the regions which are suitable with our survey platform and IHO specification of survey.

The current regional and global operational ocean models lack high horizontal and temporal resolution in small basins, such as the Minas Basin. To capture the specifications of the marine environment which is a key for sound speed error estimation for hydrographic surveys, we need to have a higher resolution model both in time and space to be able to resolve all the processes happening in the marine environment. The ocean models are run by prescribing the forcing both at the open boundaries (temperature, salinity, water level elevation) and on the surface (such as air temperature, short wave, long wave radiation, and wind). As the ocean and air continuously interact with each other, surface forcing plays an important role in the improvement of the ocean model and capturing the thermodynamic process happening under the water. Also, the spatiotemporal resolution of the surface forcing could impact the generation and evolution of the oceanic surface mixed layer and consequently other layers such as halocline or thermocline.

This study is part of a broader suite of studies (Sameoto et al., 2020) to generate a scallop species distribution map in the Bay of Fundy while incorporating the downscaled oceanographic layer. The objective of this study is to develop a higher-resolution model and assess if the model would provide a better representation of oceanographic conditions, specifically the temperature and salinity, of the Bay of Fundy in comparison to operational models. Also, in the Minas Basin, at the head of the Bay of Fundy, we experience the

highest tide in the world, a huge intertidal zone, and high current speeds. These features make a hydrographic survey very complicated in this area, and by providing a hydrographic survey insight using a hydrodynamic ocean model, we will acquire both accuracy and efficiency at the same time.

To improve our understanding of the ocean variability of the Bay of Fundy and overcome the hydrographic survey limitation in a high tidal environment, two baroclinic models are developed and evaluated for the Bay of Fundy and Minas Basin to illustrate their application to the ocean mapping routine. This study explores the use of uncertainty estimation of oceanographic variability to define how far in space and time a sound speed profile could be reliable in the hydrographic survey and includes other factors (such as wet/dry, ebb/flood window time, surface currents speed) to classify the area based on the weighted importance.

The objectives of this research are:

1- To improve the representation of existing temperature and salinity simulation using a higher-resolution baroclinic hydrodynamic model for the Bay of Fundy including Minas Basin

2- To identify the impact of spatial resolution of the atmospheric forcing on the baroclinic model

3- To implement the model output, such as temperature, salinity, and surface current speed, for the hydrographic survey planning insight

Chapter 2: Background

2.1 Study Area

2.1.1 Bay of Fundy

The Bay of Fundy, Figure 1, is a unique marine environment and home to diverse biological habitats and a strong tidal amplitude. The Bay of Fundy is located northeast of the Gulf of Maine between two Canadian Provinces, New Brunswick, and Nova Scotia. It is well-known for its special tidal behavior (6-12 m twice daily) which is predominantly semidiurnal (Swift et al., 1969) with a range varying from 6.4 m in the Grand Passage to 16 m in the spring tide at Minas Basin (Desplanque & Mossman, 2001; Garrett, 1972; Greenberg, 1983; Swift et al., 1969), which makes this region experience interesting tidal-related oceanographic processes. The funnel shape, length, and gradually decreasing depth to the head of the Bay result in it being in near resonance with the semidiurnal M_2 harmonic constituent (Desplanque & Mossman, 2001; Garrett, 1972; Redfield, 1953; Shaw et al., 2010; Swift et al., 1969). The resulting strong tidal currents are the dominant factors in the changes in surficial geology from erosion and sediment transport (Li et al., 2015; Percy, Wells, & Evans, 1997) and affect the interaction of biological, physical, and chemical conditions of the bay (Desplanque & Mossman, 2001). The main contribution of water to the bay is from Scotian Shelf water (Xue, Chai, & Pettigrew, 2000) which enters the Bay along the Nova Scotia coast undertaking mixing up to the head of the Bay (Bailey, MacGregor, & Hachey, 1954), flows out along the New Brunswick side and eastern part

of Grand Manan Island (Bigelow, 1927; Brooks, 1992; Godin, 1968; Greenberg, 1983), and combines with the Gulf of Maine circulation (Dickie, 1955; Godin, 1968; Hachey & Bailey, 1952).

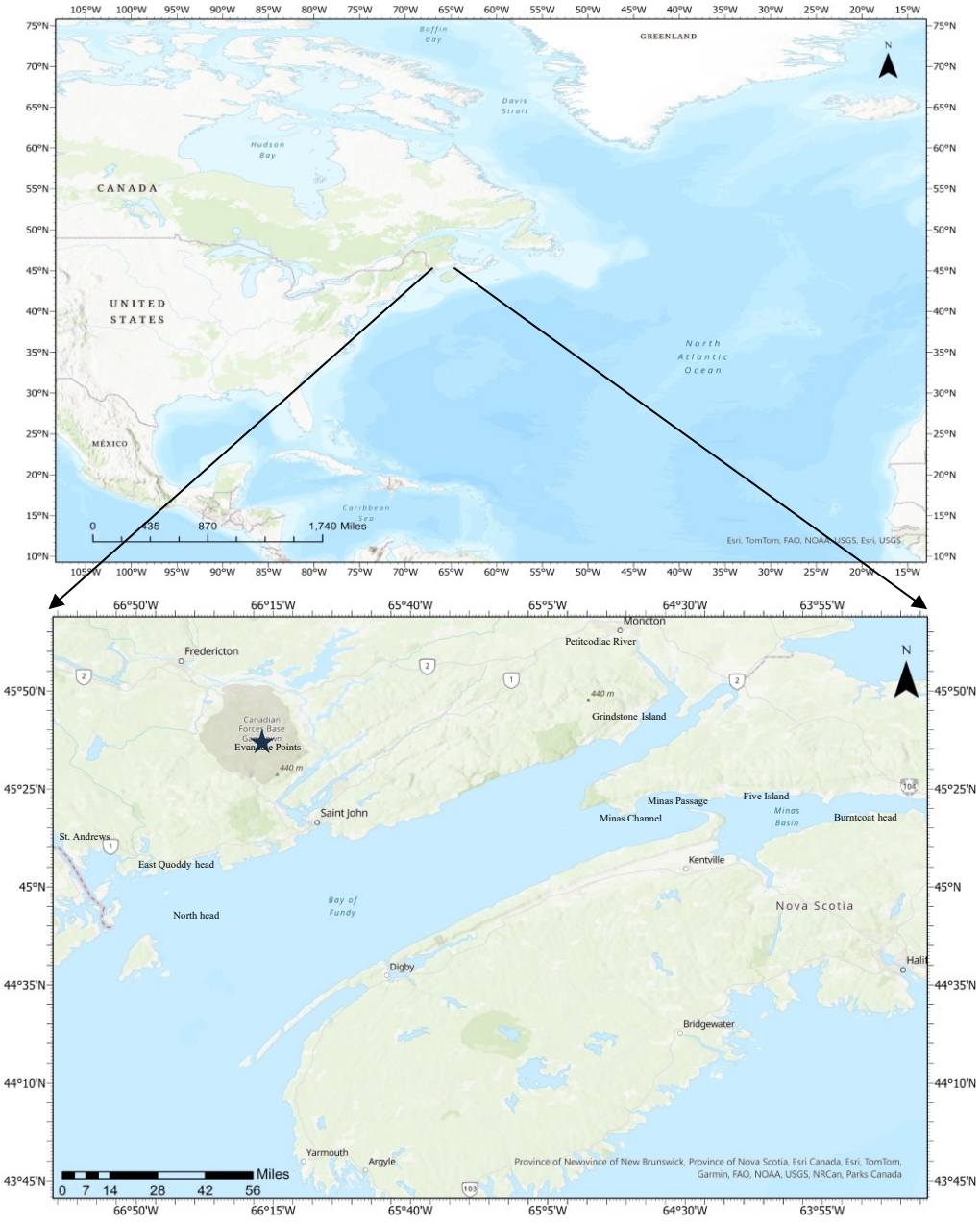

Figure 1. Bay of Fundy and the location of Evandale Point (black star).

The main source of freshwater in the Bay is the Saint John River. The lower Saint John River includes complex bathymetry, large tides, dynamic river input, and strong currents in the narrow passage. The river has a 55,000 km^2 watershed with an annual average discharge of about 1100 km^3s^{-1} (Cunjak & Newbury, 2005) with a maximum discharge of approximately 6800 km^3s^{-1} (Neu, 1960) at the freshet time. Three other important rivers discharging in the Bay of Fundy, St. Croix, Petitcodiac, and Big Salmon Rivers with an annual mean discharge of 81.6 m^3s^{-1} (The International ST. Croix River Watershed Board 2024), 27.3 m^3s^{-1}, and 11.8 m^3s^{-1}, respectively, which are very low in comparison to Saint John River discharge (Cunjak & Newbury, 2005). The near-surface circulation in the Bay is affected by the river runoff, especially in the Spring season (Aretxabaleta et al., 2008), and has less impact on the deeper part of the water column (Brooks, 1994; Chao & Boicourt, 1986). The freshwater plume joins the East Maine Coastal Current (Brooks, 1994; Brooks & Townsend, 1989; Lynch, Holboke, & Naimie, 1997) with the most flow coming from the west of Grand Manan Island (Brooks, 1994; Lynch et al., 1997; Watson, 1936) and part of it from east of the Island (Aretxabaleta et al., 2009). Also, the influence of the Saint John River provides 30 percent of freshwater contribution to the Gulf of Maine system (Apollonio, 1979; Brooks, 1994; Pettigrew et al., 1998). It is clear, therefore, that the freshwater output of the Saint John River impacts the oceanographic circulation of the Bay of Fundy.

There has been previous research on the barotropic condition of the Bay of Fundy using a different model configuration such as the structured models (Greenberg, 1979; Sankaranarayanan & McCay, 2003) and unstructured ones (Dupont et al., 2015; Wu et al., 2011, 2014). These models usually simulate the tidal and wind-derived variation of sea

levels and currents. Resolving the baroclinic condition of the Bay improves the emergency response applications (e.g., oil spill) (Paquin et al., 2020) and the transition between well-mixed and stratified zones which are important from a biological perspective (Denman & Herman, 1978; Pingree, 1975). However, few studies have focused on the baroclinic condition of the Bay, with most examining the lower parts of the Bay and Gulf of Maine. Watson (1936) showed that the counter-clockwise gyre at the mouth of Bay is mostly driven by density effects while the tidal rectification and density-driven circulation (Aretxabaleta et al., 2008) resulting from surface heating (Garrett, Keeley, & Greenberg, 1978; Greenberg, 1979) and freshwater inflow (Brooks, 1994) act as driving factors together. Also, tidal current and coastal processes may be affected by variations in temperature and salinity resulting from the surface and open boundary heat and freshwater fluxes (Katavouta & Thompson, 2016).

One contributing factor that increases model skill is how well the model can resolve the dynamic processes in the ocean domain, and this comes from the mesh resolution on which the model is running. The oceanic process properties vary on many scales which are dependent on factors such as coastline, bottom topography variation, the forcing meteorology, changing Coriolis force with latitude, and the Rossby Radius of deformation (Greenberg et al., 2007). Coastal models usually require increased spatial and temporal resolution to provide accurate forecasts (Chant, 2011; Garvine, 1995) by capturing a wider energy spectrum in the model and improving our understanding of oceanic sub-mesoscale dynamics (Soufflet et al., 2016) such as capturing the freshwater front from river discharge (Bricheno, Wolf, & Brown, 2014) or an accurate representation of sea surface temperature (Paquin et al., 2020). However, this leads to the requirement for extra computer storage

space, and a decrease in the model time steps to satisfy the computational fluid dynamic stability condition (Courant-Friedrichs-Lewy, CFL) (Bricheno et al., 2014; Greenberg et al., 2007). Koopman et al. (2014) showed that the SST increased in the Bay of Fundy from 2008 to 2012 and more surprisingly, throughout the entire water column, indicating a rate of 0.6 C increase per year since 2008. Throughout 2008-2012, the Bay of Fundy SST increased by 3.7 C, showing the same trend as the Gulf of Maine but with a different rate of change, and a 2.5 °C increase throughout the water column in the deeper part (Koopman et al., 2014). This water column temperature increase shows that even in a well-mixed, tidally driven system the enormous thermal input could change the water column variability, and having the appropriate thermal heating input improves our knowledge of our marine environment.

The seabed ecosystem is affected by human activities such as fishing, and oil and gas pollution which reduces benthic biodiversity, and without a supportive plan to manage the resources and protect the ecologically sensitive areas, the marine ecology could collapse (Worm et al., 2006). The benthic habitat mapping provides the location, condition, and extent of the marine ecosystem and the insight for decision-makers to apply precautionary practices (Brown et al., 2011; Todd et al., 2020). To provide marine protection plans and better insight into the species communities on the seafloor, marine biologists need to integrate the physical oceanographic layers such as temperature, salinity, and currents from global ocean models with biological layers to map the benthic habitat.

By understanding the baroclinic condition of the domain, biological studies, for instance, habitat mapping, and retention of organisms such as phytoplankton (Gran & Braarud, 1935), zooplankton (Fish & Johnson, 1937), and scallop larvae (Dickie, 1955); could be

better understood. To understand and predict the response of marine species to highly dynamic oceanographic conditions, habitat-based models are required to sufficiently capture the environmental variability of the domain in different spatial and temporal scales (Scales et al., 2017). Also, to improve marine species distribution models (SDMs), researchers integrate the spatiotemporal environmental data, such as temperature, salinity, and current speed retrieved from ocean models to incorporate the vertical and horizontal structure of water column (Brodie et al., 2018; Fabrizio et al., 2021; Lecours et al., 2015; Scales et al., 2017).

However, using a coarse temporal and spatial resolution in the marine habitat models results in introducing bias in the products (Scales et al., 2017) and could weaken any fine-scale habitat relationship (Winship et al., 2021). Using different resolutions of SST data, Scales et al. (2017) showed that the finer resolution model was able to capture potentially important processes such as eddies and upwelling which could improve the habitat model predictions. Also, they mentioned that the temporal resolution had a higher effect than the spatial resolution on the magnitude of inaccuracy. However, coupling the coarse spatial resolution with coarse temporal resolution (seasonal) substantially increased the model error.

Temperature plays an important role in marine species distribution and vulnerability assessment models and works directly through the thermal tolerance of a species for survival and reproduction or indirectly with its impact on the benthic food supply (e.g. affecting ice cover, zooplankton) (Renaud et al., 2019; Shackell, Ricard, & Stortini, 2014). The dominance of a species on the seafloor can fluctuate with the temperature in a region (Matishov et al., 2012). While some species are not vulnerable to +3-degree warming, some

are more vulnerable to a very small temperature increase of +0.7 (Stortini, 2015). Also, the marine species population not only is highly affected by regional temperature variation but also by smaller-scale variation processes. For this, the regional scale information is required to provide vital insight for policymakers to modify and make the structures accordingly (Shackell et al., 2014).

The water column attributes and the seafloor geological conditions affect benthic biology. The latter can be acquired by acoustic survey methods and the former can be derived from point samples of oceanographic measurement or, for better coverage, from ocean models (Anderson et al., 2008; Brown et al., 2011). While the global ocean models provide general physical oceanographic layers, the local marine environment is affected by local forces that can directly impact the marine ecosystem. Downscaled ocean models with higher spatial and temporal variability in comparison to large-scale systems, could resolve the variability close to the biological scale (Fagundes et al., 2020). An ocean model provides spatiotemporal environmental data, such as temperature, salinity, and current speed, which are essential inputs for habitat-based models and Species Distribution Models (SDMs). These models require an accurate representation of the vertical and horizontal structure of the water column to predict how marine species respond to dynamic oceanographic conditions. By generating high-quality outputs that capture the variability of the water column across different spatial and temporal scales, the model developed in this study supports habitat mapping efforts and improves our understanding of the retention and distribution of marine organisms in highly dynamic environments like the Bay of Fundy. This connection underlines the importance of ocean models in ecological and biological studies, demonstrating their relevance beyond hydrographic survey applications.

2.1.2 Minas Basin

The Minas Basin is a sub-basin in the northeast corner of the Bay and plays an important role in sediment distribution in the Bay of Fundy (Fagundes et al., 2020). The salinity ranges between 27-31 ppt and the highest currents occur in the Minas Channel as high as 3-5 m/s and about 1-2 m/s in the Basin (Amos & Joice 1977; Cameron, 1961). At the Minas Passage, the water depth reaches more than 100 m (Ashall, Mulligan, & Law, 2016; Cornett, 2010) with exposed bedrock (Parrott et al., 2008) and the depth reaches 15 m at low tide in the central part of the Basin with sand and gravel type (Amos, 1980) and finally with the intertidal mudflats at the edge of Basin (Amos, Van Wagoner, & Daborn, 1988). Suspended sediment has a huge role in controlling the physical, chemical, and biological processes happening in the coastal and estuaries environment (Miller et al., 2011) and seabed morphology, biological community structures, and light attenuation are controlled by suspended sediment concentration in the Minas Basin (Tao et al., 2014). The transport of bedload and suspended sediments has been documented by Wu et al. (2011) using a suite of methods by integrating FVCOM for simulating the tidal flows, an empirical bed load sediment transport model, and surface sediment concentration from remotely sensed images. They used a variable bottom roughness based on the sediment grain size (Li & Amos, 2001) which improved the tidal currents in the Minas Passage. They concluded that the tidal residual flow is mainly responsible for the bottom stress asymmetry and bed load transport in the Minas Basin, Passage, and Channel while M_4 and M_6 are dominant in the stress asymmetry and bed load transport in the upper part of the Minas Basin, Cobequid Bay. Also, they mentioned that the total sediment transport rate occurs mainly in the Minas Channel and Minas Passage and the sediment from Minas Passage moves eastward and

deposits in the center of the Basin, and the sediment from the eastern part of the Minas Basin moves and deposits to the center of Basin, while in Cobequid Bay the sediment moves eastward to the upper Bay. With the recent attention on tidal power extraction in the Bay of Fundy, especially in Minas Passage, understanding the dynamic of currents and the change in the bathymetry is important for the evaluation of the environmental impacts in the Minas Basin (Ashall et al., 2016). Most studies concentrate on tidal energy extraction and the side effects on sediment distribution and circulation in the Bay of Fundy. One of the forms of tidal energy extraction is using the potential energy of the tidal range (tidal barrage) and it has been documented by many researchers (Garrett et al., 1978; Greenberg, 1979, 1983; Greenberg & Amos, 1983; Shaw et al., 2010) which could affect the tidal regime in other regions. The other method is to harness the energy from the kinetic energy of tidal current (in-stream turbines) documented by (Hasegawa et al., 2011; Karsten et al., 2008; Mulligan et al., 2013), however, they concluded that high extent of tidal energy reduction may lead to a huge decrease of tidal level in Minas Basin and Passage and consequently, impact the physical (such as transport of bottom sediment) and biological processes in the area.

2.2 Surface Forcing

The quality of ocean model forecasts is highly affected by the atmospheric forcing applied as an ocean model surface boundary condition. The effect of surface heating resolution on ocean model simulation has not been studied in the Bay of Fundy which may be due to the lack of observations in the area. However, the importance of temporal and spatial resolution of surface heating on the oceanic process has been addressed in other studies. There are

different variables included in the surface heating to run an ocean model such as wind, air pressure, longwave radiation, shortwave radiation, and air temperature, and the effects of these variables on the ocean simulation could be investigated based on different spatial and temporal resolutions.

To acquire a rapid response of the ocean by considering various oceanic processes, Huthnance (2002) showed that a wind field resolution of 10 km or less with a temporal resolution of 1 to 3 h is required. The influence of high-resolution wind forcing is studied by Schaeffer et al. (2011) using three different atmospheric forcing resolution datasets, Application of Research to Operations at Mesoscale (AROME) (Seity et al., 2011) with 2.5 km and 1-hour resolution, Aire Limitée Adaptation Dynamique Développement International (ALADIN) (Fischer et al., 2005) with 9.5 km and 3-hour resolution, and Fifth-Generation Penn State/NCAR Mesoscale Model (MM5) (Brousseau et al., 2008) with 9 km and 3-hour resolution for MM5 in a 3-month hydrodynamic simulation in the Gulf of Lions and they concluded that the high-resolution surface forcing could better represent the inertial oscillations and mesoscale variability and, in comparison to temporal resolution, the spatial resolution of wind had the dominant influence on the generation of mesoscale eddy (Schaeffer et al., 2011). Considering time resolution, Lebeaupin Brossier et al. (2011) showed that even 3-6 hourly data of surface forcing is too coarse to generate a fine-scale response of the ocean, such as internal ocean boundary layer and cooling and deepening of the ocean mixed layer (Lebeaupin Brossier et al., 2011). In an attempt to compare the different spatial resolutions of surface heating, Lewis et al. (2019) assessed a regional ocean model with a 1.5 km horizontal resolution with an operational global-scale Numerical Weather Prediction (NWP) and a convective-scale regional one for a one-month

simulation and evaluated the simulated SST based on the L4 ocean buoy. They concluded that the quality of ocean forecasts is highly dependent on the applied atmospheric forcing as an open boundary forcing and the results indicate the sensitivity of simulated SSTs to the atmospheric forcing with a warm ocean bias of about 0.7 K, and 0.4 K, for global-scale, and regional-scale atmospheric models respectively. Also, the regional-scale atmospheric model shows more variability in surface heat budget and near-surface winds, however, the wind speed had less agreement with the observations in comparison to the global one (Lewis et al., 2019). They applied a sensitivity analysis to evaluate why the degraded wind forcing does not deteriorate the SST and concluded that the improvement in SST has mostly resulted from the differences in the surface heat budget between the two atmospheric forcings. Akhtar et al. (2018) showed that not only the increased resolution could improve wind speed and heat flux simulation, but also, the representation of these two variables could be enhanced by coupling between the atmosphere and ocean. He also mentioned that the poor representation of clouds in the finer mesh resolution (9 km) resulted in less accurate radiation fluxes simulation than the coarser one. Gronholz et al. (2017) concluded that the use of the higher resolution of regional atmospheric forcing improves SST prediction in the North Sea.

The impact of the spatial distribution of atmospheric forcing on the water mass formation is studied in the Mediterranean Sea using different atmospheric forcing resolutions, fine European Centre for Medium-Range Weather Forecasts (ECMWF-analyzed) (60-40 km, MED16-ECMWF), and coarse ECMWF-reanalysis (100 km, ERA40) surface field data, applied on a high-resolution ocean circulation model by Branger et al. (2010). The finer atmospheric model resolution better represented the winds in the area, also, the results of

ocean simulation with finer surface forcing (ECMWF-analyzed) showed better agreement with observations. However, applying the finer spatio-temporal resolution of surface heating in an ocean simulation does not always result in a better representation of ocean processes. The variability of mesoscale ocean processes is highly affected by improving the temporal and spatial resolution of atmospheric forcing in some coastal areas. Brossier et al. (2011) applied two Weather Research and Forecasting (WRF) atmospheric model configurations, two horizontal resolutions at 20 km and 6.7 km and two temporal resolutions at daily and three-hourly, and concluded that the ocean convection was increased where there was a fine resolution of surface forcing (which enhanced the near-surface winds), however, the convection was damped (resulting from ocean stratification) by applying higher frequency of surface forcing (Lebeaupin Brossier et al., 2011). With a change of spatial resolution from 9 to 2.5 km of wind forcing, Schaeffer et al. (2011) showed that the ocean eddies could be better represented in the Gulf of Lion while having little impact from temporal resolution. The global weather model could capture the large-scale variability, but when it comes to regional and local scale, a finer resolution is required to capture the spatio-temporal variability of the parameters in the area and enhance the representation of circulation, oceanic mixed-layer process, thermohaline circulation, and water mass formation (Artale et al., 2002; Castellari, Pinardi, & Leaman, 2000). The Bay of Fundy, known for its extreme tidal dynamics, is primarily influenced by strong tidal forcing, which dominates the circulation and mixing processes in the region. While these tidal processes have been extensively studied, the impact of surface atmospheric forcing, particularly surface heating and cooling, on oceanic processes such as temperature stratification, salinity variability, and local currents, remains largely unexplored. Surface

heating can affect the thermodynamic structure of the water column, potentially modifying stratification, influencing vertical mixing, and altering the distribution of temperature and salinity. These effects could have implications for biological productivity, habitat mapping, and other oceanographic phenomena. Understanding how surface heating interacts with the strong tidal dynamics of the Bay of Fundy is critical for improving the accuracy of ocean models and for assessing their capability to represent the region's complex physical processes under varying atmospheric conditions.

2.3 Hydrography Survey Design

The physical oceanographic condition of the ocean shows significant changes over the temporal and spatial scale of hydrographic survey and discrete oceanographic measurements are required at periods of less than a day and even hourly, depending on the oceanic condition. However, the increased processing time and the need to acquire additional data are some of the consequences of poor understanding of the oceanographic condition of the domain (Clarke, 2013; Lecours et al., 2015; Weber, Rice, & Smith, 2018). Knowledge of the baroclinic conditions of the Bay not only improves the specious distribution models but also enhances acoustic hydrographic surveys. This could be achieved by defining the areas of high sound speed variability throughout performing uncertainty evaluation from the hydrodynamic model (Church, 2020), which could provide better time, cost, and effort efficiency planning (Masetti et al., 2020).

The hydrographic surveys are usually conducted using a multibeam sonar system benefiting from a remarkable increase in swath coverage by collecting the oblique soundings, however, it comes at a cost which is bending the sounding path in the oblique

angle (Beaudoin, 2010). According to Snell's Law, this bending capability of sound path relies on the speed of sound in the different ocean layers and since it is determined by temperature, salinity, and pressure, any spatiotemporal variations from these variables affect the speed of sound which finally could result in sounding bias. Even with the recent advanced technology in the multibeam echo sounders, partial or lack of understanding of the oceanographic conditions affects the resulting uncertainty budget of the survey (Masetti et al., 2017).

Even with the current advances in the seafloor mapping system, the poor awareness of the oceanographic condition of the survey environment impacts the final product and operational efficiency (Lurton et al., 2015; Mayer et al., 2018). In this method, there is always a tradeoff between the survey efficiency and sounding accuracy, and leaning to each side could have degraded the other one, because of this trade-off, the hydrographic companies are more inclined to take the discrete and less frequent measurements if these measurements could represent the ocean spatial and temporal variability in the survey period. However, with the advent of swath sonar, more prone to refraction, it is obvious, pending the ocean domain specification, that those measurements are not enough to represent the water column variability neither in time nor in space (Clarke, Lamplugh, & Kammerer, 2000). In the second method, an MVP is used to collect the sound speed profile while the vessel is underway. In this case, there could be much more oversampling of the water column than what is required to maintain the accuracy of multibeam data, and the challenge is how many sounding profiles are sufficient to maintain the desired level of multibeam sounding accuracy (Wilson et al., 2013). As time passes, and the vessel moves forward in time and space, the previous profile is no longer appropriate to be used for ray

tracing until the next profile is captured which shows the importance of the sampling frequency of the MVP. The limitations of this method are the profile frequency, profile extrapolation, and missing data due to malfunction of the sensor.

Two possible approaches to overcome the refraction issue are 1) the real-time approach which applies the sounding profile with a specific sampling interval to the sounding which generates an artifact of abrupt step in the across-track when applying the new profile, and 2) the interpolated post-processing approach uses a time-weighted average from the closest profile before and after each ping, however, some parameters should be recorded for this method, such as the ship-head-relative azimuth and depression angle for each formed beam, and the sonar-mount-relative steering angles of the transmit and receive beams (Clarke et al., 2000). Also, the oversampling increases the risk of losing the instrument and the wear and tear (Beaudoin, 2010). Also, the appropriate frequency of sound speed profiling depends on the local oceanography, if known, the limiting of the angular sector would be removed (Clarke et al., 2000).

This issue potentially could be tackled by utilizing the local and global scales operational ocean models which provide us with the key environmental variables, such as temperature, and salinity (Masetti et al., 2020). The model data could also be used to calculate the absorption coefficient for acoustic backscatter processing (Malik, Lurton, & Mayer, 2018; Masetti et al., 2018; Montereale-Gavazzi et al., 2019) or for evaluation of multibeam sonar ray-tracing uncertainty (Church, 2020). To avoid exceeding the allowable error tolerance defined by international and national survey standards (International Hydrographic Organization, 2011; NOAA, 2019), we should try not to contaminate the collected sounding by the refraction-induced depth bias from inadequate sound speed cast frequency

(which means the spatio-temporal variability of the marine environment is not captured) (Beaudoin, 2010; Lucieer et al., 2016; Wilson et al., 2013).To overcome the poorly captured variability of the environment, either we should reduce the sonar swath angular sector, which impacts the survey efficiency, or oversampling the water column by MVP, with a high risk of loss and costs (Masetti et al., 2018).

To improve the overall sounding accuracy and determine the cast interval, Wilson et al. (2013), provided a method called, CastTime, which estimates the sampling interval by reacting to the observed variability, however, it did not include the variability in space. To improve the sounding accuracy and include the variability in space, Masetti et al. (2020) used the operational ocean model, Gulf of Maine Operational Forecast System (GoMOFS), to show the importance of the appropriate sounding cast frequency to capture the water column variability by using the ray tracing uncertainty to evaluate the adequacy level of sampling interval ranging from under-sampling to over-sampling, called ForeCast which incorporates the spatio-temporal variability of the environment. The CastTime approach considers that the modeled depth bias increases linearly with the elapsed time, while in ForeCast, by incorporating the environmental variability from GoMOFS, this spatial component improves the forecast capability of ForeCast. Also, ForeCast considers the vessel route and speed to calculate a better casting interval.

The potential application of oceanographic variability knowledge can help during the planning phase to reduce the number of large uncertainty front crossings by designing a specific survey direction or changing the survey time. The other application could be defining the calibration site with minimum environmental variability both in time and space or in the case of high variability, providing the best instrument suggestion to capture

the water column variability. In the post-processing phase, these tools can help distinguish the source of artifacts in the sonar data. Also, while performing a hydrographic survey using an uncrewed autonomous vessel, a preferred method is to undertake a risk assessment for the survey area and prioritize the region based on the survey objectives and equipment (Riding & Rawson, 2015).

The risk assessment could include different factors, some with constant features such as Marine Protected Areas (MPA), environmental factors (such as seafloor topography, MPAs, sediment type), marine traffic, vessel type, economic cost/benefit, and some with changes over time such as tidal range, weather, winds, vessel draft, surface currents, and physical oceanographic condition of the survey area. The assessment approach considers these factors to classify the survey area based on the information for the under-keel clearance such as tidal information, soundings, and navigational parameters (draft, heave) for the shallow areas, and the sound speed uncertainty analysis (using the baroclinic ocean model output) to achieve the IHO standards. Based on the intersecting layers from these factors, areas with potential concern are delineated in the survey area in time. For instance, in the ebb, for the depth shallower than a threshold, there is a high risk for grounding, or where there is a river discharge, we have a high risk of sounding uncertainty.

To tackle the above issue, hydrographic survey planning considering the changing environmental factors and vessel limitations is included in our new routine for the local basins, such as the Minas Basin. In this way, we can rely on the local ocean models to provide us the insight into water variability and ocean dynamics for the survey area in space and time, which could have the potential of improving the efficiency of hydrographic surveys. In this approach, the model data are considered as synthesized CTD casts. A model

profile is selected in the domain for the start of the survey and this profile will be used as the CTD cast in the survey domain in future time. The amount of vertical uncertainty generated by this profile is compared against the surrounding profile (true profiles in time and space) as time passes to check if the selected profile still satisfies the threshold vertical uncertainty (through raytracing, Huang, 2012). Based on the survey IHO requirement, the domain is classified as pass or failed using the selected profile

Chapter 3: Methodology

Two high-resolution models have been developed for this study, one which covers the entire Bay of Fundy including Chignecto Bay and Minas Basin, and the lower part of Saint John River to Evandale, New Brunswick, and the other one covering Minas Basin, Minas Passage, and Minas Channel. The period for the model run covers the fieldwork for the ground-truthing (towing video camera) for the benthic habitat mapping from July 1st to August 30th, 2018. The following subsections explain the model configuration, parameters, open boundary forcing, initialization, and surface forces.

3.1 Bathymetry and Coastline

The coastline dataset is extracted from the Global Self-consistent, Hierarchical, High-resolution Geography Database (GSHHG) (Wessel & Smith, 1996) with the full resolution (1:250000). The model bathymetry in the Bay of Fundy is a 100-m resolution grid derived from multibeam data collected by the CHS (Canadian Hydrographic Service) and Natural Resources Canada (NRCan) (Parrott et al., 2013). The data is a combination of different sonar systems that were performed in different years according to the data source, while areas that are not covered by this dataset (such as Chignecto Bay, the entrance of Passamaquoddy Bay, and close to Bear Cove), are digitized from CHS raster chart numbers 4010, 4011, 4012, 4013, 4117, and 4396. At the time of accessing the CHS NONNA bathymetry data, there was no vertical datum published to the dataset. Figure 2 shows the three bathymetry datasets aggregated together in the model domain.

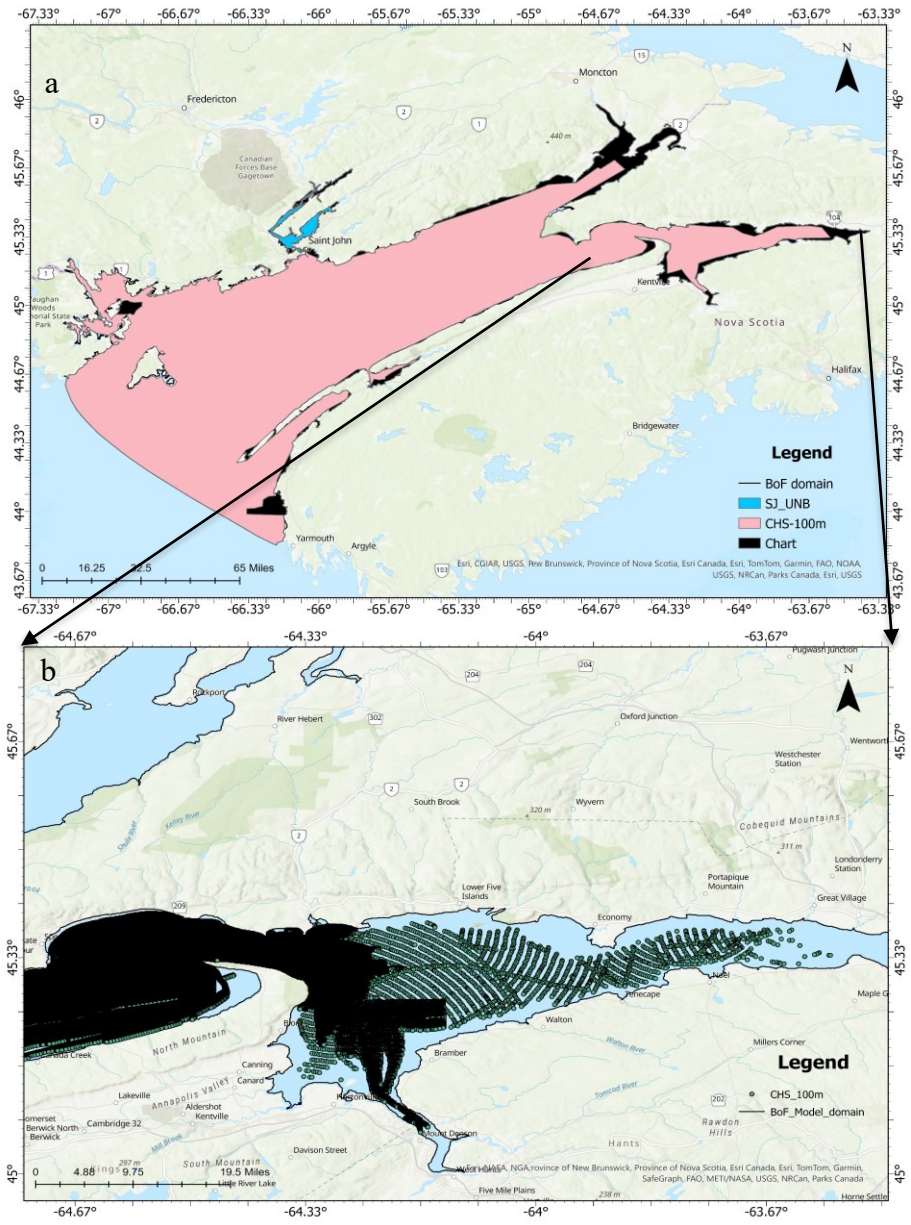

Figure 2. The three-bathymetry dataset in the model domain, a) where the pink domain is the CHS-NONA 100-m bathymetry, the dark blue domain is the Ocean Mapping Group bathymetry in the Saint John River, and the blue sections are digitized from CHS Charts. The figure at b) shows the resolution of CHS-NONNA 100-m in the Minas Basin.

The lower Saint John River is covered partially by CHS bathymetry data and the rest is 10-meter resolution bathymetry data (referenced to the CGVD28 vertical datum) from the

University of New Brunswick Ocean Mapping Group dataset (McNeill, Church, & Leger, 2018), which is a collection of surveys from 2000 to 2008.

3.2 Three-dimensional Baroclinic Hydrodynamic Model

3.2.1 Finite-Volume Coastal Ocean Model

The Finite-Volume Community Ocean Model (FVCOM), was originally developed by Chen, et al, 2003 (Chen, Liu, & Beardsley, 2003) and upgraded by the joint effort of the University of Massachusetts Dartmouth (UMAS-D) and Woods Hole Oceanographic. Institution (WHOI) (Chen, Beardsley, & Cowles, 2006) was used for this simulation. The model uses an unstructured grid and 3D primitive equations. Different modules are embedded in the model such as the sediment transport, Global Ocean Turbulence Model (GOTM) (Burchard, 2002), 3-D Wet-Dry module, and nesting modules. The equations of momentum, continuity, temperature, salinity, and density could be either in a spherical coordinate system or Cartesian, where the spherical coordinate is considered for this model configuration. For this simulation, the default MY-2.5 (Mellor & Yamada, 1982) turbulent mixing in the vertical and a Smagorinsky turbulent closure scheme in the horizontal (Smagorinsky, 1963) were used. For integration in time, the model benefits from mode split, while it uses the second-order accurate advection scheme in space for solving the transport equations such as momentum, temperature and salinity, and sediment transport. Also, to include the intertidal zone in the simulation, the Wet-Dry module is enabled horizontally. The governing equations are discretized in the flux form over the unstructured triangular mesh (Chen et al., 2003), and a generalized terrain-following coordinate. Which adapts to the bathymetry of the ocean floor, and allows better representation of water

column in regions with varying depth, is used in the vertical (Pietrzak et al., 2002). By using the unstructured grid and finite volume method the model benefits from the simple discrete computational efficiency from finite-difference and geometry flexibility from finite element methods. The accurate conservation of salt, heat, and mass is provided by the flux computational method. In the vertical, the equally spaced 40 sigma layers were used. While the number of layers is constant in the domain, the thickness of the layer changes based on the water depth and water level. FVCOM is equipped with the Message Passing Interface (MPI) parallelization which maximizes the efficiency of the model run (Chen et al., 2006). The model was run for two months of simulated time and carried out on the Atlantic Computational Excellence Network (ACEnet) high-performance computing network. It took 320 CPUs and three days to finish two months of simulation. The output was the NETCDF files which included the hourly data of water level, salinity, temperature, and west and east current velocity in forty vertical layers. For this study, FVCOM version 4.1 was used and the Coriolis effect for the nodes was included.

3.2.2 Mesh Generation

The mesh (Figure 3) is generated by the Surface Water Modeling System (SMS 12.1) (Surface-Water Modeling System, Version 11.0, Reference Manual & Tutorials, Aquaveo 2012) to create the unstructured grid for FVCOM. The unstructured mesh is a computational grid system that has an irregular shape polygon, in this case, a triangle (called an element), to discretize the ocean domain. These types of mesh are more flexible than the structured ones, which allows for easily generating a high-resolution mesh for the area of interest and reducing the resolution in less important regions. The mesh quality

recommendation for FVCOM is as follows based on the FVCOM manual (Chen et al., 2013): the minimum/maximum interior angle of each element in the mesh is 30/130 degrees, the maximum depth slope inside each element is 0.1, the adjacent element area change 0.5, and the maximum connecting elements to a node equals to 7.

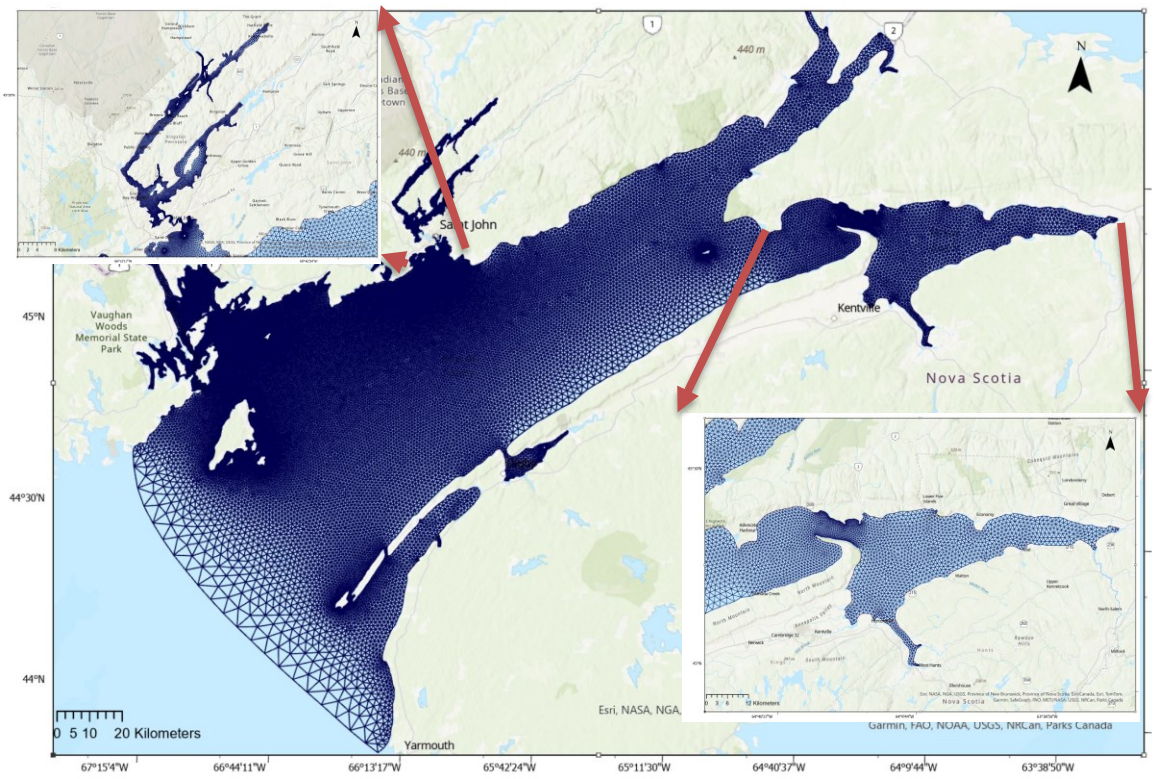

Figure 3. Unstructured mesh generated by SMS and location of two high-resolution spots.

The total number of nodes and elements is 34871 and 64765, respectively. km in the open boundary attached to the Gulf of Maine to 30 m in the Reversing Falls in the Saint John River. The open boundary at the upper part of the Saint John River is at Evandale point which is considered as the place where the salt wedge of Bay of Fundy would reach (Metcalfe et al., 1976) and the freshwater is considered as the open boundary in the model.

For time integration, the mode-split scheme is used to separate the time step between the internal (baroclinic) and external (barotropic) modes with the "isplit" equals to one. The model is set to run in 3D barotropic first with time steps set to 0.5 seconds and then it is run with 3D baroclinic mode with time step of 0.3 seconds. Spatially constant values for the minimum bottom roughness have been examined and the results are provided in section 3.3.1. Figure 4 shows the distribution of the mesh resolution in the Bay of Fundy in a color plot.

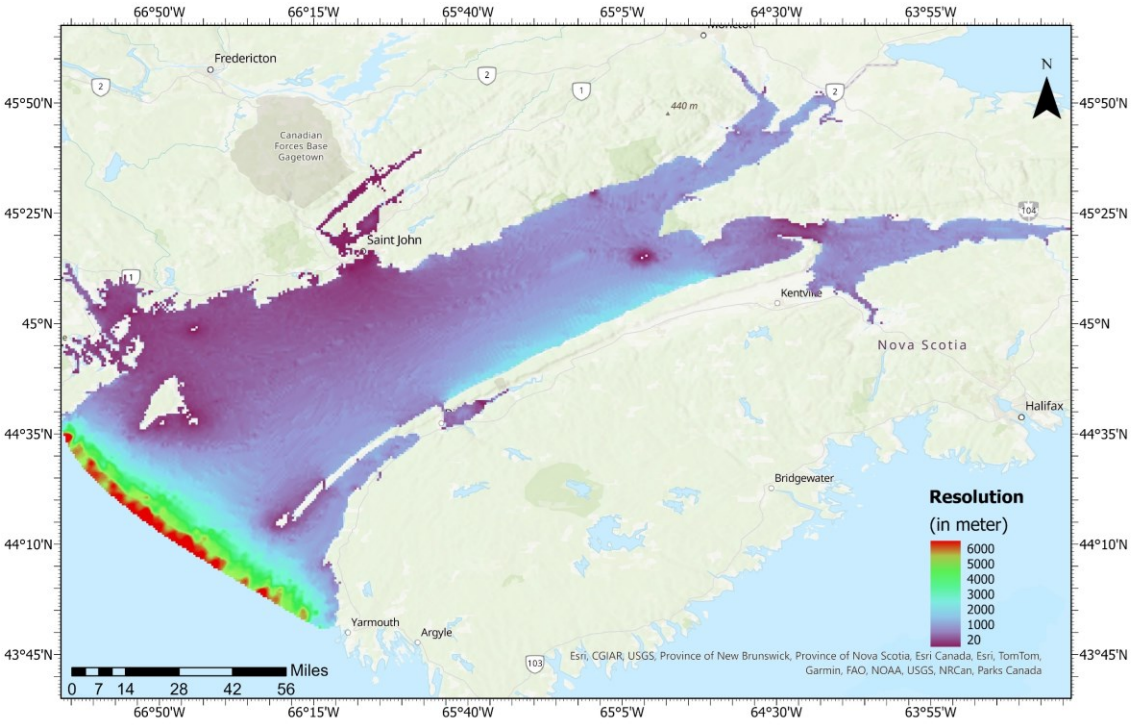

Figure 4. Mesh resolution for the Bay of Fundy model.

3.2.3 Surface Forcing

The benefits of using a high-resolution weather model are in capturing the smallest scales of motion (Skamarock & Klemp, 2008), better representation of land topography close to the coast for simulating more accurate wind patterns, and having a detailed

parameterization for cloud and precipitation processes (Milbrandt et al., 2016). Two datasets have been used as the surface heating in the model for comparison. The domain and a short description of both are provided in 3.2.3.1 and 3.2.3.2.

3.2.3.1 HRDPS

The High-Resolution Deterministic Prediction System (HRDPS) is a real-time numerical weather prediction system, that has been run by Meteorological Services of Canada (MSC) since November 2014. It provides deterministic forecasts on a regional domain with a 2.5-km horizontal resolution and a range of vertical resolution from 100 to 150 meters near the surface to coarser resolution at higher altitudes, covering a large portion of Canada using the Global Environmental Multiscale (GEM) forecast model. To reduce the spin-up time for clouds and precipitation, HRDPS uses the initial surface fields from a coupled high-resolution (2.5-km) land data assimilation system, and initial hydrometer fields from the forecast of a 2.5-km cycle. The model is run four times daily and provides a 48-hour forecast. The results have been tested and compared to the 10-km operational system and both systems were evaluated against surface observations (temperature, humidity, winds, and precipitation), fractional cloud coverage, and upper-air soundings. The evaluation shows that HRDPS generally outperformed the operational system (Milbrandt et al., 2016). The HRDPS forecasts are on a regional domain with a horizontal resolution of 0.0225° latitude and it is initialized at 0000, 0600, 1200, and 1800 UTC. Figure 5 shows the continental domain coverage of HRDPS in which the surface force was extracted.

The initial and lateral boundary conditions to run the HRDPS are provided by a Regional Deterministic Prediction System (RDPS) (Bélair et al., 2000), consisting of three main

components: a land data assimilation system, a coupled 2.5-km GEN 6-h cycle system, and a full 48-h 2.5-km GEM forecast run. The upper-air initial conditions are from RDPS analysis, the lateral boundary conditions from RDPS forecast, and the upper-boundary nesting technique (Mctaggart-Cowan et al., 2011) from RDPS hourly field is applied for levels above 10hPa. The 62 vertical levels are used for model integration.

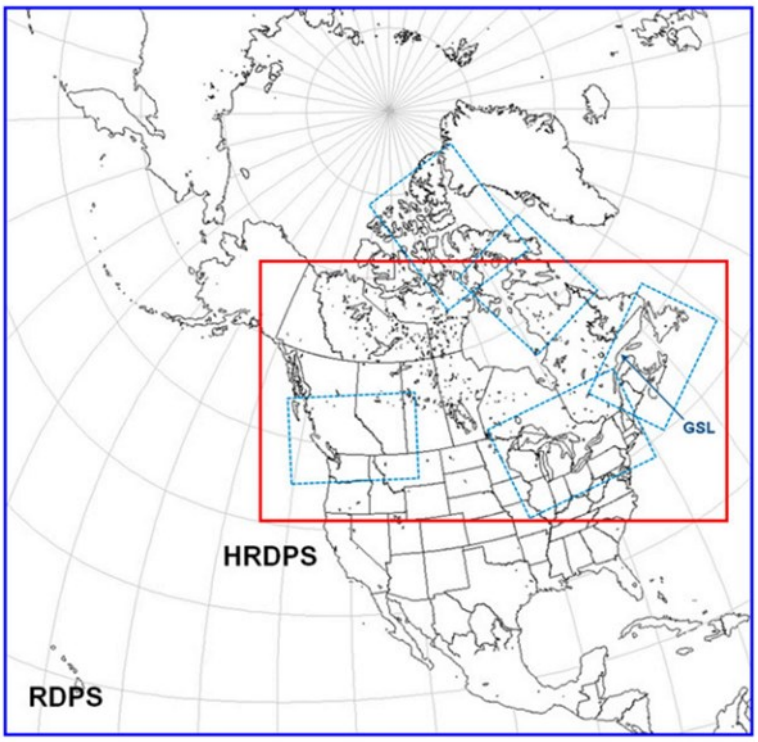

Figure 5.The computational domain for continental HRDPS (2.5 km in red), RDPS (10 km in blue), Gulf of St. Lawrence, and other experimental domains (in dashed blue), from Milbrandt et al. 2016.

A combination of Kuo transient shallow convection (Bélair et al., 2005) and the two-moment version of the (Milbrandt and Yau 2005) bulk microphysics schemes are used for cloud and precipitation. A correlated-k distribution scheme (Li & Barker, 2005) is used for radiative transfer calculation. The surface initial conditions for the mean temperature, root zone soil moisture, and snow depth are provided by a coupled 2.5-km resolution of the

Canadian Land Data Analysis System (CaLDAS), (Carrera, Bélair, & Bilodeau, 2015)) and this high resolution of CaLDAS (which is an important component of the HRDPS) increases the ability of the model to capture the moisture gradients resulting in the initiation of deep convection. The results of the comparison of HRDPS and RDPS with the observations show a slight deterioration in its performance in comparison to RDPS for the continental HRDPS domain in the summer for simulating the 2-m air temperature and 10-m wind speed (Milbrandt et al., 2016). In the Maritimes, HRDPS shows a colder bias than RDPS (both comparing against observations), and a lower wind speed. In the wintertime for the whole domain, the skill of HRDPS increases slightly for predicting the 2-m air temperature and shows a significant improvement for the 10-m wind speed. In the Maritimes, the 2-m air temperature in HRDPS is slightly closer to the observation and shows some cold and warm bias, while RDPS generally shows clod bias in this region. As to the 10-m wind speed, HRDPS mostly underestimates the wind speed while RDPS mostly overestimates the wind speed. In general, the forecast skill of the HRDPS (2 km) is generally improved over that of coarse resolution RDPS (10 km) (Milbrandt et al., 2016).

3.2.3.2 NARR

The North American Regional Reanalysis (NARR) (Mesinger et al., 2006) from the National Centers for Environmental Prediction (NCEP) is a high-resolution, 32 km in horizontal and 45 layers in the vertical, high frequency (3-hourly), atmospheric and land surface hydrology dataset for the North American domain (Figure 6) which covers a 25-yr period of 1979-2003 and is continuing in near-real time as the Regional Climate Data Assimilation System (R-CDAS). It benefits from assimilating high-quality and detailed

precipitation observations into the atmospheric analysis and consequently, provides a better reanalysis of land-atmosphere interaction than previous reanalysis. The precipitation data for the continental United States comes from the gauge dataset analyzed using PRISM at 1/8 degree and 1-degree gauge dataset from Canada and Mexico. For both initialization and the lateral boundary conditions, it uses the NCEP-DOE GR2 (Department of Energy Global Reanalysis 2). Wind and moisture datasets are provided by the surface stations and ship and buoy data and snow depth from the Air Force snow dataset. A list of data used in NARR and NCEP-DOE and the added data to improve NARR is provided in Table 1 and Table 2, respectively. There are some fixed fields as an input for the land surface model including land mask, vegetation type, soil type, surface slope category, maximum snow albedo, soil column bottom temperature, and the number of root-zone soil layers (Ek et al., 2003; Mitchell et al., 2004).

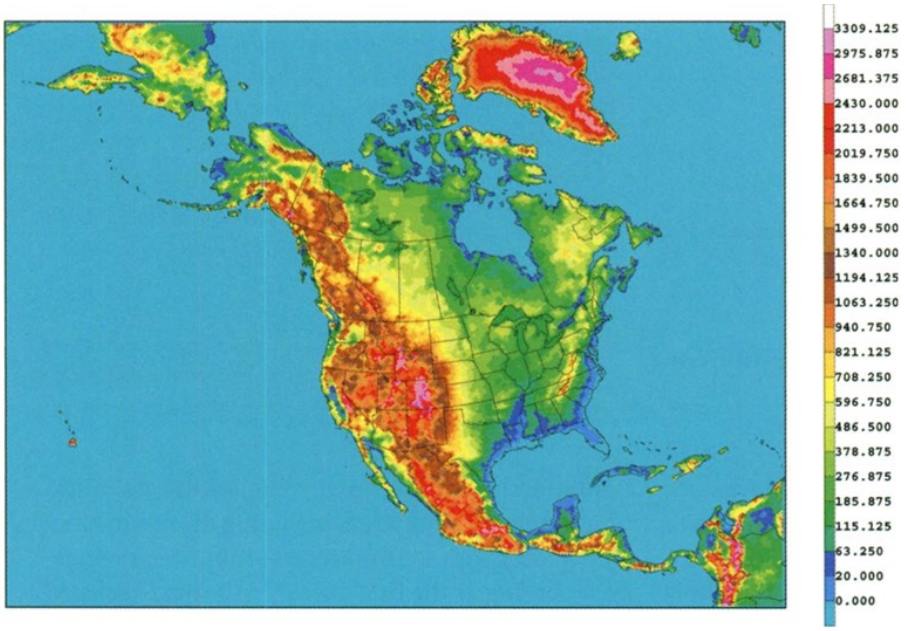

Figure 6.The NARR domain and 32-km terrain elevation(m), from Mesinger et al. 2006.

Table 1. Data used in both the NCEP-DOE Global Reanalysis and in the North American Regional Reanalysis from Global Reanalysis 2 (GR2), Mesinger et al. 2006.

Dataset	Observed variable	Source
Rawinsondes	Temperature, wind, moisture	GR2
Dropsondes	Same as above	GR2
Pibals	Wind	GR2
Aircraft	Temperature and wind	GR2
Surface	Pressure	GR2
Geostationary satellite	Cloud drift wind	GR2

Table 2. Data added or improved upon for the North American Regional Reanalysis from Mesinger et al. 2006.

Dataset	Details	Source
Precipitation, disaggregated into hours	CONUS (with PRISM), Mexico, Canada, CMAP over oceans (< 42.5 °N)	NCEP/CPC, Canada, Mexico
TOVS-lb radiances	Temperature	NESDIS
NCEP surface	Wind, moisture	GR2
MDL surface	Pressure, wind, moisture	NCAR
COADS	Ship and buoy data	NCEP/EMC
Air Force snow	Snow depth	Air Force Weather Agency
SST	1 Reynolds, with Great Lakes SSTs	NCEP/EMC, GLERL
Sea and lake ice	Contains data on Canadian lakes and Great Lakes	NCEP/EMC, GLERL, Ice Service Canada
Tropical cyclones	Locations used for blocking CMAP precipitation	Lawrance Livermore National Laboratory

The most important data addition to the NARR data assimilation is the observed precipitation which provides a more realistic hydrological cycle; however, the model does not assimilate the precipitation directly. It drives the vertical latent heat profiles from

precipitation analyses and then the model produces the NARR precipitation (Mesinger et al., 2006).

South of 27.5°N over the oceans, the CMAP (Climate Prediction Center Merged Analysis of Precipitation) 5-day global 2.5-degree precipitation analysis (Xie & Arkin, 1997) is disaggregated to hourly precipitation using the GR2 hourly precipitation forecast and then assimilated into the model. However, north of 42.5°N, there is no assimilation of precipitation over the ocean (where the CMAP is increasingly less reliable). In the case of assimilating the near-surface atmospheric observation (Near-surface wind, moisture over land) over land, it was found that the "Time" observations have a detrimental impact, and they have turned it off by applying a short time window of 30 minutes centered on the analysis time to all surface observations over land (Mesinger et al., 2006). However, being marginally helpful, the assimilation of surface wind and moisture observations is included in the runs. The sea and lake ice data comes from the satellite ice dataset (Grumbine, 1996) and interpolated to the NARR grid as logic values of 1 or 0 (ice or no ice), and alternatively, the data could be from NESDIS (National Environmental Satellite, Data, and Information Service) 25-km-daily IMS (Interactive Multisensor Snow and Ice Mapping System). For the Canadian lakes, the ice data were obtained from the ISC (Ice Service Canada). Ocean SSTs for most of the NARR period (1981 and onward) were provided by the 1° Reynold dataset (Reynolds et al., 2002), and for Canadian lakes, the interpolated values between the Pacific and Atlantic oceans are used as SST. In the winter, while the agreement between NARR and observed precipitation is extremely high on land, going from mid to high latitude over the ocean, where the assimilation is gradually degraded, it is not as good. Over summer, the same good agreement with the observations exists over land and an

improvement in comparison to winter over the ocean, but there are still some systematic underestimations. Comparison of the NARR surface data with the observations shows that it overestimates the 2-m temperature mostly in the summer (1-2 degrees) and it has a slight negative bias (underestimate, less than 1 m/s) in both winter and summer for 10-m wind (Mesinger et al., 2006). The NARR project faced several obstacles. First, the unavailability of CMAP precipitation analysis over the ocean in real-time which is replaced by the precipitation analysis from the global 8-km 30-min satellite-based CMOPRH. Second, unavailability of data for ice cover in Canada which alternatively uses daily NESDIS IMS data. However, a climatology of ice cover was used for the Great Lakes and Canadian lakes' ice cover. Finally, the unavailability of observations for the gauge precipitation in Canada resulted in no precipitation assimilation over Canada in the model.

3.2.4 Model Initialization and Open Boundary Forcing

To bring the ocean model close to realistic ocean conditions, ocean modelers set an initial condition for the state of the ocean, including but not limited to temperature, salinity, and currents, representing the ocean condition at the start of the model run period. This is a fundamental step to ensure that the model would simulate and reflect the actual ocean process and conditions. After this step, the model is prescribed by forcing both at the lateral open boundaries at the edge of the domain and also from the ocean surface due to its interaction with the air. These forces account for the energy exchange and properties between the ocean and its surroundings, including the atmosphere, other bodies of water, and rivers.

3.2.4.1 Bay of Fundy Model

The model consists of two open boundaries, one in the Saint John River with three nodes and the other adjacent to the Gulf of Maine with 23 nodes. The surface river water temperature and river water level are from Environment and Climate Change Canada, station from July 1st to September 1st, 2018. The river's open boundary is close to Oak Point station (01AP003). By using this boundary location, it is assumed that we have the freshwater inflow at that point (Metcalfe et al., 1976; Paquin et al., 2020). The time series of river water level at Oak Point is used at the open boundary due to the lack of river flow measurement in that part (Nudds et al., 2020; Paquin et al., 2020). It should be noted that the water level at this station is referenced to CGVD28 which is not the same as the vertical reference level for GoMOFS at NAVD88. To adjust the Oak Point data, three active tidal stations are considered in the region, Saint John, Yarmouth, and Halifax, where the mean water level (MWL) relative to CGV28 is 0.314, 0.299, and 0.277 m, respectively (Paquin et al., 2020). The simulated mean water level based on GoMOFS is 0.111, 0.069, and 0.106 m, which are lower than the MWL of the observations by 0.203, 0.230, and 0.171 m, respectively. The average of three offsets, 0.20 m, is used to be deducted from the observed water level at Oak Point station for the open boundary. Also, only Saint John River is considered as the river input to the model because it is the dominant contributor of freshwater into the Bay of Fundy system with an annual average discharge of around 1100 $km^3\ s^{-1}$ (Cunjak & Newbury, 2005). At the Gulf of Maine's open boundary, the forcing includes tidal elevation, temperature, and salinity. The tidal elevation, with five harmonic constituents for the Bay (M_2, N_2, S_2, K_1, and O_1), is extracted from an unstructured barotropic tidal model, the WebTide Scotia - Fundy - Maine model, which is tuned for the

Bay of Fundy (Dupont, Hannah, & Greenberg, 2005). The 6-hourly time series of temperature and salinity for the open boundary is extracted from the (GoMOFS) (Yang et al., 2016), which uses ROMS (Regional Ocean Model System) with a 700 m horizontal resolution and 30 vertical levels and is running operationally on NOAA's High-Performance Computer Systems (HPCS) predicting the water level, currents, water temperature, and salinity for 72 cycles. As the horizontal resolution of GoMOFS is 700 m, the closest GoMOFS grid point to each open boundary node is used and the Interp1 (MATLAB function) (Akima, 1970, 1974) are applied as vertical interpolation while choosing the linear and extrapolation options. The GoMOFS is also used for the initialization of currents, temperature, and salinity at the start of the simulation. Also, the closest node value of GoMOFS is assigned to the model node that is outside the GoMOFS domain. The model's sea surface is forced with hourly atmospheric data including specific humidity, 2-m air temperature, surface incoming longwave and shortwave radiation, and 10-m wind from the (HRDPS) (Milbrandt et al., 2016) at 2.5 km resolution, which is running operationally at the Canadian Center for Meteorological and Environment Prediction (CCMEP) and North American Regional Reanalysis (NARR). As the Bay of Fundy is a tidal environment and it is a dominant factor in circulation in this region, the model only needs a couple of days (based on the domain area and depth) to reflect and reach a reliable Sea Surface Height (SSH). Also, as the main focus of the model was on the bottom layer and the distribution of temperature and salinity in the water column, the initialization did not include the sea surface height. However, for a better model skill in representing the ocean surface topography and currents, improving the short-term forecast, and reducing the model drift, it is better to include the SSH in the model initialization. The

model is set to run in ‘hot-start’, where model is initialized with an input file, from 1st July to 1st September 2018.

3.2.4.2 Minas Basin Model

For the Minas Basin model, two model configurations are considered, where they both have the same mesh but with different lateral, surface forcing, and initialization. The open boundary is just at the entrance of the basin which in total includes 11 nodes. The mesh resolution distribution is provided in Figure 7. Salinity and temperature time series from the Bay of Fundy model output were used as the input to run this model. To be consistent and have a more relevant comparison with the Bay of Fundy model, the Webtide model, which is calibrated for the Bay of Fundy, with five harmonic constituents (M_2, N_2, S_2, K_1, and O_1) has been used.

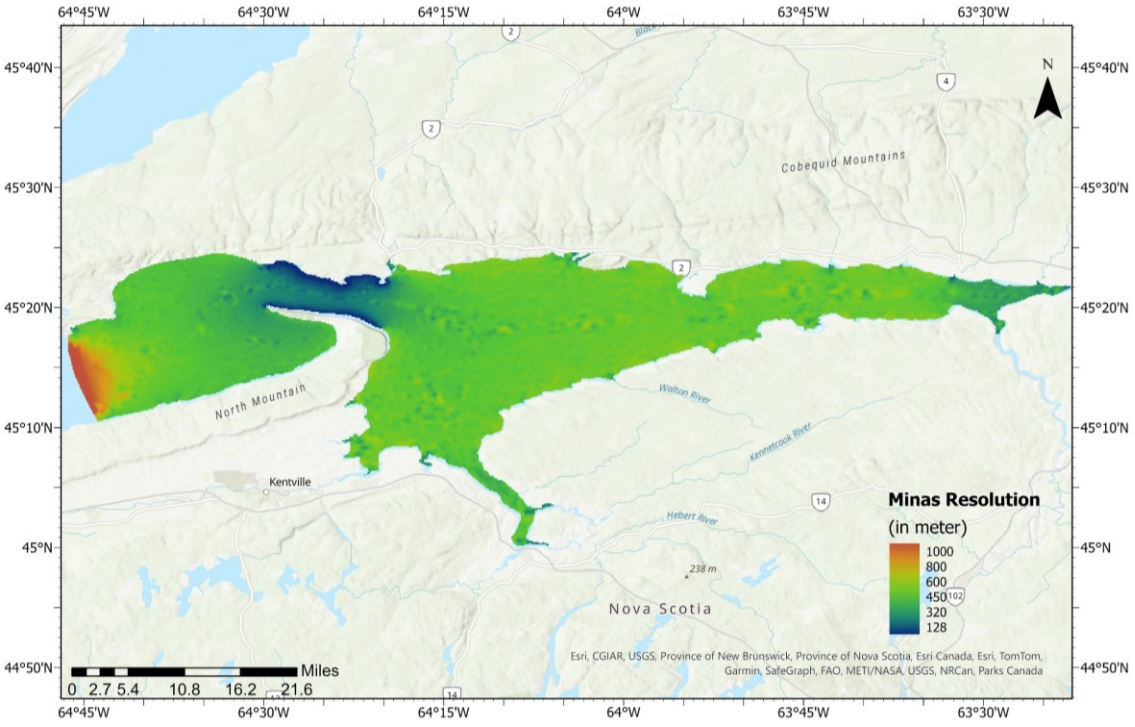

Figure 7. The mesh resolution for the Minas Basin model.

The model's initial conditions have been extracted from the result of the Bay of Fundy model, including temperature, salinity, u, and v, where an Inverse Distance Weighted (IDW) method is applied for the horizontal interpolation. The HRDPS data has been applied as the surface forcing including specific humidity, 2-m air temperature, surface incoming longwave and shortwave radiation, and 10-m wind. The model's run period is the same as the Bay of Fundy model. All other model configurations are the same as the Bay of Fundy model except for external timesteps at 0.5 seconds. The total number of nodes and elements are 10190 and 19388 with a horizontal resolution ranging from 100 to 1100 meters.

Due to the lack of availability of temperature and salinity observation in the Minas Basin in June and July 2018, and to observe and investigate the variability of the water column in that area, the second model configuration in the Minas Basin is run using the same mesh with "hot-start", but with different forcing in 2007 from April 1st to June 30th, covering the observations from MVP campaign in Minas Basin. The forcings at the open boundary (temperature and salinity) and the initial conditions (T, S, U, and V) are extracted from the FVCOM hindcast data for the Gulf of Maine available at the University of Massachusetts Dartmouth database, and the tide is extracted from Webtide. Also, the surface force is extracted from the Global Ocean Forecast System 3.1 (GOFS 3.1) National Center for Environmental Prediction weather forecast model (NCEP) (Mesinger et al., 2006). The model is evaluated against the salinity and temperature from an MVP on a survey campaign in May and June 2007 (Parrott et al., 2013).

3.3 Model Calibration and Validation

The first step for calibration is to check the model output against the tide. To do so, the model is run with different bottom roughness values, and the results are compared against the published tidal constituent for different stations in the Bay of Fundy and Minas Basin. For the validation part, the model output is compared against a tidal current dataset for the 1965 currents survey of the Bay of Fundy (Godin, 1968). Also, a tidal harmonic analysis, "T_Tide" (Pawlowicz, Beardsley, & Lentz, 2002), was performed on the simulated water level and the results were compared with the CHS tidal constituents for the M_2, N_2, S_2, O_1, and K_1 harmonic constituents.

3.3.1 Model Calibration of Bottom Roughness

The sediment erosion, deposition, resuspension, transportation, and vertical mixing are caused directly by the shear stress near the bottom. Also, the hydrodynamic properties of the flow on the bottom boundary layer affect the relationship between the near-bed sediment transport, sediment bed roughness, and tidal velocity (Cheng et al., 1999). The bottom stress is a function of shear velocity, and drag coefficient which in turn is calculated as the following equation in FVCOM:

$$\mathbf{C_d} = \mathbf{max}\left\{ \mathbf{k^2} \Big/ \mathbf{ln}\left(\frac{\mathbf{Z_{ab}}}{\mathbf{Z_0}}\right)^{\mathbf{2}}, \mathbf{0.0025} \right\} \quad \textbf{(1)}$$

, where $k = 0.4$ is the Von Karman constant, Z_0 is the bottom roughness parameter, and Z_{ab} is the height of the first layer above the bottom (Chen et al., 2006).

Based on the bottom friction coefficient equation, different values of the bottom roughness length scale are applied, and the default value of the bottom roughness minimum is changed to get the best-case scenario of the model output. Sankaranarayanan & McCay, (2003) ran a 3-d barotropic hydrodynamic model in the Bay of Fundy and tested a range of bottom roughness, from 0.001 to 0.005 m, and their results show a good agreement with the Saint John River tide data while using the 0.001m as the bottom roughness. Also, Nudds et al. (2020) used the values of 0.001m as the bottom roughness and the Cd_{min} equal to 0.02 in FVCOM in their operational model evaluation for the Bay of Fundy. While a variable bottom roughness length scale could be a closer approximation to real seafloor roughness and better sediment transport simulation (which is a topic out of the scope of this study), a constant bottom drag coefficient has been used in the model. Dupont et al. (2015) ran a 2-Dimensional finite element ocean model including wet and dry configuration for the upper part of the Bay of Fundy using a constant bottom friction coefficient of 0.0025 while Paquin et al. (2020) used three different values for three sections of their model in Bay of Fundy using 0.0025, 0.004, and 0.005 m running a high-resolution ocean model in the presence of strong tides in the Bay of Fundy.

3.3.2 Tidal Validation

To facilitate the tuning process of tides in the Bay, five primary constituents are considered which in total need 27 days of simulation data to perform the tidal analysis.

3.3.2.1 Amplitude and Phase of Constituents

A harmonic analysis (Pawlowicz et al., 2002) was performed on the simulated water level for the whole bay and the results were compared with the CHS tidal constituents for the

M_2, N_2, S_2, O_1, and K_1 harmonic constituents at eight stations in the model domain (Figure 8). The stations are Saint John River (No. 65), Digby (No. 325), St. Andrews (No.40), East Quoddy head (No.21), North head (No. 10), Grindstone Island (No. 160), Five Islands (No. 260), and Burntcoat head (270). The Saint John River Harbor tide gauge is the only active tide station in the Bay of Fundy, however, there was some period of missing data in the tide data time series during the model run period, and thus the comparison is just against one month of tidal observation.

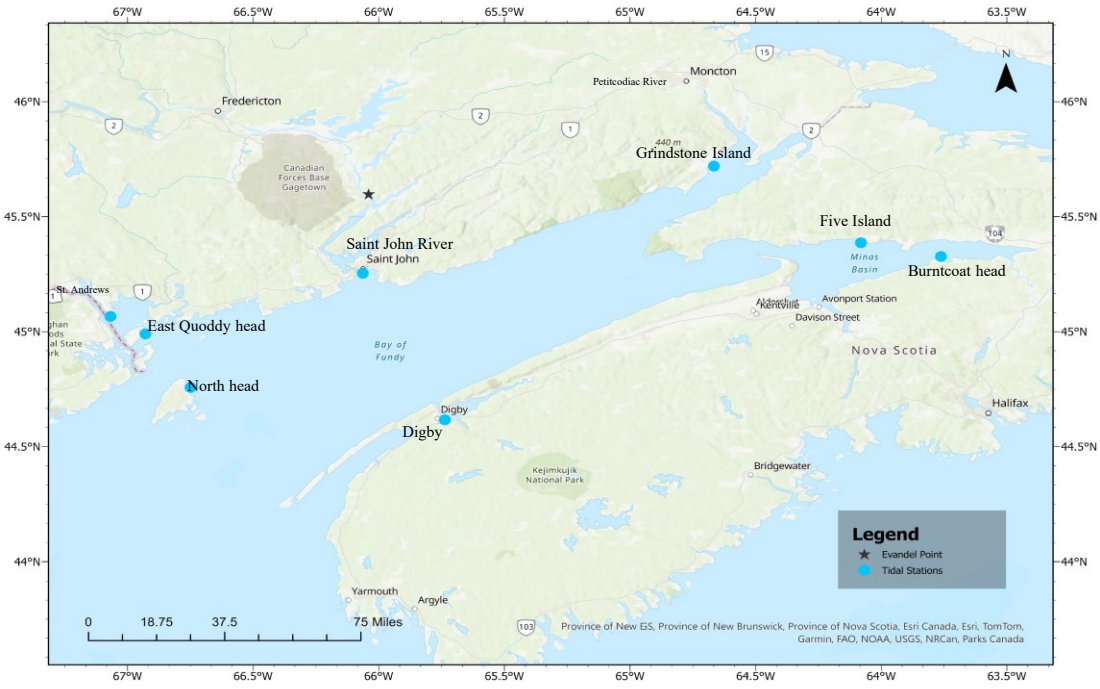

Figure 8. Location of tidal constituent analysis for the Bay of Fundy and Minas Basin (blue circles)

The error metric is the distance in the complex plane between observed (CHS constituents) and modeled constituents (Dupont et al., 2005) and is defined as follows:

$$\boldsymbol{E = \left|A_0 e^{i\emptyset_0} - A_m e^{i\emptyset_m}\right|} \quad \textbf{(2)}$$

where A_0 , $\emptyset_0$ are the amplitude and phase of the observed harmonic and A_m , $\emptyset_m$ are the amplitude and phase of the modeled harmonic. This metric combines the amplitude and phase errors in a single number for validation.

3.3.2.2 Tidal Current Ellipse

To check the simulated current speed against current observations in the Bay of Fundy, the model results are compared against a series of observations collected at 9 stations, Figure 9, by Wu et al. (2014) to validate their three-dimensional tidal model for the Gulf of Main and Bay of Fundy. However, the original data was not available (Figure 10), and the comparison is against the observation provided in a table in that article. Also, the BoF (Bay of Fundy) model and the Minas Basin model are compared against the results of Wu et al. (2014). It is worth mentioning that, the geographic location of the stations was not included in the article but it was very similar to an article on the tide and current in the Bay of Fundy (Sankaranarayanan & McCay, 2003). The latitude and longitude positions of the stations are extracted from this article. The other issue is that there were not any geographic coordinates for the two stations at the Minas Passage. The coordinate of these two stations is selected visually to be as close as possible to Wu et al. (2014).

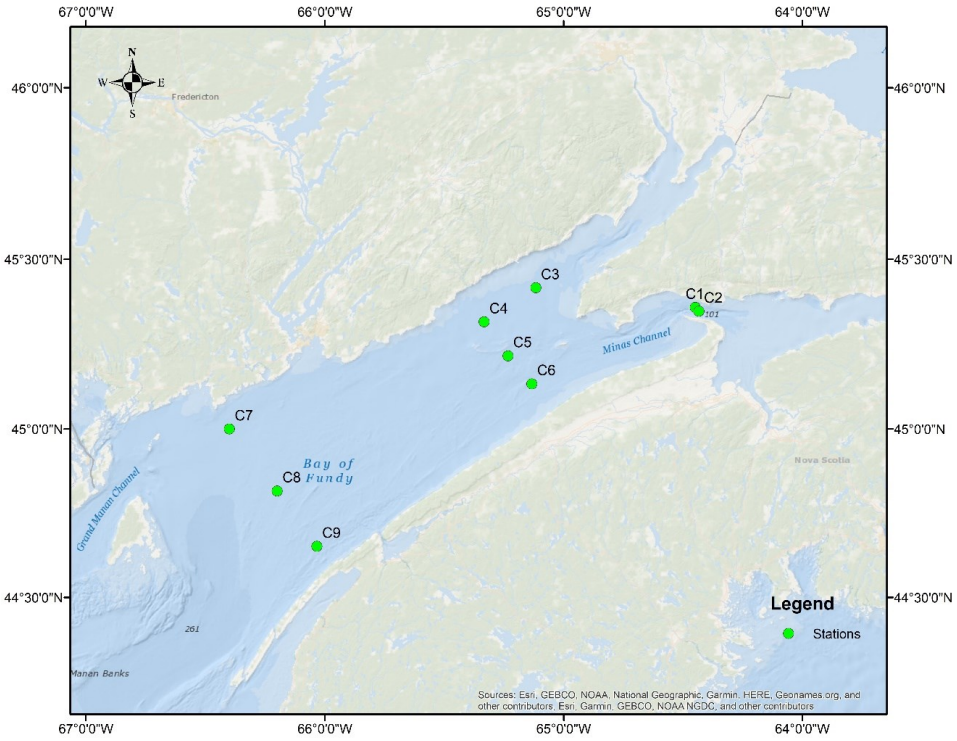

Figure 9. The location of tidal current data (green circles) is used in Tables 7, 8, 20, and 21 (C1 to C9).

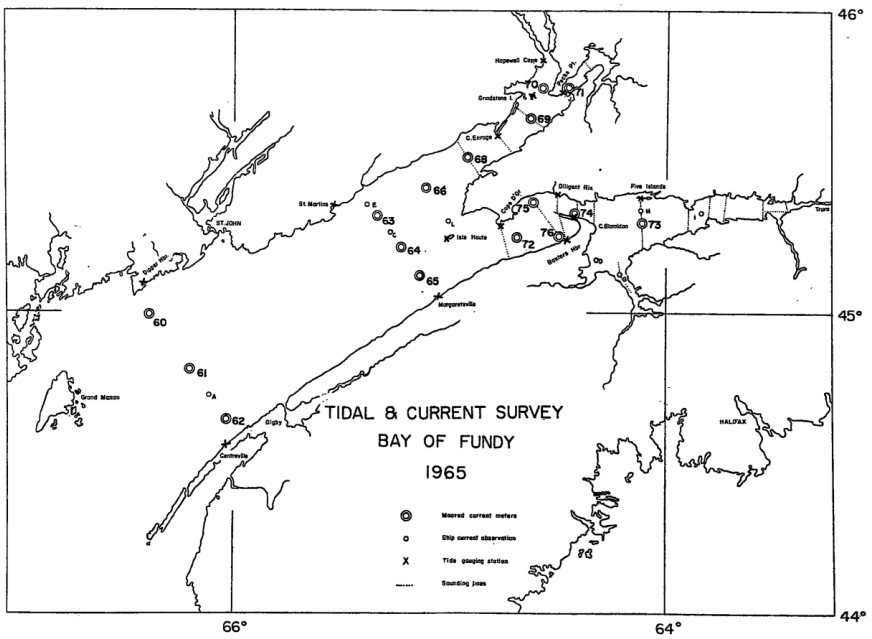

Figure 10. Location of moored current meters in the Bay of Fundy, Minas Basin, and Chignecto Bay, from Bedford Institute of Oceanography, from Godin, 1968.

3.3.3 Baroclinic Validation

The model simulation is evaluated for both the water column variability (in temperature and salinity) and the sea surface.

3.3.3.1 Skill Assessment for Surface Temperature Structure

For the sea surface, the sea surface temperature data used for the evaluation comes from a Group of High-Resolution Sea Surface Temperature (GHRSST) (Piollé et al., 2022), which is a daily gridded product by combining the complementary satellite and in-situ observations within optimal interpolation systems on a 0.054-degree grid. Since the upper 10 m layer of the ocean has a complex vertical temperature, and each satellite and in-situ measurements are different, diverse names are defined for each section of the surface 10 meters of the ocean (Figure 11) (Minnett & Kaiser-Weiss, 2012). For the comparison, the sea surface foundation temperature, the daily mean temperature at 10 m depth, is used which is the temperate excluded from the diurnal temperature variability. A quantitative technique, based on the Taylor diagram (Taylor, 2001), is provided to determine the reliability of the model simulation and compare the two model configurations, the BoF model with HRDPS and NARR.

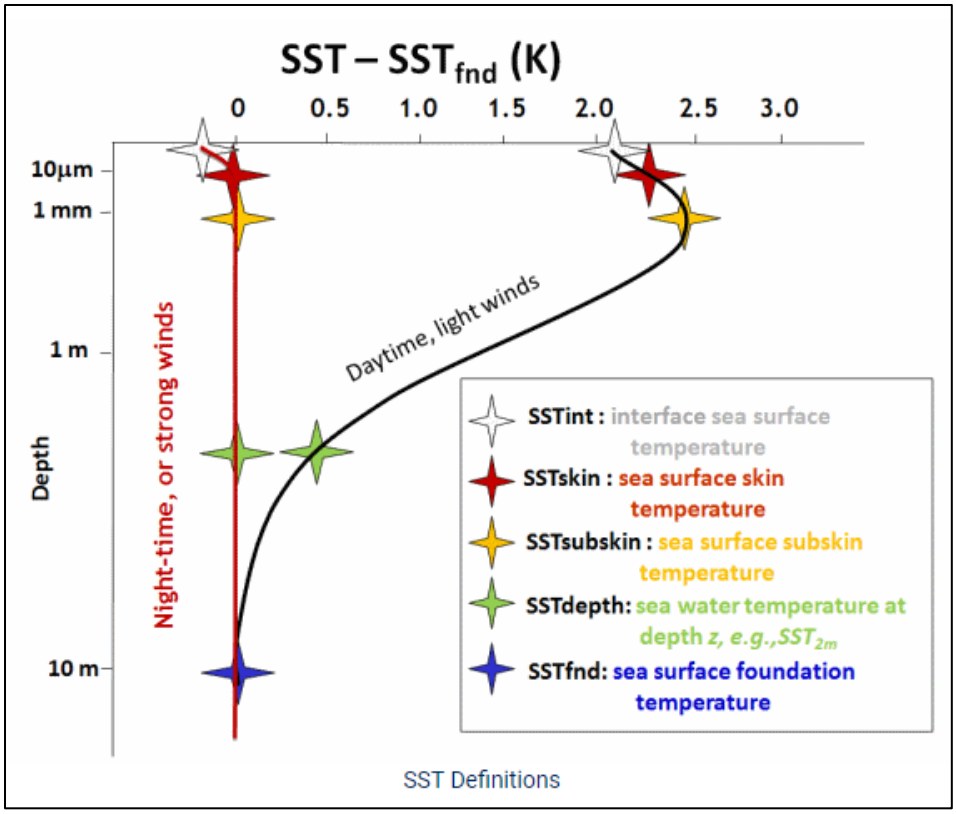

Figure 11. SST definition by GHRSST group, from Minnet and Kaiser-Weiss, 2012.

3.3.3.2 Skill Assessment of the Vertical Structure

To check the large-scale temperature and salinity vertical profiles of the local high-resolution model, the BoF model output with two coarser resolution models, including the global operational model instance of the Global Ocean Forecasting System (GOFS) 3.1 based on Hybrid isopycnal-sigma-pressure Coordinate Ocean Model (HYCOM) (Bleck, 2002), and the regional operational Gulf of Maine Operational Forecast System (GoMOFS) (Yang et al., 2016) are compared against the CTD profile data available in the Bay of Fundy.

Depending on the different specific factors, such as the goals of the modeling exercise, or the spatial and temporal importance of the output variables, the model skill criteria are

subject to change. Generally, the skill means how well the model represents the truth over a specific range of conditions, however, the model output is compared against the observations (having a range of uncertainty in both) (Stow et al., 2009), which are snapshots of observations taken at discrete locations. These are the quantitative metrics to assess the model skill based on the pairs of models and observations (Rodrigues & Fortunato, 2017; Stow et al., 2003; Willmott, 1981). The temperature and salinity output from the baroclinic run are evaluated against a set of 98 CTD casts from Nova Scotia Community College fieldwork in July and August 2018, World Ocean Database (Boyer et al., 2013), and Department of Fisheries and Oceans (DFO) Canada. The model output comparison against all 98 casts is provided in the appendix.

The Bay of Fundy is divided into three parts consisting of the upper part with 38 casts, the middle part with 22 casts, and the mouth of the Bay with 38 casts (Figure 12). Also, the water column is divided into the surface layer, middle layer, and bottom layer. For each CTD cast comparison, three layers are defined with constant depth levels, the surface layer within 10 meters from the surface (De Boyer Montegut, 2004), the bottom layer within 10 meters from the bottom, and the rest is the middle layer. There are two exceptions for this classification, one at a depth greater than 100 m which the bottom layer is considered within 30 m of the bottom, and the other one at a depth less than 25 m where the surface and the bottom layers are assumed to be within 20 percent of depth.

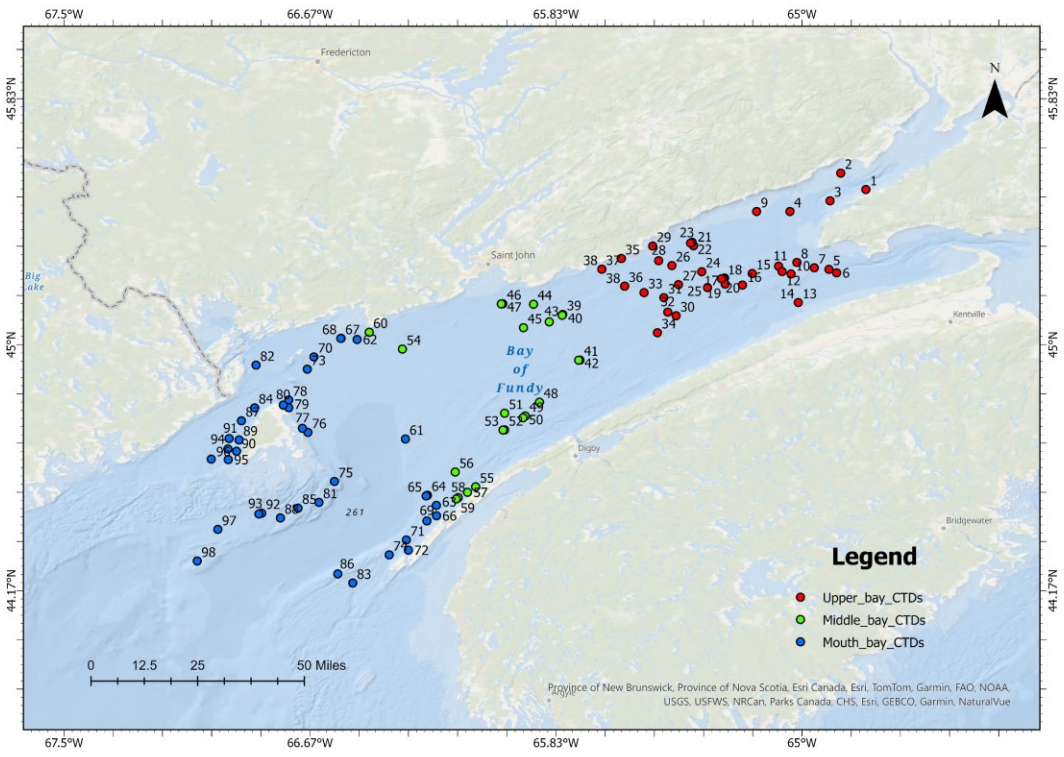

Figure 12. CTD casts from DFO, WOD, and NSCC fieldwork during July and August 2018. The color-coded points represent the head (red), middle (green), and mouth of the Bay (blue) that are being used for baroclinic assessment of the model in the water column.

For each layer, the following metrics are calculated for each section and layers where the model output (P) is compared against the CTD cast (O):

1- r: The correlation coefficient of the model predictions and observations

$$r = \frac{\sum_{i=1}^{n}(O_i - \bar{O})(P_i - \bar{P})}{\sqrt{\sum_{i=1}^{n}(O_i - \bar{O})^2 \sum_{i=1}^{n}(P_i - \bar{P})^2}} \quad \textbf{(3)}$$

2- RMSE: the root mean squared error.

$$RMSE = \sqrt{\frac{\sum_{i=1}^{n}(P_i - O_i)^2}{n}} \quad \textbf{(4)}$$

3- RI: the reliability index

$$I = exp^{\sqrt{\frac{\sum_{i=1}^{n}(log\frac{O_i}{P_i})^2}{n}}} \quad \textbf{(5)}$$

4- AE: the average error(bias)

$$AE = \frac{\sum_{i=1}^{n}(P_i - O_i)}{n} = \bar{P} - \bar{O} \quad \textbf{(6)}$$

5- AAE: the average absolute error

$$AAE = \frac{\sum_{i=1}^{n}|P_i - O_i|}{n} \quad \textbf{(7)}$$

6- ME: the modeling efficiency

$$ME = \frac{(\sum_{i=1}^{n}(O_i - \bar{O})^2 - \sum_{i=1}^{n}(P_i - O_i)^2)}{\sum_{i=1}^{n}(O_i - \bar{O})^2} \quad \textbf{(8)}$$

, where n = the number of observations, Oi = the ith of n observations, Pi = the ith of n predictions, and $\bar{O}$ and $\bar{P}$ are the observation and prediction averages, respectively.

The tendency of the observed and predicted values to vary together is measured by *r*, the correlation coefficient which ranges from -1 to 1. The *r* value will ideally be close to one,

however, the values could differ by a consistent value while still having the *r* close to one, as it does not account for biases.

The magnitude of discrepancies between the observation and prediction is measured by the root mean squared (RMSE), average error (AE), and average absolute error (AAE) with ideal values close to zero. The AE is a measure of aggregate model bias and AAE and RMSE consider the magnitude of each discrepancy rather than the direction. The average factor by which the model predictions differ from observation is calculated by the RI (Leggett & Williams, 1981) which ideally should be close to one. Finally, The ME measures the model efficiency on how well it predicts relative to the average of the observations (Loague & Green, 1991; Nash & Sutcliffe, 1970) where an ideal value of one represents a close match between model prediction and observation. A ME value close to zeros indicates that the model cannot predict each observation better than the average of observations, and for values less than zero, it is better to use the average of the observation than the model prediction. Based on the National Ocean Service (NOS) skill assessment, an ocean model has a good skill where having an RMSE of 10-20 cm and a correlation coefficient of higher than 0.9 for water level, an RMSE of 0.5-1.0 °C and 0.1- 0.5 PSU for temperature and salinity, respectively (Zhang et al., 2006).

3.4 Hydrographic Survey Planning and Uncertainty

The capability of autonomous ocean mapping systems has increased rapidly which reduces the operational costs and crew size requirements and eases access to shallow water areas. However, these autonomous systems face some challenges such as in high tidal domains, high surface currents, and river discharge. By having an insight into the hydrodynamic

situation of the domain, a better hydrographic survey could be designed to achieve all the aforementioned capabilities. In a 3D hydrodynamic model for the port of Saint John, it was shown that freshwater discharge and mixing with Bay of Fundy salt water has a significant impact on the sound speed uncertainty for a multibeam survey, and the effect of sound speed uncertainty was provided by maps of IHO order error for the Saint John Harbor (Church, 2014). Three criteria are considered to generate the survey design and calculate the uncertainties regarding each and combined criteria.

3.4.1 Sound Speed Error Estimation

From the hydrographic model, the water column variability is available both in space and time, and the sound speed could be calculated based on the spatiotemporal resolution and provide a framework to increase both the accuracy and efficiency of the hydrography survey planning. This is a step with a wider view than the survey planning based on the line spacing and depth gradient. By utilizing this method, the surveyor gets a complete overview of the survey area in space and time, and then the survey line planning would be applied accordingly.

In every survey, depending on the order requirements, the survey should not exceed the allowable error tolerance provided by international and national survey specifications (International Hydrographic Organization 2011; NOAA 2019). The maximum allowable vertical uncertainty (TVU) is defined by this equation:

$$TVH_{max} = \sqrt{a^2 + (b \times d)^2} \quad \textbf{(9)}$$

, where *a* represents the portion of the uncertainty that does not vary with the depth,

b is a coefficient that represents that portion of the uncertainty that varies with the depth, and *d* is the depth, and each survey order has its *a* and *b* values. Table 3 shows the minimum bathymetry standards for the safety of navigation for each different hydrographic order.

Table 3. Minimum bathymetry standards for the safety of navigation hydrographic survey,(*IHO-S-44_v_6.*).

Criteria	Order 2	Order 1b	Order 1a	Special	Exclusive
Area description (Generally)	**Areas where a general description of the sea floor is considered adequate.**	**Areas where under keel clearance is not considered to be an issue for the type of surface shipping expected to transit the area.**	**Areas where under keel clearance is considered not to be critical but features of concern to surface shipping may exist.**	**Areas where under keel clearance is critical**	**Areas where there are strict minimums under keel clearance and manoeuvrability criteria**
Depth THU [m] + [% of Depth]	**20 m + 10% of depth**	**5 m + 5% of depth**	**5 m + 5% of depth**	**2 m**	**1m**
Depth TVU (a) [m] and (b)	**a** = 1.0 m **b** = 0.023	**a** = 0.5 m **b** = 0.013	**a** = 0.5 m **b** = 0.013	**a** = 0.25 m **b** = 0.0075	**a** = 0.15 m **b** = 0.0075

To estimate the optimal timing and range for sound speed cast by using the uncertainty estimation of oceanographic variability, the ray-tracing error is applied to the water column. There are two approaches to performing raytracing, constant gradient velocity and constant velocity. As the sound speed in the ocean is a function of temperature, salinity, and pressure, where the latter is a function of depth, the constant gradient velocity is a better option where there are significant variations in these variables (Jensen et al., 2011; Oliveira, Lin, & Porter, 2021). Also, as the constant gradient approach is more complex, it requires more computational resources (Jensen et al., 2011; Oliveira et al., 2021). As the Bay of Fundy is under 200-meter depth, the constant velocity is more acceptable which provides sufficient accuracy for ranges less than a few hundred meters (Medwin & Clay, 1998). In this method, the ocean layer consists of n layers each with a different sound speed,

and assuming that the sound propagates at constant speed in each layer and according to Snell's Law, the beam angle is calculated in the next layer. Figure 13, (Li et al., 2018), shows the propagation of sound in a layered ocean.

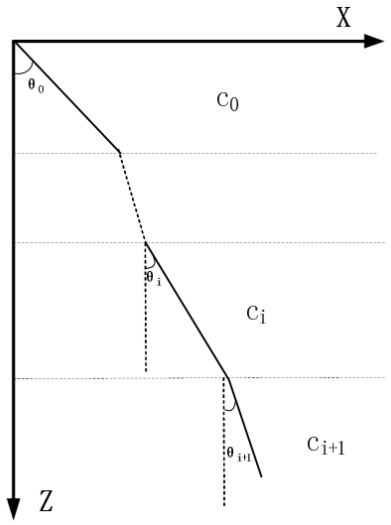

Figure 13. Sound propagation in ocean layers retrieved from Li et al. 2018.

According to the Snell's Law:

$$\frac{\mathrm{Sin}\,\theta_i}{c_i} = \frac{\sin\theta_{i+1}}{c_{i+1}} = p \qquad \textbf{(10)}$$

, where p is the Snell constant, θ_i is the angle between the sound wave of the ith layer and the normal to the horizontal plane (or incident angle of the ith layer), and C_i is the sound speed of the ith layer.

The total horizontal displacement is calculated by using the constant sound speed ray tracing method and is illustrated in Figure 14, (Li et al., 2018).

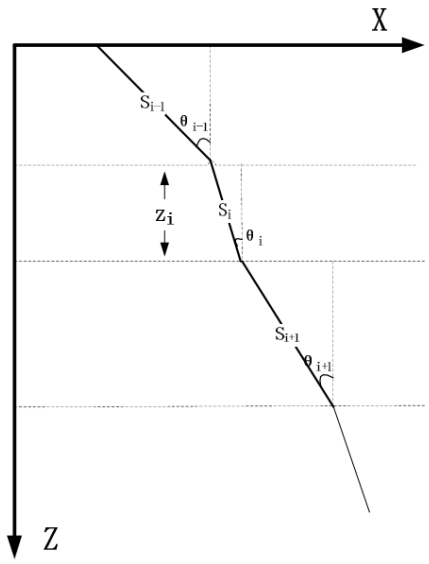

Figure 14. Constant sound speed ray tracing method, retrieved from Li et al. 2018.

According to the physical and geometrical functions we have:

$$\cos\theta_i = \frac{z_i}{S_i} \tag{11}$$

, and the horizontal displacement and time of the acoustic wave through the ith layer are:

$$x_i = x_i * \tan\theta_i = \frac{p.\ c_i.\ z_i}{\sqrt{1 - (pc_i)^2}} \tag{12}$$

$$t_i = \frac{S_i}{c_i} = \frac{z_i}{\cos\theta_i\ .\ c_i} = \frac{z_i}{c_i * \sqrt{1 - (pc_i)^2}} \tag{13}$$

The total horizontal displacement is:

$$X = \sum_{i=1}^{n} x_i = \sum_{i=1}^{n} \frac{p \,.\, c_i \,.\, z_i}{\sqrt{1 - (pc_i)^2}} \qquad \textbf{(14)}$$

, where x_i is the horizontal displacement and time t_i of the acoustic wave passing through the ith layer, S_i is the path length of sound propagated in the ith layer, and X is the total horizontal displacement. Figure 15 shows the results of ray tracing using two sound speed profiles for the adopted swath sector of 70° (Masetti et al., 2017). One profile is considered as the true CTD cast and the other one is the synthesized sound speed profile either from climatology atlases or prediction from oceanographic simulations. Then the ray tracing is applied using the synthesized profile to check how much uncertainty in both horizontal and vertical coordinates would be generated using this profile. After 45° degrees in swath angle, both horizontal and vertical bias increase.

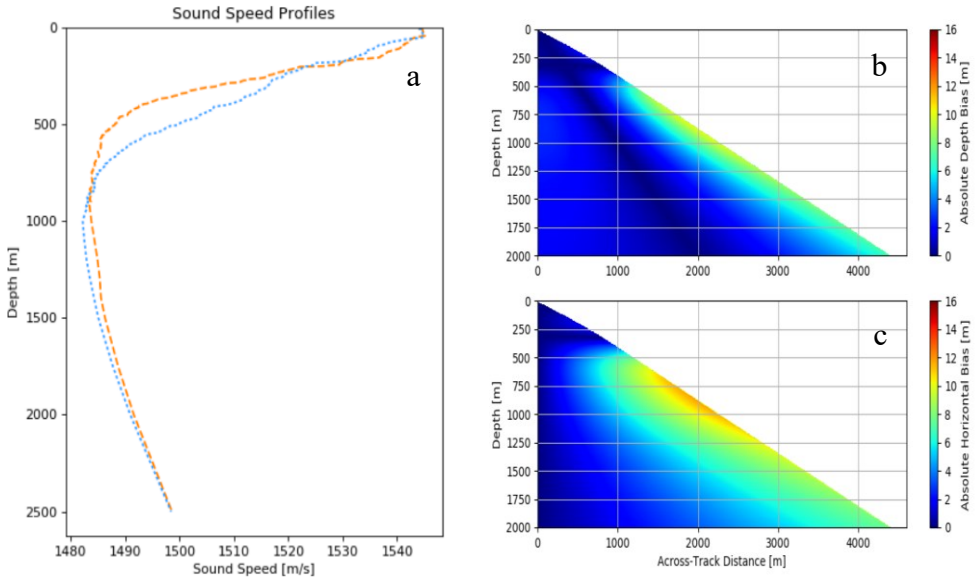

Figure 15. a) Sound speed profiles used for raytracing, one as the true CTD profile and the other as a synthesized profile, b) the absolute bias for depth, and c) horizontal bias, Masetti et al. 2017.

Considering a minimum depth and picking a starting node (in the FVCOM grid) as the first synthesized CTD, raytracing is performed for the surrounding (all nodes in the model) node profiles. The assumption here is that these nodes have the correct sound speed profile and the impact of using the wrong CTD (first synthesized) is calculated at each node location in time. Also, the measurement from the surface sound speed probe and correction of sound speed at the sonar head could ensure that there is no error related to beam steering from surface sound speed. If the depth bias, the vertical difference between the raytracing using the correct sound speed profile and synthesized CTD profile, at the user-defined angular sector is higher than a certain threshold, then it is considered as the area where it needs another sound profile. Using this method, the survey area is classified for each time step based on the survey-required accuracy level and depth bias calculated from raytracing.

Some criteria need to be met before performing the raytracing. The huge tidal range in the Bay of Fundy and Minas Basin generates tidal flats which are one of the challenges in the survey design objectives, specifically in the Minas Basin where the large tidal flat makes the acoustic survey impossible, and these areas are rarely covered by hydrographic survey. Usually, in shallow areas where the hydrographic survey is demanding, LIDAR (Light Detection and Ranging) would be an alternative option, however, the mud flat with a high concentration of clay sediment in the water column could generate turbid water, which makes the LIDAR survey less accurate and useful (Zhao et al., 2018). Also, based on the vessel type, its draft, and the maximum surface current speed, the operatable areas should be considered for that boat. Combining all these criteria and standards, the survey design procedure receives the environmental variability in space and time, CTD cast, and provides the time window for a different part of the survey area, the casting requirement, anchoring

points, and finally after the survey area partitioning, other automated survey line planning can be used. In the case of Minas Basin, a proposed survey plan would have a big boat starting outside the Basin and the Autonomous Surface Vessel (ASV) goes in on flood and retreat with the ebb.

3.4.2 Tide

The model output variable zeta (Sea Surface Height), ζ, and the bathymetry are used to reach the total water depth at any time step. By having the vessel draft a threshold could be specified for the total water depth. The available depth between the lowest point from the ship keel to the seafloor at any given location *L* and a given time t is called Under- Keel Clearance (UKC) (Figure 16) (CIDCO n.d.).

$$UKC(P,t) = Z(P) + T(P,t) - (d + h(t)) \quad \textbf{(15)}$$

, where:

UKC(P,t) is the under-keel clearance at any position and time,

Z(P) is the sounding at the location *P*, which is referenced to the Chart Datum,

T(P,t) is the water level at position *P* and time *t*,

d is the vessel draft, and

h(t) is the vessel's heave at time *t*.

Then, based on a certain threshold (coming from the vessel specification), the areas with a high chance of grounding or being hazardous for surveying could be depicted and predicted.

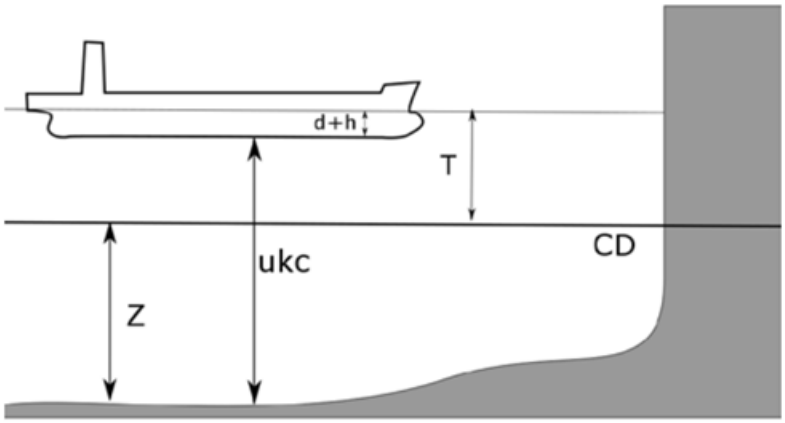

Figure 16. Under-keel clearance definition. The UKC is the instantaneous under-keel clearance, T is the instantaneous water level, d is the vessel draft, h is the vessel heave, the CD is the Chart Datum, and Z is the sounding referenced to the CD.

3.4.3 Surface Currents

There is a high risk of drifting due to surface currents, especially for autonomous vehicles that could be susceptible to strong surface currents which could affect the vessel trajectory (Schmidt, 2020; Stateczny et al., 2020) and their battery consumption. While performing the hydrographic survey, gaps could be generated in the data. The other concerning issue is the energy consumption in these survey platforms where their requirement to keep the survey line would apply more work on the vessel's propulsion system and drain the battery in the presence of strong currents. Also, finding an anchorage site that can satisfy the vessel draft and is less prone to high surface currents could be beneficial for the survey.

The bearing and speed magnitude will be derived from the ocean surface current velocity with the components u and v in the x and y direction, respectively. For each time step, the survey area could be classified as the potential areas where there is a high and low risk of

drift. Figure 17 shows an example of a drift polygon with a low and high probability of drift using the Global Ice Prediction System (GIOPS) (Chénier, Abado, & Martin, 2018).

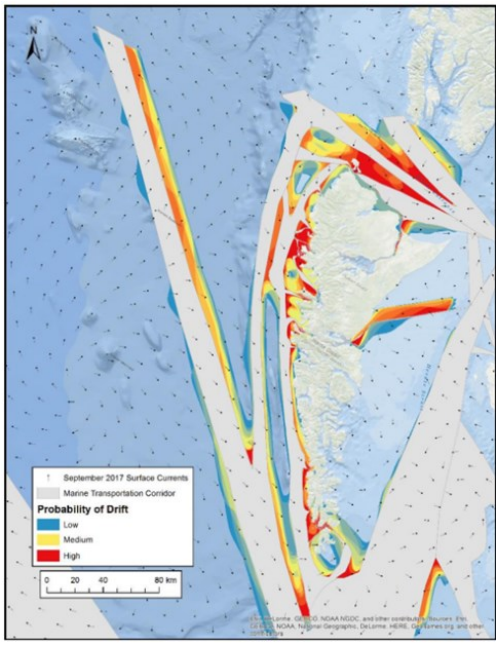

Figure 17. Predicted drift polygon, from Chenier et al. 2018.

3.4.4 Weighted Criteria Matrix

Multi-Criteria Decision Making (MCDM) plays an important role across different industries where we have different criteria to consider, and we need to get the best combination of these criteria to reach the desired goal. The MCDM could be used in structuring the sustainability of asset management, marine risk management, investigating the optimal wind farm setting, or environmental and disaster management (Brodny & Tutak, 2023; Jeong et al., 2018; Jiang et al., 2024).

These three steps are followed to create an MCDM model but more specific details are provided by Hansen and Devlin 2019. (Hansen & Devlin, 2019):

1- Defining the relevant criteria

2- Generate the score for each criterion.

3- Determining the weights for each criterion

The criteria should be relevant to decision-makers, in this case, the surveyable area while satisfying the survey vessel limitations, without any overlaps, and independent. The water depth (depth and instantaneous water level from tide), current speed (the magnitude of west and east velocity), and sound speed error estimation (based on the sound speed raytracing) are picked as the criteria for this study. The next step is to generate the scoring for each criterion. The criteria could be either qualitative (good or bad) or quantitative (value assigned). The latter needs to be quantified at different levels and get a proper numerical score based on the performance. The scoring for each criterion is usually normalized from 0 to 1 in which zero means the worst performance and 1 the best one. This scoring could be conducted based on a value function (Equation 16) which relates possible outcomes to a scale that shows the decision maker's preferences (Malczewski & Rinner, 2015). In that step, weighting the criteria; the relative importance is determined for each criterion to decision-makers by assigning their relative weights which sum to unity across all criteria (Hansen & Devlin, 2019; Malczewski & Rinner, 2015).

$$v(a_{ik}) = \left(\frac{\max\{a_{ik}\} - a_{ik}}{r_k}\right)^p \quad \textbf{(16)}$$

, where a_{ik} is the level of the k-th criterion (k =1, 2…, n) for the i-th alternative (i =1,2,…,m), r_k is the k-th criterion range, $v(a_{ik})$ is the standardized score value ranging

from 0 (least desirable) to 1 (most desirable), and p is equal to one for the linear value function.

For each time step, the water depth and current speed are considered as the first criteria and apply score and weight to generate a base layer for sound speed error estimation to create the final output. To provide a normalized scoring for water depth and current speed, a specific scenario is proposed. The idea is that in a domain like Minas Basin, the mother ship could only do a cast once on the safe part of the domain and the ASV is not able to perform a cast on the shallow regions on its own. This is the only cast that the survey planning relies on. The minimum water depth is 5 meters to satisfy the limitation of the mother ship, and the maximum surface current speed for the survey vessel is 1 m/s (ex. Odetti et al., 2020), which considers the ASV limitation on a high surface current speed environment. Figure 18 and Figure 19 show the unitless normalized scores for both criteria which have the range from 0 to 1 and are multiplied by 100. For normalizing the depth, a minimum depth of 5 meters is considered, where depth equal to or less than 5 meters is assigned zero, and depth higher than 5 to the maximum depth gets values between zero and one (with the maximum depth getting 1). The maximum depth is assigned to one and in this way, different survey vessels could enter the domain if their draft is less than the maximum depth. For the surface current normalization, the same procedure is used while the current speed criteria are set to 1m/s. The surface current speed less than 1 m/s gets 1 and where the surface current speed is higher than 1 m/s up to the maximum surface current speed, these regions are linearly weighted to zero. Then based on the importance and the objectives of the survey and domain, the criterion weights of 0.7 and 0.3 are assigned to water depth and surface current speed, respectively (Figure 18, Figure 19). As a

precautionary step, values that are higher than 31 are accepted as the low-risk nodes to be considered as a safe base layer for performing the IHO standardization check. The value 31 comes from the fact that the area with a depth shallower than 5 meters has the same normalized weight of zero and when there is a zero normalized weight from depth, it is not clear what the depth is (any depths between 0 to 5m). As the surface current speed gets the total weight between 0 and 30, (0 to 100 multiplied by 0.3), if the best scenario where the surface speed total weight is 30, there should be at least a small amount of weight from depth to escape the 0-5 meter range (with 0 weight), this small amount could be any values higher than zero, in this case one. To do this, the total weight of a node is just from the normalized weighted surface current speed, and since the maximum weight comes from the speed lower than 1m/s (at 100), the normalized value of 100 is multiplied by the weight of surface current (0.30) which ends up 30 (total weight = (0.7 *(depth weight from 0-5 which is zero) + 0.30 *(weight of current at zero m/s which is 100))=30). Based on the weighted-sum model Equation 17 (Triantaphyllou, 2000), the nodes having values higher than 31 are accepted and are used to generate the base layer.

$$A_j^{WSM} = \sum_j^n w_j a_{ij} \quad for\ i = 1,2,3,..m \tag{17}$$

, where w_j is the relative weight, a_{ij} is the performance value and A_j^{WSM} is the total importance.

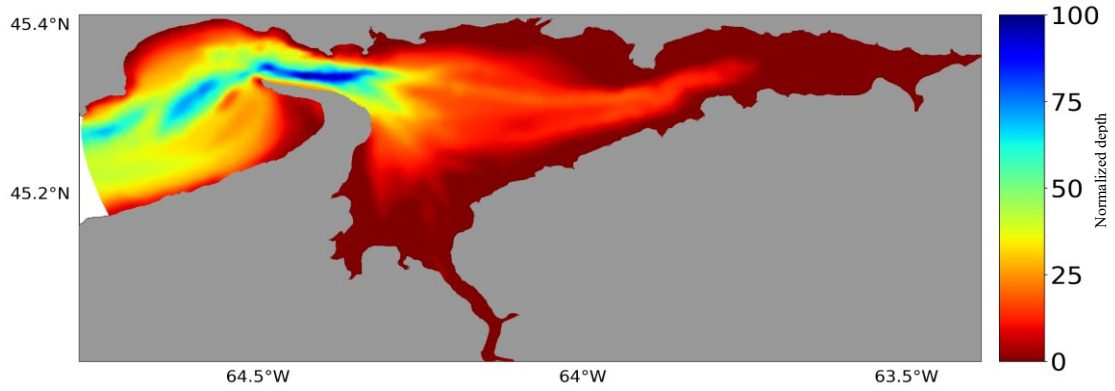

Figure 18. The weighted normalized depth higher than 5 meters at a one-time stamp. The dark red areas are regions with depths shallower than 5 meters, while the blue areas are deep parts.

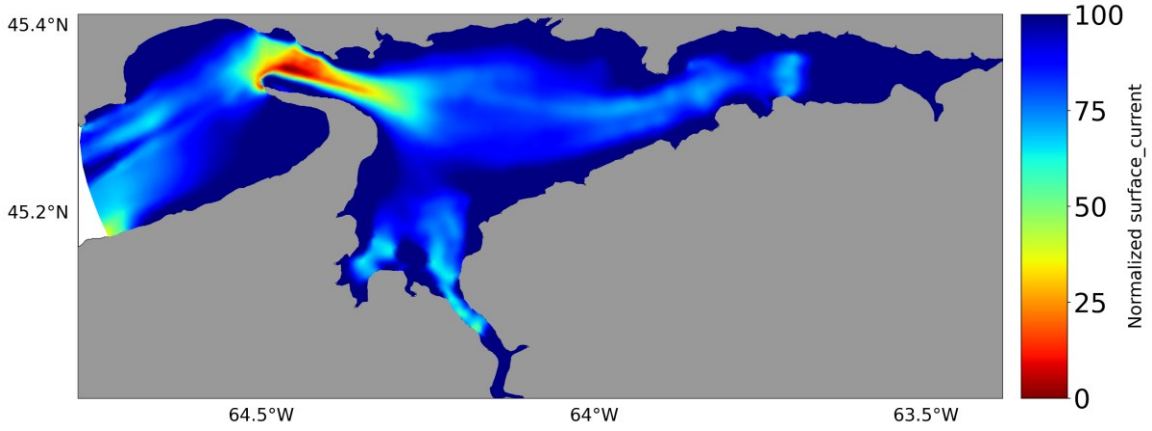

Figure 19. The weighted normalized surface current speed lower than 1 m/s at a one-time stamp. The blue areas are the regions where the surface speed is less than one and close to zero (dark blue) and the red areas are very high surface current speed regions (close to or higher than 1 m/s).

The sum of weighted normalized depth and surface current speed is plotted in Figure 20 showing the rejected areas as white regions having a weight less than 30.

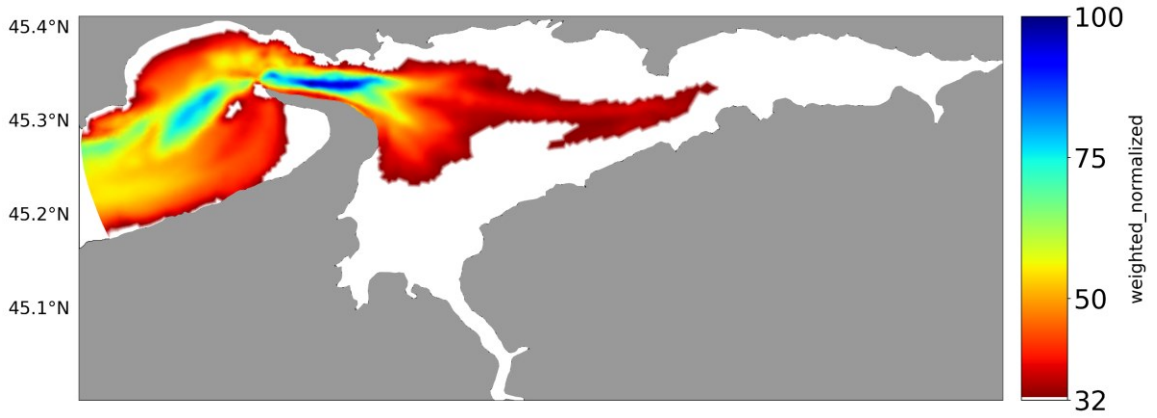

Figure 20. The weighted normalized depth (>5 m) and surface current speed (<1 m/s) at the one-time stamp. The white areas are the places where the combination of both criteria does not satisfy values higher than 31.

Now a refined-based layer is generated to be used for raytracing. To perform this, as the Minas Basin is a very dynamic environment and well-mixed, a node is picked at the entrance of the model to have some different water mass from the inside of the Basin for better depiction of plots. Considering this as the first CTD, the raytracing is performed against the remaining nodes to check how far in space and time we could rely on the first node based on the required IHO order. The Total Vertical Uncertainty (TVU) is calculated only for nodes that were not rejected and compared with the raytracing results to check whether it satisfies that order (Figure 21). Also, Figure 22 shows the percentage of depth error for using the sound speed profile at the first time step and applying that for the half tidal cycle. Based on this computation, maps that show the surveyable area are provided based on either criterion (depth or surface current speed) or both together for one tidal cycle and used to plan the hydrography survey more efficiently and less challenging.

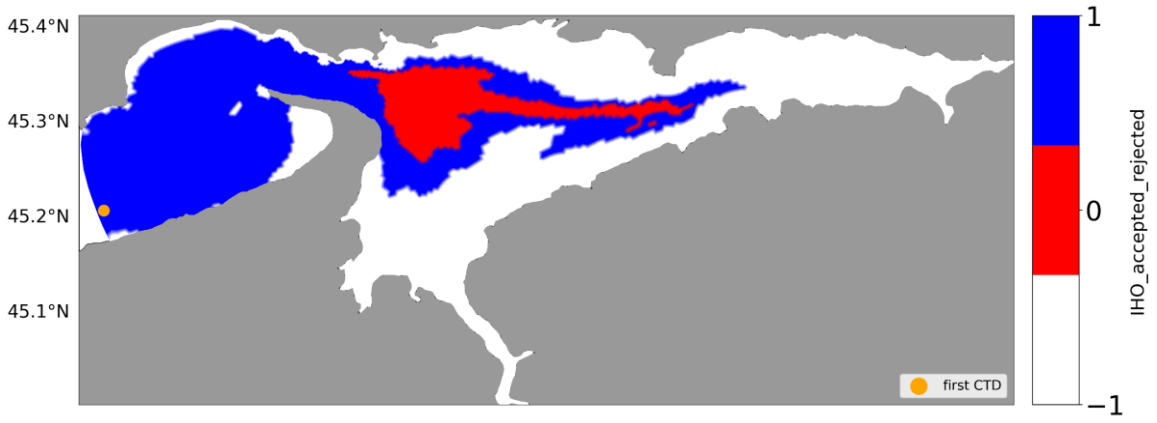

Figure 21. The IHO order 1 results, based on using the sound speed profile from the open boundary node (orange node at the first time step as synthesized CTD). The blue area is accepted, red is rejected, and white areas are excluded from raytracing.

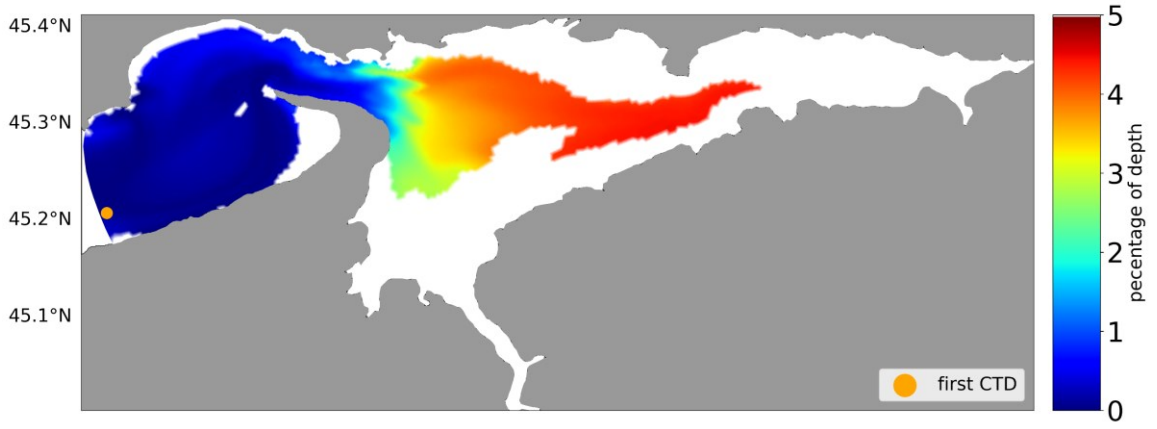

Figure 22.The percentage of depth error for using the sound speed profile at the open boundary node (at the first time step). The dark brown area is excluded from the error calculation since it did not satisfy the weight criteria.

Chapter 4: Analysis

4.1 Bay of Fundy

In this section the results of the BoF model are compared against the published tidal constituents (M_2, N_2, S_2, K_1, and O_1), CTD casts, and SST from GHRSST.

4.1.1 Model Calibrations

The model was run with different values of the bottom roughness coefficient to evaluate which value provides a better representation of tidal propagation for the domain. A range of bottom roughness length scales, 0.007 to 0.015 m, and bottom roughness minimum, 0.002 to 0.018 m, were used in this process. A harmonic analysis (Pawlowicz et al., 2002) was performed and the breakdown of the total errors against the published CHS tidal constituents in the Bay of Fundy (Dupont, Hannah, & Greenberg, 2005) for each of the five principal constituents is provided in the following tables (Table 4, Table 5, Table 6, Table 7, and Table 8). For the model run, between all pairs of bottom roughness and minimum bottom roughness, the bottom roughness at 0.001m and the minimum bottom drag at 0.01 m provided better calibration for all five constituents at eight stations in the Bay of Fundy, Minas Basin, and Chignecto Bay. For the M_2 (Table 4), the minimum amplitude difference happens at the East Quoddy head and Saint John Harbor with 5 and 7 cm, respectively, while Five Island and Grindstone Island in the Minas Basin and Chignecto Bay experience the highest amplitude differences at 30 cm. While six stations have phase differences of equal or less than one degree against the observation, the

maximum phase difference happens at Five Island at 3.3 degrees. By combining both amplitude and phase difference and calculating the total error, the model faces the smallest total error at Saint John Harbor and East Quoddy Head and the largest one at Five Island. In the case of N_2 (Table 5), Table 5 shows the results of the same comparison for the N_2 constituent with the highest and lowest total error at Five Island and East Quoddy Head at 0.29 and 0.04 m, respectively.

Table 4. The model amplitude(m) and phase (Degree-local) comparison against the CHS published constituents and discrepancies (CHS-Model) for M_2 with a bottom coefficient of 0.001 and a minimum drag of 0.01.

M_2	Amplitude(m)			Phase (°)			Error(m)
	Obs.	Model	Diff.	Obs.	Model	Diff.	
65-SJ Harbor	3.01	2.93	0.07	342.1	341.54	0.56	0.07
325-Digby	3.14	2.95	0.19	333.7	333.80	-0.10	0.18
40-St. Andrews	2.72	2.58	0.14	350.6	353.88	-3.28	0.20
21-East Quoddy Head	2.47	2.41	0.05	339.7	340.87	-1.17	0.07
10-North Head	2.52	2.37	0.14	338.6	338.35	0.25	0.14
160-Grindstone Island	4.71	4.40	0.30	351.1	351.15	-0.05	0.30
260-Five Island	5.42	5.11	0.30	8.90	5.53	3.37	0.43
270-Burntcoat Head	5.64	5.45	0.19	14.0	12.90	1.10	0.21
Mean			0.18			-0.35	0.22
Absolute			0.18			1.53	
RMS			0.20			2.11	

The model shows the highest error at Five Island at 0.29m and the minimum at East Quoddy head at 0.04 m. At Saint John Harbor, Digby, and Grindstone Island, the model shows almost the same error around 0.12 m. The next important constituent in the Bay of Fundy system is the S_2 (Table 6), with a maximum total error of 0.27 m at the Burntcoat Head and a minimum of 0.10 m at the East Quoddy Head. This total error mostly results from the high phase difference between the model results and the observation, while the amplitude difference is small.

The result of the diurnal tidal component shows smaller errors. For the K_1 (Table 7), the maximum error at the Burntcoat head is at 0.06 m (which is almost 40% of amplitude error from the observation) with 0.04 amplitude difference and 12.7 degrees phase difference. The rest of the stations show a minimum error of around 0.02 m (almost 14% of amplitude error from observation) with a very small amplitude difference.

Table 5. The model amplitude(m) and phase (Degree-local) comparison against the CHS published constituents and discrepancies (CHS-Model) for N_2 with a bottom coefficient of 0.001 and a minimum drag of 0.01.

N_2	Amplitude(m)			Phase (°)			Error(m)
	Obs.	Model	Diff.	Obs.	Model	Diff.	
65-SJ Harbor	0.59	0.70	-0.11	313.80	311.16	2.64	0.12
325-Digby	0.62	0.71	-0.09	308.40	303.68	4.72	0.11
40-St. Andrews	0.54	0.61	-0.07	324.60	325.99	-1.39	0.08
21-East Quoddy Head	0.56	0.59	-0.03	312.60	310.10	2.50	0.04
10-North Head	0.35	0.58	-0.23	314.40	307.66	6.74	0.24
160-Grindstone Island	1.15	1.04	0.11	315.00	321.67	-6.67	0.17
260-Five Island	1.21	1.17	0.04	351.70	337.62	14.08	0.29
270-Burntcoat Head	1.09	1.24	-0.15	351.00	346.14	4.86	0.18
Mean			-0.03			2.7	0.15
Absolute			0.11			5.1	
RMS			0.12			6.3	

Table 6. The model amplitude(m) and phase (Degree-local) comparison against the CHS published constituents and discrepancies (CHS-Model) for S_2 with a bottom coefficient of 0.001 and a minimum drag of 0.01.

S_2	Amplitude(m)			Phase (°)			Error(m)
	Obs.	Model	Diff.	Obs.	Model	Diff.	
65-SJ Harbor	0.48	0.43	0.05	17.50	33.10	-15.60	0.13
325-Digby	0.50	0.44	0.06	10.10	24.78	-14.68	0.13
40-St. Andrews	0.40	0.37	0.03	30.90	49.70	-18.80	0.13
21-East Quoddy Head	0.34	0.35	-0.01	13.70	30.49	-16.79	0.10
10-North Head	0.42	0.35	0.07	9.80	27.79	-17.99	0.14
160-Grindstone Island	0.74	0.66	0.08	34.90	46.90	-12.00	0.17
260-Five Island	0.78	0.75	0.03	54.00	67.38	-13.38	0.18
270-Burntcoat Head	0.83	0.81	0.02	59.00	78.09	-19.09	0.27
Mean			0.05			-16.5	0.17
Absolute			0.05			16.5	
RMS			0.06			16.7	

For the next diurnal tidal component, O_1 (Table 8), all the stations show very small errors around 0.02 m (almost 16% of amplitude error from observation), which is mostly coming from the high phase differences against the observations. The amplitude difference is less than 0.02 m at most stations.

Table 7. The model amplitude(m) and phase (Degree-local) comparison against the CHS published constituents and discrepancies (CHS-Model) for K_1 with a bottom coefficient of 0.001 and a minimum drag of 0.01.

K_1	Amplitude(m)			Phase (°)			Error(m)
	Obs.	Model	Diff.	Obs.	Model	Diff.	
65-SJ Harbor	0.15	0.15	0.00	136.20	126.98	9.22	0.02
325-Digby	0.14	0.15	-0.01	131.70	122.77	8.93	0.03
40-St. Andrews	0.15	0.16	-0.01	136.30	136.61	-0.31	0.01
21-East Quoddy Head	0.14	0.15	-0.01	133.30	126.58	6.72	0.02
10-North Head	0.16	0.15	0.01	136.00	126.00	10.00	0.03
160-Grindstone Island	0.17	0.17	0.00	138.50	130.36	8.14	0.02
260-Five Island	0.16	0.18	-0.02	147.50	136.72	10.78	0.04
270-Burntcoat Head	0.14	0.18	-0.04	154.00	141.27	12.73	0.06
Mean			-0.01			7.6	0.02
Absolute			0.01			7.7	
RMS			0.01			8.5	

Table 8. The model amplitude(m) and phase (Degree-local) comparison against the CHS published constituents and discrepancies (CHS-Model) for O_1 with a bottom coefficient of 0.001 and a minimum drag of 0.01.

O_1	Amplitude(m)			Phase (°)			Error(m)
	Obs.	Model	Diff.	Obs.	Model	Diff.	
65-SJ Harbor	0.11	0.11	0.00	117.70	112.68	5.02	0.01
325-Digby	0.11	0.12	-0.01	118.90	108.01	10.89	0.02
40-St. Andrews	0.11	0.12	-0.01	120.60	119.62	0.98	0.01
21-East Quoddy Head	0.10	0.11	-0.01	114.70	111.20	3.50	0.02
10-North Head	0.09	0.11	-0.02	117.10	110.65	6.45	0.02
160-Grindstone Island	0.14	0.13	0.01	120.60	114.52	6.08	0.02
260-Five Island	0.12	0.13	-0.01	134.50	119.63	14.87	0.03
270-Burntcoat Head	0.12	0.13	-0.01	140.00	123.90	16.10	0.04
Mean			0.00			7.4	0.02
Absolute			0.01			7.4	
RMS			0.01			8.9	

4.1.2 Model Validation- Currents

The model output is validated against the tidal currents, CTD casts, and sea surface temperatures available in the area. However, for the Minas Basin model, the output is compared against the tidal currents and the CTD data from the moving vessel profile during 2007.

4.1.2.1 Predicted Tidal Currents

The predicted depth-averaged currents are compared against the 9 current data (Figure 9, Figure 10) which were used in a three-dimensional tidal model for the Bay of Fundy and Gulf Maine by Wu et al. (2014). The M_2 is the most dominant tidal component in the Bay of Fundy with a magnitude of four times greater than the next largest tidal constituent (Greenberg, 1983). For this reason, only the comparison for the M_2 constituent is provided in Table 9. At the Minas Passage, the model predicts the depth-averaged semi-major current with the same order of magnitude as the observations but, it overestimates the current amplitude along the major axis of 0.5 and 0.2 m/s for C1 and C2, respectively. The difference in the semi-minor axis is very small at 0.01 m/s for C1 and -0.05 m/s for C2. The modeled inclinations are 162 and 161 degrees which are slightly different from the observations by 3.2 and -1 degrees and finally, there is a phase delay of 9.4 and 11.7 degrees for these two stations. The modeled current amplitudes show a very good agreement regarding the semi-major, semi-minor, and phase values against the observed values at the head of Bay, at stations C4, C5, and C6. The model predicts the weaker semi-major amplitude at C4, C5, and C6 by -0.03, -0.15, and -0.03 m/s, respectively. Also, the predicted semi-minor values are -0.01, -0.01, and 0.01 m/s compared to the observed values

of 0.0, 0.05, and 0.02 m/s. Considering the phase difference, the modeled phase lagged by -0.1 and -1.8 degrees at stations C4 and C5, while it was ahead of observation on station C6 by 2.4 degrees. At the entrance of the Bay, stations C7, C8, and C9; the model does not show a good agreement in the case of inclination and phase, specifically at station C9 showing the same issue (not good inclination and phase) as in Wu et al. (2014), but the semi-major and semi-minor axes show a good agreement but smaller amplitude. As Table 9 shows, the model was able to capture a trend in current amplitude that was reported by Wu et al. (2014). The current amplitude increases from north to south from station C4 to C6 in the upper Fundy and the entrance of the Bay from station C7 to C9. This feature shows that in the Bay of Fundy, the current speed is higher on the Nova Scotia side and lower on the New Brunswick side. As the water enters from the Gulf of Maine to the Bay of Fundy, it travels close to the Nova Scotia side to the head of the Bay, while facing some mixing on its way. On the way back, it experiences a counter-clockwise turn at the head of the Bay and continues on the New Brunswick side where the speed and the magnitude of current have reduced compared to the Nova Scotia side.

Table 9. Model data comparison of the depth-average tidal ellipse for M_2. The location of sites is in Figure 8 (Units of semi-major and minor are in m/s and the difference in angles are in degrees).

	Observed					Modeled					Difference			
	Semi-Major	Semi-Minor	Incline-action	Phase		Semi-Major	Semi-Minor	Incline-action	Phase		Maj-diff	Min-diff	Inc-diff	Pha-diff
C1	2.70	-0.03	158.8	210.6		3.20	-0.04	162.0	220		0.50	-0.01	3.2	9.4
C2	2.87	-0.10	162.0	209.3		3.10	-0.05	161.0	221		0.23	0.05	-1.0	11.7
C3	0.73	0.03	30.1	18.3		0.77	0.00	35.8	16.6		0.04	-0.03	5.7	-1.7
C4	0.89	0.00	29.0	20.0		0.86	-0.01	34.6	19.9		-0.03	-0.01	5.6	-0.1
C5	1.09	0.05	31.1	21.9		0.94	-0.01	33.9	20.1		-0.15	-0.06	2.8	-1.8
C6	1.04	0.02	38.1	20.7		1.01	0.01	30.7	23.1		-0.03	-0.01	-7.4	2.4
C7	0.72	0.10	26.2	25.8		0.51	0.02	32.2	15.6		-0.21	-0.08	6.0	-10.2
C8	0.98	0.11	37.4	20.8		0.70	-0.07	41.2	10.4		-0.28	-0.18	3.8	-10.4
C9	1.09	0.13	22.1	16.8		0.84	-0.02	41.0	4.4		-0.25	-0.15	18.9	12.4

4.1.2.2 Water Column Variability with HRDPS Surface Forcing

Two types of comparison are provided to assess the baroclinic component of the run. In the first one, the water column variability of the simulated temperature and salinity are analyzed against the CTD data. In the second one, the simulated sea surface temperature (SST) is compared against the observed SST from satellite data.

The simulated temperature and salinity from the baroclinic run are evaluated against the available CTD data for the period of the model run. These CTD casts are gathered from the fieldwork accomplished by the Nova Scotia Community College survey, the Department of Fisheries and Oceans Canada (DFO), and the World Ocean Database (WOD) (Boyer et al., 2013). A total of 98 CTD casts were used and plots of comparison between observed and modeled temperature and salinity are provided in Appendix A. The Bay of Fundy is divided into three sections (Figure 12) to check if there is any area in that model that performs better. The entrance of the Bay with 38 casts, the middle part with 22

casts, and the head of the Bay with 38 casts (three instances are provided for each section and the rest of the plots are in the Appendix A section). In each figure, three different scenarios are depicted, the highest, medium, and lowest RMSE with respect to FVCOM_HRDPS and CTD casts. These CTD casts are picked based on the average RMSE of three layers where the lowest RMSE is considered as the best model simulation and the highest RMSE is the worst one at each section of the Bay (tables in Appendix B). However, there is no specific trend in the temperature and salinity profile at each section which means having the best agreement at some locations inside each section and at the same time a deviation of 1 degree in temperature in another location in the same section. These discrepancies are not uniform in the head of the Bay to find a normal trend in the model prediction; however, a small surface thermohaline feature happens at the head of the bay and is captured by the model. Figure 23 shows the temperature and salinity profile for both the simulated and the observation at the head of the Bay. In the middle of the Bay, the temperature and salinity stratification become more significant at the surface in comparison to the head of the Bay (Figure 24). The model was able to capture the features in the CTD cast in this section. At the entrance of the Bay (Figure 25), not only do we have the stratification on the surface layer, but also, at some locations, CTD 83, colder and saltier (based on the salinity plots in the appendix) water layer present at depth 65, and the model was able to capture it.

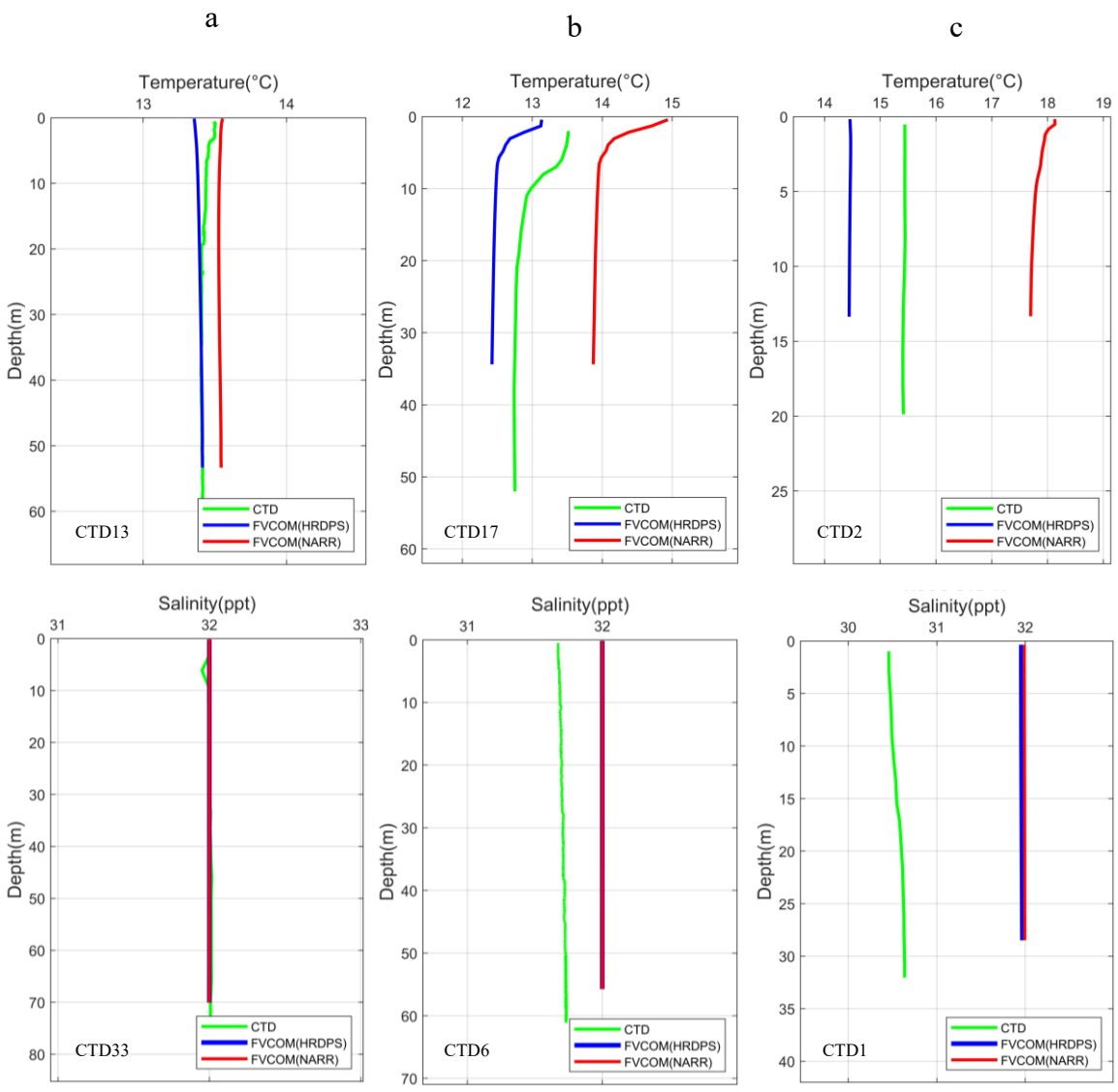

Figure 23. The temperature (top) and salinity (bottom) from FVCOM_HRDPS and FVCOM_NARR comparison against CTD cast at the head of the Bay of Fundy. The first column (a), second (b), and third (c) columns represent the lowest, medium, and highest RMSE from FVCOM_HRDPS against CTD casts, respectively.

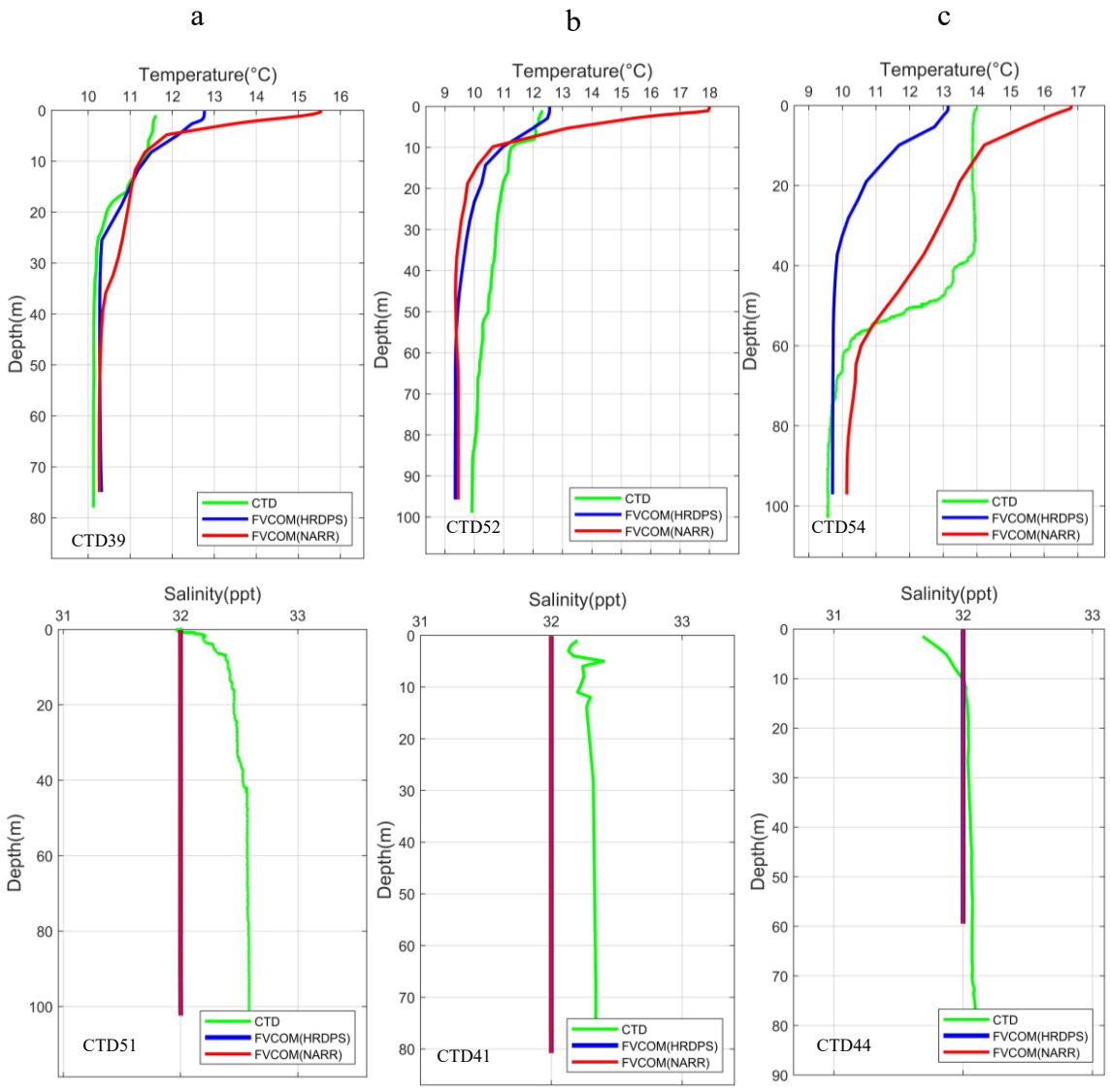

Figure 24. The temperature (top) and salinity (bottom) from FVCOM_HRDPS and FVCOM_NARR comparison against CTD casts at the middle of the Bay of Fundy. The first column (a), second (b), and third (c) columns represent the lowest, medium, and highest RMSE from FVCOM_HRDPS against CTD casts, respectively.

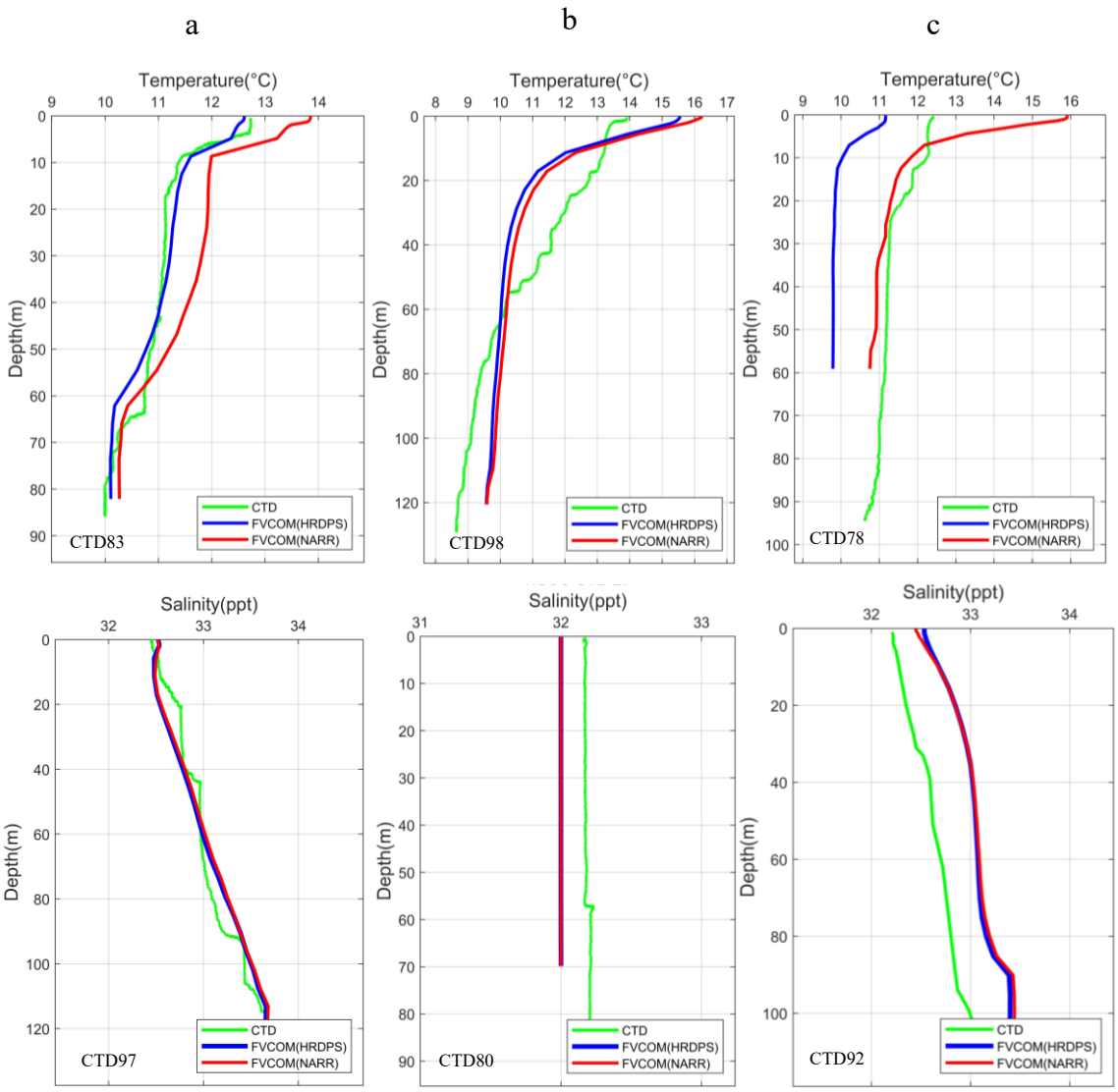

Figure 25. The temperature (top) and salinity (bottom) from FVCOM_HRDPS and FVCOM_NARR comparison against CTD casts at the entrance of the Bay of Fundy. The first column (a), second (b), and third (c) columns represent the lowest, medium, and highest RMSE from FVCOM_HRDPS against CTD casts, respectively.

4.1.2.3 Baroclinic Model Skill Assessment for Temperature

To provide a performance metric for the model, a statistical analysis was run on all 98 CTD casts. Also, to check the large-scale temperature and salinity structure of the local high-

resolution model, the FVCOM output is compared with coarser resolution models, including the global operational model instance of GOFS 3.1 and GoMOFS (Yang et al., 2016). The results of this comparison are provided in Table 10, Table 11, and Table 12 for the temperature at the bottom, middle, and surface layers, respectively.

For the bottom layer in the whole Bay, Table 10, both FVCOM_HRDPS (Bay of Fundy model run with HRDPS) and FVCOM_NARR (Bay of Fundy model run with NARR) show better correlations than other two models at 0.95 and 0.96, while FVCOM_HRDPS provides less RMSE, RI, AE, and AAE in comparison to FVCOM_NARR. Regarding the Model efficiency (ME), the best results are provided by the FVCOM_HRDPS, GoMOFS, and FVCOM_NARR at 0.9, 0.8, and 0.6, respectively.

Considering each section and correlations, the four models have higher correlation at the head of the Bay than mouth and middle of the Bay, which might be due to not less stratification in the head, while FVCOM_HRDPS and FVCOM_NARR show the highest of them all. The statistics breakdown for each section of the Bay is included in this table for each model.

Table 10. Bottom layer temperature skill assessment for GOFS3.1, FVCOM_HRDPS, FVCOM_NARR, and GoMOFS against the 98 CTS casts.

Model/Bottom	Number of CTD	r	RMSE	RI	AE	AAE	ME
Upper Fundy	38						
FVCOM_HRDPS		0.95	0.4	1.014	-0.2	0.3	0.8
FVCOM_NARR		0.94	1.5	1.045	1.2	1.3	-1.1
GOFS		0.84	2.1	1.086	-1.4	1.7	-3.2
GoMOFS		0.85	0.9	1.030	0.7	0.7	0.3
Middle Fundy	22						
FVCOM_HRDPS		0.75	0.6	1.024	-0.1	0.5	0.4
FVCOM_NARR		0.75	0.8	1.032	0.2	0.7	-0.1
GOFS		0.22	2.9	1.159	-2.4	2.5	-13.8
GoMOFS		0.82	1.0	1.038	0.7	0.8	-0.6
Mouth Fundy	38						
FVCOM_HRDPS		0.82	0.7	1.030	-0.2	0.6	0.6
FVCOM_NARR		0.87	0.6	1.028	0.3	0.5	0.6
GOFS		0.55	2.2	1.117	-1.7	2.1	-3.7
GoMOFS		0.79	0.8	1.032	0.3	0.5	0.5
Whole Fundy	98						
FVCOM_HRDPS		0.95	0.6	1.024	-0.2	0.5	0.9
FVCOM_NARR		0.96	1.1	1.036	0.6	0.9	0.6
GOFS		0.81	2.4	1.117	-1.7	2.0	-0.7
GoMOFS		0.94	0.8	1.033	0.5	0.6	0.8

Regarding the model efficiency alone at each section of the Bay, upper_fundy, middle_fundy, and mouth_fundy, the FVCOM_HRDPS performs better at the upper part, middle, and in a common place with FVCOM_NARR at the mouth of the Bay at 0.8, 0.4, and 0.6. In general, FVCOM_NARR shows warmer RMSE in this layer for the head, middle Fundy than FVCOM_HRDPS, and this impacts its total ME.

For the middle layer, Table 11, considering the whole Bay and ME, FVCOM_HRDPS ranks first (at 0.7), followed closely by the FVCOM_NARR and GoMOFS at the second and third places at 0.5 and 0.4, respectively. At the head of the Bay, FVCOM_HRDPS and GoMOFS show better ME (at 0.8 and 0.4) than the FVCOM_NARR (at -0.8), while FVCOM_NARR outperform the three models in the middle and entrance of the Bay at 0.2

and 0.1. The four models still show higher correlations in the upper Fundy than the other two sections, with the two FVCOM models having the highest correlations. At the middle layer, the FVCOM_NARR has a higher RMSE than FVCOM_HRDPS and GoMOFS, while it has a lower RMSE at the middle and mouth of the Bay.

Table 11. Middle layer temperature skill assessment for GOFS3.1, FVCOM_HRDPS, FVCOM_NARR, and GoMOFS against the 98 CTS casts.

Model/Middle	Number of CTD	r	RMSE	RI	AE	AAE	ME
Upper Fundy	38						
FVCOM_HRDPS		0.95	0.5	1.015	-0.2	0.4	0.8
FVCOM_NARR		0.94	1.4	1.043	1.2	1.3	-0.8
GOFS		0.88	1.7	1.068	-1.1	1.4	-1.7
GoMOFS		0.85	0.8	1.029	0.6	0.7	0.4
Middle Fundy	22						
FVCOM_HRDPS		0.73	0.9	1.038	-0.6	0.7	0.0
FVCOM_NARR		0.88	0.9	1.034	0.0	0.8	0.2
GOFS		0.62	2.2	1.109	-2.0	2.0	-6.1
GoMOFS		0.60	0.9	1.036	0.3	0.7	0.1
Mouth Fundy	38						
FVCOM_HRDPS		0.57	0.9	1.038	-0.6	0.8	-0.4
FVCOM_NARR		0.68	0.8	1.031	0.1	0.6	0.1
GOFS		0.54	2.0	1.102	-1.4	1.8	-3.7
GoMOFS		0.43	1.4	1.053	0.8	0.9	-2.6
Whole Fundy	98						
FVCOM_HRDPS		0.92	0.8	1.031	-0.5	0.6	0.7
FVCOM_NARR		0.94	1.1	1.037	0.5	0.9	0.5
GOFS		0.86	1.9	1.092	-1.4	1.7	-0.3
GoMOFS		0.81	1.1	1.041	0.6	0.8	0.4

For the surface layer, Table 12, the FVCOM_HRDPS shows better ME in the whole Bay (at 0.4) followed by FVCOM_NARR (at 0.1), and the other two models share the third place (at 0.5). Regarding each section, the same pattern as the middle layer repeats here where the FVCOM_HRDPS has better ME (at 0.7) in the upper Bay, while FVCOM_NARR has better ME (at 0.1 and -0.9) at the middle and entrance of the Bay.

Regarding the correlation, the same pattern as the bottom and middle layers repeats here. In total, the FVCOM_HRDPS and FVCOM_NARR outperform the other two models in simulating the temperature for the whole Bay and each section of the Bay, while between the two, FVCOM_HRDPS shows better results.

Table 12. Surface layer temperature skill assessment for GOFS3.1, FVCOM_HRDPS, FVCOM_NARR, and GoMOFS against the 98 CTD casts.

Model/Surface	Number of CTD	r	RMSE	RI	AE	AAE	ME
Upper Fundy	38						
FVCOM_HRDPS		0.93	0.6	1.018	-0.3	0.5	0.7
FVCOM_NARR		0.93	1.4	1.043	1.3	1.3	-0.8
GOFS		0.70	1.1	1.036	0.7	0.9	0.0
GoMOFS		0.82	0.8	1.028	0.5	0.6	0.4
Middle Fundy	22						
FVCOM_HRDPS		0.33	1.1	1.041	-0.5	0.9	-0.3
FVCOM_NARR		0.84	0.9	1.032	0.4	0.8	0.1
GOFS		0.17	1.7	1.059	1.1	1.4	-1.9
GoMOFS		0.58	1.4	1.049	1.0	1.1	-1.0
Mouth Fundy	38						
FVCOM_HRDPS		0.42	1.1	1.043	-0.9	1.0	-1.8
FVCOM_NARR		0.43	0.9	1.035	0.3	0.7	-0.9
GOFS		0.08	1.7	1.059	0.7	1.2	-5.4
GoMOFS		0.38	2.0	1.068	1.5	1.5	-8.0
Whole Fundy	98						
FVCOM_HRDPS		0.82	0.9	1.035	-0.6	0.7	0.4
FVCOM_NARR		0.89	1.2	1.038	0.7	1.0	0.1
GOFS		0.56	1.5	1.051	0.8	1.1	-0.5
GoMOFS		0.58	1.5	1.051	1.0	1.1	-0.5

4.1.2.4 Baroclinic Model Skill Assessment for Salinity

The results of the skill assessment are provided in Table 13, Table 14, and Table 15 for the bottom, middle, and surface layers. For the bottom layer, Table 13, both FVCOM_HRDPS and FVCOM_NARR show better ME against the other two models for the whole Bay at 0.6. and these two models almost have the same ME at each section of the Bay. Both FVCOM_HRDPS and FVCOM_NARR have a better ME in the mouth of the Bay followed

by the middle and upper Bay. At the mouth of the Bay, these two models have higher correlations, lower RMSE, AE, and AAE in comparison to the other two sections of the Bay, especially at the head of the Bay, where the models experience higher errors.

Table 13. Bottom layer salinity skill assessment for GOFS3.1, FVCOM_HRDPS, FVCOM_NARR, and GoMOFS against the 98 CTD casts.

Model/Bottom	Number of CTD	r	RMSE	RI	AE	AAE	ME
Upper Fundy	38						
FVCOM_HRDPS		0.53	0.6	1.008	0.4	0.5	-0.9
FVCOM_NARR		0.53	0.6	1.008	0.4	0.5	-0.9
GOFS		0.05	0.6	1.009	0.5	0.5	-1.1
GoMOFS		0.87	1.0	1.014	0.9	0.9	-4.1
Middle Fundy	22						
FVCOM_HRDPS		0.48	0.3	1.004	-0.2	0.3	-0.5
FVCOM_NARR		0.53	0.3	1.004	-0.1	0.2	-0.4
GOFS		0.52	0.3	1.004	0.2	0.3	-0.6
GoMOFS		0.88	0.6	1.008	0.6	0.6	-4.5
Mouth Fundy	38						
FVCOM_HRDPS		0.90	0.3	1.004	0.0	0.2	0.6
FVCOM_NARR		0.89	0.3	1.004	0.0	0.2	0.6
GOFS		0.62	0.5	1.006	0.1	0.4	-0.1
GoMOFS		0.76	0.7	1.009	0.6	0.7	-1.3
Whole Fundy	98						
FVCOM_HRDPS		0.77	0.4	1.006	0.1	0.3	0.6
FVCOM_NARR		0.77	0.4	1.006	0.1	0.3	0.6
GOFS		0.73	0.5	1.007	0.2	0.4	0.4
GoMOFS		0.87	0.8	1.011	0.7	0.7	-0.5

For the middle layer, Table 14, GOFS provides better model efficiency at 0.4 followed by FVCOM_HRDPS and FVCOM_HRDPS at 0.3 for the whole Bay. Considering sections separately for ME, FVCOM_HRDPS has better ME at the upper Bay, while GOFS is better in the middle of the Bay and finally FVCOM_HRDPS and FVCOM_NARR have higher ME than the other two models. The FVCOM_HRDPS and FVCOM_NARR have higher correlation, and lower RMSE, AE, and AAE at the mouth of the Bay, while these errors increase reaching to the head of the Bay.

Table 14. Middle layer salinity skill assessment for GOFS3.1, FVCOM_HRDPS, FVCOM_NARR, and GoMOFS against the 98 CTD casts.

Model/Middle	Number of CTD	r	RMSE	RI	AE	AAE	ME
Upper Fundy	38						
FVCOM_HRDPS		0.53	0.6	1.009	0.5	0.5	-0.9
FVCOM_NARR		0.52	0.7	1.009	0.5	0.5	-1.0
GOFS		-0.13	0.6	1.009	0.4	0.5	-1.0
GoMOFS		0.87	1.0	1.014	1.0	1.0	-4.0
Middle Fundy	22						
FVCOM_HRDPS		-0.01	0.4	1.005	-0.1	0.3	-0.2
FVCOM_NARR		0.16	0.3	1.005	-0.1	0.3	-0.1
GOFS		0.75	0.2	1.003	0.1	0.2	0.4
GoMOFS		0.77	0.7	1.009	0.7	0.7	-3.5
Mouth Fundy	38						
FVCOM_HRDPS		0.75	0.3	1.004	-0.1	0.2	0.3
FVCOM_NARR		0.78	0.3	1.004	-0.1	0.2	0.3
GOFS		0.65	0.4	1.005	-0.2	0.3	0.2
GoMOFS		0.14	0.6	1.008	0.3	0.5	-2.4
Whole Fundy	98						
FVCOM_HRDPS		0.61	0.5	1.006	0.1	0.4	0.3
FVCOM_NARR		0.62	0.5	1.006	0.1	0.3	0.3
GOFS		0.75	0.5	1.007	0.1	0.3	0.4
GoMOFS		0.55	0.8	1.011	0.7	0.7	-1.0

Table 15 shows the salinity at the surface layer for the three sections and the whole Bay. The FVCOM_HRDPS and FVCOM_NARR show better model efficiency at 0.1 for the whole Bay. In each section, these two models almost show the same ME, with one exception at the mouth of Bay. Also, the correlations are very close for these two models in three sections, while all error metrics increase from the mouth to the head of the Bay.

Table 15. Surface layer salinity skill assessment for GOFS3.1, FVCOM_HRDPS, FVCOM_NARR, and GoMOFS against the 98 CTD casts.

Model/Surface	Number of CTD	r	RMSE	RI	AE	AAE	ME
Upper Fundy	38						
FVCOM_HRDPS		0.52	0.7	1.009	0.5	0.5	-1.0
FVCOM_NARR		0.50	0.7	1.009	0.5	0.5	-1.0
GOFS		-0.76	0.7	1.010	0.4	0.5	-1.2
GoMOFS		0.85	1.1	1.015	1.0	1.0	-4.0
Middle Fundy	22						
FVCOM_HRDPS		0.24	0.4	1.005	0.0	0.3	0.0
FVCOM_NARR		0.50	0.4	1.005	0.0	0.3	0.0
GOFS		-0.18	0.7	1.009	-0.4	0.5	-2.4
GoMOFS		-0.60	0.7	1.010	0.6	0.6	-3.2
Mouth Fundy	38						
FVCOM_HRDPS		0.52	0.3	1.004	-0.1	0.2	-0.2
FVCOM_NARR		0.56	0.3	1.004	-0.1	0.2	-0.1
GOFS		-0.18	0.6	1.008	-0.4	0.4	-4.0
GoMOFS		-0.50	0.5	1.007	0.2	0.5	-3.8
Whole Fundy	98						
FVCOM_HRDPS		0.46	0.5	1.007	0.1	0.4	0.1
FVCOM_NARR		0.46	0.5	1.007	0.1	0.4	0.1
GOFS		-0.24	0.6	1.009	-0.1	0.5	-0.5
GoMOFS		0.06	0.8	1.011	0.6	0.7	-1.5

In general, the two FVCOM models have better performance in simulating the salinity for the surface and bottom layer for the whole and each section of the Bay than GOFS and GoMOFS. While both FVCOM models are driven by GoMOFS at the open boundaries, the surface forcings for the BoF models are from a higher-resolution weather model that could better represent the local wind patterns, and improved heat flux accuracy to enhance model the resolved simulated temperature, salinity, and the ocean stratification.

4.1.2.5 Sea Surface Temperature Variability

Here, the SST from both runs with HRDPS and NARR are compared against the daily time series of GHRSST. As before, the Bay of Fundy is divided into three sections, Figure 12,

Head_Bay, Middle_Bay, and Entrance_Bay, however, the Minas Basin is added for this comparison. The GHRSST data with 5 km resolution are interpolated to the FVCOM grid, and then for each grid point the mean, standard deviation, root-mean-square, and correlation are calculated. Then, for each section (Head, Middle, Entrance, Minas) all the statistical parameters are averaged to achieve one single value for each section. The results are plotted in a Taylor plot for each section. Figure 26 shows the Taylor Diagram for the entrance of the Bay. The radial axis (black) shows the standard deviation, the angular axis (blue) shows the correlation coefficient, and the green dashed line shows the root-mean-square of the modeled SST. The GHRSST is depicted as the 'Obs' in the plot and 'E-HRDPS' and 'E-NARR' represent the results for the entrance (E) using HRDPS and NARR, respectively.

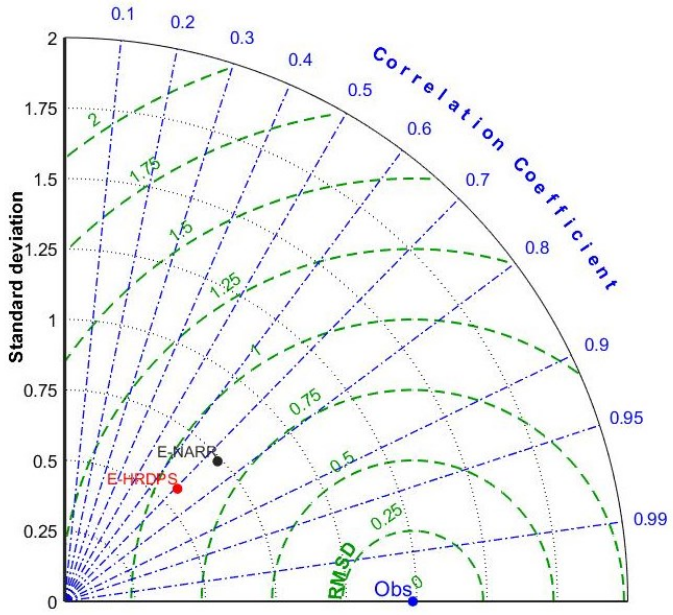

Figure 26. STD, RMS, and R for the SST at the Bay entrance for the model run with HRDPS and NARR.

Both models almost have the same correlation coefficient and the root-mean-square around 0.7 and 0.8 degrees at the entrance, respectively. Considering the STD, the E_NARR shows a wider range of variability than E_HRDPS. In the Middle of the Bay (Figure 27), where the same trend repeats for both M_NARR and M_HRDPS with a little higher value of RMS and lower values of correlation. The variability (STD) of the GHRSST increases in the middle of the Bay compared to the Bay entrance and both model runs also show this small change as well.

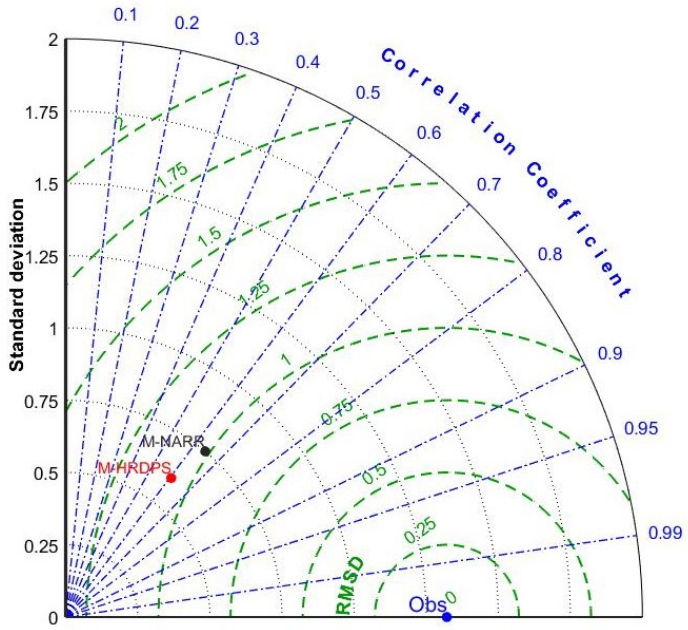

Figure 27. STD, RMS, R for the SST at the middle of Bay for the model run with HRDPS and NARR.

So far, both model runs showed almost the same statistical trend at the entrance and the middle of the bay. However, at the head of the Bay, the improvement in SST from the HRDPS model run is obvious. Figure 28 shows that both models' runs provide better results

at the head of the Bay compared to the entrance and middle of the Bay. The correlation for H_HRDPS and H_NARR reaches 0.91 and 0.84, respectively with a smaller RMS for H_HRDPS. In the case of standard deviation, both model runs are close to the GHRSST variability at 1.4 degrees, while H_NARR shows a little higher variability and H_HRDPS provides low variability.

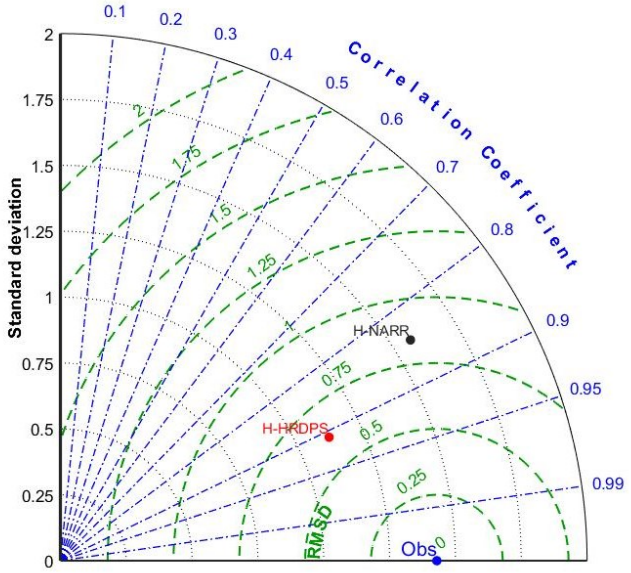

Figure 28. STD, RMS, R for the SST at the head of Bay for the model run with HRDPS and NARR.

For the last part of the comparison, both models are compared in a smaller area (Minas Basin) in the Bay of Fundy to check if any improvement is achieved in the SST. Figure 29 shows the same trend as the head of the Bay of Fundy. While Mi_NARR shows a better correlation at 0.9 with the GHRSST, it suffers from higher RMS at 1.25 degrees. Also, it provides much higher variability at 2.6 degrees Celsius compared to the GHRSST at 1.8 degrees Celsius. The Mi_HRDPS provides a lower correlation at 0.87 while showing less RMS at 1 degree Celsius. As with the other locations in the Bay, Mi_HRPDS depicts lower variability at 1.4 degrees compared to the GHRSST at 1.8 degrees Celsius.

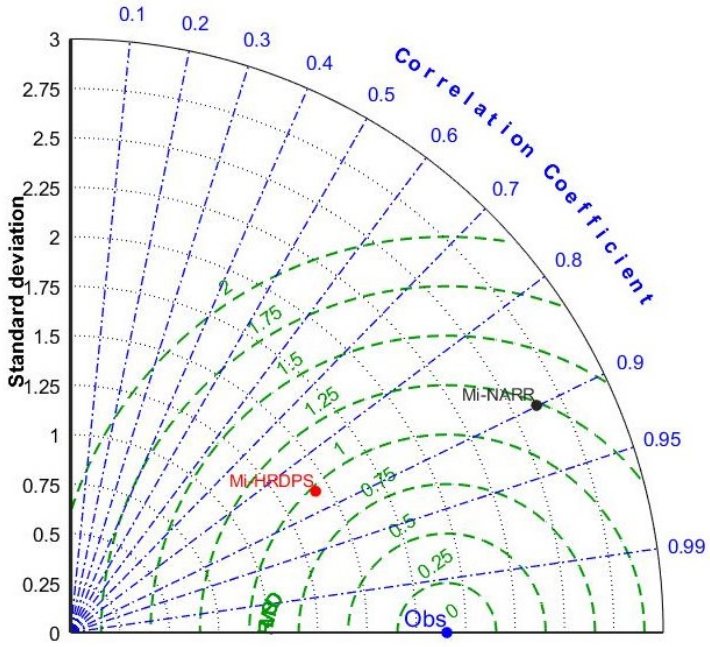

Figure 29. STD, RMS, R for the SST at the Minas Basin for the model run with HRDPS and NARR.

In total, the FVCOM_HRDPS got better results at the head of the Bay and Minas Basin compared to the entrance and middle of the Bay. In the case of SST variability (STD), both model outputs provide better results at the head of the Bay while the smallest variability is happening at the entrance of the Bay. One possible reason could be the vertical resolution of the model in the entrance and the head of the Bay. The model vertical resolution is 2 meters and 1m at the entrance and head of the Bay, respectively. At the depth of 70 meters, the vertical resolution is 2 meters and as the depth increases to 200 meters, it becomes 5.2 meters. Having this coarse vertical resolution might decrease the model's capability to capture the temperature variability at the surface. In the Minas Basin, at 20 meters depth,

the vertical resolution reaches 0.5 meters, and the model provides a close STD to the GHRSST.

Another reason could be the horizontal resolution of the model in these areas. At the entrance, having the coarsest resolution, the resolution is 6 km and reaches 300 meters at the head of the Bay and Minas Basin (Figure 30).

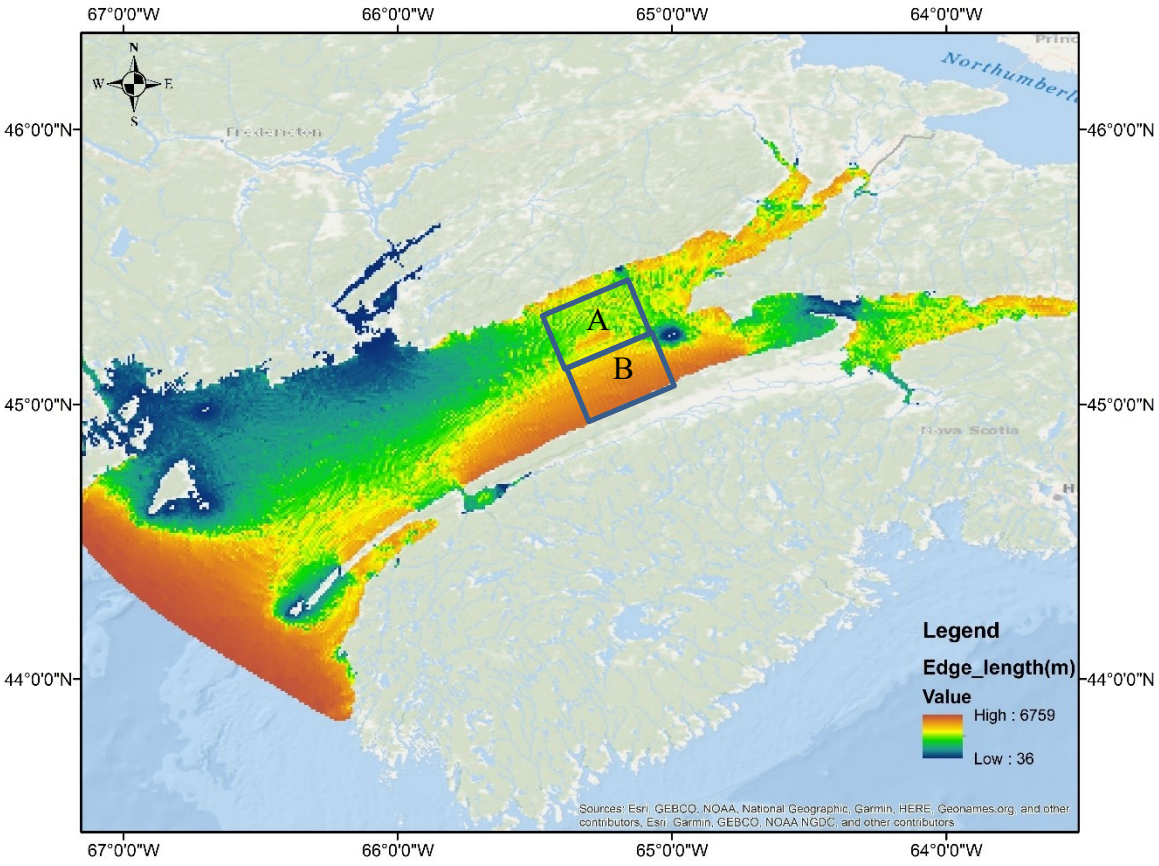

Figure 30. The histogram equalized the mesh edges in meters and showed two sections, a) with high(high_res) and b) low(low_res) resolution mesh.

The distribution of the mesh resolution is not uniform in the Bay of Fundy. Where there is a constrained area or shallow section, such as Minas Passage and Saint John Harbor, the resolution has increased. Even at the head of the bay, where we approach from the Digby

area to the Minas Basin, there is a reduction of mesh resolution, while, on the other side of the coastline in New Brunswick side where there is more coastline complexity, the mesh resolution is finer. To quantify the effect of the horizontal resolution of the Bay of Fundy model, a comparison has been provided for the upper part of the Bay, where the model shows better agreement with the GHRSST data. Based on Figure 30, the head of the Bay is divided into coarse and fine resolutions. The "A" shows high horizontal resolution ranging from 600 to 1400 meters, while the "B" section represents coarse resolution with a range of 900 to 2500 meters. In this case, the results of the model run using the HRDPS are compared against the GHRSST in each section. Figure 31 shows the results of the statistical analysis for section A. While the STD of GHRSST is about 1.40 degrees, the model shows a good STD agreement with the observation at 1.15 degrees. Also, the correlation and RMS at 0.92 and 0.59 degrees indicate the capability of the model to simulate the SST close to the observation. In the case of section B with a coarse resolution, Figure 32, the model output experienced less agreement against the GHRSST data. The model correlation reduces at section B to 0.86 compared to 0.92 for section A, and model SST shows less variability at 0.80 degrees (0.4-degree difference with GHRSST), while there is an increase in the RMS at 0.7 degrees in section B.

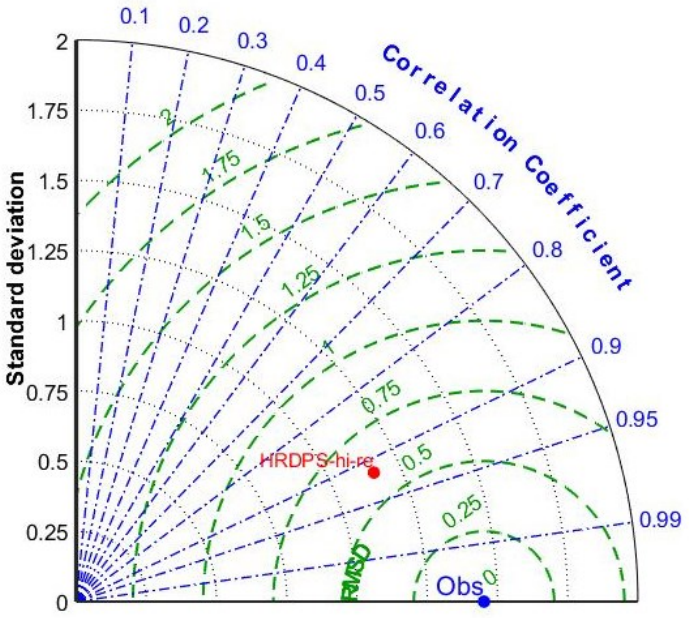

Figure 31. Taylor plot for the Head of Bay at "A" section with higher resolution.

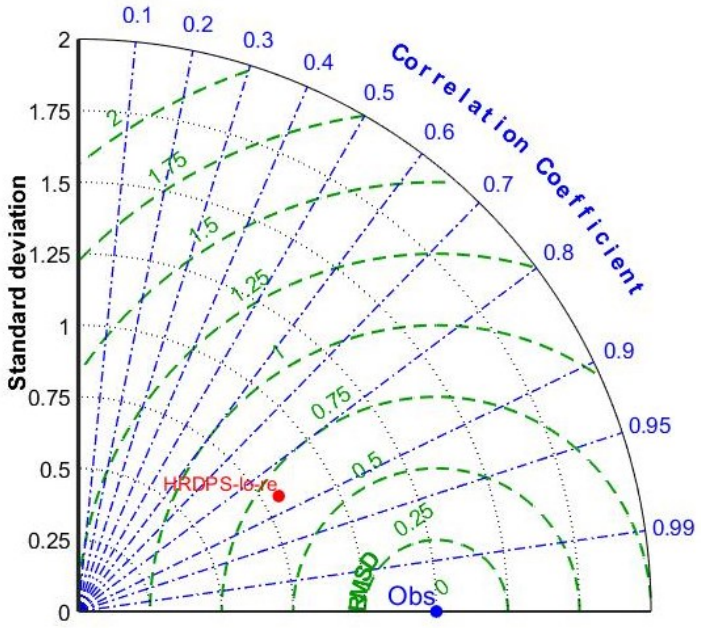

Figure 32. Taylor plot for the Head of Bay at "B" section with coarse resolution.

4.1.3 Impact of Surface Forcing on the Ray-Tracing Error

The Bay of Fundy model was run with two different surface forcing, NARR, and HRDPS. In this section, a comparison is provided to check how the applied surface forcing in the ocean model could impact the vertical error budget in the hydrography survey and how much vertical error is introduced by using the modeled data. The CTD casts (Figure 12) and the corresponding model output is being used to do the raytracing and the calculation of depth error in each 98 CTD location. Then, the results are checked against the IHO-order 1a at 70 swath degrees. Figure 33 indicates the amount of error that we introduce to the hydrographic survey using the model output profile from the FVCOM_HRDPS model run.

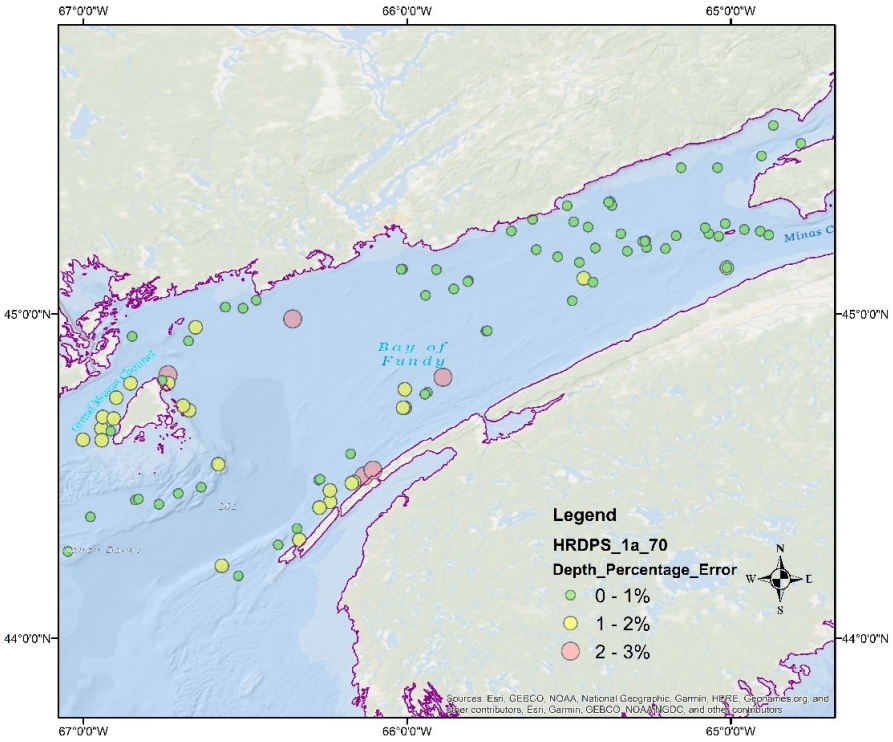

Figure 33. The depth percentage error by using the FVCOM_HRDPS model profile.

From the Saint John River to the head of the Bay, the depth error is less than 1%. Most of the higher depth errors are distributed around the west of Grand Manan Island and the shoreline of Grand Passage and there are only 5 locations with a depth error between 2 and 3%. Only 12 percent (Figure 34) of modeled profiles (FVCOM_HRDPS) are rejected at IHO order 1a at a 70-degree swath angle. The same plots are provided for the modeled profile output from FVCOM_NARR data in Figure 35 and Figure 36.

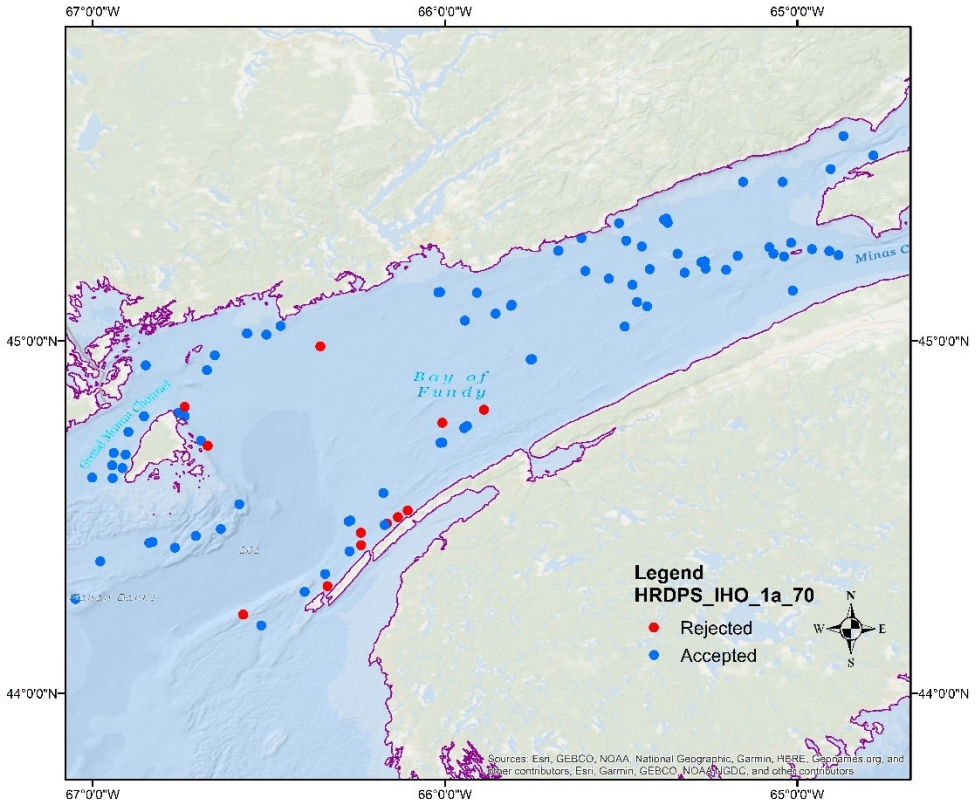

Figure 34. The accepted or rejected model profile after raytracing using FVCOM_HRDPS output at order 1a at a 70-degree swath angle. Red dots are rejected, and blue dots are accepted.

At the head of the Bay, where the FVCOM_HRDPS showed the best results, the FVCOM _NARR provides a poor performance regarding the depth percentage error. At some locations, in particular the entrance of Chignecto Bay, the depth error reaches 3-4%. Also, the number of locations with 2-3% depth error has increased at the head of the Bay. In general, the FVCOM_NARR is warmer at the head of the bay from the surface to the bottom of the water column, and since the head is a well-mixed area, the whole water column is warmer than FVCOM_HRDPS. This results in a higher depth uncertainty and being more rejected at the head of the Bay.

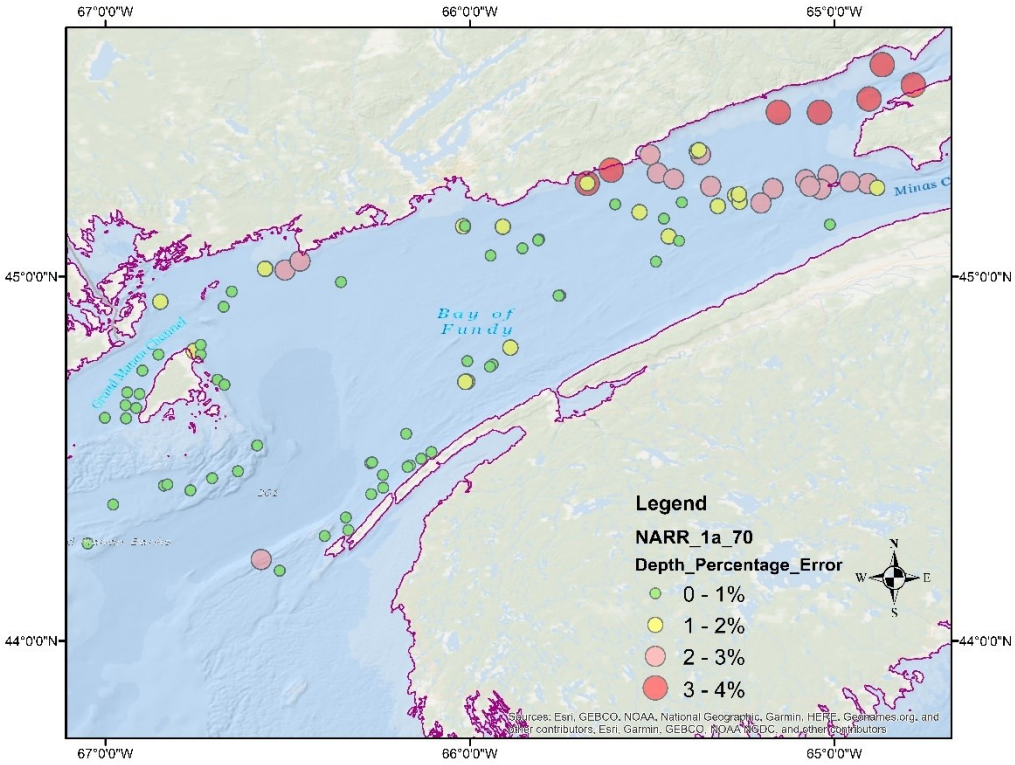

Figure 35. The depth percentage error by using the FVCOM _NARR model profile.

However, going to the deeper parts, middle to the mouth of the Bay, the surface layer is still warmer, but it gets enough time to reach the CTD cast below 10 m depth and follow

the same pattern as the CTD, with a little offset, to the bottom of the water column. This in turn will reduce the depth uncertainty at the deeper area and less profile rejection.

At the entrance of the Bay, especially around the Grand Manan Island, the modeled profiles show good results by having up to 1% depth percentage error. Regarding the IHO order 1a, the total rejection is 25%, almost double the FVCOM _HRDPS rejections, while those rejections are at the head of the Bay. However, there is less rejection at the entrance of the Bay compared to FVCOM _HRDPS. In total, the FVCOM _HRDPS provided better acceptance for the IHO order 1a at a 70-degree swath angle in the Bay of Fundy and introduced less vertical error in the sound speed raytracing.

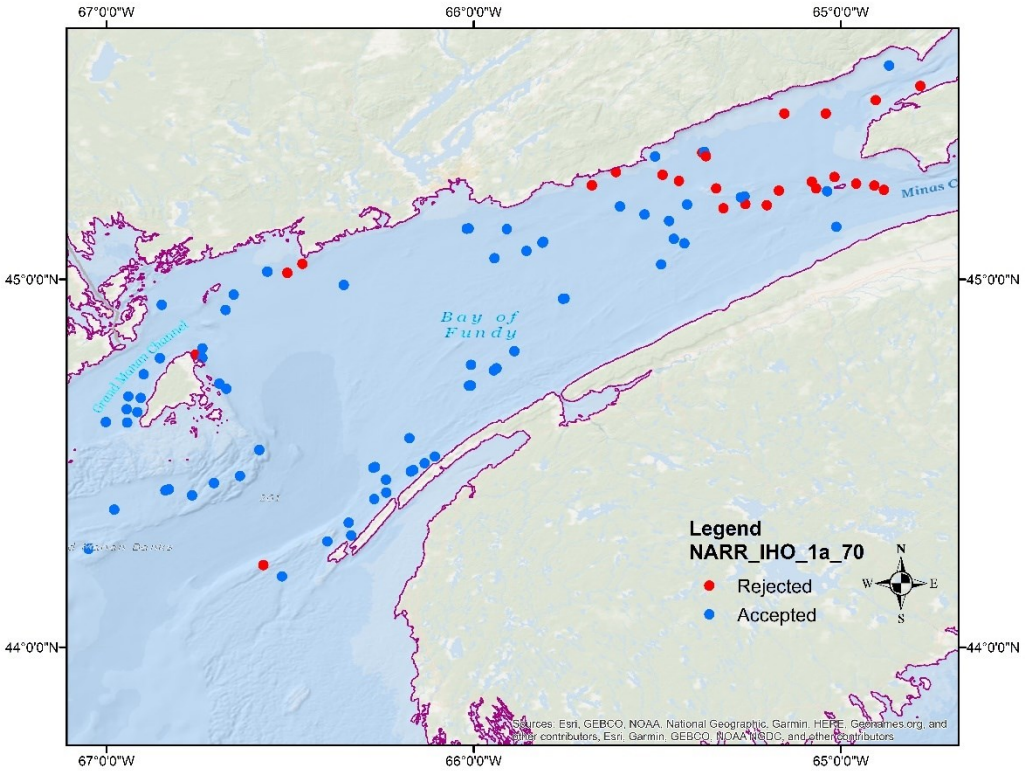

Figure 36. The accepted or rejected model profile after raytracing using FVCOM _NARR output at order 1a at a 70-degree swath angle. Red dots are rejected, and blue dots are accepted.

4.2 Minas Basin Model

The same calibration is performed for the Minas Basin model. However, in this case, the best model results come from the minimum drag coefficient of 0.025 (Wu et al., 2011) and the bottom roughness length scale of 0.001 meters. The predicted water level comparison against the CHC-published tidal constituents for two locations, Five Island and Burntcoat are provided in Table 16 to Table 20 for the Five constituents.

4.2.1 Model Calibration

The modeled water level is compared against the same two stations, Five Island and Burntcoat Head. For the M2, Table 16, the amplitude difference is less than 20 cm for the two stations, and compared to the Bay of Fundy model results (Table 4), there is a good improvement in Five Island and a 1 cm higher amplitude error in the Burntcoat station. As to the phase, at Five Island, the model is leading the observation by 2.45 degrees while it is lagged by 1.88 degrees at Burntcoat Head. Considering the total error for M_2 (last column), in comparison to the Bay of Fundy model, the Minas model has a lower error in Five Island and a little higher error in Burntcoat.

Table 16. The model Amplitude (m) and Phase (°, local) comparison against the CHS published constituents and discrepancies (CHS-Model) for M_2 with a bottom coefficient of 0.001m and minimum drag of 0.025.

M_2	Amplitude(m)			Phase (°)			Error(m)
	Obs.	Model	Diff.	Obs.	Model	Diff.	
260-Five Island	5.42	5.24	0.18	8.90	6.45	2.45	0.29
270-Burntcoat Head	5.64	5.44	0.20	14.00	15.88	-1.88	0.27
Mean			0.19			0.28	0.28
Absolute			0.19			2.1	
RMS			0.19			2.1	

The same feature is happening for the N_2, Table 17, at both stations with amplitude differences of 0.43 and 0.33 m for Five Island and Burntcoat Head. The phase lag has increased to 8.7 degrees at Burntcoat Head and is leading from the observations by 5.61 degrees at Five Island. Also, compared to the Bay of Fundy model results (Table 5), the Minas model has a higher total error in both stations in Five Island and Burntcoat.

Table 17. The model Amplitude(m) and Phase (°, local) comparison against the CHS published constituents and discrepancies (CHS-Model) for N_2 with a bottom coefficient of 0.001m and minimum drag of 0.025.

N2	Amplitude(m)			Phase (°)			Error(m)
	Obs.	Model	Diff.	Obs.	Model	Diff.	
260-Five Island	1.21	0.78	0.43	351.70	346.09	5.61	0.44
270-Burntcoat Head	1.09	0.76	0.33	351.00	359.75	-8.75	0.36
Mean			0.38			-1.5	0.4
Absolute			0.38			7.1	
RMS			0.38			7.3	

For the S_2 component, Table 18, the Five Island provides better results against the observation by the total error of 0.12 m. Also, the minas model performs better (lower total error) than the Bay of Fundy model for both stations for the S_2 constituent. In the case of diurnal tidal components, K_1 and O_1, Table 19 and Table 20, the differences in amplitude are very small and become zero for the O_1. Regarding the total error, the Minas model has a lower error than the Bay of Fundy model for both diurnal constituents in the two stations.

Table 18. The model Amplitude(m) and Phase (°, local) comparison against the CHS published constituents and discrepancies (CHS-Model) for S_2 with a bottom coefficient of 0.001m and minimum drag of 0.025.

S2	Amplitude(m)			Phase (°)			Error(m)
	Obs.	Model	Diff.	Obs.	Model	Diff.	
260-Five Island	0.78	0.69	0.09	54.00	47.82	6.18	0.12
270-Burntcoat Head	0.83	0.67	0.16	59.00	61.81	-2.81	0.16
Mean			0.12			1.6	0.14
Absolute			0.12			4.4	
RMS			0.12			4.8	

Table 19. The model Amplitude(m) and Phase (°, local) comparison against the CHS published constituents and discrepancies (CHS-Model) for K_1 with a bottom coefficient of 0.001m and minimum drag of 0.025.

K1	Amplitude(m)			Phase (°)			Error(m)
	Obs.	Model	Diff.	Obs.	Model	Diff.	
260-Five Island	0.17	0.18	-0.01	147.50	139.92	7.58	0.02
270-Burntcoat Head	0.14	0.17	-0.02	154.00	146.04	7.96	0.03
Mean			-0.02			7.7	0.02
Absolute			0.02			7.7	
RMS			0.02			7.7	

Table 20. The model Amplitude(m) and Phase (°, local) comparison against the CHS published constituents and discrepancies (CHS-Model) for O_1 with a bottom coefficient of 0.001m and minimum drag of 0.025.

O1	Amplitude(m)			Phase (°)			Error(m)
	Obs.	Model	Diff.	Obs.	Model	Diff.	
260-Five Island	0.13	0.13	0.00	134.50	121.28	13.22	0.03
270-Burntcoat Head	0.12	0.12	0.00	140.00	133.09	6.91	0.01
Mean			0			10	0.02
Absolute			0			10	
RMS			0			10.5	

4.2.2 Model Validation

Due to the lack of CTD cast observations in the Minas Basin, the Minas Basin model is just validated against the tidal current observations and GHRSST data.

4.2.2.1 Predicted Tidal Current

The same comparison as for the Bay of Fundy model is used for comparing the predicted tidal currents against the observation for the Minas Basin model. Table 21 shows the results of depth-averaged current analysis for semi-major, semi-minor, inclination, and phase at stations C1 and C2 for the M_2 in the Minas Basin passage.

Table 21. Model data comparison of the depth-averaged tidal ellipse for M_2. The location of sites is in Fig. 8 (Units of Semi-major and minor are in m/s and the difference in angles are in degrees).

	Observed					Modeled					Difference			
	Semi-Major	Semi-Minor	Incline-action	Phase		Semi-Major	Semi-Minor	Incline-action	Phase		Semi-Major	Semi-Minor	Incline-action	Phase
C1	2.70	-0.03	158	210.6		2.80	-0.3	162	225		0.1	-0.27	3.2	14.4
C2	2.87	-0.1	162	209.3		2.90	-0.05	164	227		0.03	0.05	2	17.7

The Minas model shows a good agreement at the semi-major axis at both C1 and C2 stations at 2.8 and 2.9, respectively. The model is slightly stronger at these two stations at 0.1 m/s at C1 and 0.03 m/s at C2. The modeled semi-minor axis at C1 is stronger by 0.27 m/s and it is weaker by 0.05 m/s at C2. The modeled inclination is slightly larger than the observation by 3.2 and 2 degrees for C1 and C2, respectively. Regarding the phase, the model phase lagged by 14.4 and 17.7 degrees at these two stations.

Comparing the Bay of Fundy model and the Minas Basin model shows that the semi-major axis has improved at both C1 and C2 in the Minas Basin model in comparison to the Bay of Fundy model. Table 22 shows the results of this comparison.

Table 22. Model data comparison of the depth-averaged tidal ellipse for M_2 for the Bay of Fundy and Minas Basin model against the observations at C1 and C2.

	Bay of Fundy model					Minas Basin model			
	Semi-Major-diff	Semi-Minor-diff	Inclination-diff	Phase-diff		Semi-Major-diff	Semi-Minor-diff	Inclination-diff	Phase-diff
C1	0.5	-0.01	3.2	9.4		0.1	-0.27	3.2	14.4
C2	0.23	0.05	-1	11.7		0.03	0.05	2	17.7

At C1, the semi-major difference is 0.5 and 0.1 m/s at BoF and Minas models, respectively. They both provided the same inclination difference at 3.2 degrees, while for semi-minor and phase differences, the BoF model shows a better agreement against the observation. At C2, they both have the same semi-minor difference against the observation at 0.05 m/s, while the Minas Basin model performs better than the BoF model for the semi-major axe with a small difference of 0.03 m/s. However, the BoF model shows better results for the phase and inclination difference compared to the observation in this station.

4.2.2.2 Sea Surface Temperature Variability in Minas Basin

For the Minas Basin, due to the lack of a CTD database to compare with the predicted water column temperature, only the Minas model SST is compared against the GHRSST data. Also, an SST comparison for both BoF and Minas Models is provided in Figure 37. The Minas model was run by the HRDPS surface forcing, it is compared against the BoF model with the HRDPS only. In comparison to the BoF model, the Minas Basin model provides better agreement against the GHRSST data. The correlation and STD have

improved and reached 0.89 and 1.5 degrees. Also, the RMS error has decreased to 0.82 compared to 0.96 degrees from the BoF model. The only difference between the Minas model and the Bay of Fundy model is the horizontal resolution of the mesh. While the vertical resolution of the model is the same for both models, the Minas Basin has a finer horizontal resolution.

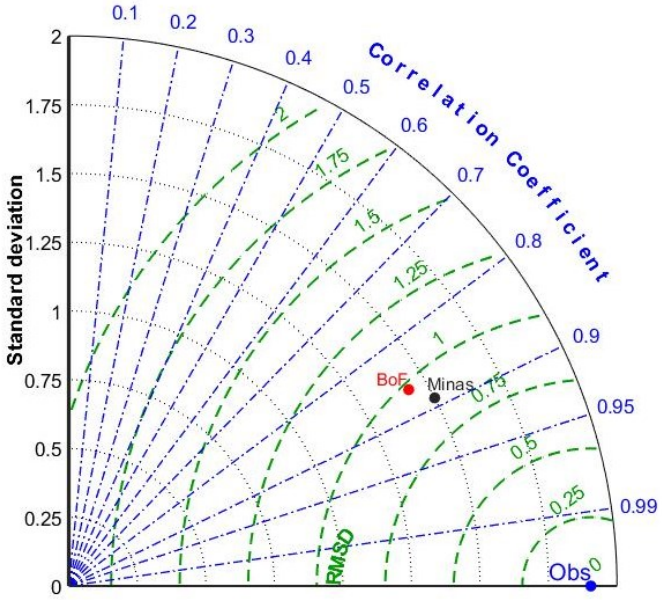

Figure 37. Taylor plot for Minas Basin comparing GHRSST against the SST from Minas and BoF models.

4.2.2.3 Salinity and Temperature Variability in the Water Column

A comparison between the Minas model run in 2007 against the MVP data is provided in Figure 38 and Figure 39 for 6 profiles in the area. As the water reaches into the Minas Channel and Minas Basin, both salinity and temperature become less variable due to the huge effect of tidal mixing in the area, however, there are still small variations on the entrance of the Basin. The Minas Basin model can capture the variability in all 6 transects,

but there are some discrepancies regarding the structure of the temperature and salinity. At the Minas Basin and Minas Passage, Figure 38 a, b, and c; the model shows a cold bias in temperature while the simulated salinity provides better agreement with the MVP data. The same cold bias in temperature repeats at the Minas Channel, Figures 39a, and b, while it represents a better salinity profile against the observation. At the entrance of the Minas Passage, Figure 39c the model, however, shows a warm bias in the temperature and less salty water than the observations. In general, the maximum bias in temperature is less than 0.7 °C and less than 0.3 ppt for the salinity for the Minas model.

Capturing the Basin dynamics and variability of temperature and salinity requires a good open boundary condition and a higher resolution of surface forcing, higher than NCEP, for providing the local wind regime in that area. Also, high-resolution bathymetry data could significantly improve the ocean model performance for the domain, by providing a detailed topographic feature of the seafloor through better bottom roughness representation. However, the lack of high-resolution bathymetry data in the Minas Basin generates more bias and errors in the ocean model due to the inability of the model to resolve the small-scale seafloor features from coarse bathymetry. The huge tidal range, resulting in the generation of a vast intertidal zone; and the short hydrographic survey window make it difficult to plan a comprehensive hydrographic survey plan in this area and an insight into the ocean variability and its dynamic could make a huge difference in hydrographic pre-planning procedure.

It is important to distinguish between the purposes of a bathymetric survey and an ocean model. While a high-resolution bathymetric survey enhances the input data quality for an ocean model, the model itself provides insights into water column dynamics, current

structures, and environmental variability, which are crucial for applications like hydrographic survey planning, habitat mapping, and coastal management. Therefore, bathymetry improves the ocean model's ability to simulate realistic conditions, which, in turn, supports the effective planning of future bathymetric surveys or other marine studies.

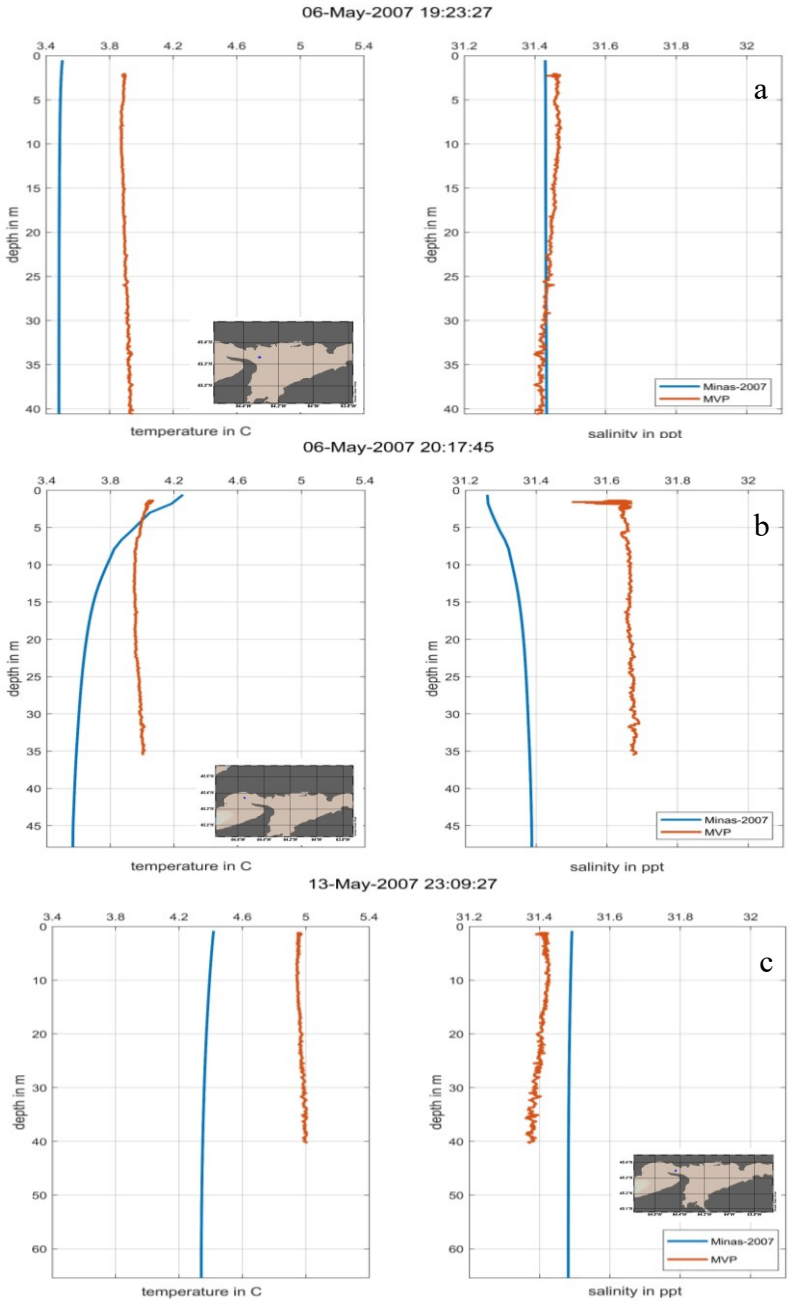

Figure 38. Temperature (left column) and Salinity (right column) profiles for the Minas_model (blue) and MVP data (orange) at a and c) Minas Basin on May 6th at 19:23 and 20:17, b) Minas Passage on May 13th at 23:09.

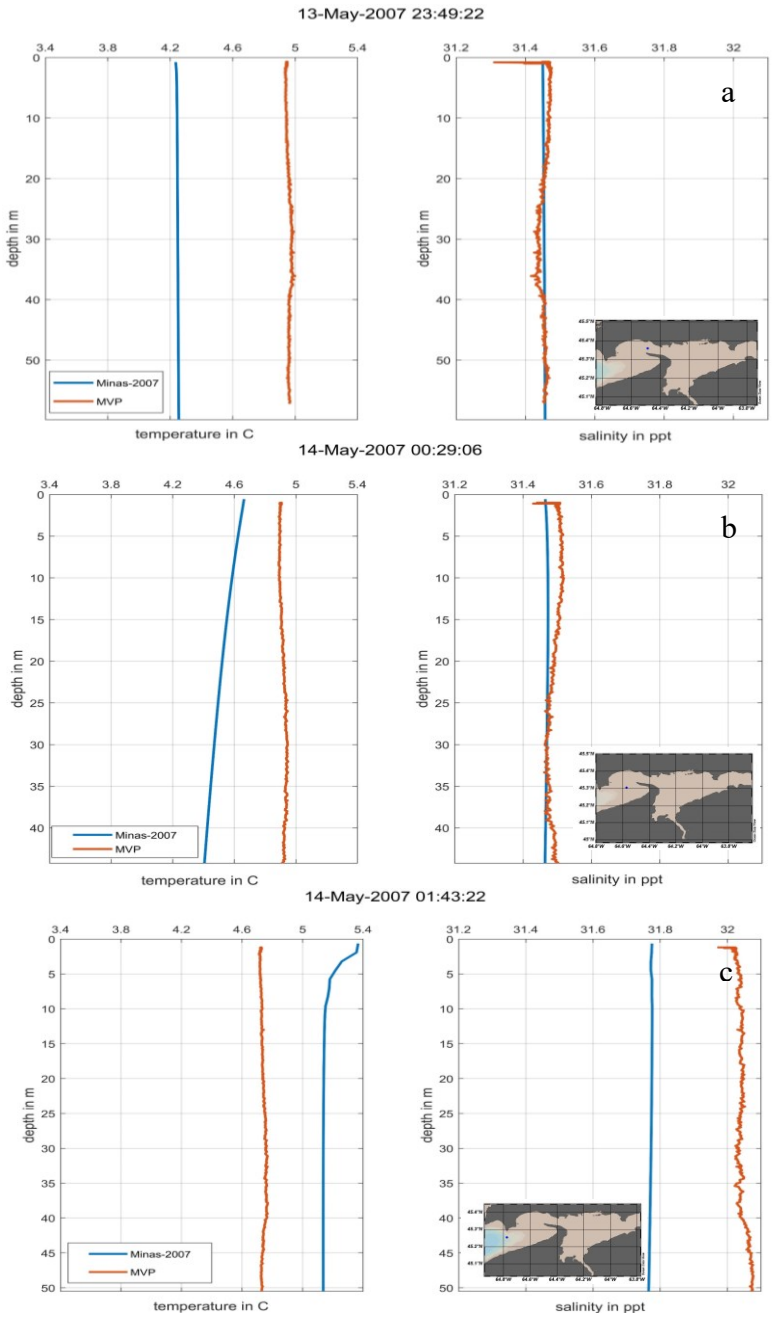

Figure 39. Temperature (left column) and Salinity (right column) profiles for the Minas_model (blue) and MVP data (orange) at a) Minas Passage on May 13 at 23:49, b) Minas Channel on May 14th 00:29, and c) entrance of Minas Passage on May 14th at 01:43.

4.3 Hydrography Survey Planning

Simulations for the Bay of Fundy and Minas Basin models are provided in this section. Each of these includes different scenarios based on the hypothetical survey requirements.

4.3.1 Saint John Harbor

Saint John River (SJ River) is the main source of freshwater discharge in the Bay of Fundy and features complex oceanography and hydrography which make the hydrographic survey more challenging. Based on the proposed hydrographic survey design, all aspects of the survey design such as high tidal range, surface current speed, and oceanographic variability, due to the discharge of freshwater on the surface layer and entrance of salt-water from the bottom layer (Church, 2014), are involved in this area. Different IHO orders could be considered and evaluated for the surface current speed of 1 m/s and depth higher than 5 meters. A synthetic CTD cast, generated from BoF model output, has been chosen at the outer part of the Harbor and the effect of under-sampling of the CTD on the hydrographic survey is demonstrated in the following figures. A scenario is considered, with a minimum depth of 5m, a surface current speed limit of 1 m/s, a 140-degree multibeam swath angle, and applying the IHO exclusive order for half tidal cycle. A model output profile (including temperature, salinity, and total depth) is picked and is considered the first synthesized CTD cast for the survey area. Then, this CTD is used for doing the ray tracing against the other modeled profiles in Saint John Harbor. The total depth, including bathymetry, predicted water level from the model (zeta), and vessel draft, is normalized to the 5-meter depth and is multiplied by 100. Figure 40 shows four stages of the tide on August 15th, starting at a) 02:00 am, b) 05:00 am, c) 08:00 am, and d) 11:00 am.

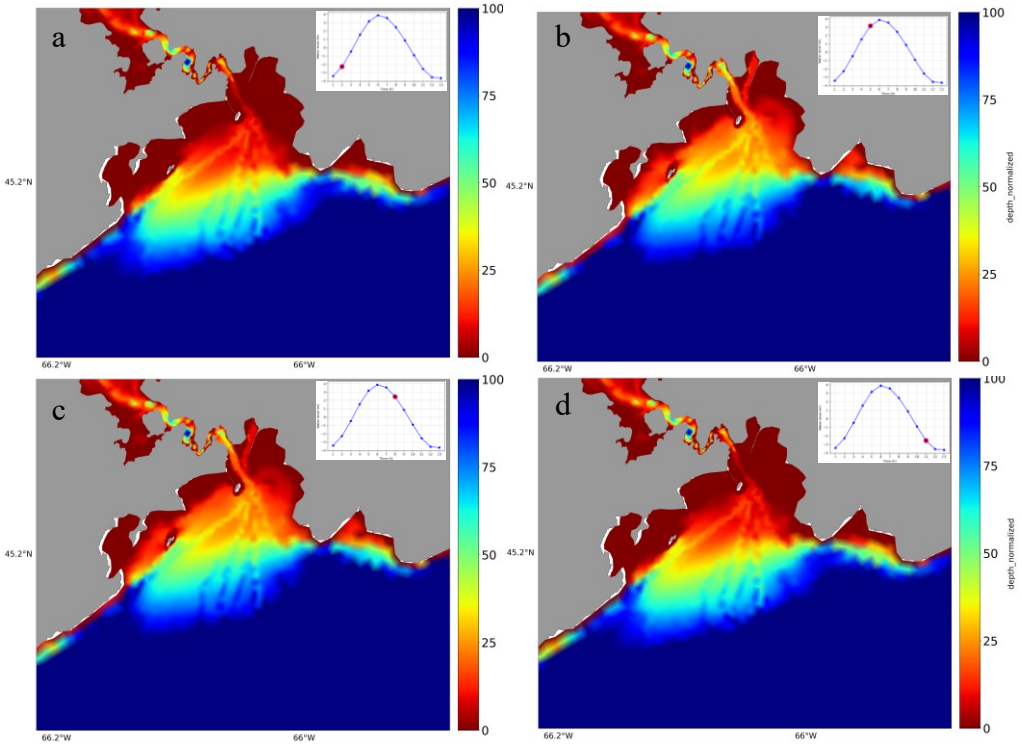

Figure 40. The normalized depth to 5 meters on 2018-08-15 at a) 02:00 at the start of the flood and b) at 05:00 at the flood, c) at 08:00 start of ebb, and d) at 11:00 at ebb.

The values close to 100 show the deep area and the ones close to zero indicate very shallow areas (close to or lower than 5m). The dark brown areas are where the domain did not satisfy the instance depth higher than 5 meters, and the rest shows how the normalized depth has changed as the tide goes in and out. The surveyable area in a half tidal cycle could be presented in percentages showing how far the platform could reach based on the depth-only criteria. Figure 41 shows that the channel in the Harbor is surveyable more the 80 percent of the half tidal cycle, however going further away from the deep part of the Harbor, it reaches 50 to 20 percent.

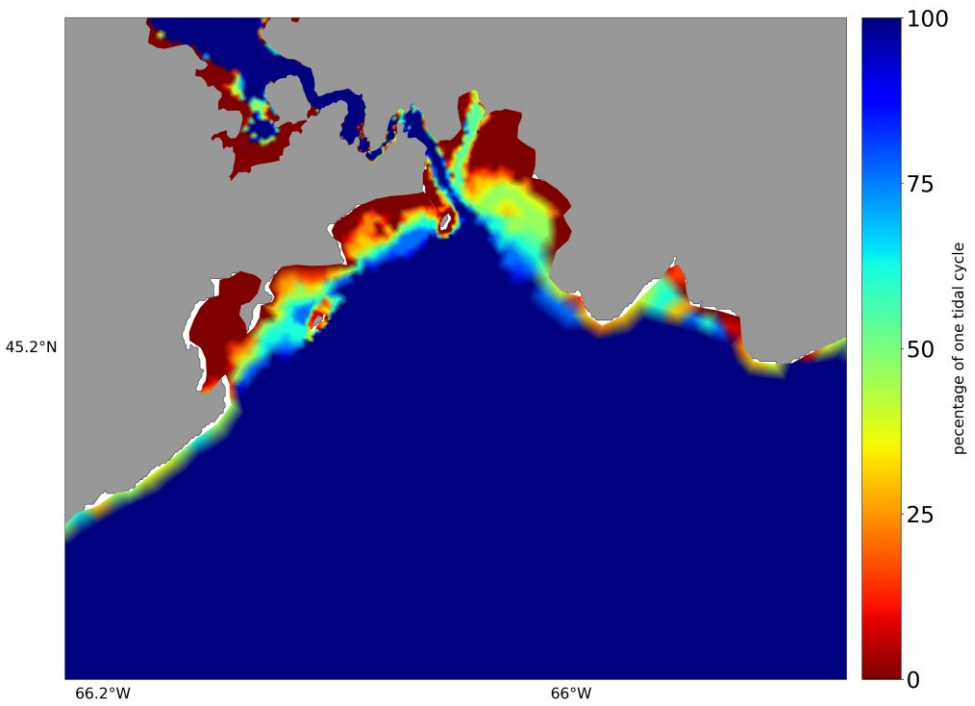

Figure 41. The percentage of time in half tidal cycle with a total depth greater than 5m.

Using the next criterion, the surface current speed lower than 1 m/s could be beneficial for the remotely operated vehicles to check for challenging areas based on the vessel's limitations and operational capabilities. As Figure 42 shows, most of the area has a surface speed lower than 1 m/s except for some limited areas close to the Reversing Falls, Saint John Harbor bridge, and Cape Spenser, which features some high current speed. At 02:00 am (Figure 42a), a small section at the Reversing Falls, the Courtenay Bay Breakwater, and a large section around Cape Spencer show higher surface current speed than 1 m/s. At 05:00 am (Figure 42b), the Reversing Falls show higher surface speed in the domain. At 11:00 am (Figure 42d), other than the Reversing Falls and the outer part of the Harbor, a small section close to the Saint John bridge has a higher surface current than 1 m/s.

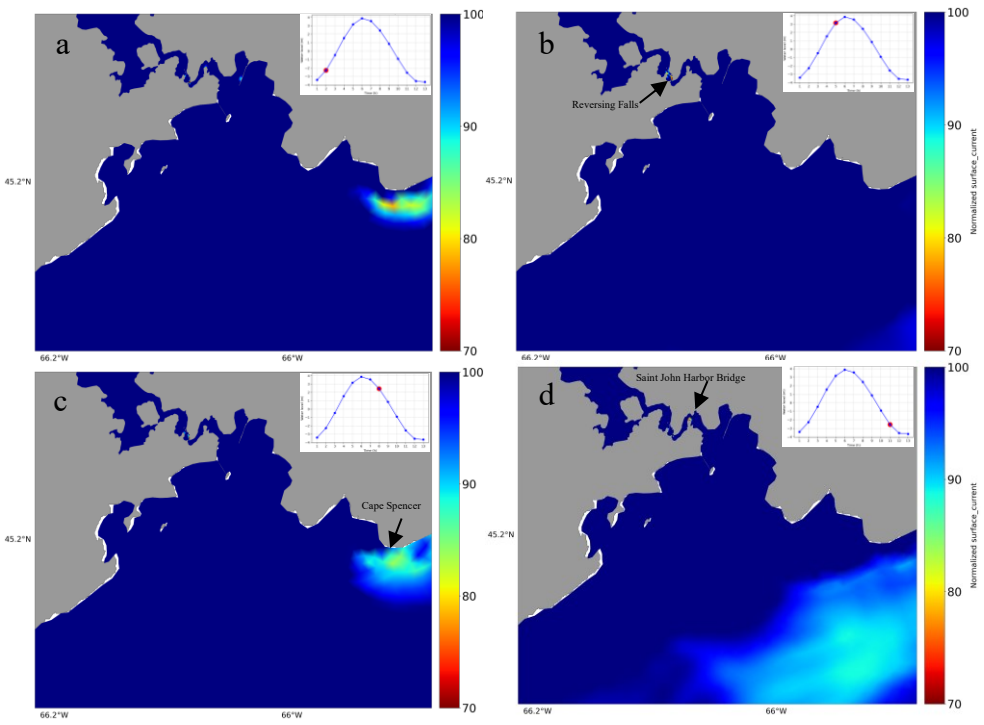

Figure 42. The weighted normalized surface current speed was less than 1 m/s on 2018-08-15 at a) 02:00 at the start of the flood b) at 05:00 at the flood, c) at 08:00 start of ebb, and d) at 11:00 at ebb.

Considering the surface speed variability in one tidal cycle, Figure 43, depicts that most of the domain satisfies the surface speed of less than 1 m/s, however, the Reversing Falls and close to the Harbor bridge are the areas where they show the surface speed is lower than 1 m/s at 50 to 70 percent of a tidal cycle.

These plots, Figure 40 to Figure 43, have considered each criterion separately and in the next step, the effect of the joint criteria is considered. Based on the survey vessel specification, a different weight could be assigned to each of those criteria, minimum depth, and surface current speed.

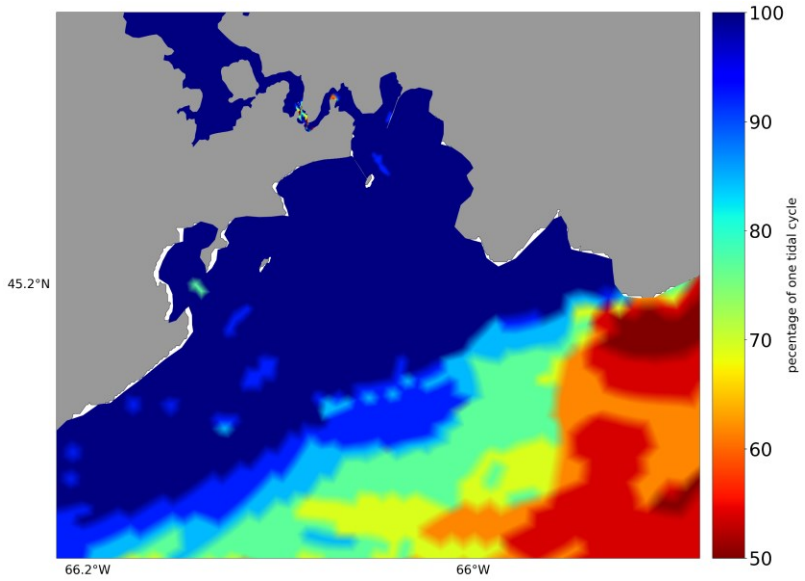

Figure 43. The percentage of time in half tidal cycle with surface current speed lower than 1 m/s.

The weight of depth is assigned as 0.7 and the surface current speed's weight is assigned as 0.3, satisfying the sum of both weights as 1, and finally multiplied by 100. This dataset ranges from 0 to 100 showing the effects of both criteria. Figure 44 depicts the areas where the weighted values for both total depth and the surface current speed are higher than 31. The white areas are where the values are less than 31 and are excluded from being a safe domain and not considered in the base layer for further IHO evaluation.

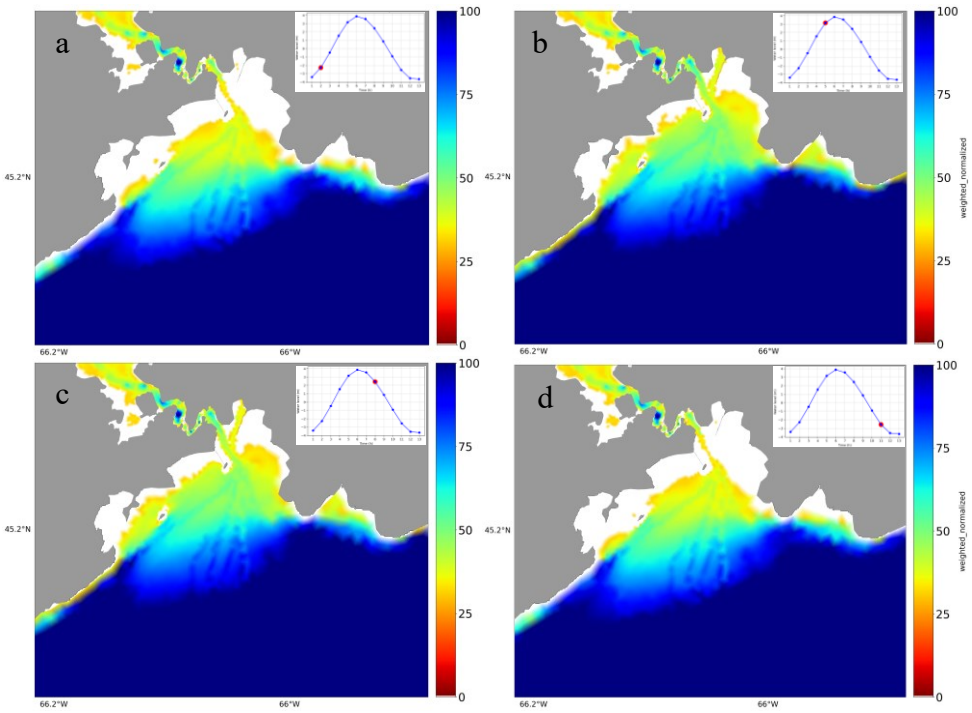

Figure 44. The weighted normalized total depth and surface current speed on 2018-08-15 at a) 02:00 at the start of the flood and b) at 05:00 at the flood, c) at 08:00 start of ebb, and d) at 11:00 at ebb.

The blue areas are getting a high value satisfying both the depth and surface speed criteria and as it reaches the red colors it becomes less favorable. At 02:00 am (Figure 44a), the rejected nodes (white colors) are mostly scattered in the shallow areas, also at some point close to Reversing Falls. As the water enters the Harbor, Figure 44b, the number of rejected nodes decreases and there are more surveyable areas satisfying both criteria. This layer is considered the base layer for performing the raytracing and calculating the depth percentage error due to using a synthetic CTD cast from the model output and then checking the IHO order, (exclusive order) in each time step. Figure 45 shows the percentage of depth error that the survey would achieve if using the synthetic CTD cast (orange dot) at the beginning of the survey. This CTD cast at that specific time step is used

for the raytracing against other modeled profiles at later times. Closer to the CTD cast, the error reaches zero and as it goes further to the Harbor area (Figure 45a), the depth error reaches 2 to 3 percent of depth. The distribution of depth error percentage changes during half a tidal cycle in Figure 45 b, c, and d. Then, by performing the IHO exclusive order check, Figure 46 shows almost the same pattern on accepted and rejected areas as the depth percentage error.

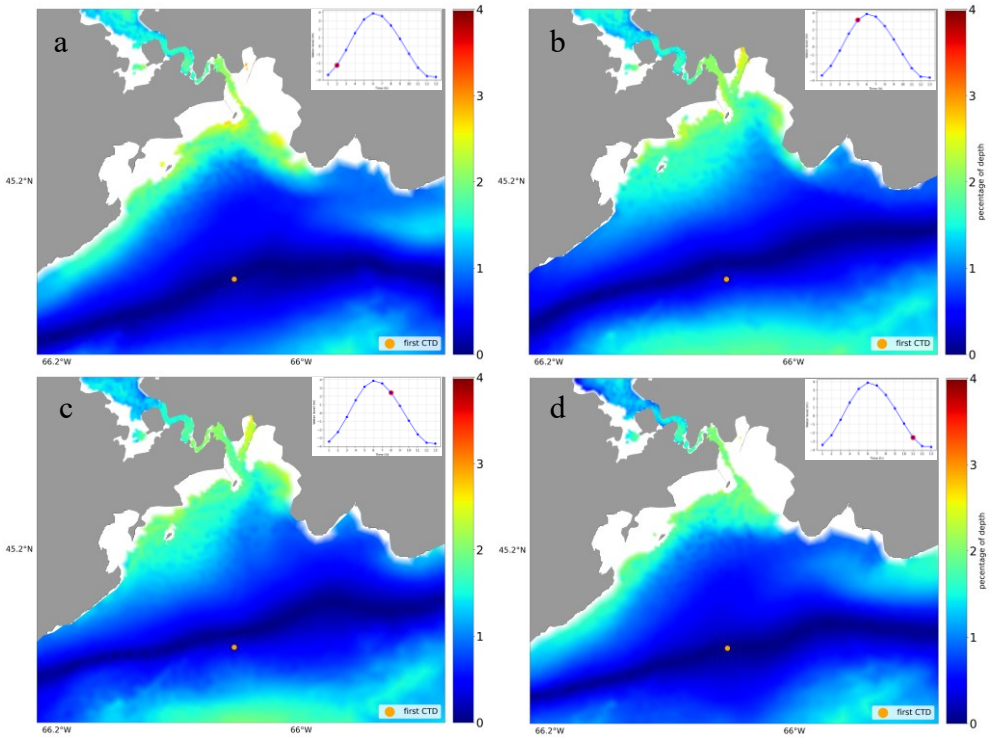

Figure 45. The percentage of depth error introduced by using a modeled profile (as synthetic CTD cast, orange dot) on 2018-08-15 at a) 02:00 the start of the flood and b) at 05:00 at the flood, c) at 08:00 start of ebb, and d) at 11:00 at ebb.

The blue and red areas show the accepted and rejected exclusive order, respectively, based on the CTD cast at the first time step. At the beginning of the flood at 02:00 am, Figure 46a, some part of SJ River at the Harbor passes the exclusive order, having about a 2% depth error.

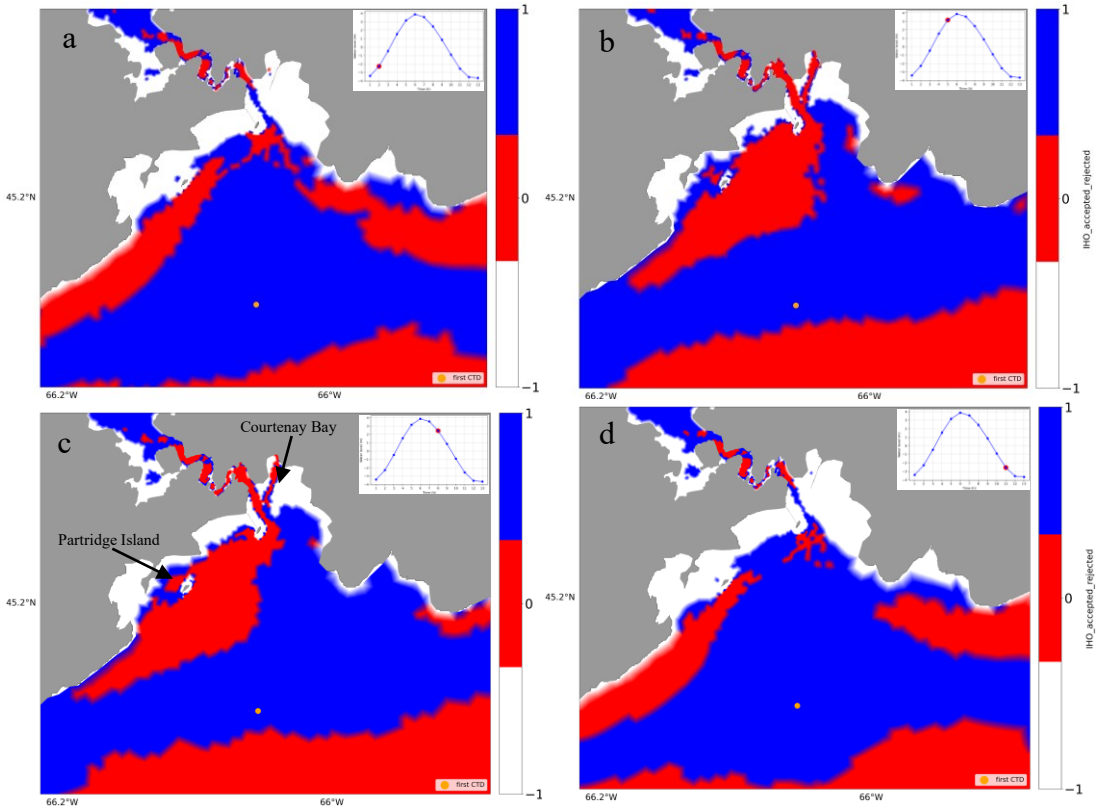

Figure 46. The IHO exclusive order was accepted or rejected on 2018-08-15 at a) 02:00 at the start of the flood and b) at 05:00 at flood, c) at 08:00 start of ebb, and d) at 11:00 at ebb. The red and blue colors are accepted and rejected orders, and the white areas did not pass the base layer criteria.

At this time at the outer part of the Harbor, areas with higher depth percentage error, especially at the edge of the base layer are rejected and only the middle part is accepted. At 05:00 am, Figure 46b, most of SJ River, including Courtenay Bay, from the Harbor to the upper part of Reversing Falls fails the exclusive order. At this point, the freshwater

discharge of SJ River flows on the top of the saltier Bay of Fundy water to Partridge Island and creates a different water mass and stratification in that area. The rejected areas remain the same in the entire domain in the next three hours at 08:00 am, Figure 46c. Also, a high section of areas surrounding Patridge Island is rejected compared to the start of the tidal cycle. Considering a half tidal cycle, a layer showing the percentage of the tidal cycle in Saint John Harbor is created which depicts which areas are more susceptible in the case of rejecting the IHO order (Figure 47).

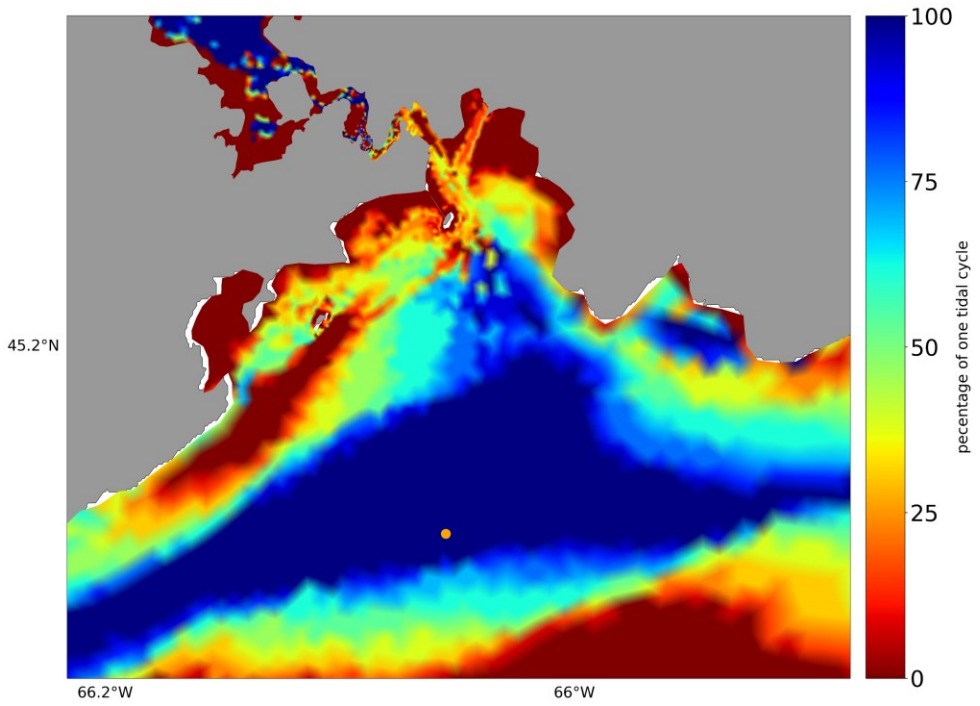

Figure 47. The percentage of half tidal cycle that the survey would satisfy exclusive order based on the first CTD cast.

As depicted in Figure 47, the blue section would meet the exclusive order in 90 or 100 percent of the half tidal cycle, while the green areas only satisfy that order just 50 percent of the time. In the Harbor area, this percentage reduces to 40 to 25 percent of the half tidal cycle, showing a very dynamic environment and more challenging to meet a high standard

such as exclusive order. This layer provides valuable insight in terms of survey planning and getting more insight into the variability of the survey domain and how to plan a more beneficial survey in terms of survey time and costs. It is worth mentioning that some parts of the upper part of Saint John River always are accepted for this IHO order, while the synthetic CTD cast is very far from this location and could have a different water mass. Figure 45 shows that for this region, the percent of depth error is always less than 2, while closer to the Reversing Falls, the depth error increases. At the Reversing Falls, the water column faces a huge mixing and density gradient change, that could be very different than the location of the synthesized CTD cast. However, at the upper part of the bay, the effect of intensive mixing and layering decreases and depth error decreases, leading to being accepted for the IHO order.

4.3.2 Minas Basin

Minas Basin is a tidal environment with a huge tidal range and tidal flats in the upper part of the Basin which makes the hydrography survey, specifically using multibeam, a very complicated and demanding project. Using a remotely operated vehicle or autonomous survey platform could ease the process, however, these platforms face some limitations. For the first scenario, the survey vessel could safely transit in the surface water speed of less than 1m/s and a water depth greater than 5 meters. Also, the survey should satisfy the IHO order 1a in the survey area using the 140-degree swath angle for the multibeam.

Two scenarios are considered to showcase the differences in the water mass in the Minas Basin, one choosing the synthesized CTD cast at the open boundary, and the other one in the Minas Basin. Figure 48 shows the normalized depth at the start of the tidal cycle, at

02:00 am and every three hours until 11:00 am. As the tide enters the Basin, the water level increases up to the head of the Basin. But there are still huge tidal flats and areas less than five meters depicted in dark red. If a surveyor or an autonomous platform is more concerned about the total depth of the domain in one tidal cycle, it would be useful to have a plot that represents the percentage of the half tidal cycle for the model domain having a depth higher than 5 meters. Figure 49 depicts the percentage time of the half tide cycle for the whole domain in which the total depth is higher than 5 meters.

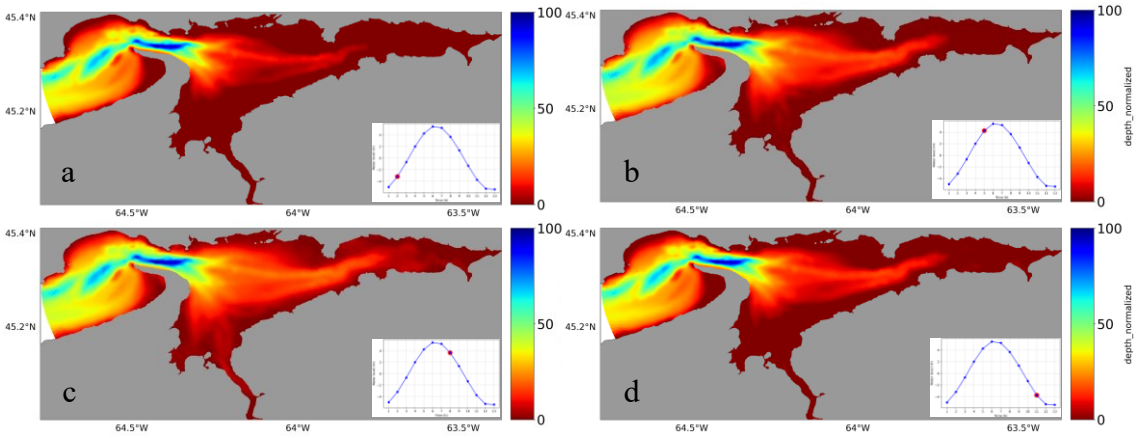

Figure 48. The normalized depth to 5 meters on 2018-08-15 at a) 02:00 at the start of the flood and b) at 05:00 at the flood, c) at 08:00 start of ebb, and d) at 11:00 at ebb.

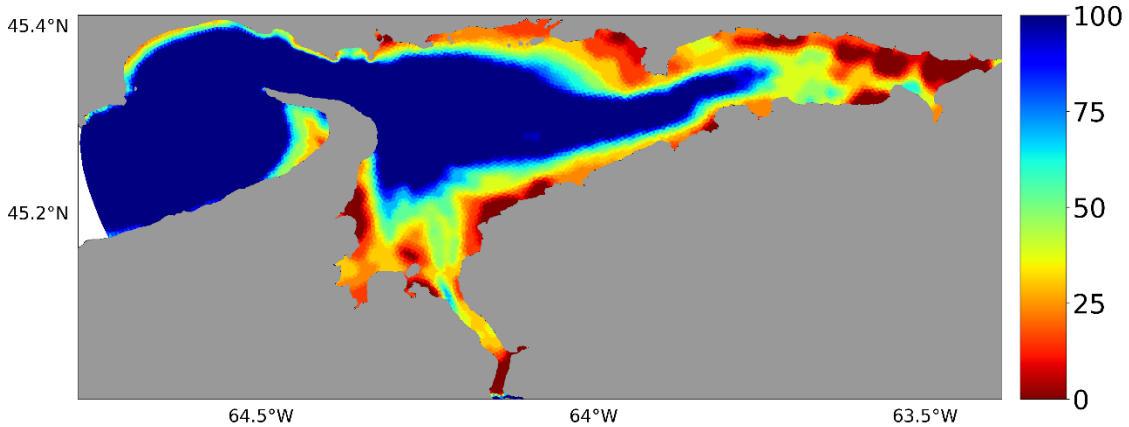

Figure 49. The percentage of time in half tidal cycle with a total depth higher than 5m.

Most of the areas have a total depth higher than 5 meters in more than 80 percent of one tidal cycle. The rest of the Basin is 50 percent or less in one tidal cycle for the transition. This alone could provide insight into the survey planning before performing the hydrography survey. Also, during the survey, it could be used to predict the safe transit (based on total depth) for the survey vessel in a new environment.

In the next step, the normalized surface current speed lower than 1 m/s is generated. The current speed higher than 1m/s gets values close to zero, based on the maximum range of surface current speed, and the speed lower than 1 m/s gets values at 100. Figure 50 provides the normalized surface current speed for starting at 02:00 am every three hours, until 11:00 am.

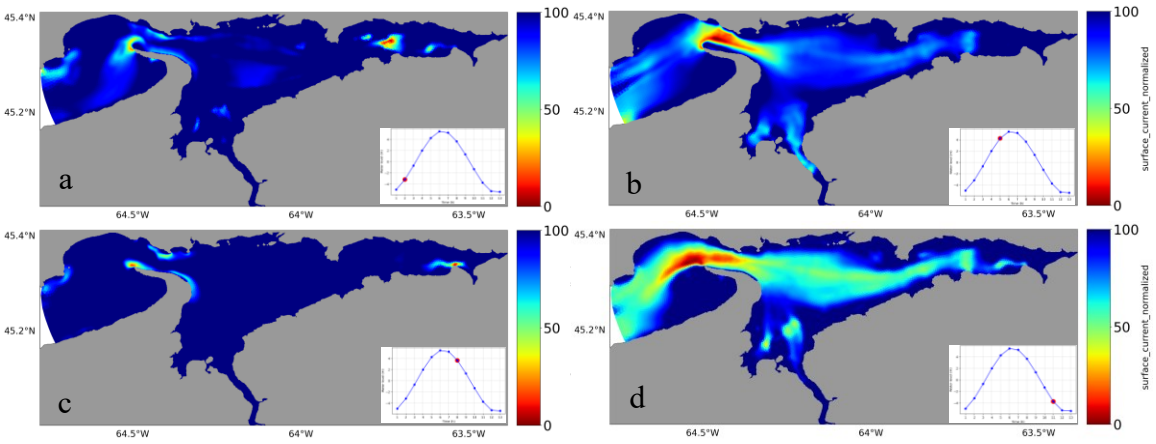

Figure 50. The normalized surface current speed to 1m/s on 2018-08-15 at a) 02:00 at the start of the flood and b) at 05:00 at the flood, c) at 08:00 start of ebb, and d) at 11:00 at ebb. Dark blue is the area with a surface speed lower than 1m/s and green and red have a higher surface speed than 1m/s.

The areas in blue are more appropriate if there is any surface speed limitation for the autonomous survey platform, while the red areas are more prone to the higher surface current speed. As in the normalized depth, Figure 51 shows the percentage of time of one

tidal cycle where the surface current speed is lower than 1m/s. The Minas Basin experiences high tidal currents and Figure 51 indicates that most of the Basin (red color) has less than 25 percent of one tidal cycle with a speed lower than 1m/s, especially in the middle part of the Basin and the Minas Channel and Passage.

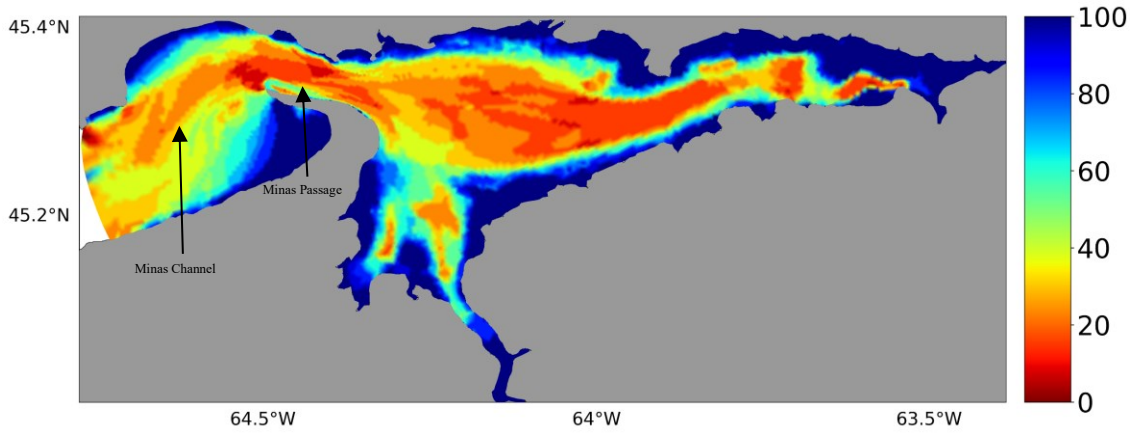

Figure 51. The percentage of time in half tidal cycle with surface current speed lower than 1m/s.

Figure 49 and Figure 51 are the results of applying two different criteria to the Minas model output. However, if the two criteria are to be considered for a specific survey, it will provide the areas in which the domain satisfies the total depth higher than 5 m and surface current speed lower than 1 m/s. Figure 52 shows the combination of these two criteria after applying the weight to each criterion in a tidal cycle. The blue color indicates that more than 80 percent of a tidal cycle, the entrance of Minas Basin close to Cape Split, satisfies both criteria, while the red sections, which are mostly at the head of Minas Basin and Minas Passage, have a very short tidal window (less than 25 percent of the half tidal cycle) to do so.

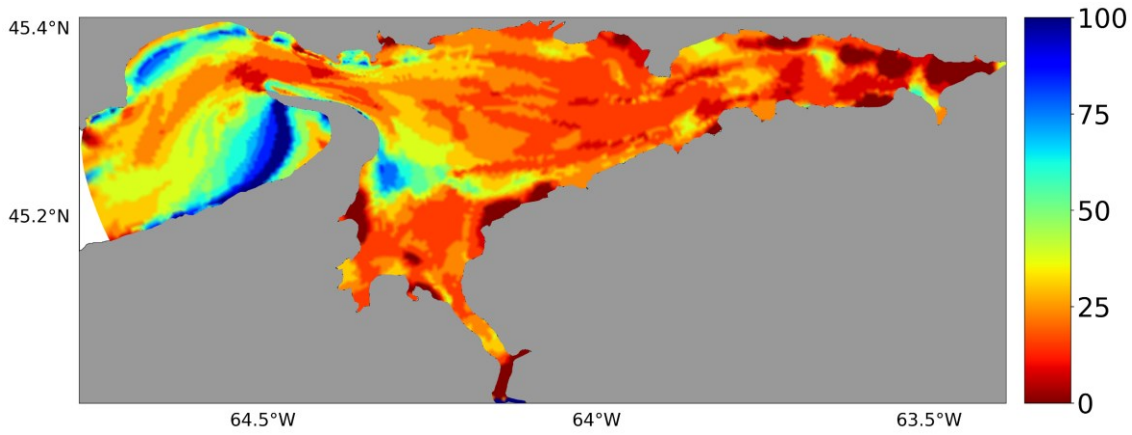

Figure 52. The percentage of time in half tidal cycle with surface current speed lower than 1m/s and depth higher than 5 m.

These plots, Figure 49 to Figure 52, provide some important information on the nature and specification of the environment and do not consider the operational limitation of hydrographic survey standards. The base layer is generated by excluding the high-risk zones, where the total depth is lower than 5 meters and the surface current speed is higher than 1 m/s. Also, based on the survey platform specification, the surveyor could apply specific criteria and different weights to these criteria. In some cases, the domain could have a huge tidal range, high surface current speed, or both together. For instance, a weight value of 0.70 and 0.30 are considered for the depth and surface current speed criteria, respectively. These weights have been applied to the normalized depth and surface current speed layer for the Minas Basin. Figure 53 depicts the weighted normalized of total depth and surface current speed for the four parts of half a tidal cycle, a) on 02:00, b) 05:00 am, 08:00 am, and 11:00 am. The remaining area is where it has both the safety of navigation (total depth greater than 5 m) and operatable (surface current speed lower than 1m/s) by the survey platform.

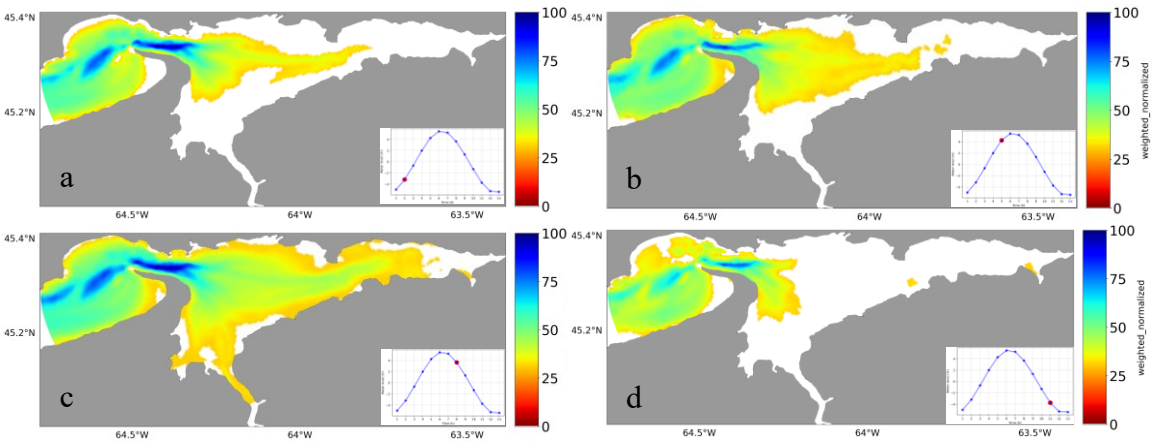

Figure 53. The weighted normalized total depth and surface current speed on 2018-08-15 at a) 02:00 at the start of the flood and b) at 05:00 at the flood, c) at 08:00 start of ebb, and d) at 11:00 at ebb. The white areas have weighted normalized values of less than 31.

This layer is used to provide the sound speed ray-tracing uncertainty calculation using the modeled temperature and salinity profiles and check how much depth error is introduced in our measurement by relying on a profile from model output and considering that as the first CTD cast at the entrance of Minas Basin and whether the rest of the domain satisfy the IHO order 1a or not. Figure 54 depicts the results of the raytracing using a random modeled profile from the model at the entrance of Minas Basin and checking this cast in other parts of the domain to check how much depth error would be introduced in the raytracing.

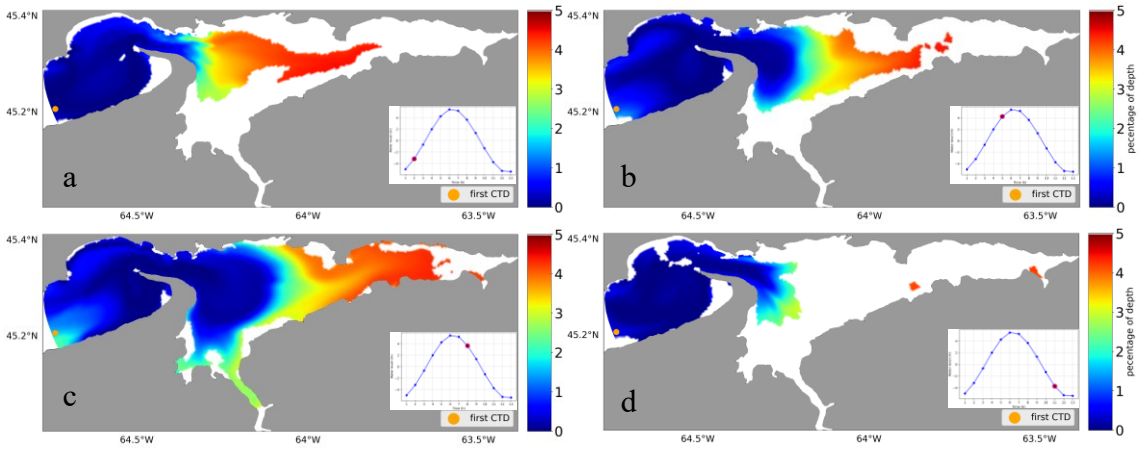

Figure 54. The percentage of depth error introduced by using a modeled profile (the orange dot as synthetic CTD cast) at the entrance of Minas Basin on 2018-08-15 at a) 02:00 the start of the flood and b) at 05:00 at the flood, c) at 08:00 start of ebb, and d) at 11:00 at ebb.

At the beginning of the tidal cycle, Figure 54a, the Minas Channel shows a low percentage of depth error of about 1%, reaching 2% at the Minas Passage, and finally 4% at the middle of Minas Basin. After 6 hours, Figure 54c, while using the same modeled profile for the raytracing, the distribution of the depth error has changed by the flood condition of the tide. Close to the CTD location at the Minas Channel, the depth percentage error is almost at 2%, less depth percentage error of about 1-2% at the Minas Passage and Minas Basin, and a 4-5% depth error at the head of the Basin. Then, the results of these depth errors are compared against the TVU at IHO order-1a for the whole domain. Figure 55 provides the final result of whether the survey would satisfy the IHO order-1a by using only CTD cast at the entrance of the Minas Basin model.

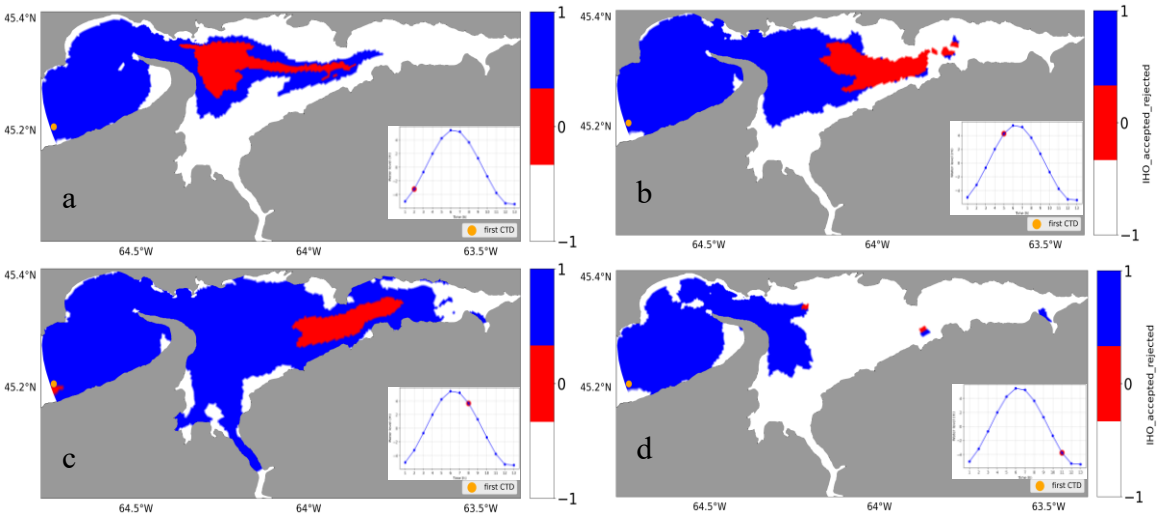

Figure 55. The IHO order 1a was accepted or rejected on 2018-08-15 at a) 02:00 at the start of the flood and b) at 05:00 at flood, c) at 08:00 start of ebb, and d) at 11:00 at ebb. The red is rejected, the blue is accepted, and the white did not satisfy the depth and surface speed criteria.

At the beginning of the tidal cycle, Figure 55a, the hydrography survey was accepted at order-1a in the Minas Channel and Minas Passage, but as the depth percentage error increased and depth decreased at the Minas Basin, the survey was rejected at this IHO order. However, 6 hours later, in Figure 55c, due to the increase in the depth percentage error at the Minas Channel, the survey started to be rejected close to the CTD location. However, it is still accepted at this IHO order in the Minas Passage and the entrance of Minas Basin. At the head of Minas Basin, where the depths are shallower and the depth percentage error is higher, the survey is rejected as well. In general, the depth portion of TVU plays a more important role in rejecting the IHO order 1a in Minas Basin. Also, the upper part of the Minas Basin is a little saltier and warmer which generates slightly a different water body than the entrance of the Minas Basin. This oceanographic feature

along with the higher depth in the head of Minas Basin has resulted in rejected IHO order in that area.

In another case, the criteria are the same as before (depth >5m and current speed <1 m/s), but the synthesized CTD (a modeled profile) location has changed and now it is at the entrance of Minas Basin after the Minas Passage. The results of depth percentage error and IHO order-1a accepted or rejected are provided in Figure 56 and Figure 57, respectively. At the beginning of the tidal cycle (Figure 56a), there is a small depth error around the CTD location at the Minas Basin less than 1%, while at the Minas Channel, the depth percentage error reaches 4%. At the Minas Passage, at the deep part, the error is less than 2%, but as it goes further to the shallow side of the Passage, the depth percentage error becomes 3%. In 6 hours, Figure 56c, the depth error distribution has changed, and the maximum depth error reaches 5% at the entrance of the Minas model (close to Huntington Point). At the head of the Basin, the depth error is still around 1%, while in the middle of the Basin, the error is about 3%. Almost the same depth error distribution is happening at the Minas Passage and more shallow areas are getting a higher depth error at 3%.

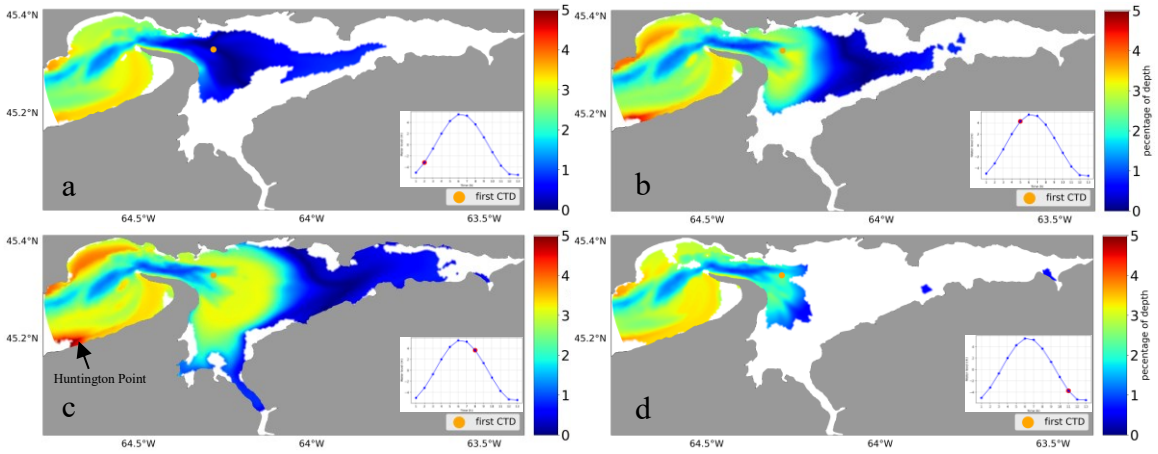

Figure 56. The percentage of depth error introduced by using a modeled profile (as CTD cast) at the middle of Minas Basin on 2018-08-15 at a) 02:00 the start of the flood and b) at 05:00 at the flood, c) at 08:00 start of ebb, and d) at 11:00 at ebb.

Figure 57 shows where the hydrography survey would satisfy the IHO order-1a by comparing the calculated depth error against the TVU. Most of the Minas Channel is rejected (Figure 57a) due to high depth percentage error except for two small sections in the middle of the channel, where the depth percentage error is around 1%. However, the majority of areas are rejected both at the start and 6 hours (Figure 57c) into the tidal cycle. At Minas Basin areas around the CTD cast, at the beginning of the flood, the survey is all accepted, but in 6 hours, they are all rejected, due to high percentage error, except some areas in the Minas Passage. The central Minas Basin, the Southern Bight, and some parts of Cobequid Bay are mostly accepted (lower depth percentage error). The rest of the domains, where the error is around 1%, are accepted.

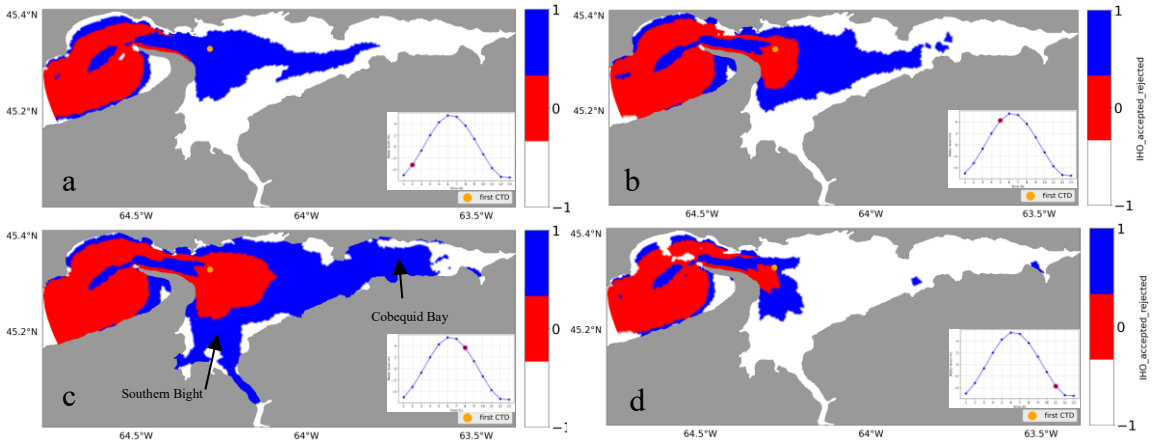

Figure 57. The IHO order 1a was accepted or rejected on 2018-08-15 at a) 02:00 at the start of the flood and b) at 05:00 at flood, c) at 08:00 start of ebb, and d) at 11:00 at ebb. The red is rejected, the blue is accepted, and the white did not satisfy the depth and surface speed criteria.

These criteria for the minimum depth and surface current speed could be changed by the hydrographic surveyor, and also, to the location of the first modeled profile as the CTD cast. Depending on where you pick the first CTD cast you can see the evolution of the depth error both in the time and space and then come up with a survey plan within your area. It should be noted that these are some static examples of using a synthetic CTD cast for half a tidal cycle, while one could pick different points in time and space and check the evolution of the accepted and rejected IHO order as one wishes.

Chapter 5: Discussion

Not only barotropic condition of the Bay of Fundy impact the hydrography survey design in different parts of the Bay, but also the baroclinic condition could have considerable influence on the depth bias on the outer swath angle of a multibeam survey. The interpretation of each of the three thesis questions is discussed in the following subsections.

5.1 Hydrodynamic Models

5.1.1 Water Level

Regarding the predicted water level, the BoF model shows a good agreement against the observation of the amplitude and phase of tidal constituents at different stations around the Bay. However, the model performance is reduced as it reaches the upper part of the Bay at the Minas Basin where the coastline complexity and presence of huge tidal flats play an important role in capturing the correct water level by the model. One reason could be the lower resolution of the model at the Minas Basin and the other one is the low resolution of bathymetry data in the Minas Basin.

Regarding the Minas Basin model, having higher horizontal resolution than the Bay of Fundy modal at Minas Basin, 600 versus 1000 m, it reduces the amplitude error of the M_2 constituent by half and the phase difference by 1 degree compared to the BoF model at Five Island, while there was no further improvement for the Burntcoat Head. This could have resulted from the coarse bathymetry resolution in the Minas Basin, mostly from single beam survey, where the Burntcoat Head is further east exposed to a coarser bathymetry, in which case difficult for the Minas model to get the tide correct in this location. While the model horizontal resolution has increased in the Minas Basin model, the bathymetry still

has the same resolution as the BoF model, and the bathymetric features are not resolved using fine mesh resolution.

An increase in the resolution of the bathymetry from multibeam sonar surveys in the area could improve the ocean model to better capture the ocean currents and dynamics. This in turn provides a better water level simulation which could benefit the hydrographic survey by providing the tidal level or datum for areas with no tidal station.

For both models, using the variable bottom roughness might improve the predicted water in the Minas Basin (Wu, et al., 2014). Even though the Bay of Fundy has less sediment distribution variability with fewer features on the seafloor, however, in some parts of the Bay, mostly the eastern part, some unique features and seabed forms could affect the shear stress and the current velocity on the bottom layer. Also, in the Minas Basin, especially at the Channel and Passage, the exposed bedrock and dunes could impact the circulation and currents, and quantifying the bottom roughness could improve the water level simulated by the model. M_2 constituent is the most dominant tidal constituent in the Bay of Fundy, but the effects of other components should not be neglected or underestimated. For this study, the five main components (M_2, N_2, S_2, K_1, and O_1) are considered for the open boundary. The minor semi-diurnal components (L_2, NU_2, K_2, and $2N_2$) have a considerable contribution to the water level in the Bay of Fundy, for instance, 19cm, 15cm, 13cm, and 5.5cm at Saint John Harbor respectively (Paquin et al., 2020). However, for tidal analysis, the use of five components benefits from the shorter simulation period, 27 days; also, it minimizes the time-consuming model calibration based on the bottom roughness.

5.1.2 Tidal Currents

In the case of predicted tidal currents at locations C_1 and C_2 in the Minas Passage Figure 9, there is a considerable improvement in the semi-major axes for the Minas Basin model in comparison to the BoF model, while the phase discrepancy against the observations has increased in Minas Basin model. In the case of the BoF model, the model has a lower difference (compared to observations) of 0.50 and 0.14 m/s for semi-major and semi-minor axes, respectively. For the inclination and phase differences, other than C9, the model has a difference lower than 7.4 degrees (for inclination) and 11.7 degrees (for phase). Regarding the Minas Basin model, the semi-major axis improved (compared to the BoF model) for both C1 and C2, while it slightly degraded for the semi-minor axis at C1, and phase differences at both stations. It is worth mentioning that the geographic coordinates of stations C_1 and C_2 were not published in Wu et al. (2014) and they are picked visually to be close to the published paper. This could be the result of a high discrepancy in the semi-major axe at the C_1 location in which the depth gradient is high in the Minas Passage. The predicted tidal current by the BoF model follows the same trend as published by Wu et al. (2014), showing an increased tidal current speed (semi-major) going from the east to west at the head (C_4, C_5, C_6) and entrance of the Bay (C_7, C_8, C_9), Figure 9. Also, the phase differences against the observations are increasing from the head to the entrance of the Bay. This increase in the phase discrepancy could have originated from the coarser resolution of the mesh at the entrance of the Bay where it is getting close to the open boundary while at the head, the mesh resolution is finer, and the model could capture the tidal currents and its direction closer to the observations (Lynch & Naimie, 1993).

5.2 Surface Forcing

The predicted temperature by the BoF model, having the HRDPS as surface forcing provides better agreement than NARR run in the water column against the CTD casts in the Bay of Fundy. However, there are some cases in which FVCOM_NARR shows an improvement in the predicted temperature profiles. At the surface, the FVCOM_HRDPS shows a higher model skill in the entire domain, followed by the FVCOM_NARR. However, at the entrance and middle of the Bay, the FVCOM_NAR provides slightly a better model skill for simulating sea SST. Some factors could impact the model performance including the horizontal resolution of both the ocean model and the atmospheric surface forcing. At the head of the Bay, where the BoF model mesh resolution increases on the section A of the Bay (Figure 30), the FVCOM_HRDPS has higher correlation, lower RMSE, and better STD (compared to the GHRSST), while the performance (with regards to the three statistics) degrades with the same surface forcing (HRDPS) in the section B. The other important factor is the vertical spacing of each layer in the water column, i.e. the vertical resolution. FVCOM benefits from the sigma layer in the vertical direction and as the vertical resolution increases from the entrance of the Bay to the head (from between 2 and 3 m at the entrance to 0.5 m at the head), the model experiences better performance. It is worth mentioning that, at the head of the Bay, the FVCOM_HRDPS outperforms the GoMOFS. While GoMOFS has a uniform horizontal resolution and higher resolution at the open boundary than FVCOM_HRDPS, 700m vs 6 km, the FVCOM_HRDPS resulted in a better model performance at the head of the Bay, where the FVCOM_HRDPS has a horizontal resolution more than 1000 m. The Bay of Fundy models have better skills than the GoMOFS at the surface and middle layers at the

mouth of the Bay while showing almost the same skill as the GoMOFS at the bottom, which could be the result of prescribing a higher-resolution surface forcing, HRDPS. The FVCOM_HRDPS model outperforms the GoMOFS in the surface, middle, and bottom layers throughout the rest of the Bay. In the case of salinity, both model configurations, with HRDPS and NARR show almost the same performance in all parts of the Bay and the three layers.

The two model configurations have different impacts on the sound raytracing in the water column and total vertical uncertainty in different parts of the Bay. Based on the results in Figure 33 and Figure 35, the depth errors are geographically distributed for each model configuration. For the FVCOM_NARR, it is mostly rejected at the head of the Bay where the width of the Bay shrinks. The NARR is a coarse surface forcing and, especially close to the shoreline, its skill would depend on the percentage of land included in each cell, being able to capture the microclimate between land can ocean, and the biases introduced in the model by data assimilation. Consequently, the air temperature would be affected and result in generating a stronger thermocline in the water column. At the head of the Bay, a quarter or higher portion of the cell is contaminated by the land air temperature, while in the wider mouth of the Bay, a very small portion of the cell covers the land, mostly apparent near Digby's neck. In the case of FVCOM_HRDPS, the rejected profiles are mostly distributed randomly in the entrance of the Bay, and around Digby neck.

Table 23 provides the summary (Tables 10, 11, and 12) of RMSE (the magnitude of bias) and AE (cold or warm bias) for the temperature at the upper and mouth of the Bay for the FVCOM_HRDPS and FVCOM_NARR.

At the head of the Bay, FVCOM_NARR has higher RMSE and positive AE (Average Error) (warm bias) in surface temperature in comparison to FVCOM_HRDPS where it has lower RMSE and smaller negative AE (cold bias). The performance of the FVCOM_NARR in the water column at the upper part of the Bay, table 10 to 12, shows that this configuration overpredicts the temperature for the three layers, having bigger RMSE and positive AE, which indicates a warmer temperature in these layers. This could result in a higher sound speed propagation and a higher chance of larger refraction through the water column, which would finally exceed the maximum allowable vertical uncertainty (TVU). The other important factor in exceeding this allowable uncertainty is that the RMSE in temperature increases going from the middle layer to the bottom layer. This implies a higher sound speed in the last layer potentially causing more horizontal and vertical uncertainties and generating a frown-like artifact. While the RMSE in salinity is small and almost the same in both FVCOM_HRDPS and FVCOM_NARR in these layers, and the area is not very deep, the temperature plays a dominant role in defining the sound speed in this area. In the case of FVCOM_HRDPS in this section, the model underpredicts the temperature in the three layers and shows lower RMSE (than FVCOM_NARR) with a negative AE, indicating a colder water column. In this case, the calculated sound speed is slower (than FVCOM_NARR), and the chance of exceeding the vertical allowable uncertainty decreases. Also, the RMSE in temperature decreases in the water column from the surface to the bottom, which could potentially cause less sound speed deviation from its original path through the water column. At the mouth of Bay, FVCOM_NARR has lower RMSE and positive AE (warm bias), while FVCOM_HRDPS has higher RMSE with higher negative AE (cold bias).

Table 23. The RMSE (magnitude of bias) and AE (cold or warm bias) of temperature for the two model configurations for the upper and mouth of the Bay, were retrieved from Tables 10, 11, and 12.

Temperature					
Upper Bay	**FVCOM_NARR**			**FVCOM_HRDPS**	
	RMSE	**AE**		**RMSE**	**AE**
Surface	1.4	1.3		0.6	-0.3
Middle	1.4	1.2		0.5	-0.2
Bottom	1.5	1.2		0.4	-0.2
Mouth of Bay					
Surface	0.9	0.3		1.1	-0.9
Middle	0.8	0.1		0.9	-0.6
Bottom	0.6	0.3		0.7	-0.2

At the mouth of the Bay, the pattern in RMSE in temperature is opposite of the upper Bay, in which the FVCOM_NARR has a smaller RMSE in each layer than FVCOM_HRDPS. However, both models show the same positive (FVCOM_NARR) and negative (FVCOM_HRDPS) AE in all three layers as in the upper part. Also, in this section, the RMSE in temperature decreases from the surface to the bottom in both models. FVCOM_NARR has both lower RMSE and AE than the FVCOM_HRDPS in this section where the latter gets more profiles rejected based on the TVU limit. A combination of higher RMSE (than FVCOM_NARR), negative AE, and being in the deeper part of the Bay could potentially generate a smile-like artifact that exceeds the allowable vertical uncertainty for the mouth of the Bay. In the case of FVCOM_NARR in comparison to the upper Bay, the difference is that the RMSE decreases from surface to bottom in the mouth of the Bay, while it increases from the middle layer to the bottom layer in the upper Bay.

5.3 Hydrography Survey Design

Ocean modeling and hydrographic survey are both closely connected and the improvement in one could benefit the other one. This is evident in a challenging domain with a huge tidal regime such as the Bay of Fundy, specifically Minas Basin, where there is no active tide gauge, most of the Basin has not been surveyed with multibeam sonar, and the bathymetry has a coarse resolution. Not only could ocean models provide insight into the water level variability and tidal window in this area, but they also can provide an appropriate insight into the water column variability in salinity and temperature that has a high impact on the sound speed raytracing and refraction in different water mass layers. On the other hand, high-resolution bathymetric data could capture all the seafloor features and complexities which could be beneficial in resolving the ocean dynamics by ocean models and improve model performance.

Some considerations are required on how to apply the survey design insight for planning an autonomous surface vessel. In a domain like Minas Basin, the mother ship could only do a cast once on the safe part of the domain and the ASV is not able to perform a cast on the shallow regions on its own. This is the only cast that the survey planning relies on. In this way, using only a synthetic CTD cast from the ocean model and applying our proposed method could provide insight into the rest of the domain. The generated plots could lead the surveyor to see where there are different bodies of water in the area and when the area is more exposed to an abrupt change in water density. As in the Minas Basin, there were two different bodies of water, one at the head of the Basin, and the other at the entrance of Minas. Knowing this before doing any survey design could enhance our survey design and lower the survey costs.

In addition, the model output could be used at different locations and times as the survey reaches the uncertainty threshold, and the plan would be to use the synthetic CTD as the survey progresses and this is not confined to just a single CTD from the mother ship. It is worth mentioning that in a well-mixed shallow water environment, the sound speed profile could be calculated by using the measured surface sound speed (by Sound Velocity probe), temperature probe, calculated surface salinity (from sound speed and temperature), and the depth of water.

As the Minas model ran for 2007 and the comparison against the MVP data showed, in this domain, water column variability could be expected. By applying the proposed method based on an ocean model product, hydrographic survey vessel limitation, and raytracing uncertainty calculation, the survey planning could be more efficient in terms of the duration of the survey and cost. Depending on the project specification and limitations of the vessel, different scenarios could be run to get more information for the survey pre-plan campaign. The more information you have from your domain, the better the decision could be made on the right equipment for the survey. Not only does this method provide the IHO standard based on a synthetic CTD cast from the model output, but also it includes some other ancillary layers. For instance, the ASV could benefit from tidal current direction to go by the current and use less power of the propulsion. In the Minas Basin where there is a variable and small survey window, this method can provide insight into how much time you have to survey some specific area, when you should be at the survey domain, and when you should leave the area before being stranded in the shallow area when the ebb happens. In the case of the remotely operated survey vessel or autonomous surface vessels, a combination of both the water depth limit and surface current speed criteria makes the

survey planning more robust. The other useful information generated by this method is by showing the domains or areas where the vessel should not be in a tidal cycle based on each criterion or both together. By combining all these pieces of information, a supervised survey planning could be generated. The survey design in the Minas Basin was mostly under the influence of the high tidal range or huge tidal flats, and high surface current speed at the Passage. It was less affected by the variability of temperature and salinity in the water column, however, at some locations, the effect of ocean baroclinity could be a dominant factor in the survey design results.

The Saint John River is where a high amount of freshwater is discharged to the Bay of Fundy and contributes to the surface circulation of the Bay, and it deposits a high amount of sediment to Saint John Harbor and the Bay of Fundy. The surface current speed is not an important element in that area except at some points close to the Reversing Falls. The depth criterion still plays an important role in the survey design due to the high tidal range. The impact of the baroclinic effect imposes a higher limit than the other two criteria combined. However, the ocean model's performance is highly dependent on how well the river water specifications such as water level, salinity, and temperature are introduced at the open boundary at Evandale Point. Also, due to the complexity of the Saint John River coastline, a high-resolution mesh is required to resolve all of the coastline's features up to the open boundary. These are some limitations that could impact the accuracy and performance of an ocean model with a high discharge of fresh water, in which difficulties to fully capture these features could consequently affect the accuracy of the survey design. The model output, both BoF and Minas models have proved to be beneficial in the hydrographic survey design and in providing the baroclinic condition of the Bay of Fundy.

The model output could be used where there is a lack of active tidal stations, defining the anchorage sites, and safe survey domain in both high tidal environments and high oceanic water column variability.

5.4 Recommendation for Future Works

Based on this thesis, these are some potential topics that could be used for feature improvement and consideration, including:

- Increasing the model resolution in the upper part of the Saint John River to improve and capture the river completely,
- Adding more vertical layers both close to the surface and close to the seafloor to capture the surface mixed layer and seafloor features respectively,
- Using the variable bottom roughness in the model configuration instead of the fixed roughness length scale to include the different features on the seafloor and improve the bottom current estimation,
- Including 9 tidal constituents at the open boundary to capture the total water variability in the Bay of Fundy,
- For the survey design, specifically for ROVs or AUVs, the wave height and period play important roles in the operational and maneuverability of these vessels, and by including the wave in the model configuration, the wave height could be added as another criterion,
- Adding the capability of the method to accept the operational ocean model output or other ocean model types, such as ROMS or NEMO, and

- The models could also be used to calculate the absorption coefficient for acoustic backscatter processing.
- Comparing the model results against the available sound speed measurements from hydrographic surveys.

Chapter 6: Conclusion

A pair of high-resolution three-dimensional baroclinic hydrodynamic models have been developed for the Bay of Fundy and Minas Basin to improve our understanding of the variability of the water column in the Bay. Also, a method was introduced by incorporating the model output to generate a hydrographic survey design plan based on the depth and surface current speed criteria and the associated IHO-order requirement. The model was able to reproduce the water levels, salinity, and temperature within the model domains. The model simulation periods covered a habitat mapping-focused sampling campaign in July and August 2018.

The model output was evaluated both quantitatively and qualitatively against the available published tidal constituents, tidal ellipses, CTD profiles gathered during the fieldwork in 2018, WOD and DFO CTD datasets, and GHRSST data. The models showed good skill in simulating water levels in different parts of the model domain, with a little higher discrepancy at the Minas Basin, where the model resolution decreases, and the bathymetry data is not as high-resolution as the Bay of Fundy. Regarding the temperature and salinity in the water column, it provides better results than GoMOFS at the middle and head of the Bay. Overall, the model showed good agreement against the observations.

Two different surface atmospheric forcings were applied, each having a different spatiotemporal resolution to investigate if a higher surface forcing could improve the thermodynamic feature of an ocean model. The evaluations against the observations showed that using a coarse surface forcing (NARR) generates a warm bias for the SST while the higher resolution one (HRDPS) outperformed. A high-resolution surface forcing

could improve the ocean model simulation and enhance its application in hydrographic survey design, especially if the ocean domain is the same or smaller in order of magnitude as the surface forcing horizontal resolution. In the two model configurations for the Bay of Fundy, FVCOM_NARR simulation showed higher profile rejections in the upper Bay while FVCOM_HRDPS passed all those profiles. However, only a higher horizontal resolution of surface forcing does not always guarantee a better ocean model simulation result, because other important components in the weather models should be considered. In the case of ocean model application in the hydrography survey design insight, the higher-resolution surface forcing generally decreased the number of rejected profiles and generated fewer depth errors. The same phenomena were captured in the Minas Basin where the domain is small in comparison to the NARR resolution. The other improvement in SST was shown for the model performance while having a higher horizontal resolution at the head of the Bay. Also, by comparing the vertical resolution at the open boundary and the head of the Bay, the model shows better skill in capturing the SST variability where the vertical resolution was higher (head of the Bay).

The model was able to provide hydrographic survey insights for a highly tidal environment, the Minas Basin, and a baroclinic environment at Saint John Harbor. It could also provide some other model byproduct by depicting the surveyable area by considering one or multiple criteria. The model output could be used where there is no CTD observation available for performing the ray tracing and also for providing the time of ebb or flood and the survey window for the hydrographic survey. Our proposed survey design procedure could represent a good complementary approach to the existing methods in hydrography

survey design and could be a better alternative under certain ocean environments, such as Minas Basin.

This model development showed that not only regional or global surface forcing plays an important role in the thermodynamic simulation of ocean conditions, but also the surface forcing resolution could impact the ocean model performance. Also, the vertical and horizontal resolution of the ocean model affects how well the model could capture the oceanic variability in the Bay of Fundy.

In conclusion, the development and application of this high-resolution three-dimensional hydrodynamic model have significantly enhanced our understanding of the Bay of Fundy's complex oceanographic dynamics and demonstrated its practical value for hydrographic survey planning. While the findings highlight the importance of surface forcing resolution and vertical model resolution in improving ocean model performance, they also underscore the need for continued refinement of input datasets, such as bathymetry, particularly in highly dynamic regions like the Minas Basin. Looking forward, this model sets the stage for future advancements in both regional ocean modeling and hydrographic survey methodologies, paving the way for broader applications in tidal energy research, habitat mapping, and other coastal management efforts. By addressing both present challenges and opportunities, this work provides a foundation for more accurate, efficient, and insightful oceanographic studies in similarly complex environments worldwide.

References

Akhtar, N., Brauch, J., & Ahrens, B. (2018). Climate modeling over the Mediterranean Sea: impact of resolution and ocean coupling. *Climate Dynamics*, *51*, 933-948. doi: 10.1007/s00382-017-3570-8.

Akima, H. (1970). A new method of interpolation and smooth curve fitting based on local procedures. *Journal of the ACM (JACM)*, *17*(4), 589-602. doi: 10.1145/321607.321609.

Akima, H. (1974). A method of bivariate interpolation and smooth surface fitting based on local procedures. *Communications of the ACM*, *17*(1), 18-20. doi: 10.1145/360767.360779.

Amos, C. L., and Joice, G. H. E. (1977). 'The Sediment Budget of the Minas Basin, Bay of Fundy, N.S.' Data Series Report, BI-D-77-3.

Amos, C. L., Van Wagoner, N. A., & Daborn, G. R. (1988). The influence of subaerial exposure on the bulk properties of fine-grained intertidal sediment from Minas Basin, Bay of Fundy. *Estuarine, Coastal and Shelf Science*, *27*(1), 1-13.

Amos, C. L., & Long, B. F. N. (1980). The sedimentary character of the Minas Basin, Bay of Fundy. In *Proc. Coastlines Canada Conf., Halifax, NS*.

Anderson, J. T., Van Holliday, D., Kloser, R., Reid, D. G., & Simard, Y. (2008). Acoustic seabed classification: current practice and future directions. *ICES Journal of Marine Science*, *65*(6), 1004-1011. doi: 10.1093/icesjms/fsn061.

Apollonio, S. (1979). The Gulf of Maine. *Courier of Maine Books*.

Artale, V., Iudicone, D., Santoleri, R., Rupolo, V., Marullo, S., & d'Ortenzio, F. (2002). Role of surface fluxes in ocean general circulation models using satellite sea surface temperature: Validation of and sensitivity to the forcing frequency of the Mediterranean thermohaline circulation. *Journal of Geophysical Research: Oceans*, *107*(C8), 29-1. doi: https://doi.org/10.1029/2000JC000452.

Aretxabaleta, A. L., McGillicuddy Jr, D. J., Smith, K. W., & Lynch, D. R. (2008). Model simulations of the Bay of Fundy Gyre: 1. Climatological results. *Journal of Geophysical Research: Oceans*, *113*(C10). doi: 10.1029/2007JC004480.

Ashall, L. M., Mulligan, R. P., & Law, B. A. (2016). Variability in suspended sediment concentration in the Minas Basin, Bay of Fundy, and implications for changes due to tidal power extraction. *Coastal Engineering*, *107*, 102-115.

Bailey, W. B., MacGregor, D. G., & Hachey, H. B. (1954). Annual variations of temperature and salinity in the Bay of Fundy. *Journal of the Fisheries Board of Canada*, *11*(1), 32-47. doi: 10.1139/f54-005.

Beaudoin, J. (2010). 'Real-Time Monitoring of Uncertainty Due to Refraction in Multibeam Echo Sounding'. *The Hydographic Journal, 134,3–13*.

Bélair, S., Mailhot, J., Girard, C., & Vaillancourt, P. (2005). Boundary layer and shallow cumulus clouds in a medium-range forecast of a large-scale weather system. *Monthly weather review*, *133*(7), 1938-1960. doi: https://doi.org/10.1175/MWR2958.1.

Bélair, S., Méthot, A., Mailhot, J., Bilodeau, B., Patoine, A., Pellerin, G., & Côté, J. (2000). Operational implementation of the Fritsch–Chappell convective scheme in the 24-km Canadian regional model. *Weather and Forecasting*, *15*(3), 257-274. doi: https://doi.org/10.1175/1520-0434(2000)015<0257:OIOTFC>2.0.CO;2.

Béranger, K., Drillet, Y., Houssais, M., Testor, P., Bourdallé-Badie, R., Alhammoud, B., Bozec, A., Mortier, L., Bouruet-Aubertot, P., and Crépon, M. (2010). Impact of the spatial distribution of the atmospheric forcing on water mass formation in the Mediterranean Sea. *Journal of Geophysical Research: Oceans*, *115*(C12). doi: 10.1029/2009JC005648.

Bigelow, H. B. (1927). Dynamic oceanography of the Gulf of Maine. *Eos, Transactions American Geophysical Union*, *8*(1), 206-211. doi: 10.1029/TR008i001p00206.

Bleck, R. (2002). An oceanic general circulation model framed in hybrid isopycnic-Cartesian coordinates. *Ocean modelling*, *4*(1), 55-88. doi: https://doi.org/10.1016/S1463-5003(01)00012-9.

Boyer, T. P., Antonov, J. I., Baranova, O. K., Coleman, C., Garcia, H. E., Grodsky, A., Johnson, D. R., Locarnini, R. A., Mishonov, A. V., O'Brien, T. D., Paver, C. R., Reagan, J. R., Seidov, D., Smolyar, I. V., and Zweng, M. M. (2013). World Ocean Database 2013. *Silver Spring, MD*. doi: 10.25607/OBP-1454.

Béranger, K., Drillet, Y., Houssais, M. N., Testor, P., Bourdallé-Badie, R., Alhammoud, B., Bozec, A., Mortier, L., Bouruet-Aubertot, P., & Crépon, M. (2010). Impact of the spatial distribution of the atmospheric forcing on water mass formation in the Mediterranean Sea. *Journal of Geophysical Research: Oceans*, 115(C12).

Bricheno, L. M., Wolf, J. M., & Brown, J. M. (2014). Impacts of high resolution model downscaling in coastal regions. *Continental Shelf Research*, *87*, 7-16. doi: 10.1016/j.csr.2013.11.007.

Brodie, S., Jacox, M. G., Bograd, S. J., Welch, H., Dewar, H., Scales, K. L., Maxwell, S. M., Briscoe, D. M., Edwards, C. A., Crowder, L. B., Lewison, R. L., and Hazen, E. L. (2018). Integrating dynamic subsurface habitat metrics into species distribution models. *Frontiers in Marine Science*, *5*, 219. doi: 10.3389/fmars.2018.00219.

Brodny, J., & Tutak, M. (2023). Assessing the energy security of European Union countries from two perspectives–A new integrated approach based on MCDM methods. *Applied Energy*, *347*, 121443. doi: https://doi.org/10.1016/j.apenergy.2023.121443.

Brooks, D. A. (1992). A brief overview of the physical oceanography of the Gulf of Maine. In *Proceedings of the Gulf of Maine scientific workshop. Urban Harbors Institute, University of Massachusetts, Boston* (pp. 51-74).

Brooks, D. A. (1994). A model study of the buoyancy-driven circulation in the Gulf of Maine. *Journal of Physical Oceanography*, *24*(11), 2387-2412. doi: 10.1175/1520-0485(1994)024<2387:AMSOTB>2.0.CO;2.

Brooks, D. A., and Townsend, D. W. (1989). Variability of the coastal current and nutrient pathways in the eastern Gulf of Maine. *Journal of Marine Research 47(2):303–21.* doi: 10.1357/002224089785076299.

Brossier, C. L., Béranger, K., Deltel, C., & Drobinski, P. (2011). The Mediterranean response to different space–time resolution atmospheric forcings using perpetual mode sensitivity simulations. *Ocean Modelling*, *36*(1-2), 1-25. doi: https://doi.org/10.1016/j.ocemod.2010.10.008.

Brousseau, P., Bouttier, F., Hello, G., Seity, Y., Fischer, C., Berre, L., Montmerle, T., Auger, L., & Malardel, S. (2008). A prototype convective-scale data assimilation system for operation: *The Arome-RUC. HIRLAM Techn. Report*, 68(23–30), 48.

Brown, C. J., Smith, S. J., Lawton, P., & Anderson, J. T. (2011). Benthic habitat mapping: A review of progress towards improved understanding of the spatial ecology of the seafloor using acoustic techniques. *Estuarine, Coastal and Shelf Science*, *92*(3), 502-520. doi: 10.1016/j.ecss.2011.02.007.

Burchard, H. (2007). Applied turbulence modelling in marine waters (Vol. 100). Springer.

Cameron, H. L. (1961). Interpretation of high-altitude small-scale photography. *The Canadian Surveyor*, *15*(10), 567-573. doi: 10.1139/tcs-1961-0054.

Carrera, M. L., Bélair, S., & Bilodeau, B. (2015). The Canadian land data assimilation system (CaLDAS): Description and synthetic evaluation study. *Journal of Hydrometeorology*, *16*(3), 1293-1314. doi: 10.1175/JHM-D-14-0089.1.

Castellari, S., Pinardi, N., & Leaman, K. (2000). Simulation of water mass formation processes in the Mediterranean Sea: Influence of the time frequency of the atmospheric forcing. *Journal of Geophysical Research: Oceans*, *105*(C10), 24157-24181. doi: https://doi.org/10.1029/2000JC900055.

Chant, R. J. (2011). 2.11-Interactions between Estuaries and Coasts: River Plumes–Their Formation, Transport, and Dispersal. In *Treatise on estuarine and coastal science* (pp. 213-235). Elsevier Inc.

Chao, S. Y., & Boicourt, W. C. (1986). Onset of estuarine plumes. *Journal of Physical Oceanography*, *16*(12), 2137-2149. doi: 10.1175/1520-0485(1986)016<2137:ooep>2.0.co;2.

Chen, C., Beardsley, R., Cowles, G., Qi, J., Lai, Z., Gao, G., Stuebe, D., Xu, Q., Xue, P., Ge, J., Hu, S., and Ji, R. (2013). An Unstructured Grid, Finite-Volume Coastal Ocean Model FVCOM – User Manual. Cambridge, *MA, USA: Sea Grant College Program, Massachusetts Institute of Technology*.

Chen, C., Beardsley, R. C., Cowles, G., Qi, J., Lai, Z., Gao, G., & Stuebe, D. (2006). An unstructured grid, finite-volume coastal ocean model: FVCOM user manual. *SMAST/UMASSD*, *6*, 78.

Chen, C., Liu, H., & Beardsley, R. C. (2003). An unstructured grid, finite-volume, three-dimensional, primitive equations ocean model: application to coastal ocean and estuaries. *Journal of atmospheric and oceanic technology*, *20*(1), 159-186. doi: 10.1175/1520-0426(2003)020<0159:AUGFVT>2.0.CO;2.

Cheng, R. T., Ling, C. H., Gartner, J. W., & Wang, P. F. (1999). Estimates of bottom roughness length and bottom shear stress in South San Francisco Bay, California. *Journal of Geophysical Research: Oceans*, *104*(C4), 7715-7728.

Chénier, R., Abado, L., & Martin, H. (2018). CHS Priority Planning Tool (CPPT)—A GIS model for defining hydrographic survey and charting priorities. *ISPRS international journal of geo-information*, *7*(7), 240. doi: 10.3390/ijgi7070240.

Church, I. W., (2014). Modelling the Estuarine Circulation of the Port of Saint John (Doctoral Dissertation). *University of New Brunswick.*

Church, I. W. (2020). Multibeam sonar ray-tracing uncertainty evaluation from a hydrodynamic model in a highly stratified estuary. *Marine Geodesy*, *43*(4), 359-375. doi: 10.1080/01490419.2020.1717695.

CIDCO. n.d. Examination of Navigation Risk Assessment Methodologies with Particular Relevance to Arctic Regions. Le Centre Interdisciplinaire de Développement En Cartographie Des Océans (CIDCO)'. 1–54.

Clarke, J. E. H. (2013). Optimal Use of Multibeam Technology in the Study of Shelf Morphodynamics. Pp. 1–28 in Vol. 44.

Clarke, J. E. H., Lamplugh, M. & Kammerer, E. (2000). Integration of Near-Continuous Sound Speed Profile Information. In *Proceedings of Canadian Hydrographic Conference 2000*.

Cornett, A., Durand, N., and Bourban, S. (2010). 3D Modelling and Assessment of Tidal Current Energy Resources in the Bay of Fundy. In *Proceedings of the 3rd International Conference on Ocean Energy (January 2014):2–7*.

Cunjak, R. A., & Newbury, R. W. (2005). Atlantic coast rivers of Canada. In *Rivers of North America* (pp. 938-980). Academic Press.

De Boyer Montégut, C., Madec, G., Fischer, A. S., Lazar, A., & Iudicone, D. (2004). Mixed layer depth over the global ocean: An examination of profile data and a profile-based climatology. Journal of Geophysical Research: Oceans, 109(C12). doi: 10.1029/2004JC002378.

Denman, K., & Herman, A. (1978). Space-Time Structure of a Continental Shelf Ecosystem Measured by a Towed Porpoising Vehicle. *Journal of Marine Research 36:693–714.*

Desplanque, C., & Mossman, D. J. (2001). Bay of Fundy tides. *Geoscience Canada*.

Dickie, L. M. (1955). Fluctuations in abundance of the giant scallop, Placopecten magellanicus (Gmelin), in the Digby area of the Bay of Fundy. *Journal of the Fisheries Board of Canada*, *12*(6), 797-857.

Dupont, F., Higginson, S., Bourdallé-Badie, R., Lu, Y., Roy, F., Smith, G. C., Lemieux, J. F., Garric, G., and Davidson, F. (2015). A high-resolution ocean and sea-ice modelling system for the Arctic and North Atlantic oceans. *Geoscientific Model Development*, *8*(5), 1577-1594. doi: 10.5194/gmd-8-1577-2015.

Dupont, F., Hannah, C. G., & Greenberg, D. (2005). Modelling the sea level of the upper Bay of Fundy. *Atmosphere-Ocean*, *43*(1), 33-47.

Ek, M. B., Mitchell, K. E., Lin, Y., Rogers, E., Grunmann, P., Koren, V., Gayno, G., and Tarpley, J. D. (2003). Implementation of Noah land surface model advances in the National Centers for Environmental Prediction operational mesoscale Eta model. *Journal of Geophysical Research: Atmospheres*, *108*(D22). doi: https://doi.org/10.1029/2002JD003296.

Fabrizio, M. C., Tuckey, T. D., Bever, A. J., & MacWilliams, M. L. (2021). The Extent of Seasonally Suitable Habitats May Limit Forage Fish Production in a Temperate Estuary. *Frontiers in Marine Science*, *8*, 706666. doi: 10.3389/fmars.2021.706666.

Fagundes, M., Litvin, S. Y., Micheli, F., De Leo, G., Boch, C. A., Barry, J. P., Omidvar, S., and Woodson, C. B. (2020). Downscaling global ocean climate models improves estimates of exposure regimes in coastal environments. *Scientific Reports*, *10*(1), 14227. doi: 10.1038/s41598-020-71169-6.

Fischer, C., Montmerle, T., Berre, L., Auger, L., & Ştefănescu, S. E. (2005). An overview of the variational assimilation in the ALADIN/France numerical weather-prediction system. Quarterly Journal of the Royal Meteorological Society: A *Journal of the Atmospheric Sciences, Applied Meteorology and Physical Oceanography*, 131(613), 3477–3492.

Fish, C. J., & Johnson, M. W. (1937). The biology of the zooplankton population in the Bay of Fundy and Gulf of Maine with special reference to production and distribution. *Journal of the Biological Board of Canada*, 3(3), 189-322.

Garrett, C. J. R., Keeley, J. R., & Greenberg, D. A. (1978). Tidal mixing versus thermal stratification in the Bay of Fundy and Gulf of Maine. *Atmosphere-ocean*, *16*(4), 403-423. doi: 10.1080/07055900.1978.9649046.

Garrett, C. (1972). Tidal resonance in the Bay of Fundy and Gulf of Maine. *Nature*, *238*(5365), 441-443. doi: 10.1038/238441a0.

Garvine, R. W. (1995). A dynamical system for classifying buoyant coastal discharges. *Continental Shelf Research*, *15*(13), 1585-1596. doi: 10.1016/0278-4343(94)00065-U.

Godin, G. (1968). *The 1965 current survey of the Bay of Fundy: a new analysis of the data and an interpretation of the results* (Vol. 8). O.Ottawa: marine sciences branch.

Goyert, H. F., Bassett, R., Christensen, J., Coleman, H., & Coyne, M. (2021). Characterizing spatial distributions of deep-sea corals and chemosynthetic communities in the US Gulf of Mexico through data synthesis and predictive modeling. *US Department of the Interior, Bureau of Ocean Energy Management Available at: https://espis. boem. gov/final% 20reports/BOEM_2021-027. pdf*.

Gran, H. H., & Braarud, T. (1935). A quantitative study of the phytoplankton in the Bay of Fundy and the Gulf of Maine (including observations on hydrography, chemistry and turbidity). *Journal of the Biological Board of Canada*, *1*(5), 279-467.

Greenberg, D. A., & Amos, C. L. (1983). Suspended sediment transport and deposition modeling in the Bay of Fundy, Nova Scotia—a region of potential tidal power development. *Canadian Journal of Fisheries and Aquatic Sciences*, *40*(S1), s20-s34. doi: 10.1139/f83-266.

Greenberg, D. A. (1979). A numerical model investigation of tidal phenomena in the Bay of Fundy and Gulf of Maine. *Marine Geodesy*, *2*(2), 161-187. doi: 10.1080/15210607909379345.

Greenberg, D. A. (1982). Modelling the mean barotropic circulation in the Bay of Fundy and Gulf of Maine. *Journal of Physical Oceanography*, *13*(5), 886-904. doi: 10.1175/1520-0485(1983)013<0886:MTMBCI>2.0.CO;2.

Greenberg, D. A., Dupont, F., Lyard, F. H., Lynch, D. R., & Werner, F. E. (2007). Resolution issues in numerical models of oceanic and coastal circulation. *Continental Shelf Research*, *27*(9), 1317-1343. doi: 10.1016/j.csr.2007.01.023.

Gronholz, A., Gräwe, U., Paul, A., & Schulz, M. (2017). Investigating the effects of a summer storm on the North Sea stratification using a regional coupled ocean-atmosphere model. *Ocean Dynamics*, *67*, 211-235. doi: 10.1007/s10236-016-1023-2.

Grumbine, R. W. (1996). Automated sea ice concentration analysis at NCEP. *World Meteorological Organization-Publications-Wmo Td, 8-20*.

Hachey, H. B., & Bailey, W. B. (1952). *The General Circulation of the waters of Bay of Fundy. MS Rep. Biol. 669 Sta* (p. 100). No. 455, Tech. rep., Fish. Res. Bd. Canada, St. Andrews, NB, Canada.

Hansen, P., & Devlin, N. (2019). Multi-criteria decision analysis (MCDA) in healthcare decision-making. In *Oxford research encyclopedia of economics and finance*. doi: 10.1093/acrefore/9780190625979.013.98.

Hasegawa, D., Sheng, J., Greenberg, D. A., & Thompson, K. R. (2011). Far-field effects of tidal energy extraction in the Minas Passage on tidal circulation in the Bay of Fundy and Gulf of Maine using a nested-grid coastal circulation model. *Ocean Dynamics*, *61*, 1845-1868. doi: 10.1007/s10236-011-0481-9.

Huang, X. (2012). A comprehensive study of the Bellhop algorithm for underwater acoustic channel modelings. *The Journal of the Acoustical Society of America*, *132*(3_Supplement), 1942-1942. doi: 10.1121/1.4755149.

Huthnance, J. M. (2002). Wind-driven circulation in coastal and marginal seas. *Canadian journal of remote sensing*, *28*(3), 329-339. doi: 10.5589/m02-032.

Jensen, F. B., Kuperman, W. A., Porter, M. B., & Schmidt, H. (2011). Fundamentals of Ocean Acoustics. In F. B. Jensen, W. A. Kuperman, M. B. Porter, & H. Schmidt (Eds.), *Computational Ocean Acoustics* (pp. 1–64). Springer New York. https://doi.org/10.1007/978-1-4419-8678-8_1.

Jeong, B., Oguz, E., Wang, H., & Zhou, P. (2018). Multi-criteria decision-making for marine propulsion: Hybrid, diesel electric and diesel mechanical systems from cost-environment-risk perspectives. *Applied energy*, *230*, 1065-1081. doi: 10.1016/j.apenergy.2018.09.074.

Jiang, F., Li, J., Ma, L., Dong, Z., Chen, W., Broyd, T., & Wang, G. (2024). Sustainable urban road planning under the digital twin-MCDM-GIS framework considering multidisciplinary factors. *Journal of Cleaner Production*, *469*, 143097. doi: https://doi.org/10.1016/j.jclepro.2024.143097.

Karsten, R. H., McMillan, J. M., Lickley, M. J., & Haynes, R. D. (2008). Assessment of tidal current energy in the Minas Passage, Bay of Fundy. *Proceedings of the Institution of Mechanical Engineers, Part A: Journal of Power and Energy*, *222*(5), 493-507. doi: 10.1243/09576509JPE555.

Katavouta, A., Thompson, K. R., Lu, Y., & Loder, J. W. (2016). Interaction between the tidal and seasonal variability of the Gulf of Maine and Scotian Shelf region. *Journal of Physical Oceanography*, *46*(11), 3279-3298. doi: 10.1175/JPO-D-15-0091.1.

Koopman, H. N., Westgate, A. J., Siders, Z. A., & Cahoon, L. B. (2014). Rapid subsurface ocean warming in the Bay of Fundy as measured by free-swimming basking sharks. *Oceanography*, *27*(2), 14-17. doi: 10.5670/oceanog.2014.32.

Kosowska-Stamirowska, Z., Ducruet, C., & Rai, N. (2016). Evolving structure of the maritime trade network: evidence from the Lloyd's Shipping Index (1890–2000). *Journal of Shipping and Trade*, *1*(1), 10. https://doi.org/10.1186/s41072-016-0013-3.

Lecours, V., Devillers, R., Schneider, D. C., Lucieer, V. L., Brown, C. J., & Edinger, E. N. (2015). Spatial scale and geographic context in benthic habitat mapping: review and future directions. *Marine Ecology Progress Series*, *535*, 259-284. doi: 10.3354/meps11378.

Lewis, H. W., Siddorn, J., Castillo Sanchez, J. M., Petch, J., Edwards, J. M., & Smyth, T. (2019). Evaluating the impact of atmospheric forcing and air–sea coupling on near-coastal regional ocean prediction. *Ocean Science*, *15*(3), 761-778. doi: 10.5194/os-15-761-2019.

Li, J., & Barker, H. W. (2005). A radiation algorithm with correlated-k distribution. Part I: Local thermal equilibrium. *Journal of the atmospheric sciences*, *62*(2), 286-309. doi: 10.1175/JAS-3396.1.

Li, J., Gu, Q., Chen, Y., Sun, G., & Huang, H. (2018). A Combined Ray Tracing Method for Improving the Precision of the USBL Positioning System in Smart Ocean. *Sensors*, 18(10). https://doi.org/10.3390/s18103586.

Li, M. Z., & Amos, C. L. (2001). SEDTRANS96: the upgraded and better calibrated sediment-transport model for continental shelves. *Computers & Geosciences*, *27*(6), 619-645. doi: https://doi.org/10.1016/S0098-3004(00)00120-5.

Li, M. Z., Hannah, C. G., Perrie, W. A., Tang, C. C., Prescott, R. H., & Greenberg, D. A. (2015). Modelling seabed shear stress, sediment mobility, and sediment transport in the Bay of Fundy. *Canadian Journal of Earth Sciences*, *52*(9), 757-775. doi: 10.1139/cjes-2014-0211.

Lucieer, V., Huang, Z., & Siwabessy, J. (2016). Analyzing uncertainty in multibeam bathymetric data and the impact on derived seafloor attributes. *Marine Geodesy*, *39*(1), 32-52. doi: 10.1080/01490419.2015.1121173.

Lurton, X., Lamarche, G., Brown, C., Lucieer, V., RIce, G., Schimel, A., & Weber, T. (2015). Backscatter measurements by seafloor-mapping sonars. *Guidelines and recommendations*, *200*.

Lynch, D. R., Holboke, M. J., & Naimie, C. E. (1997). The Maine coastal current: spring climatological circulation. *Continental Shelf Research*, *17*(6), 605-634. doi: 10.1016/S0278-4343(96)00055-6.

Malczewski, J., & Rinner, C. (2015). *Multicriteria decision analysis in geographic information science* (Vol. 1, pp. 55-77). New York: Springer.

Malik, M., Lurton, X., & Mayer, L. (2018). A framework to quantify uncertainties of seafloor backscatter from swath mapping echosounders. *Marine Geophysical Research*, *39*, 151-168. doi: 10.1007/s11001-018-9346-7.

Masetti, G., Gallagher, B., Calder, B. R., Zhang, C., & Wilson, M. (2017). Sound Speed Manager: An open-source application to manage sound speed profiles. *The International Hydrographic Review*.

Masetti, G., Kelley, J. G., Johnson, P., & Beaudoin, J. (2018). A ray-tracing uncertainty estimation tool for ocean mapping. *IEEE Access*, *6*, 2136-2144. doi: 10.1109/ACCESS.2017.2781801.

Masetti, G., Smith, M. J., Mayer, L. A., & Kelley, J. G. (2020). Applications of the Gulf of Maine Operational Forecast System to Enhance Spatio-Temporal

Oceanographic Awareness for Ocean Mapping. *Frontiers in Marine Science*, *6*, 804.

Matishov, G., Moiseev, D., Lyubina, O., Zhichkin, A., Dzhenyuk, S., Karamushko, O., & Frolova, E. (2012). Climate and cyclic hydrobiological changes of the Barents Sea from the twentieth to twenty-first centuries. *Polar biology*, *35*, 1773-1790. doi: 10.1007/s00300-012-1237-9.

Mayer, L., Jakobsson, m., Allen, G., Dorschel, B., Falconer, R., Ferrini, V., Lamarche, G., Snaith, H., & Weatherall, P. (2018). The Nippon Foundation-GEBCO Seabed 2030 Project: The Nippon Foundation—GEBCO seabed 2030 project: The quest to see the world's oceans completely mapped by 2030. *Geosciences*, *8*(2), 63. doi: 10.3390/geosciences8020063.

McNeill, P., Church, I. W., & Leger, M. (2018). Integrating Bathymetric Datasets in the Lower Saint John River to Produce a Common Reference Surface. *Victoria: Canadian Hydrographic Conference.*

McTaggart-Cowan, R., Girard, C., Plante, A., & Desgagné, M. (2011). The utility of upper-boundary nesting in NWP. *Monthly weather review*, *139*(7), 2117-2144. doi: 10.1175/2010MWR3633.1.

Medwin, H., & Clay, C. S. Fundamentals of Acoustical Oceanography 1998 Academic Press.

Mellor, G. L., & Yamada, T. (1982). Development of a turbulence closure model for geophysical fluid problems. *Reviews of Geophysics*, *20*(4), 851-875. doi: 10.1029/RG020i004p00851.

Mesinger, F., DiMego, G., Kalnay, E., Mitchell, K., Shafran, P. C., Ebisuzaki, W., Jović, D., Woollen, J., Rogers, E., Berbery, E. H., Ek, M. B., Fan, Y., Grumbine, R., Higgins, W., Li, H., Lin, Y., Manikin, G., Parrish, D., & Shi, W. (2006). North American regional reanalysis. *Bulletin of the American Meteorological Society*, *87*(3), 343-360. doi: 10.1175/BAMS-87-3-343.

Metcalfe, C. D., Dadswell, M., Gillis, G. F., & Thomas, M. L. H. (1976). Physical, Chemical, and Biological Parameters of the Saint John River Estuary, New Brunswick, Canada. *Fish. Mar. Serv. Res. Dev. Tech. Rep. 686: 42 pp.*

Milbrandt, J. A., Bélair, S., Faucher, M., Vallée, M., Carrera, M. L., & Glazer, A. (2016). The pan-Canadian high resolution (2.5 km) deterministic prediction system. *Weather and Forecasting*, *31*(6), 1791-1816. doi: 10.1175/WAF-D-16-0035.1.

Milbrandt, J. A., & Yau, M. K. (2005). A multimoment bulk microphysics parameterization. Part II: A proposed three-moment closure and scheme

description. *Journal of the atmospheric sciences*, *62*(9), 3065-3081. doi: 10.1175/JAS3535.1.

Miller, R. L., Liu, C. C., Buonassissi, C. J., & Wu, A. M. (2011). A multi-sensor approach to examining the distribution of total suspended matter (TSM) in the Albemarle-Pamlico estuarine system, NC, USA. *Remote Sensing*, *3*(5), 962-974. doi: 10.3390/rs3050962.

Minnett, P., & Kaiser-Weiss, A. (2012). Near-surface oceanic temperature gradients. *GHRSST Discussion Doc*, *7*.

Mitchell, K. E., Lohmann, D., Houser, P. R., Wood, E. F., Schaake, J. C., Robock, A., Cosgrove, B. A., Sheffield, J., Duan, Q., Luo, L., Higgins, R. W., Pinker, R. T., Tarpley, J. D., Lettenmaier, D. P., Marshall, C. H., Entin, J. K., Pan, M., Shi, W., Koren, V., Meng, J., Ramsay, B. H., & Baily, A. A. (2004). The multi-institution North American Land Data Assimilation System (NLDAS): Utilizing multiple GCIP products and partners in a continental distributed hydrological modeling system. *Journal of Geophysical Research: Atmospheres*, *109*(D7).

Montereale-Gavazzi, G., Roche, M., Degrendele, K., Lurton, X., Terseleer, N., Baeye, M., Francken, F., & Van Lancker, V. (2019). Insights into the short-term tidal variability of multibeam backscatter from field experiments on different seafloor types. *Geosciences*, *9*(1), 34.

Mulligan, R. P., Smith, P. C., Hill, P. S., Tao, J., & Van Proosdij, D. (2013). Effects of tidal power generation on hydrodynamics and sediment processes in the upper Bay of Fundy. In *4th Specialty Conference on Coastal, Estuary and Offshore Engineering* (Vol. 10).

Neu, H. A. (1960). Hydrographic survey of Saint John Harbour, N. B. (Mechanical Engineering Report (*National Research Council of Canada. Division of Mechanical Engineering*); No. MH-97). doi: https://doi.org/10.4224/40001823.

NOAA, 2019. Hydrographic Surveys Specifications and Deliverables.

Nudds, S., Lu, Y., Higginson, S., Haigh, S. P., Paquin, J., O. Flaherty-sproul, M., Taylor, S., Blanken, h., Marcotte, G., Smith, G. C., Bernier, N. B., Macaulay, P., Wu, Y., Zhai, L., Davidson, F. J. M., & Page, F. (2020). Evaluation of Structured and Unstructured Models for Application in Operational Ocean Forecasting in Nearshore Water. *Journal of Marine Science and Engineering*, *8*(7), 484. https://doi.org/10.3390/jmse8070484.

Odetti, A., Bruzzone, G., Altosole, M., Viviani, M., & Caccia, M. (2020). SWAMP, an Autonomous Surface Vehicle expressly designed for extremely shallow waters. *Ocean Engineering*, *216*, 108205. doi: https://doi.org/10.1016/j.oceaneng.2020.108205.

Oliveira, T. C. A., Lin, Y.-T., & Porter, M. B. (2021). Underwater Sound Propagation Modeling in a Complex Shallow Water Environment. *Frontiers in Marine Science*, 8. https://doi.org/10.3389/fmars.2021.751327.

Paquin, J. P., Lu, Y., Taylor, S., Blanken, H., Marcotte, G., Hu, X., Zhai, L., Higginson, S., Nudds, S., Chanut, J., Smith, G. C., Bernier, N., & Dupont, F. (2020). High-resolution modelling of a coastal harbour in the presence of strong tides and significant river runoff. *Ocean Dynamics*, *70*, 365-385. doi: 10.1007/s10236-019-01334-7.

Parrott, D. R., Todd, B. J., Shaw, J., Clarke, J. E. H., Griffin, J., Macgowan, B., Lamplugh, M., & Webster, T. (2008). Integration of multibeam bathymetry and LiDAR surveys of the Bay of Fundy, Canada. In *Proceedings of the Canadian hydrographic conference and national surveyors conference* (pp. 6-2).

Parrott, D. R., Hayward, S., Fraser, P., Lamplugh, M., & Griffon, J. (2013). *Cruise Report Matthew 2007006 and 2007016, Bay of Fundy, 3 May-16 June 2007* (p. 6474). Geological Survey of Canada.

Pawlowicz, R., Beardsley, B., & Lentz, S. (2002). Classical tidal harmonic analysis including error estimates in MATLAB using T_TIDE. *Computers & geosciences*, *28*(8), 929-937. doi: 10.1016/S0098-3004(02)00013-4.

Percy, J. A., Wells, P. G., & Evans, A. J. (1997). Bay of Fundy Issues: A Scientific Overview. Environment Canada - Atlantic Region, Occasional Report No. 8. Sackville, NB: Environment Canada.

Pettigrew, N. R., Townsend, D. W., Xue, H., Wallinga, J. P., Brickley, P. J., & Hetland, R. D. (1998). Observations of the Eastern Maine Coastal Current and its offshore extensions in 1994. *Journal of Geophysical Research: Oceans*, *103*(C13), 30623-30639. doi: 10.1029/98jc01625.

Pietrzak, J., Jakobson, J. B., Burchard, H., Vested, H. J., & Petersen, O. (2002). A three-dimensional hydrostatic model for coastal and ocean modelling using a generalized topography following co-ordinate system. *Ocean Modelling*, *4*(2), 173-205. doi: 10.1016/S1463-5003(01)00016-6.

Pingree, R. D. (1975). The advance and retreat of the thermocline on the continental shelf. *Journal of the Marine Biological Association of the United Kingdom*, *55*(4), 965-974. doi: 10.1017/S0025315400017859.

Piollé, J., Armstrong, E., Casey, K., & Donlon, C. (2022). The Recommended GHRSST Data Specification (GDS). doi: 10.5281/ZENODO.6984989.

Redfield, A. C. (1953). Interference Phenomena in the Tides of the Woods Hole Region. *Journal of Marine Research 12(1):121–40*.

Renaud, P. E., Wallhead, P., Kotta, J., Włodarska-Kowalczuk, M., Bellerby, R. G., Rätsep, M., Slagstad, D., & Kukliński, P. (2019). Arctic sensitivity? Suitable habitat for benthic taxa is surprisingly robust to climate change. *Frontiers in Marine Science*, *6*, 538. doi: 10.3389/fmars.2019.00538.

Reynolds, R. W., Rayner, N. A., Smith, T. M., Stokes, D. C., & Wang, W. (2002). An improved in situ and satellite SST analysis for climate. *Journal of climate*, *15*(13), 1609-1625. doi: 10.1175/1520-0442(2002)015<1609:AIISAS>2.0.CO;2.

Riding, J., & Rawson, A. (2015). LINZ Hydrography Risk Assessment Methodology Update. *Marico Marine Report*, (15NZ322).

Rodrigues, M., & Fortunato, A. B. (2017). Assessment of a three-dimensional baroclinic circulation model of the Tagus estuary (Portugal). doi: 10.3934/environsci.2017.6.763.

Sameoto, J. A., Keyser, F., Keith, D., Brown, C. J., & Church, I. (2020). Proceedings of the Bay of Fundy seafloor mapping forum: Dartmouth, Nova Scotia, March 13, 2020. *Canadian Technical Report of Fisheries and Aquatic Sciences, 3395*.

Sankaranarayanan, S., & McCay, D. F. (2003). Three-dimensional modeling of tidal circulation in Bay of Fundy. *Journal of waterway, port, coastal, and ocean engineering*, *129*(3), 114-123. doi: 10.1061/(ASCE)0733-950X(2003)129:3(114).

Scales, K. L., Hazen, E. L., Jacox, M. G., Edwards, C. A., Boustany, A. M., Oliver, M. J., & Bograd, S. J. (2017). Scale of inference: on the sensitivity of habitat models for wide-ranging marine predators to the resolution of environmental data. *Ecography*, *40*(1), 210-220. doi: 10.1111/ecog.02272.

Schaeffer, A., Garreau, P., Molcard, A., Fraunié, P., & Seity, Y. (2011). Influence of high-resolution wind forcing on hydrodynamic modeling of the Gulf of Lions. *Ocean Dynamics*, *61*, 1823-1844. doi: 10.1007/s10236-011-0442-3.

Schmidt, V. (2020). Hydrographic survey with autonomous surface vehicles. *The International Hydrographic Review*, 24. https://ihr.iho.int/articles/hydrographic-survey-with-autonomous-surface-vehicles.

Seity, Y., Brousseau, P., Malardel, S., Hello, G., Bénard, P., Bouttier, F., Lac, C., & Masson, V. (2011). The AROME-France convective-scale operational model. *Monthly Weather Review*, 139(3), 976–991.

Shackell, N. L., Ricard, D., & Stortini, C. (2014). Thermal habitat index of many Northwest Atlantic temperate species stays neutral under warming projected for 2030 but changes radically by 2060. *PLoS One*, *9*(3), e90662. doi: 10.1371/journal.pone.0090662.

Shaw, J., Amos, C. L., Greenberg, D. A., O'Reilly, C. T., Parrott, D. R., & Patton, E. (2010). Catastrophic tidal expansion in the Bay of Fundy, Canada. *Canadian Journal of Earth Sciences*, *47*(8), 1079-1091. doi: 10.1139/E10-046.

Skamarock, W. C., & Klemp, J. B. (2008). A time-split nonhydrostatic atmospheric model for weather research and forecasting applications. *Journal of computational physics*, *227*(7), 3465-3485. doi: https://doi.org/10.1016/j.jcp.2007.01.037.

Smagorinsky, J. (1963). General circulation experiments with the primitive equations: I. The basic experiment. *Monthly weather review*, *91*(3), 99-164.

Soufflet, Y., Marchesiello, P., Lemarié, F., Jouanno, J., Capet, X., Debreu, L., & Benshila, R. (2016). On effective resolution in ocean models. *Ocean Modelling*, *98*, 36-50.

Stateczny, A., Burdziakowski, P., Najdecka, K., & Domagalska-Stateczna, B. (2020). Accuracy of Trajectory Tracking Based on Nonlinear Guidance Logic for Hydrographic Unmanned Surface Vessels. *Sensors,* 20(3). doi: https://doi.org/10.3390/s20030832.

Stortini, C. H., Shackell, N. L., Tyedmers, P., & Beazley, K. (2015). Assessing marine species vulnerability to projected warming on the Scotian Shelf, Canada. *ICES Journal of Marine Science*, *72*(6), 1731-1743.

Stow, C. A., Jolliff, J., McGillicuddy Jr, D. J., Doney, S. C., Allen, J. I., Friedrichs, M. A., Rose, K. A., & Wallhead, P. (2009). Skill assessment for coupled biological/physical models of marine systems. *Journal of Marine Systems*, *76*(1-2), 4-15. doi: 10.1016/j.jmarsys.2008.03.011.

Stow, C. A., Roessler, C., Borsuk, M. E., Bowen, J. D., & Reckhow, K. H. (2003). Comparison of estuarine water quality models for total maximum daily load development in Neuse River Estuary. *Journal of Water Resources Planning and Management*, *129*(4), 307-314. doi: 10.1061/(ASCE)0733-9496(2003)129:4(307).

Surface-Water Modeling System, Version 11.0, Reference Manual & Tutorials, Aquaveo, LLC. 2012. 'SMS'.

Swift, D. J., Pelletier, B. R., Lyall, A. K., & Miller, J. A. (1969). Sediments of the Bay of Fundy-a preliminary report. *Atlantic Geology*, *5*(3), 95-100. doi: 10.4138/1801.

Tao, J., Hill, P. S., Mulligan, R. P., & Smith, P. C. (2014). Seasonal variability of total suspended matter in Minas Basin, Bay of Fundy. *Estuarine, Coastal and Shelf Science*, *151*, 169-180. doi: https://doi.org/10.1016/j.ecss.2014.10.005.

Taylor, K. E. (2001). Summarizing multiple aspects of model performance in a single diagram. *Journal of Geophysical Research: Atmospheres*, 106(D7), 7183–7192. https://doi.org/10.1029/2000JD900719.

The International ST. Croix River Watershed Board. 2024. International ST. Croix River Board 2023 Annual Report. IJC: International Joint Commission.

Todd, B. J., Brown, C. J., Curtis, B., Kirchhoff, S., Lacharité, M., Sameoto, J. A., & Church, I. (2020). Seabed habitats of the Bay of Fundy, Atlantic Canada. In *Seafloor Geomorphology as Benthic Habitat* (pp. 243-265). Elsevier.

Triantaphyllou, E., & Triantaphyllou, E. (2000). *Multi-criteria decision-making methods* (pp. 5-21). Springer Us. 44. doi: 10.1007/978-1-4757-3157-6.

Watson, E. E. (1936). Mixing and Residual Currents in the Tidal Waters as Illustrated in the Bay of Fundy. *Journal of the Biological Board of Canada*, *2*(2), 141-208.

Weber, T. C., Rice, G., & Smith, M. (2018). Toward a standard line for use in multibeam echo sounder calibration. *Marine Geophysical Research*, *39*, 75-87. doi: 10.1007/s11001-017-9334-3.

Wessel, P., & Smith, W. H. (1996). A global, self-consistent, hierarchical, high-resolution shoreline database. *Journal of Geophysical Research: Solid Earth*, *101*(B4), 8741-8743. doi: 10.1029/96jb00104.

Willmott, C. J. (1981). On the validation of models. Physical Geography 2(2):184–94. doi: 10.1080/02723646.1981.10642213.

Wilson, M., Beaudoin, J., & Smyth, S. (2013). Water-Column Variability Assessment for Underway Profilers to Improve Efficiency and Accuracy of Multibeam Surveys. *U.S. Hydrographic Conference.*

Winship, A., Williams, B., Salgado, E., Poti, M., Hourigen, T., Frometa, J., Etnoyer, P., Coyne, M., Coleman, H., Christensen, J., Bassett, R., & Goyert, H. (2021). Characterizing Spatial Distributions of Deep-sea Corals and Chemosynthetic Communities in the US Gulf of Mexico through Data Synthesis and Predictive Modeling. *US Department of the Interior, Bureau of Ocean Energy Management.*

Worm, B., Barbier, E. B., Beaumont, N., Duffy, J. E., Folke, C., Halpern, B. S, Jackson, J., Lotze, H., Micheli, F., Palumbi, S., Sala, E., Selkoe, K., Stachowicz, J., & Watson, R. (2006). Impacts of biodiversity loss on ocean ecosystem services. *science*, *314*(5800), 787-790. doi: 10.1126/science.1132294.

Wu, Y., Chaffey, J., Law, B., Greenberg, D. A., Drozdowski, A., Page, F., & Haigh, S. (2014). A three-dimensional hydrodynamic model for aquaculture: a case study in the Bay of Fundy. *Aquaculture Environment Interactions*, *5*(3), 235-248. doi: 10.3354/aei00108.

Wu, Y., Chaffey, J., Greenberg, D. A., Colbo, K., & Smith, P. C. (2011). Tidally-induced sediment transport patterns in the upper Bay of Fundy: a numerical study. *Continental Shelf Research*, *31*(19-20), 2041-2053. doi: 10.1016/j.csr.2011.10.009.

Xie, P., & Arkin, P. A. (1997). Global precipitation: A 17-year monthly analysis based on gauge observations, satellite estimates, and numerical model outputs. *Bulletin of the american meteorological society*, *78*(11), 2539-2558. doi: 10.1175/1520-0477(1997)078<2539:GPAYMA>2.0.CO;2.

Xue, H., Chai, F., & Pettigrew, N. R. (2000). A model study of the seasonal circulation in the Gulf of Maine. *Journal of Physical Oceanography*, *30*(5), 1111-1135. doi: 10.1175/1520-0485(2000)030<1111:AMSOTS>2.0.CO;2.

Yang, Z., Richardson, P., Chen, Y., Kelley, J. G., Myers, E., Aikman, F., Kelley, J. G. W., Peng, M., & Zhang, A. (2016). Model development and hindcast simulations of NOAA's Gulf of Maine operational forecast system. *Journal of Marine Science and Engineering*, *4*(4), 77. doi: 10.3390/jmse4040077.

Zhang, A., Hess, K. W., Wei, E. J., & Myers, E. P. (2006). Implementation of model skill assessment software for water level and current in tidal regions. *NOAA Technical Report NOS CS 24, Silver Spring, MD.* Available online at https://repository.library.noaa.gov/view/noaa/2204.

Zhao, X., Zhao, J., Zhang, H., & Zhou, F. (2018). Remote Sensing of Suspended Sediment Concentrations Based on the Waveform Decomposition of Airborne LiDAR Bathymetry. *Remote Sensing*, 10(2). https://doi.org/10.3390/rs10020247.

Appendix A

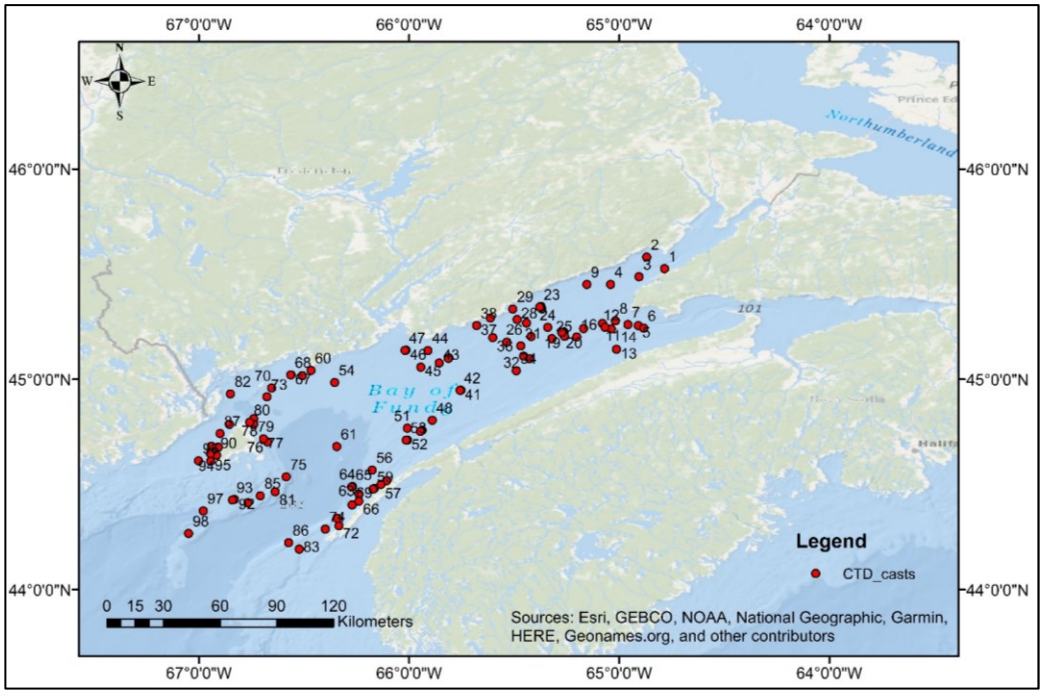

A 1. CTD cast from NSCC field work, DFO, and WOD for the 2 months, July and August 2018. used for comparison.

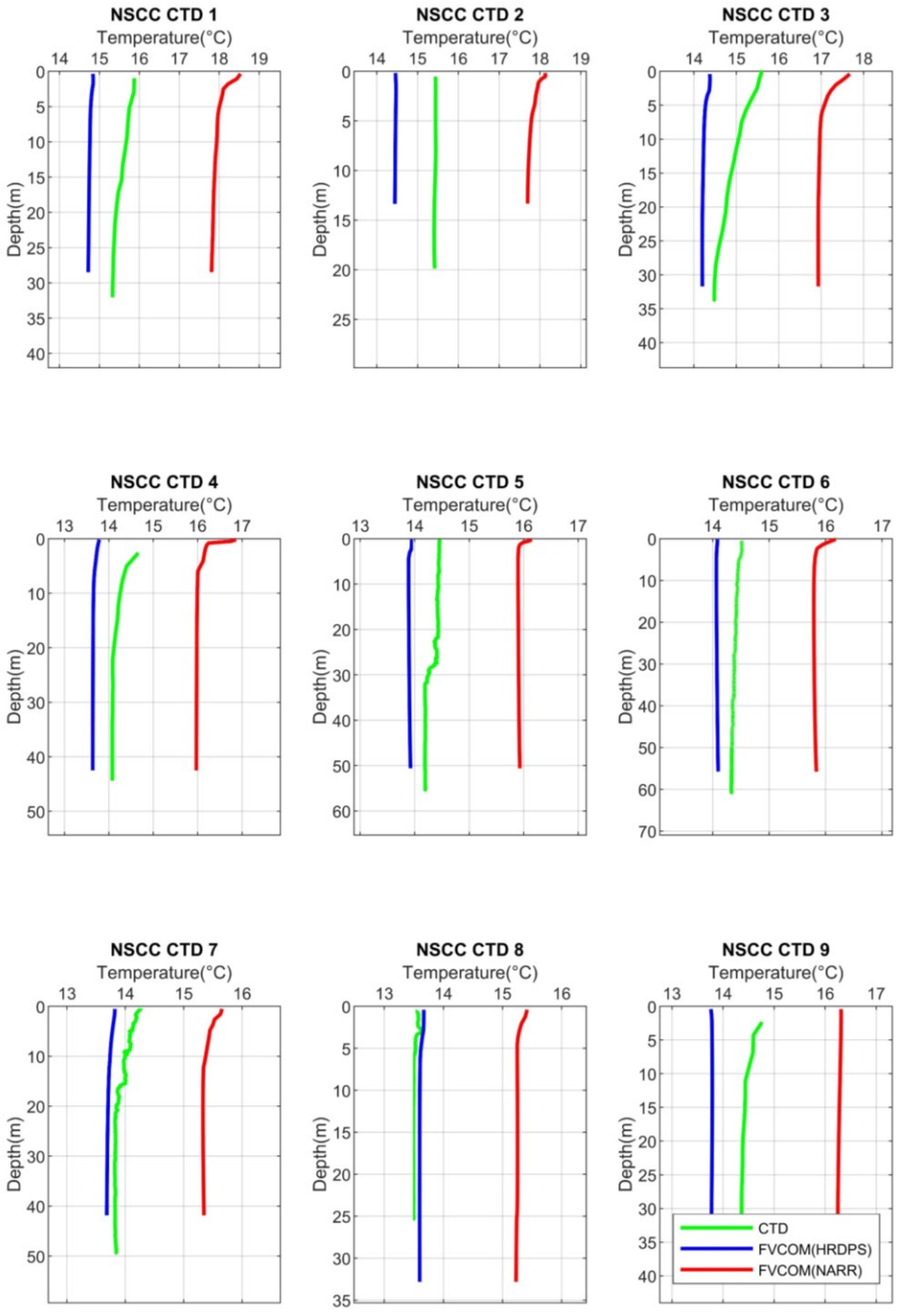

A 2. Temperature profiles for the CTD (green), FVCOM_HRDPS (blue), and FVCOM_NARR (red).

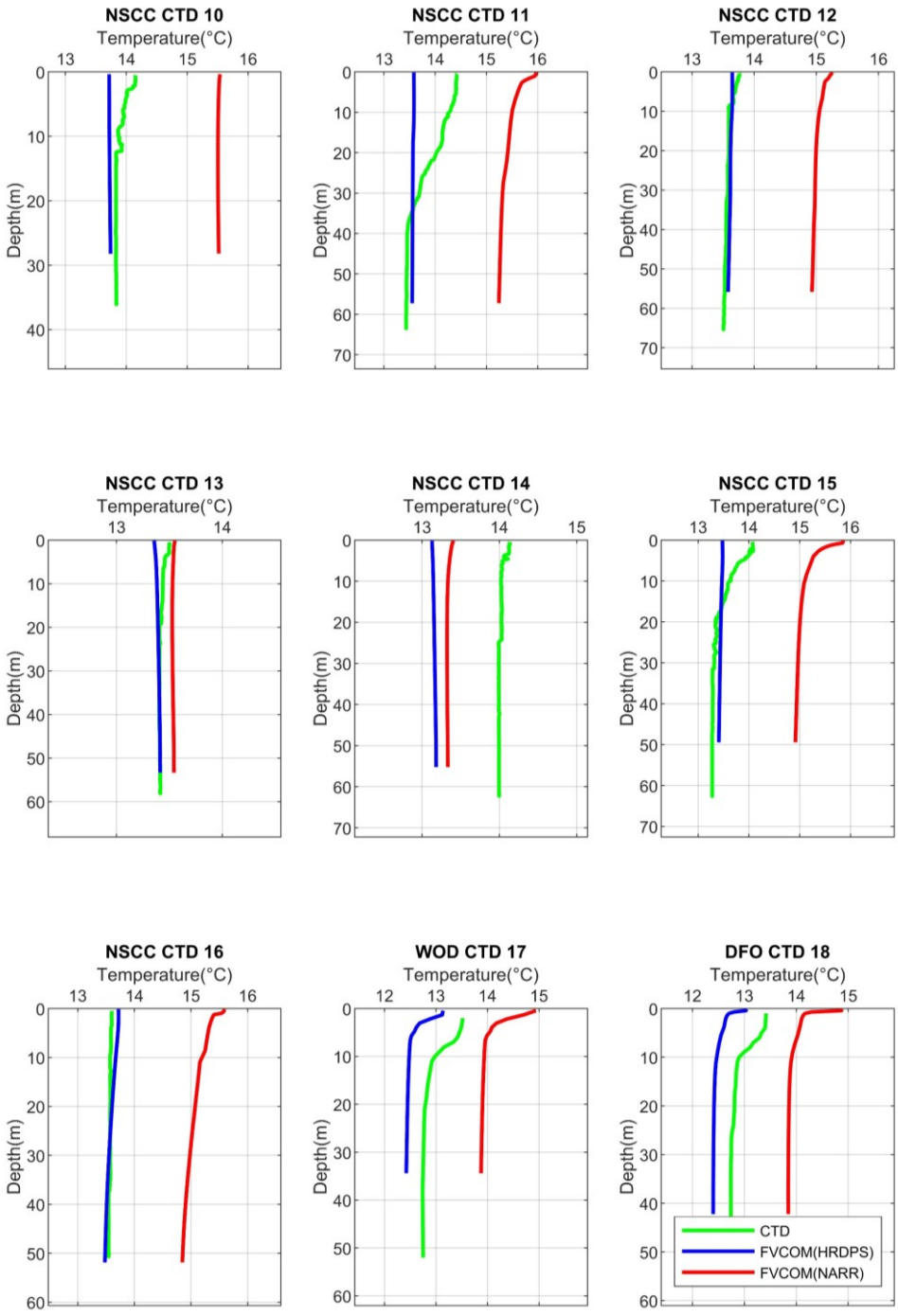

A 3. Temperature profiles for the CTD (green), FVCOM_HRDPS (blue), and FVCOM_NARR (red).

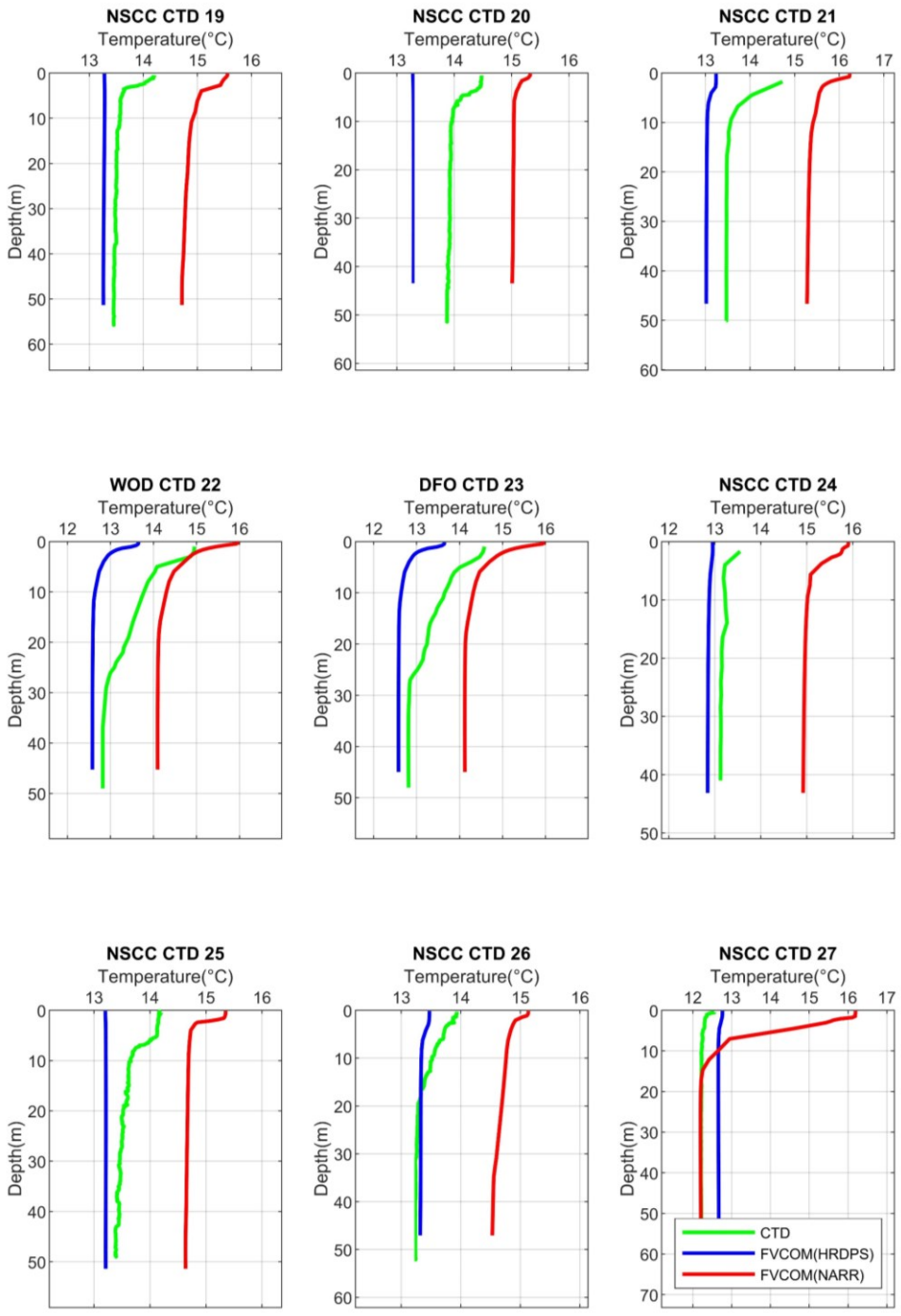

A 4. Temperature profiles for the CTD (green), FVCOM_HRDPS (blue), and FVCOM_NARR (red).

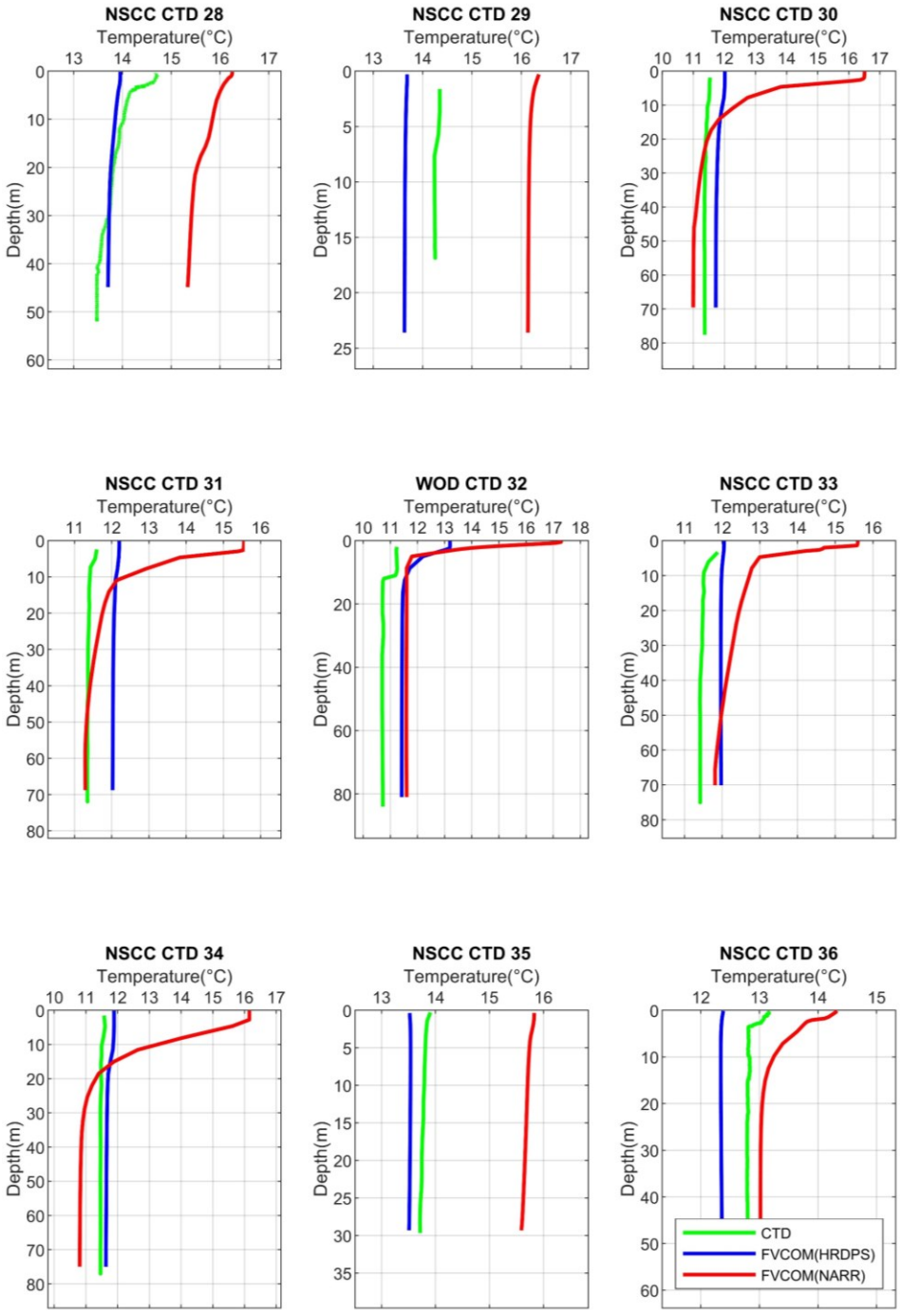

A 5. Temperature profiles for the CTD (green), FVCOM_HRDPS (blue), and FVCOM_NARR (red).

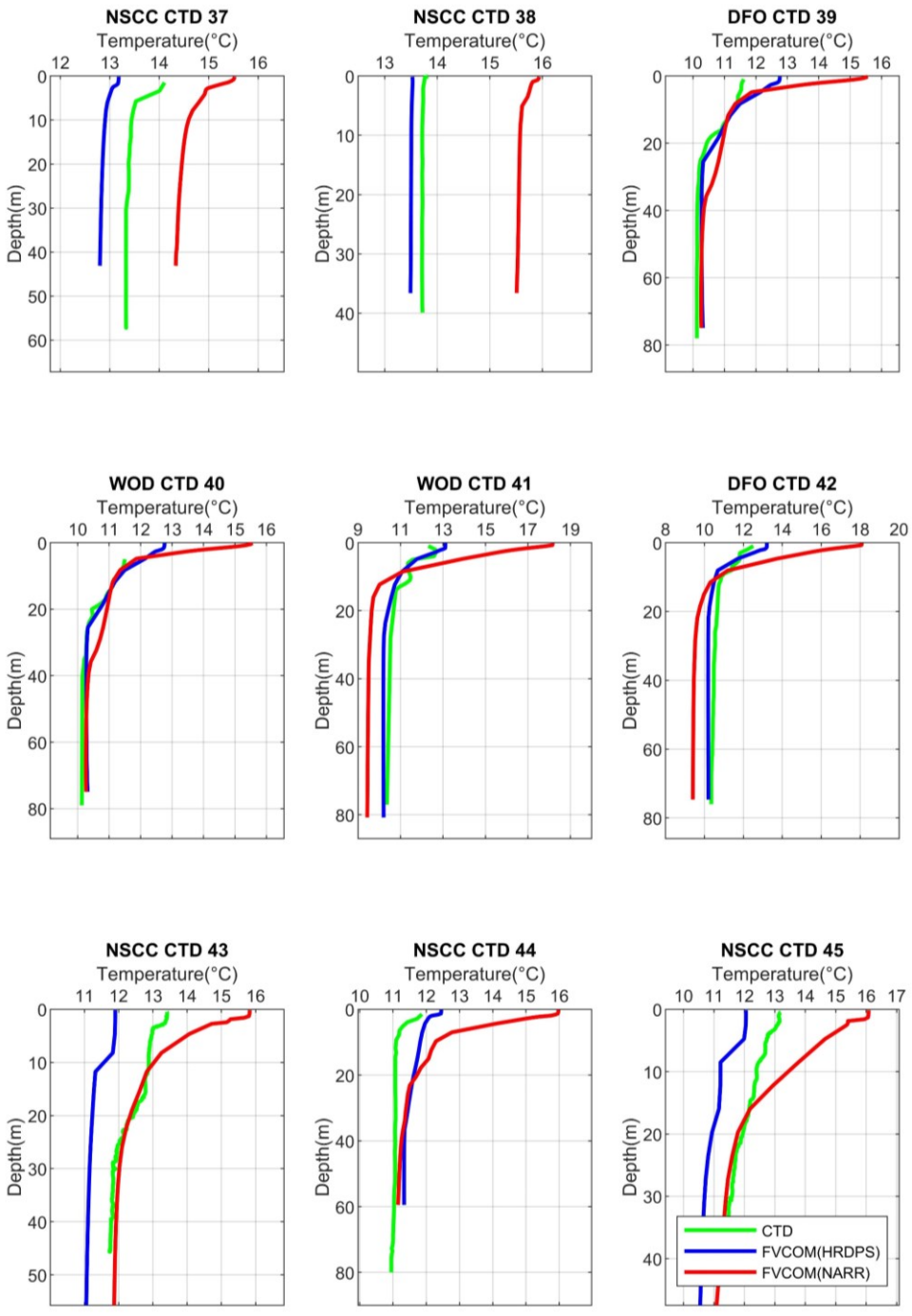

A 6. Temperature profiles for the CTD (green), FVCOM_HRDPS (blue), and FVCOM_NARR (red).

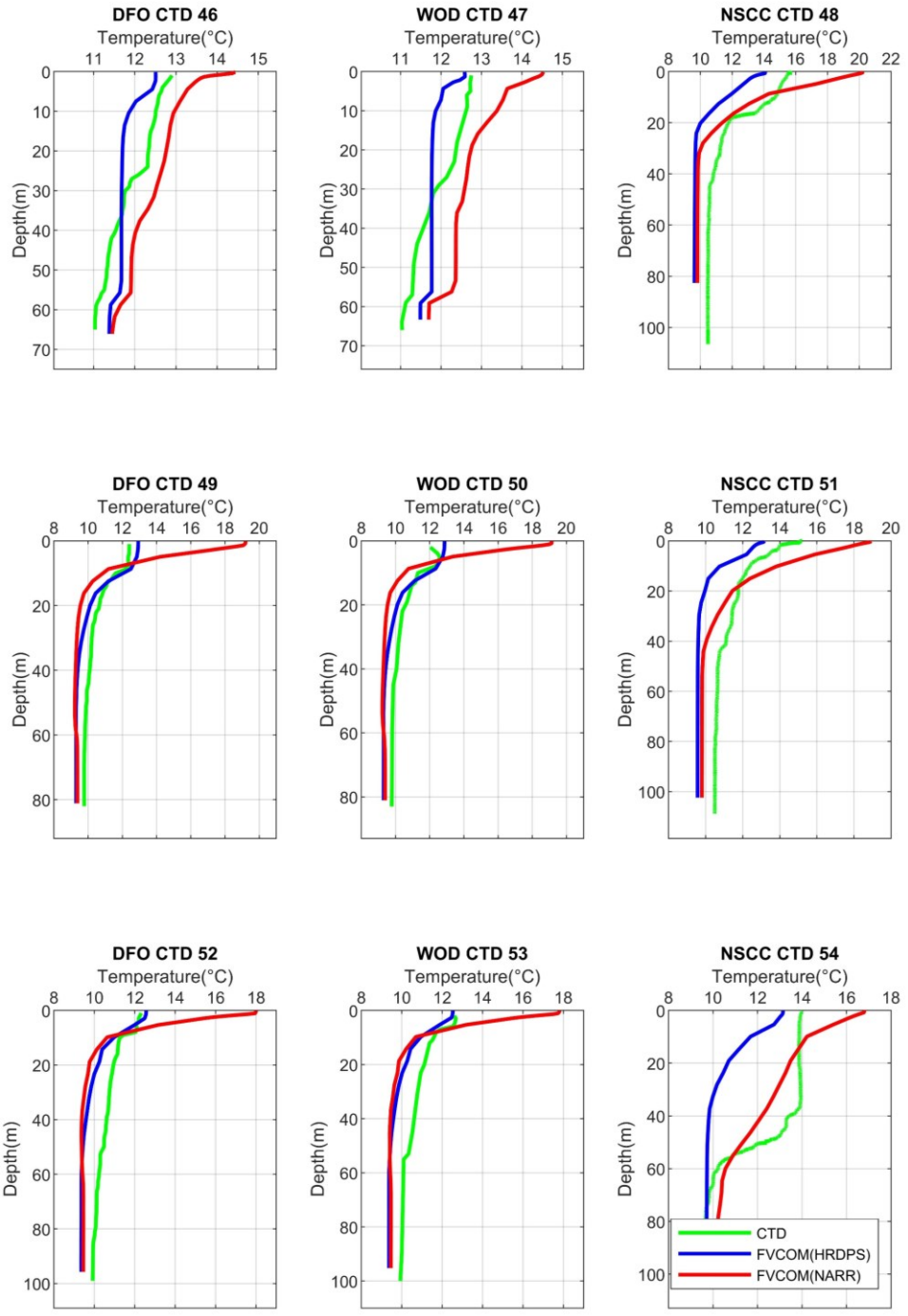

A 7. Temperature profiles for the CTD (green), FVCOM_HRDPS (blue), and FVCOM_NARR (red).

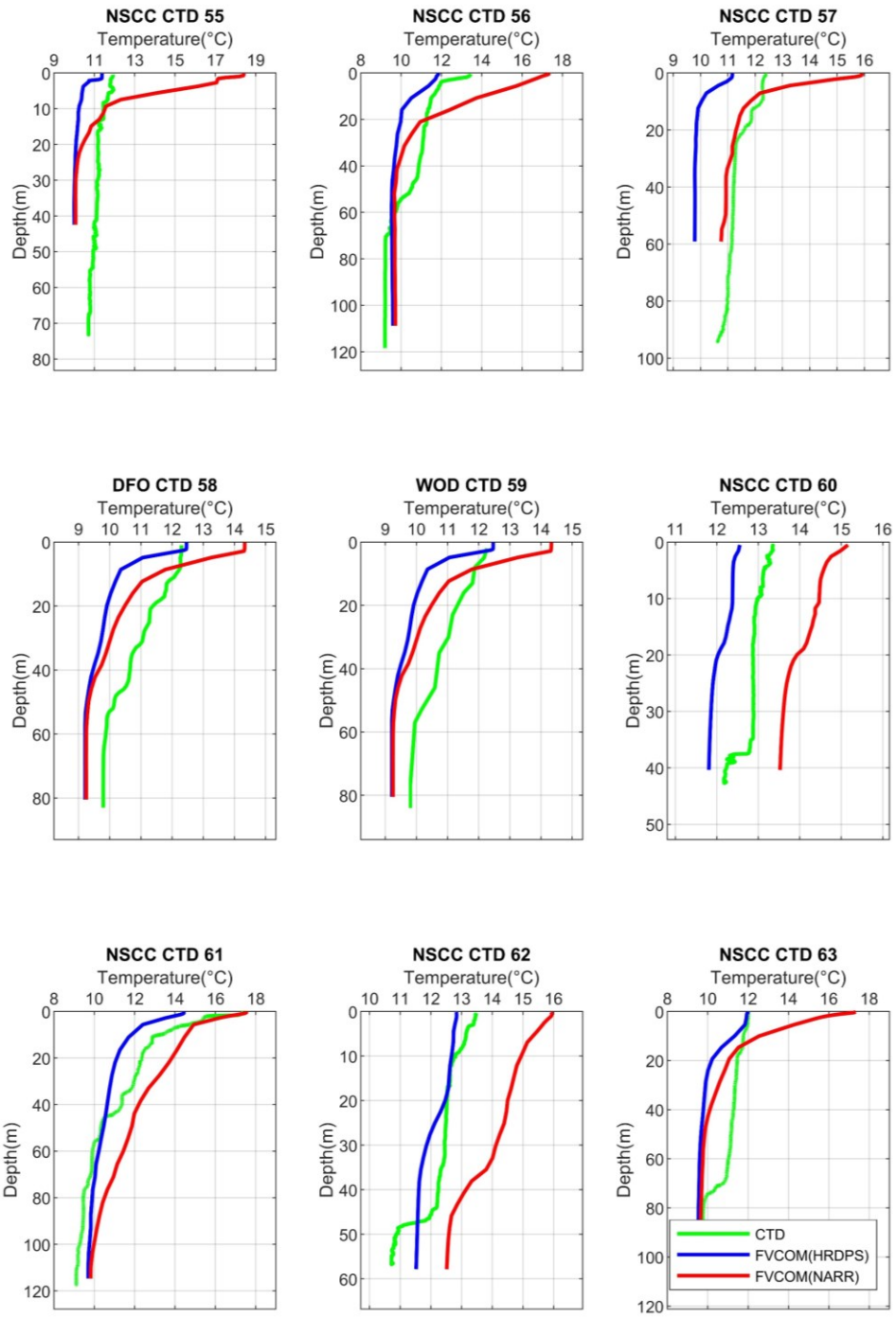

A 8. Temperature profiles for the CTD (green), FVCOM_HRDPS (blue), and FVCOM_NARR (red).

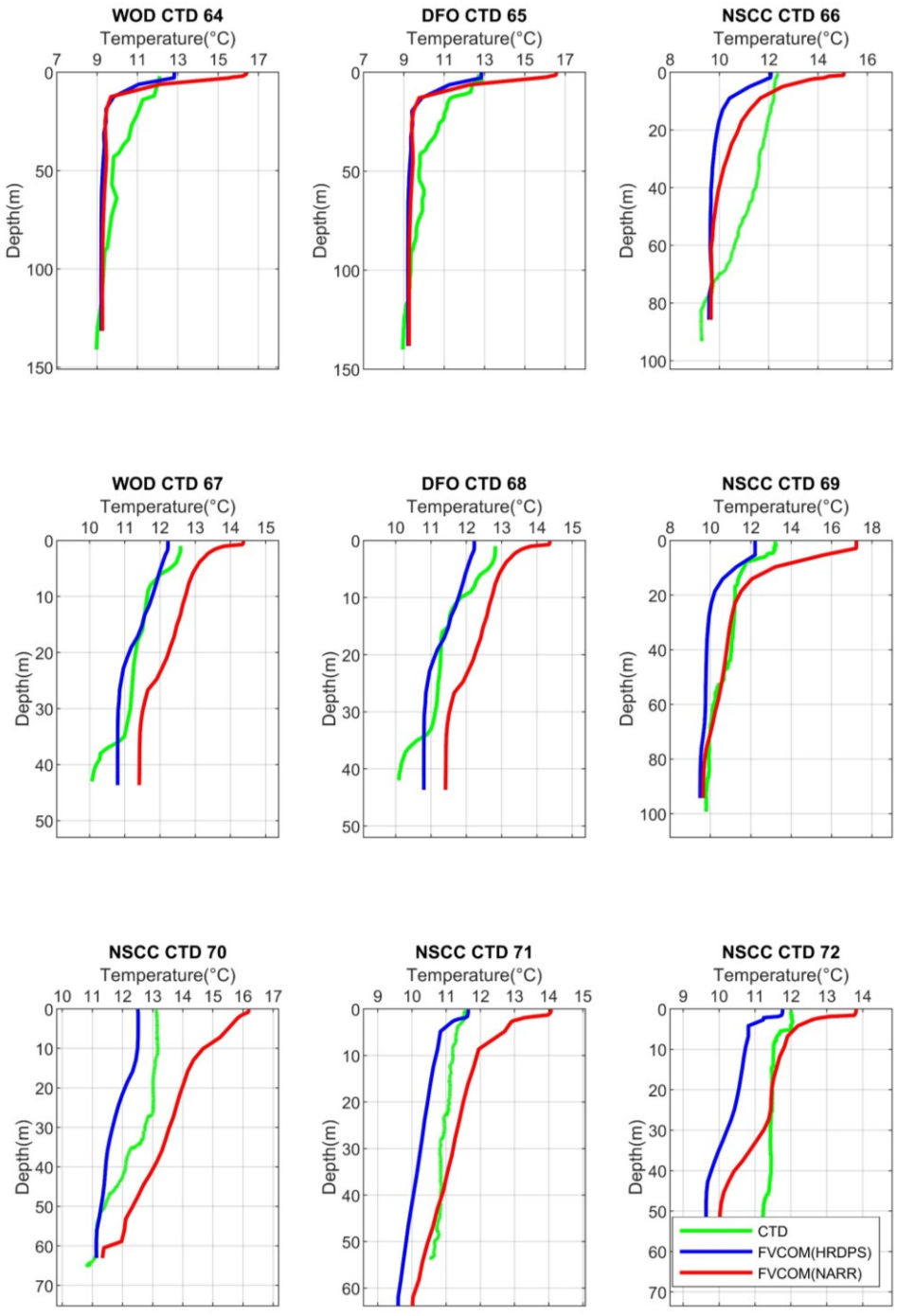

A 9. Temperature profiles for the CTD (green), FVCOM_HRDPS (blue), and FVCOM_NARR (red).

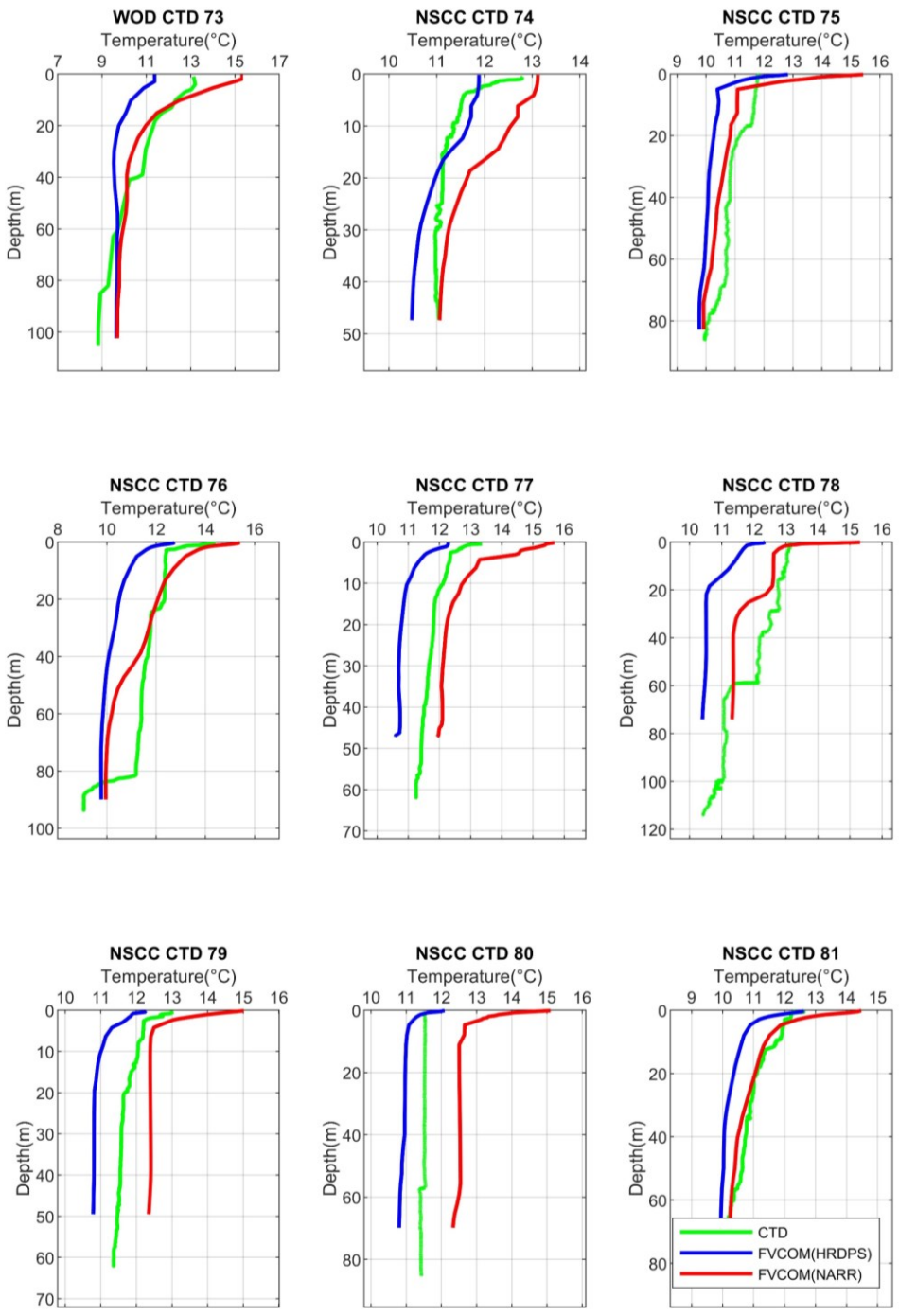

A 10. Temperature profiles for the CTD (green), FVCOM_HRDPS (blue), and FVCOM_NARR (red).

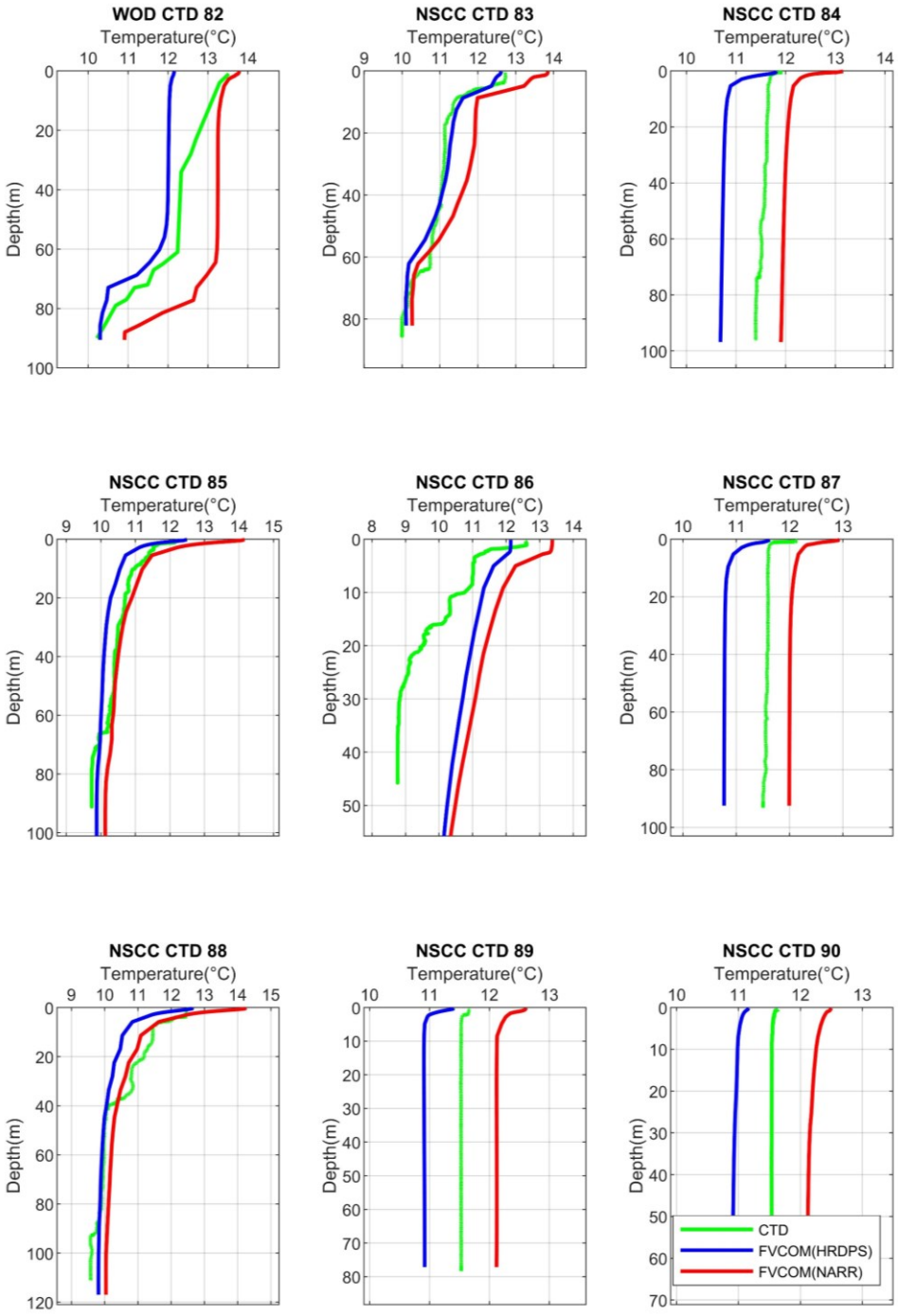

A 11. Temperature profiles for the CTD (green), FVCOM_HRDPS (blue), and FVCOM_NARR (red).

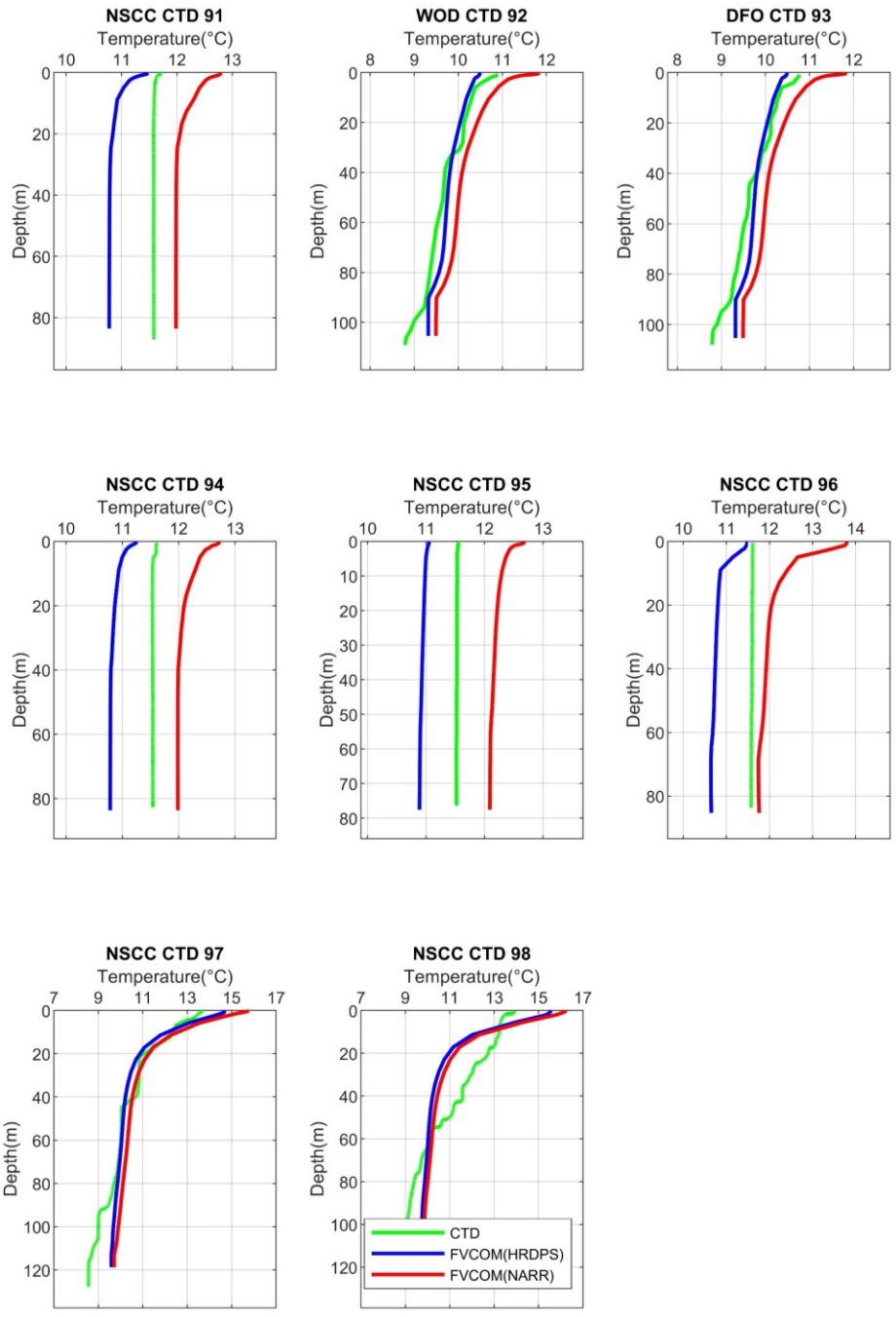

A 12.Temperature profiles for the CTD (green), FVCOM_HRDPS (blue), and FVCOM_NARR (red).

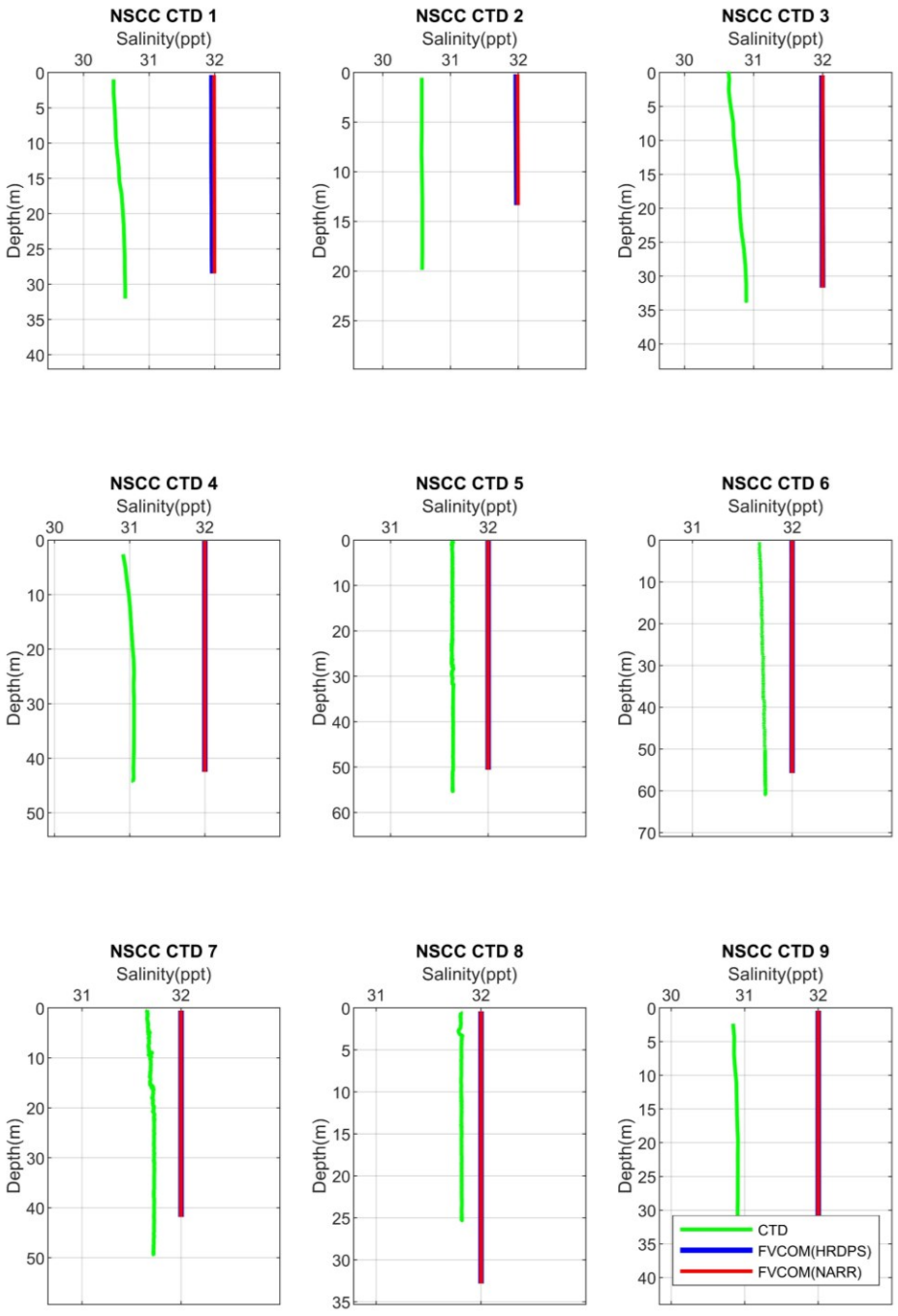

A 13. Salinity profiles for the CTD (green), FVCOM_HRDPS (blue), and FVCOM_NARR (red).

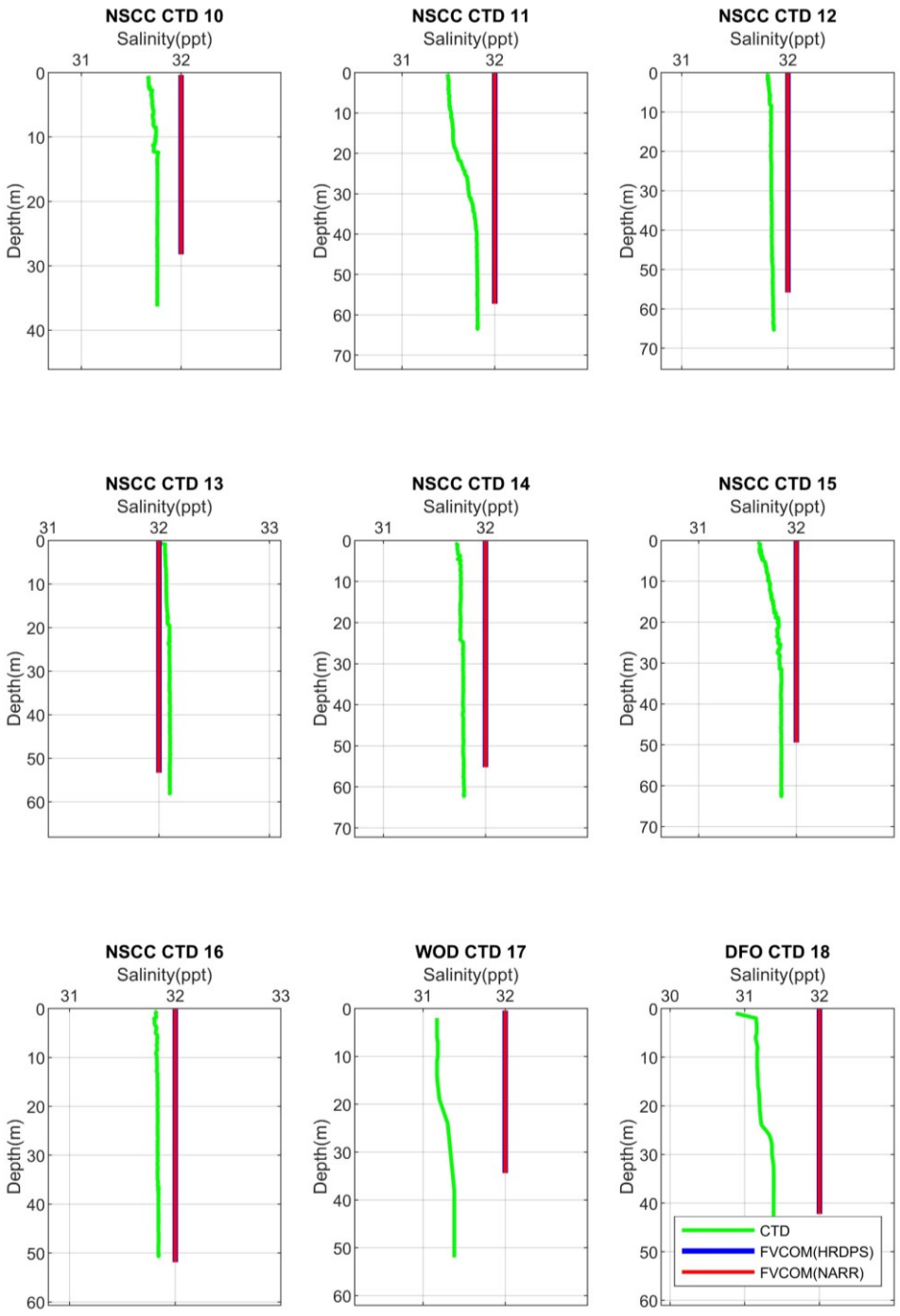

A 14. Salinity profiles for the CTD (green), FVCOM_HRDPS (blue), and FVCOM_NARR (red).

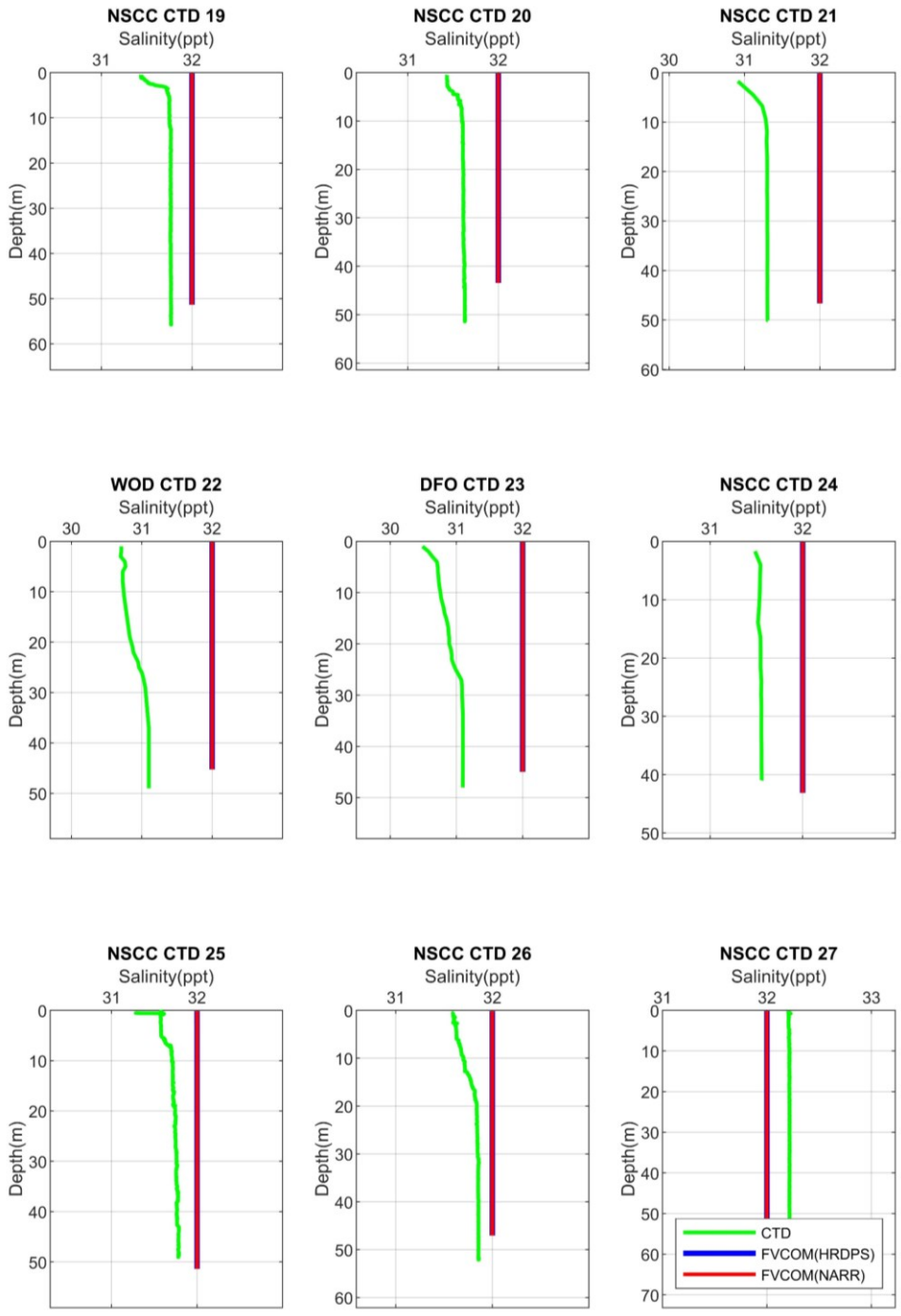

A 15. Salinity profiles for the CTD (green), FVCOM_HRDPS (blue), and FVCOM_NARR (red).

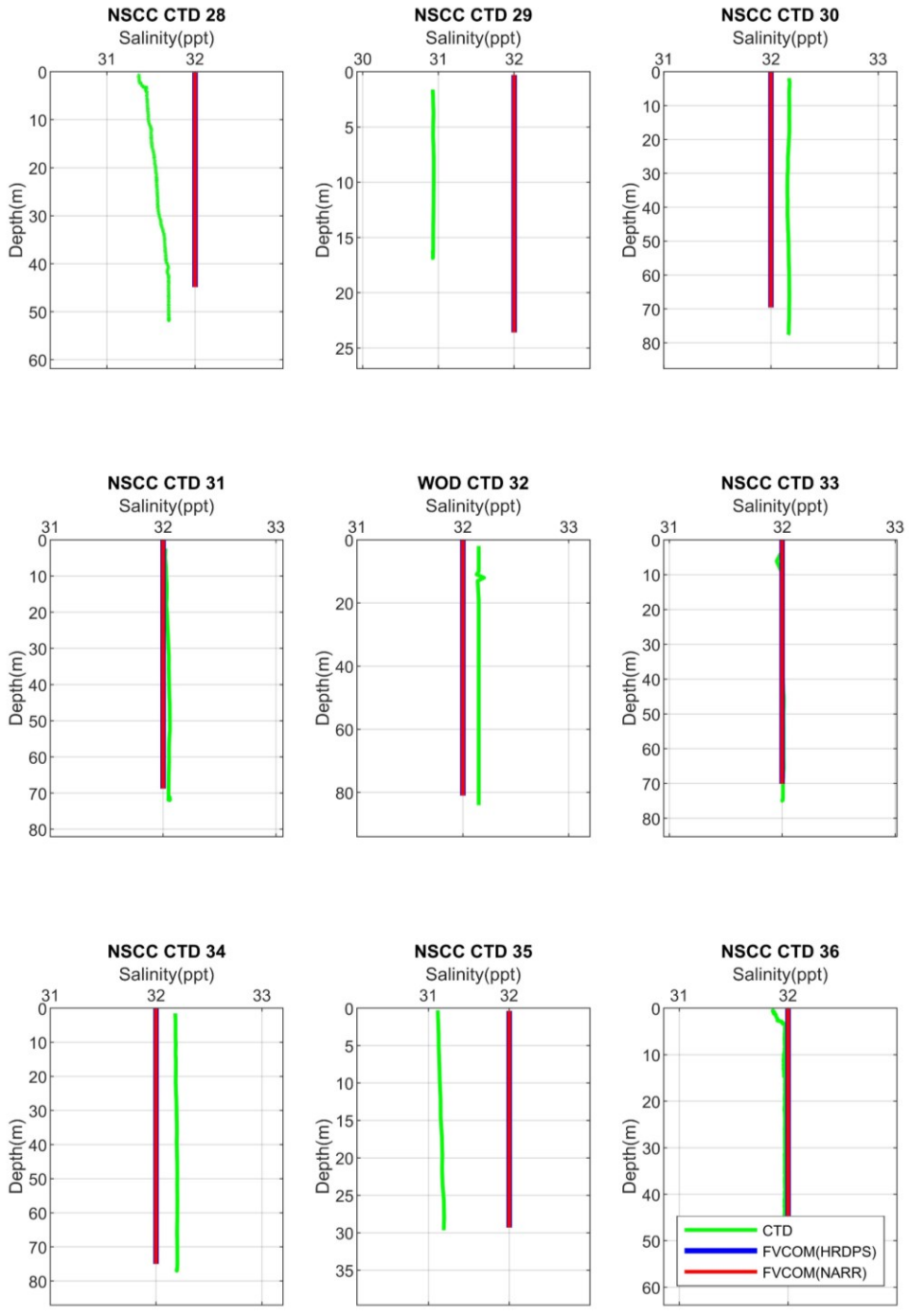

A 16. Salinity profiles for the CTD (green), FVCOM_HRDPS (blue), and FVCOM_NARR (red).

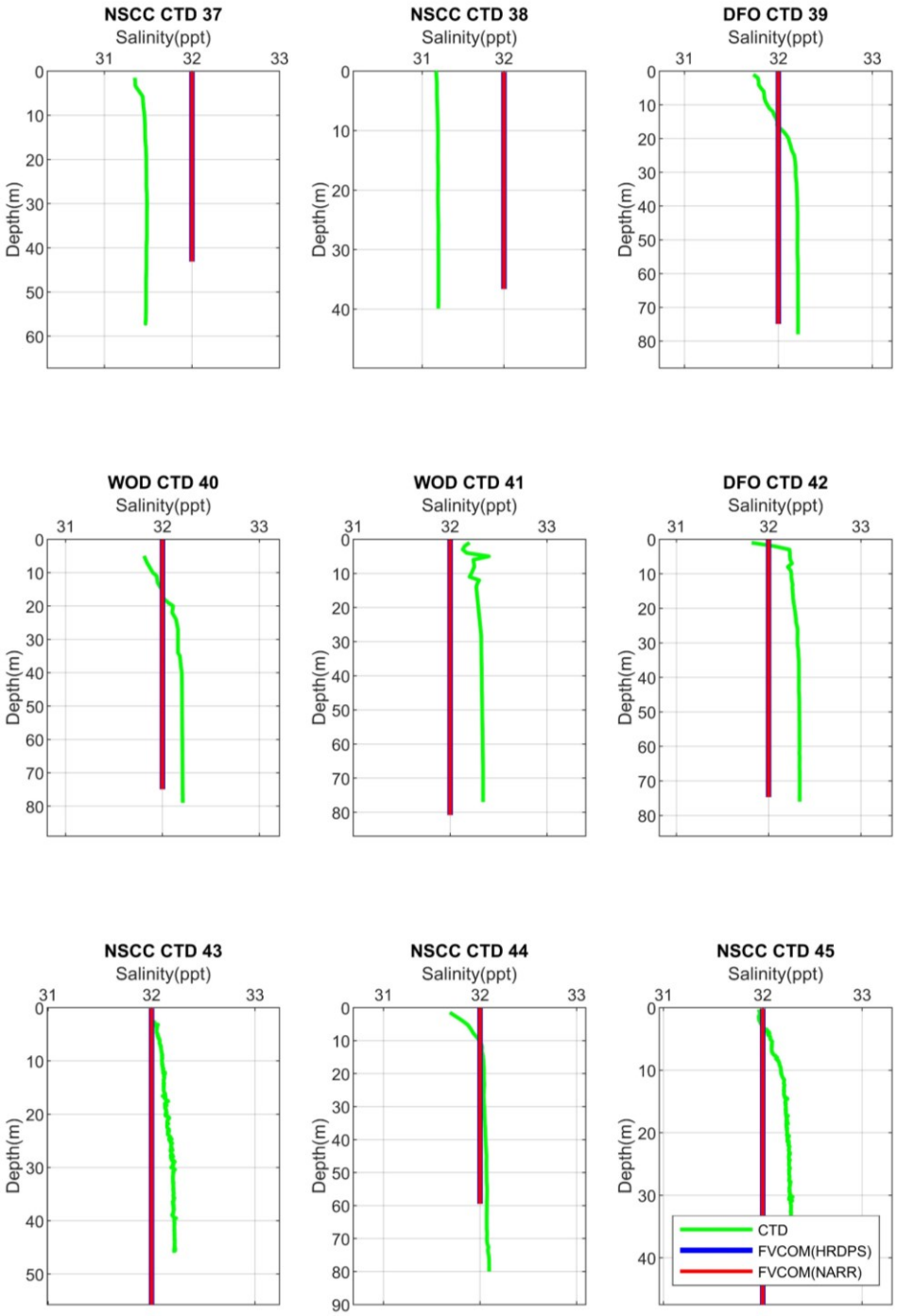

A 17. Salinity profiles for the CTD (green), FVCOM_HRDPS (blue), and FVCOM_NARR (red).

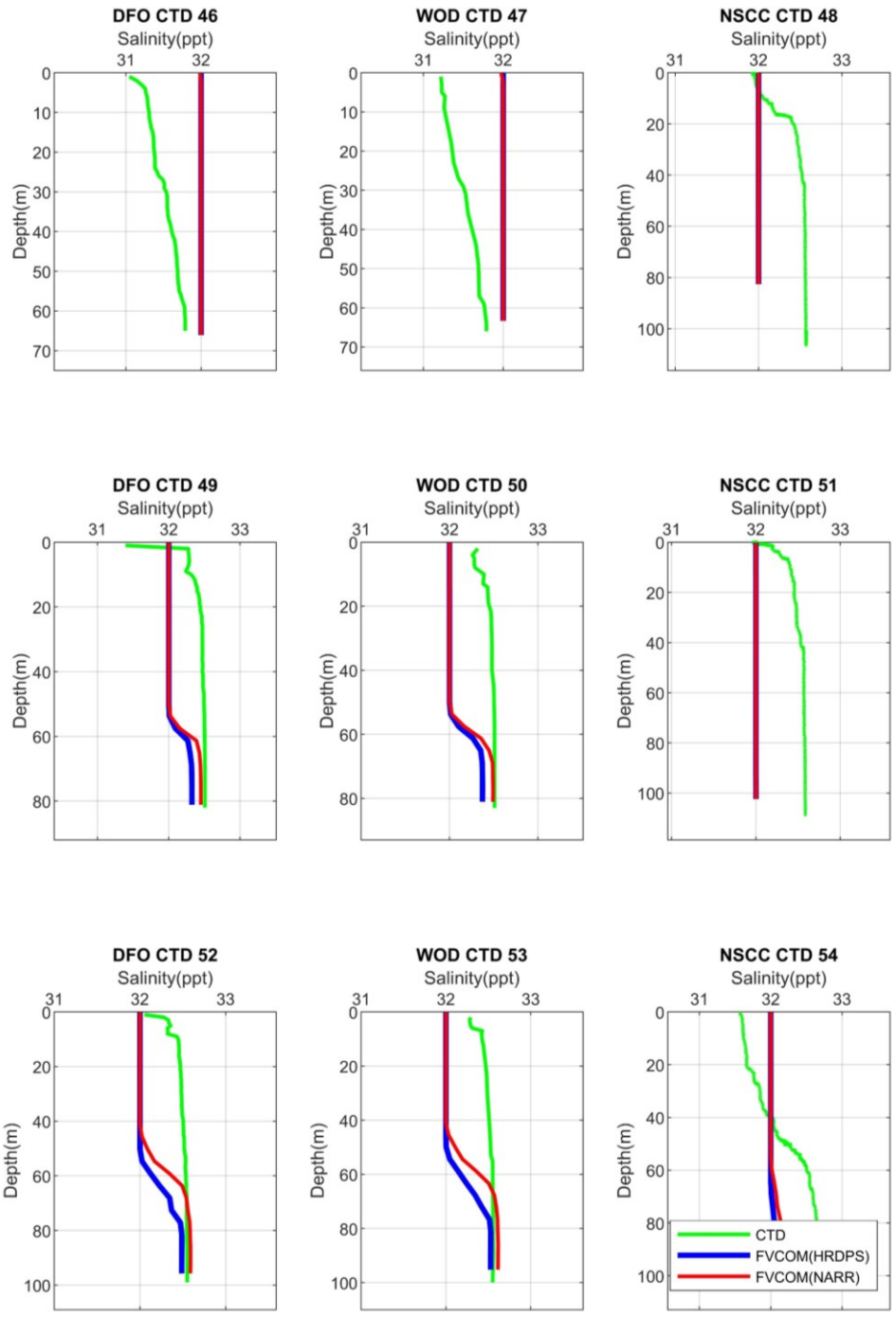

A 18.Salinity profiles for the CTD (green), FVCOM_HRDPS (blue), and FVCOM_NARR (red).

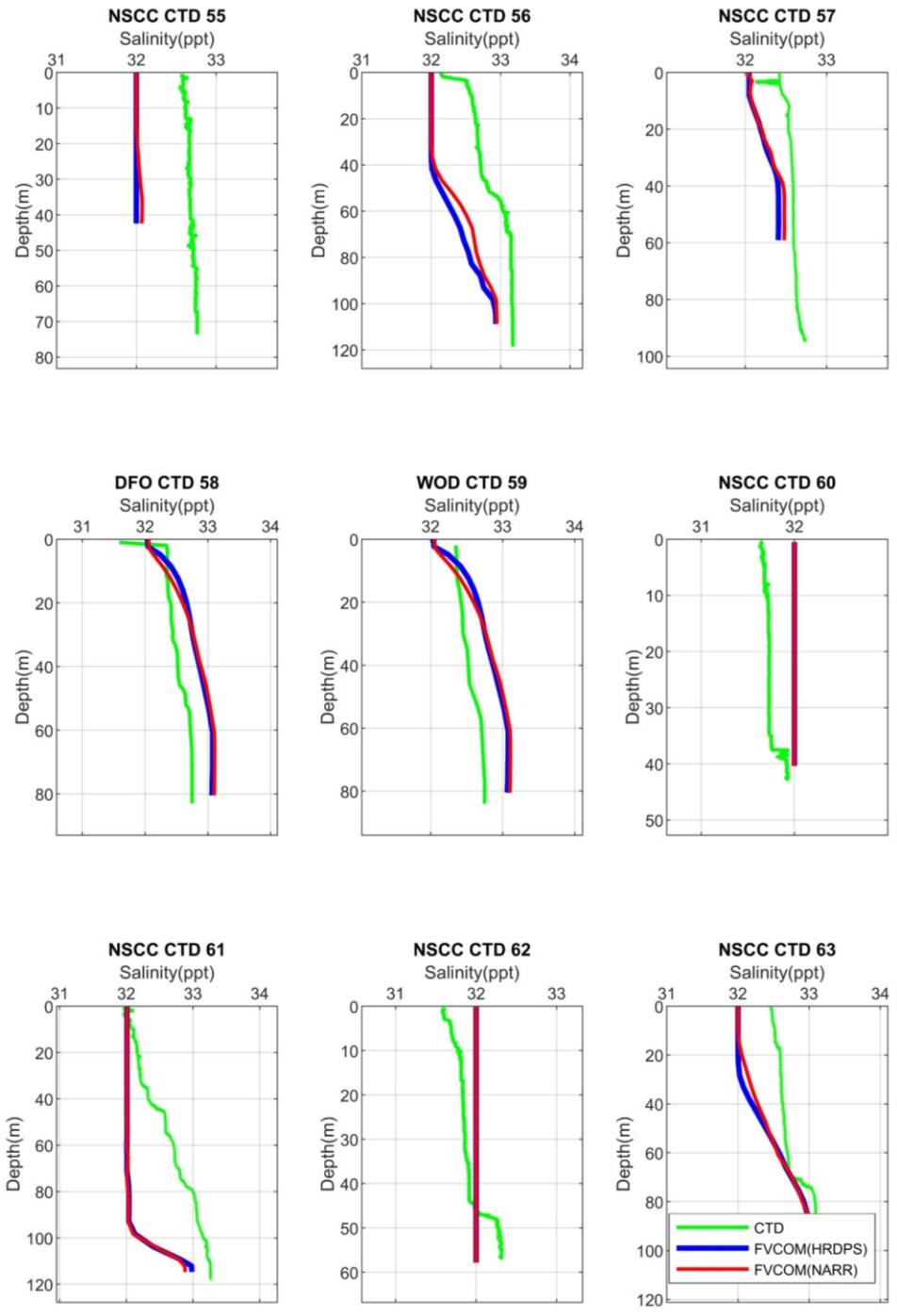

A 19. Salinity profiles for the CTD (green), FVCOM_HRDPS (blue), and FVCOM_NARR (red).

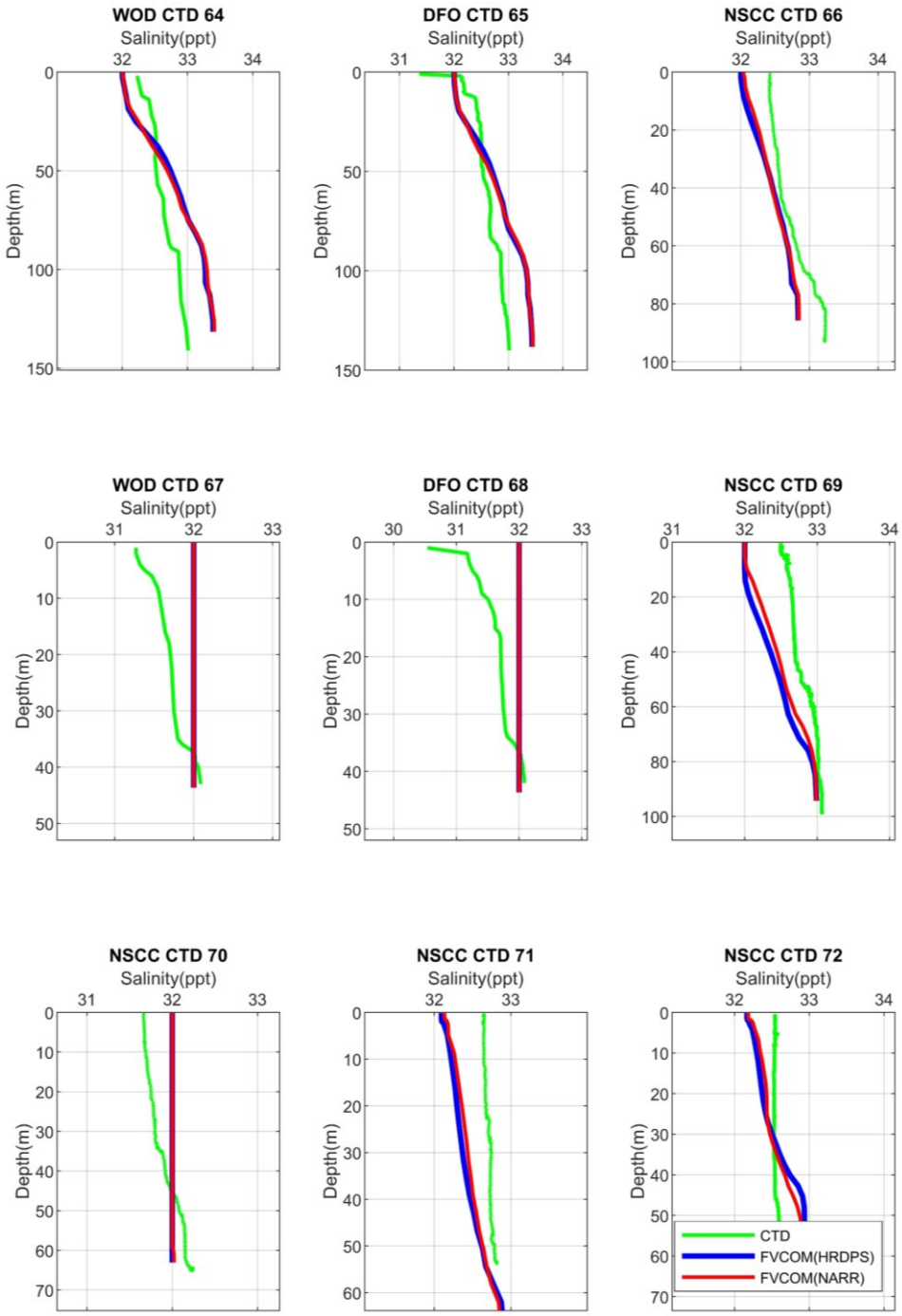

A 20. Salinity profiles for the CTD (green), FVCOM_HRDPS (blue), and FVCOM_NARR (red).

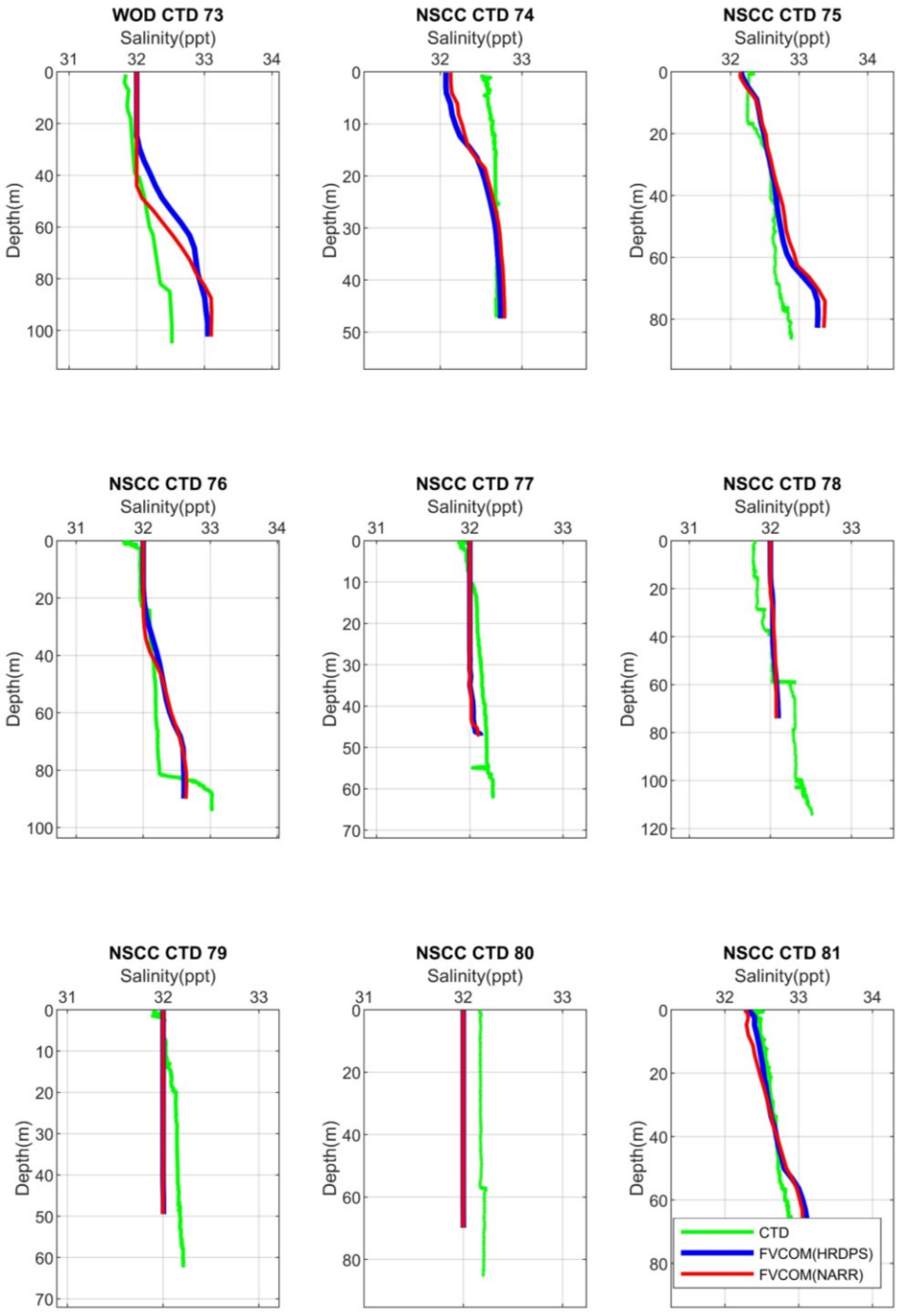

A 21. Salinity profiles for the CTD (green), FVCOM_HRDPS (blue), and FVCOM_NARR (red).

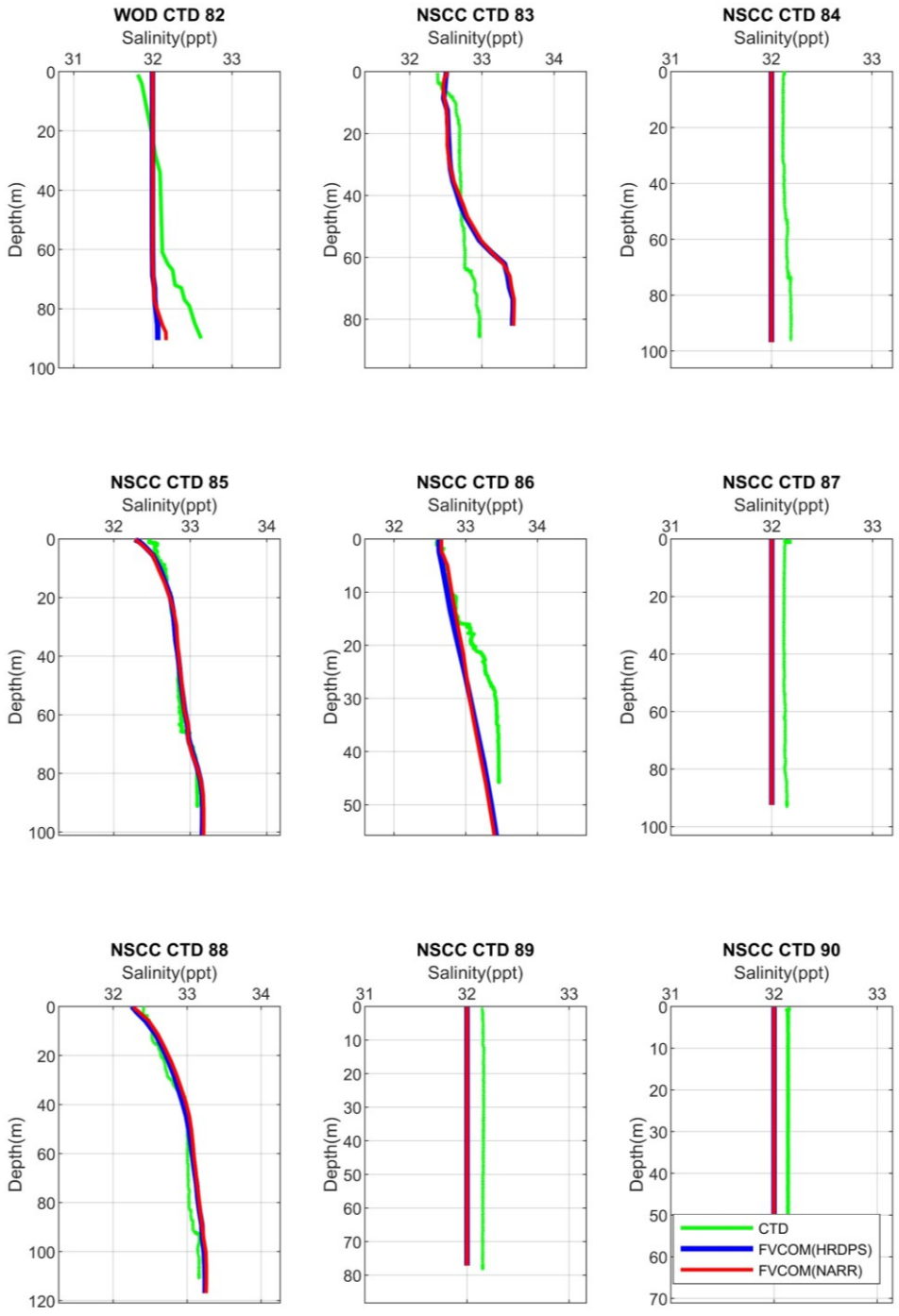

A 22. Salinity profiles for the CTD (green), FVCOM_HRDPS (blue), and FVCOM_NARR (red).

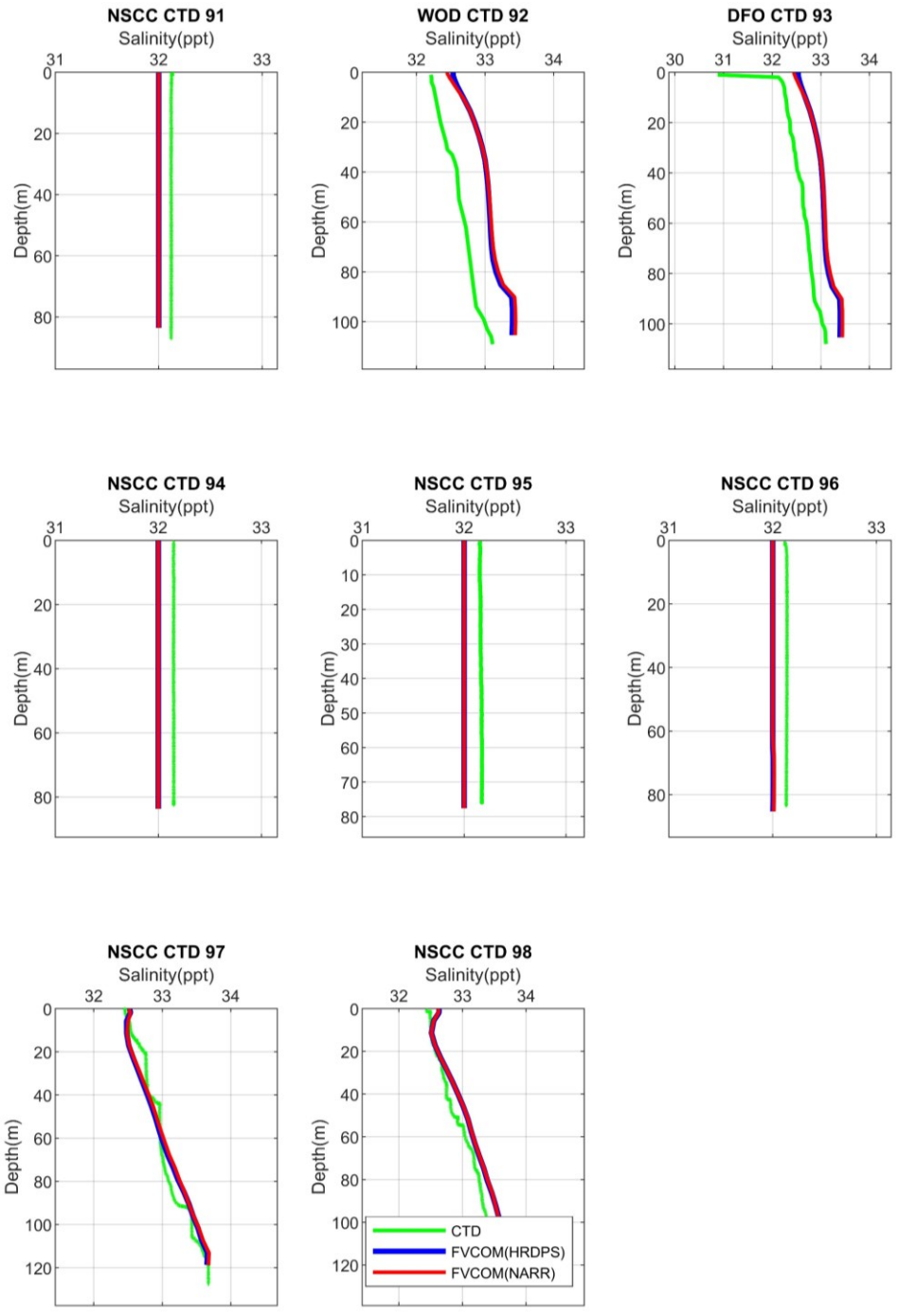

A 23.Salinity profiles for the CTD (green), FVCOM_HRDPS (blue), and FVCOM_NARR (red).

Appendix B

B 1. Ranking the three CTD casts (best, good, bad) based on the mean of RMSE at three layers at the upper part of the Bay for temperature and salinity.

Upper Bay RMSE					
	Temperature	**Surface**	**Middle**	**Bottom**	**Mean RMSE**
1	CTD 13	0.05	0.00	0.00	0.02
2	CTD 17	0.44	0.38	0.31	0.38
3	CTD 2	0.97	0.98	0.97	0.97
	Salinity				
1	CTD 33	0.00	0.00	0.00	0.00
2	CTD 6	0.30	0.28	0.27	0.28
3	CTD 1	1.44	1.42	1.33	1.40

B 2. Ranking the three CTD casts (best, good, bad) based on the mean of RMSE at three layers at the middle part of the Bay for temperature and salinity.

Middle of Bay RMSE					
	Temperature	**Surface**	**Middle**	**Bottom**	**Mean RMSE**
1	CTD 39	0.06	0.13	0.19	0.12
2	CTD 52	0.66	1.02	0.07	0.58
3	CTD 54	2.18	3.05	0.13	1.7
	Salinity				
1	CTD 51	0.02	0.04	0.07	0.04
2	CTD 41	0.20	0.32	0.34	0.28
3	CTD 44	0.40	0.56	0.58	0.51

B 3. Ranking the three CTD casts (best, good, bad) based on the mean of RMSE at three layers at the mouth part of the Bay for temperature and salinity.

Mouth of Bay RMSE					
	Temperature	**Surface**	**Middle**	**Bottom**	**Mean RMSE**
1	CTD 83	0.24	0.07	0.10	0.14
2	CTD 98	1.20	0.09	0.87	0.72
3	CTD 78	2.15	1.45	1.37	1.7
	Salinity				
1	CTD 97	0.06	0.01	0.02	0.03
2	CTD 80	0.16	0.17	0.21	0.18
3	CTD 92	0.62	0.66	0.70	0.66

Curriculum Vitae

Candidate's full name: Ahmadreza Alleosfour

Universities attended:

B.Sc., physics, Persian Gulf University, 2005

M.Sc., physical oceanography, Tarbiat Modares University, 2008

Publications:

- Misiuk B., Tan Y.L., Li M.Z., Trappenberg T., Alleosfour A., Church I.W., Ferrini V., Brown C.J., 2024. Multivariate mapping of seabed grain size parameters in the Bay of Fundy using convolutional neural networks.
- Alleosfour, A., Church, I., 2022. Hydrographic survey planning uncertainty from ocean model surface forcing, Proceeding of the Canadian Hydrographic Conference, Gatineau, Ottawa, Canada,
- Alleosfour, A., Church, I., 2020. Down-scaled oceanographic modeling in the Bay of Fundy (Canadian Technical Report of Fisheries and Aquatic Sciences No. 3395), Proceedings of the Bay of Fundy Seafloor Mapping Forum: Dartmouth, Nova Scotia, March 13, 2020. Fisheries and Oceans Canada, Bedford Institute of Oceanography,
- Alleosfour, A., Church, I., Brown, C., 2020. Modeling the Baroclinic Conditions of Bay of Fundy – FVCOM Case Study. Geomatics Atlantic, Online,
- Alleosfour, A., Church, I., 2020. Augmenting hydrographic data with high-resolution ocean modeling, Proceedings of the Canadian Hydrographic Conference, Quebec, QC, Canada.